Tabletop Fast Neutron Sources Driven by High Repetition Rate Ultrashort Laser Systems

by

Nicholas J. Peskosky

A dissertation submitted in partial fulfillment
of the requirements for the degree of
Doctor of Philosophy
(Nuclear Engineering and Radiological Sciences)
at the University of Michigan
2023

Doctoral Committee:

Professor Karl Krushelnick, Chair
Professor Almantas Galvanauskas
Professor Igor Jovanovic
Assistant Research Scientist Milos Burger
Research Scientist John Nees

Nicholas J. Peskosky

njpeskos@umich.edu

ORCID iD: 0009-0009-2296-7072

Dedicated to my mom and dad, and my loving wife Claire.

ACKNOWLEDGMENTS

The completion of this doctoral dissertation would not have been possible without the support, guidance, mentorship, and encouragement of several individuals. First and foremost, to my advisor Prof. Karl Krushelnick, thank you for guiding my curiosity within the field of plasma physics and for sponsoring my various research endeavors over these past five years. Your patience and steering were instrumental to my experimental success in our various labs. While not direct advisors, thank you to Prof. Alex Thomas and Prof. Louise Willingale for your advice, thoughtful insight and encouragement over the years. Thank you Prof. Igor Jovanovic for the liberal use of your neutron science laboratory and for your help in all things pertaining to the detection of neutrons. To Prof. Almantas Galvanauskas, thank you for trusting me to work in your fiber lab and for your many thought-provoking conversations regarding the direction of our collaboration.

To Research Scientist John Nees, whether you planned to all along or just continuously nudged me in the right direction, I can declare that I am truly a 'laser jock' today because of your countless hours of teaching, extracurricular discussion and hands-on instruction. To Research Scientist Milos Burger, your encouragement was always perfectly timed and I could not have made such quality light 'donuts' without your insight.

Thanks to my fellow High Field Science cohort members, in particular Jason Cardarelli for his constant help in unpacking theory, Stephen DiIorio for an endless supply of coffee and unmatched aid on everything computational, Brendan Stassel for his constant help through both semesters of intermediate plasma physics, and Mario Balcazar for thoughtful discussion and for lending a random high vacuum odd or end when my experiments needed it most. To my co-Krushlenick advisees Jon Murphy and Nick Ernst, thank you for helping me navigate

graduate level plasma physics as a lowly engineer! Thank you to my lambda cubed lab mates Hao Huang, Tanner Nutting, Lauren Ibon, Jinpu Lin, Xuan Xiao - it was a pleasure to work and learn from you all!

Many thanks to my collaborators in the Galvanauskas' fiber laboratory, especially Alex Rainville for his breadth of optics and photonics knowledge and passion for seeing our joint experiment become a reality, Mat Whittlesey and Yanwen Jing for the thankless job of taming system gremlins and running the pulse stackers and FPGA, and Chris Pasquale for riding along on the crazy adventure that panned out from inventing, designing, and building our GMNA fiber setup.

To my family, thank you for believing in me all these years and for helping me pursue my passion for science and engineering. Lastly and most importantly, to my wife Claire, there is nothing I can do or say that will reflect my undying gratitude for your understanding and patience, especially through the many late nights spent away from you in the laser lab.

TABLE OF CONTENTS

LIST OF FIGURES

LIST OF ABBREVIATIONS

AO Adaptive Optics

CBC Coherent Beam Combination

CPA Chirped Pulse Amplification

CPSA Chirped Pulse Stacking Amplification

DM Deformable Mirror

DPSSL Diode-Pumped Solid-State Laser

EHD Electrohydrodynamic

FROG Frequency-Resolved Optical Gating

FOM Figure-of-Merit

FWHM Full Width at Half Maximum

GA Genetic Algorithm

GMNA Gain-Managed Nonlinear Amplification

GTI Gires-Tournois Interferometer

LDNS Laser-Driven Neutron Source

LG Laguerre-Gaussian

LPA Laser-Plasma Accelerator

nTOF Neutron Time-of-Flight

OAM Orbital Angular Momentum

OAP Off-Axis Parabolic Mirror

OPCPA Optical Parametric Chirped Pulse Amplification

PIC Particle-in-Cell

PMT Photomultiplier Tube

PSD Pulse Shape Discrimination

PSP Pulse Shape Parameter

SHG Second Harmonic Generation

SPP Spiral Phase Plate

Ti:Sa Titanium doped Sapphire

TMP Turbomolecular Pump

TNSA Target Normal Sheath Acceleration

USPL Ultrashort Pulsed Laser

YDFL Ytterbium doped Fiber Laser

ABSTRACT

The interaction of high-intensity ultrashort laser pulses with matter can generate extreme acceleration gradients and localized plasma temperatures suitable for nuclear fusion. To date, experimental campaigns at various laboratories have successfully demonstrated sources of relativistic electrons, and multi-MeV ions as well as secondary radiation in the form of intense ultrashort (fs-ps) pulses of x-rays, gamma rays, relativistic positrons, and neutrons from light-matter interaction. Historically, the chirped pulse amplification (CPA) lasers capable of generating Terawatt/Petawatt (high-field) peak power density necessary to drive such laser-plasma accelerators (LPA) have been limited to repetition rates of 1-10 Hz. Recently, solid-state diode-pumped optical parametric chirped-pulse amplifiers, Y^{3+} doped thin-disk amplifiers, and large mode area fiber optic amplifiers have demonstrated unprecedented scaling toward delivery of 0.1-1 J, <100 fs laser pulses at 1-10kHz. These advances in the field of high-power laser engineering have ushered in the era of third-generation femtosecond technology (3FST) with the stated objective of delivering terawatt-scale peak power at kilowatt-scale average power. Such "TW at a kW" photonic systems are ideal for driving high-brightness tabletop fast neutron sources.

This thesis work addresses the challenge of scaling relativistic laser targets to the kHz repetition regime with specific application to ultrashort laser-driven neutron sources (LDNS). First, the design, development, and testing of a novel pulsed electrohydrodynamic (EHD) microjet nozzle is presented. Proof-of-principle experiments carried out at 0.480 kHz on the University of Michigan relativistic λ^3 laser resulted in 4×10^4 n/sec/sr isotropic yield from

laser-driven D(d,n)^{3}He fusion reactions in a 2.7 μm deuterated microjet. This fast neutron flux is confirmed via bubble dosimeters, solid-state ^{6}Li-doped microstructured semiconductor neutron detectors, ^{3}He proportional detectors, and a neutron time-of-flight (nTOF) detection scheme using pulse shape discrimination enabled and time-gated EJ-309 liquid scintillation detectors. Building upon the suite of high repetition neutron diagnostics developed for the EHD targetry campaign, an experiment exploring neutron generation from relativistic optical vortex beams is presented. Irradiation of free-flowing D_2O liquid microjets with orbital angular momentum (OAM) beams of topological charge $l = 1$ and $l = 5$ was shown to generate record D-D neutron yield in excess of 10^6 n/sec/sr. To explain this marked source enhancement, a basic particle-in-cell (PIC) computational model is constructed to validate OAM self-focusing, and subsequent filamentation due to plasma density inhomogeneity at the overdense target-vacuum boundary.

Lastly, the results from a collaborative experimental LDNS campaign utilizing a novel ultrashort fiber CPA laser based on coherent beam combination and coherent pulse stacking amplification are discussed. To the best of our knowledge, this experiment demonstrates the first high repetition (2-10 kHz) tabletop neutron source driven by an all-fiber femtosecond laser. As part of this effort, a synchronous off-color ultrashort laser backlighter was developed as a high repetition optical diagnostic. This novel probe system is capable of arbitrary femtosecond-to-millisecond delay and is based on the application of gain-managed nonlinear amplification (GMNA) in Yb-doped fibers. Proof-of-principle operation is experimentally demonstrated through time-resolved imaging of a propagating laser-driven shock front with the frequency-doubled GMNA output beam.

CHAPTER 1

Introduction

1.1 Current paradigms of neutron science

Neutrons are unique subatomic particles in that they do not have an associated electrostatic charge and can therefore freely penetrate an electron cloud and freely interact with an atomic nucleus. The neutron was first discovered by Sir James Chadwick in 1932 [17], and the importance of this discovery to the field of nuclear physics is reflected in the fact that he was awarded the 1935 Nobel Prize in Physics for his groundbreaking experimental work. The control and manipulation of the neutron ushered in the Atomic Age of human history, and its role in sustained nuclear chain reactions is principally responsible for the invention of nuclear weapons and civilian nuclear power alike. Neutron-induced transmutation of the atomic nucleus is instrumental to various scientific, industrial, and medical applications. Within the field of discovery science the detection of neutrons is a fundamental diagnostic for measuring the success of inertial and magnetic confinement fusion schemes, similarly, neutron scattering measurements provide unique insight into the structure of novel materials and intense neutron fluxes replicate the penetrating radiation fields ejected from black holes. Industrially, neutrons are used to pinpoint the location of geological petrochemical deposits, non-destructive radiographic imaging with neutrons provides a complementary technique for microscopic inspection of light nuclei materials, and many commercially relevant radionuclides are bred with intense neutron fluxes. Within the field of medicine, boron-neutron

capture therapy and diagnostic radiotherapy procedures are enabled by the engineered application of powerful neutron beams.

Common sources of neutrons span a gamut of nuclear technologies, energies, physical sizes, and available flux levels - each representing trade-offs in shielding required, complexity, portability, cost, and regulatory burden for operation. Radioisotope sources and beam-target tube generators are arguably the most widely disseminated sources because of their moderate intensity, compact footprint, and limited licensing overhead. Facility-scale sources can deliver the greatest man-made neutron fluences $\sim 10^{12-17}$ n/cm^2·s and are associated with high operational cost, specific siting restrictions, and significant operational overhead. This category of neutron sources includes accelerator beamlines, spallation sources, fusion confinement devices, Z-pinch and dense plasma focus experiments, and conventional critical and subcritical fission reactors. As a type of pulsed generator, laser-driven neutron sources (LDNS) have historically blurred the line between tabletop and building-sized systems. Recent advances in the front-end photonic drivers and back-end target generation schemes are simultaneously shrinking the physical size of laser-based sources while exponentially increasing source brightness and up-time availability. A review of the historic scientific advances that have made this paradigm shift possible is given below to frame the motivation for this thesis work.

The first working laser was demonstrated in 1960 [18] and almost immediately these new 'tools of light' were recognized as a means to create energetic plasmas. As early as 1961, a team of scientists under John Nuckolls surmised that lasers were an ideal candidate for the indirect initiation of inertial confinement fusion because of their ability to concentrate extremely large quantities of energy in both time and space. [19] Following a public demonstration at the World's Fair in 1965, the U.S. Atomic Energy Commission (known later as the Department of Energy) began what has now been a multi-decade campaign to achieve break-even terrestrial thermonuclear fusion driven by high-intensity lasers. A parallel effort under Nikolai Basov's scientific leadership in then Soviet Russia was ultimately credited with

the first demonstration of achieving a single detectable D-D fusion neutron event in 1968 by irradiation of LiD with ∼20J picosecond laser pulses from a Nd:Glass laser [20]. Continued research in laser science over the next two decades saw the invention of Q-switching and mode-locking, techniques that further increased the peak power of lasers past the regime of non-linear optics and to the threshold of perturbing atomic potentials. Continued experiments across the globe with multi-beam laser systems and various forms of cryogenic D_2 resulted in fast neutron yields exceeding the 10^6 n/shot/sr in the mid-1970s. Although these efforts were made in hopes of practical realization of direct drive fusion hypothesized by Nuckolls *et al.* [21], they ultimately set the stage for laser-driven tabletop neutron generation by a new breed of high-intensity lasers with ultrashort pulse durations.

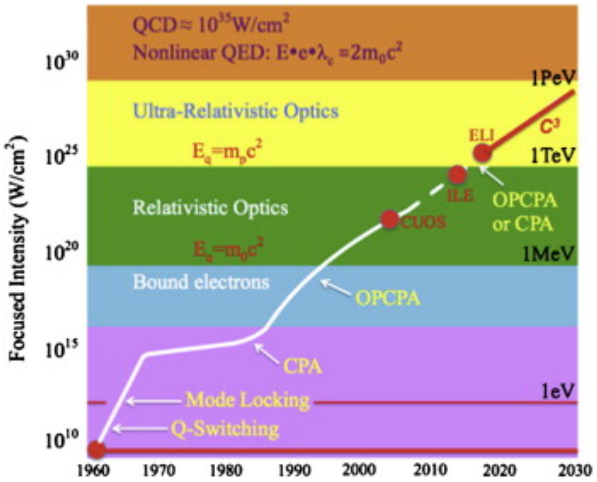

Figure 1.1: Historical scaling of the peak focused optical intensity achievable with lasers. Used from Ref. [1] with permission.

The groundbreaking work by Mourou and Strickland in 1985 [22] on so-called Chirped Pulse Amplification (CPA) ushered a new era of laser science capable of synthesizing femtosecond (10^{-15} second) duration laser pulses. Applying this technique, relativistic optical intensities (and now supra-relativistic) shown in Figure 1.1 were for the first time practically realized in the laboratory environment. Coupled with the demonstration of broadband lasing in the solid-state gain material Ti:Sapphire (Ti^{3+}:Al_2O_3) by Peter Moulton in 1986 [23] and passive Kerr-lens mode locking of a Ti:Sapphire (Ti:Sa) oscillator in 1994 [24, 25], moderate

repetition rated CPA laser systems became ubiquitous workhorses of the university scale laser laboratory. Coupled with the proliferation of CPA lasers, researchers across the globe rapidly demonstrated new ion acceleration mechanisms suitable for driving bright secondary radiation sources.

1.2 Trends in second-generation high-power ultrashort lasers

Traditionally, the practical engineering of Ultrashort Pulsed Lasers (USPLs) has resulted in a functional schism in the availability of compressed pulse energy and repetition rate at which such fs pulses may be generated. From a technical standpoint, this categorical division is a result of: (1) the finite spectral gain bandwidth associated with different laser gain media (2) the availability and repetition rate of suitably intense in-band pump sources, (3) host material thermal birefringence resulting in undesired resonator lensing at high average powers, (4) the finite damage threshold of gain media and relay optics, (5) the undesirable nonlinear optical processes resulting from high intracavity fluence, and (6) thermal engineering limitations due to heat removal from the quantum defect of active optical elements comprising the laser system.

As a canonical representation for large aperture solid-state amplifier-based systems, Ti:Sa CPA lasers now regularly achieve multi-petawatt peak output powers but with repetition rates largely limited to $\leq$ 10 Hz. Currently fielded systems are rate limited by the stringent pump requirement placed by the short (3.6 μs) upper-state lifetime of the Ti^{3+} ion. Further, all practical pump sources in the λ = 450-540 nm peak absorption band of Ti:Sa are frequency doubled solid-state lasers with nanosecond pulse durations. Joule-class pump lasers of this type are usually flash-lamp pumped, and true system repetition limits are a product of both amplifier thermal recovery time and pulsed power charge cycling. Diode-pumped solid-state lasers (DPSSL) providing mJ-class operation fare slightly better and are capable of scaling to

multi-kHz operation but with peak pump pulse energies of (∼120 mJ). Coupled with suitable cryogenic cooling, CPA architectures pumped with DPSSL technology can achieve TW peak power at kHz repetition rates. By definition, this makes any USPL based on Ti:Sapphire (or any other indirectly pumped gain media) an *indirect CPA* architecture. Correspondingly, the moderate quantum defect associated with green-blue Ti:Sa pulsed optical pumping results in considerable parasitic amplifier thermal load. Ultimately, this limits the average system output power to no more than a few hundred watts.

In contrast, rare earth-doped glass architectures routinely boast 0.01-100 MHz repetition rates but with compressed pulse energies in the μJ-mJ range. As a consequence of narrower gain bandwidth, transform-limited pulses in the infrared (IR) are $\sim$ 100 fs in duration or longer, yielding effective peak powers typically of a few GW. Yb^{3+}-doped glass fiber lasers exemplify *direct CPA* architectures because the upper state lifetime is of order 1-2 ms and continuous wave (CW) pumping is therefore achievable with widely available NIR telecommunications grade laser diodes. The scalability of fiber systems with multiple parallel amplifier channels and the possibility of all-fiber photonic integration make fiber-based lasers an attractive alternative to solid-state CPA lasers for mobile or aerospace applications. Fiber amplifiers also benefit from a large surface area to thermal mass which allows for heat management by simple liquid-cooled heat exchangers. At present, further scaling of energy extraction from active fiber lasers is primarily limited by complex trade-offs in mode field diameter (MFD). The extractable pulse energy from fiber amplifiers scales proportionally with the diameter of the active fiber but there are finite limits on this scaling. Ultimately these are imposed by the optical necessity of maintaining single-mode operation to preserve output beam quality and volume-to-surface-area ratios required for sufficient thermal extraction under heat load. Furthermore, the long interaction lengths suitable for gain extraction from Yb-doped fiber amplifiers (YDFAs) are ultimately clamped by detrimental effects of nonlinear phase accumulation by propagating pulses. Taken together, these design parameters place upper limits on total pulse energy extracted from such fiber lasers. To date, stan-

dalone single-channel ultrashort fiber systems have not demonstrated parity with solid-state architectures in delivering kHz pulses with on-target relativistic intensity.

1.3 Towards third-generation femtosecond technologies

Note that Ti:Sa lasers and YDFLs are not the only candidates for high-intensity ultrashort pulse lasers. Their introduction serves to highlight many of the representative limitations of laboratory-fielded solid-state and fiber technologies categorically labeled second-generation femtosecond technology (2FST) [26]. Contemporary research trends have therefore focused on technology hybridization techniques as a route toward continued scaling of high-peak and high-average power ultrashort photonic systems. The primary objective of third-generation femtosecond technology (3FST) is to deliver terawatt-scale peak powers with kilowatt-scale average powers [26]. When physically realized, these systems will usher in a new era of laser-plasma acceleration schemes in the relativistic and ultra-relativistic regimes.

In the context of bolstering system average power output, researchers have focused on developing advanced solid-state amplifier designs which incorporate gain media with larger surface area and improved volumetric thermal management. Leading this effort are investigations of slab and thin-disk amplifiers based on diode-bar-pumped Yb:YAG and Yb:CaF_2. Originally developed for high-throughput materials microprocessing applications, Yb:YAG thin-disk technology was recently scaled to multi-kW power levels and its suitability for ultrashort use was revisited.

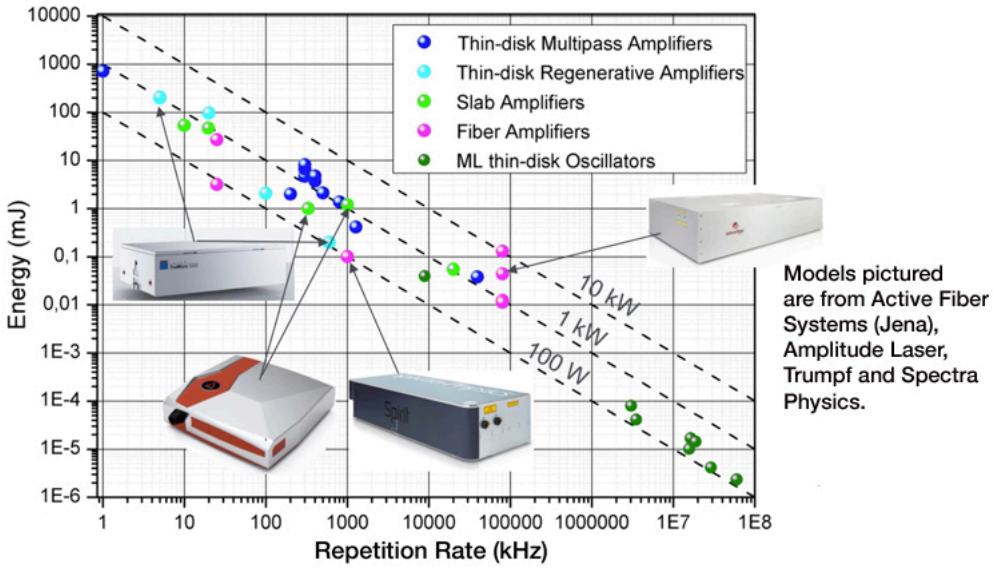

Figure 1.2: Scaling data for the attainable pulse energy versus repetition rate for various advanced multi-kHz ultrashort laser architectures. [2]

To further reduce nonlinear phase effects in active fibers, researchers have looked to implement fiber chirped-pulse amplification (FPCA) schemes using photonic band-gap fibers, chirally coupled core (CCC) fibers, and photonic crystal rod amplifiers. These large MFD active fibers can further bolster total system output through massive parallelization in laser architectures utilizing modular amplifiers and coherent pulse combination techniques [27, 28]. Recently, coherent pulse stacking amplification (CPSA) has been demonstrated as a promising technique to further scale fiber optic lasers toward 3FST design targets [29].

Compression-after-compressor (CafC) [30] has emerged as a pulse compression scheme that can further enhance the peak power of virtually all high-repetition ultrashort systems. Whether executed with gas-filled hollow-core fibers or multi-pass cells [31], nonlinear plate cells [32, 33], or filaments [34, 35], the CafC technique utilizes photoionization or Kerr-nonlinearities to spectrally broaden a moderate intensity pulse. If specific care is taken to manage both the sign and magnitude of the imparted residual pulse chirp, dispersion management (i.e., prisms, double-chirped mirrors, gratings, bulk optical materials) techniques may be employed to compress the ultra-broadband output. This promising technique

has been shown to generate octave spanning spectral content, kHz multi-millijoule level pulses, and 10-30x pulse compression resulting in few or even single-cycle optical pulses with correspondingly extreme peak power (multi-TW) [31, 36].

Together, these technologies provide a viable path toward the realization of a USPL system capable of delivering 100 mJ / 100 fs / 10 kHz laser pulses, colloquially known as a 'terawatt at a kilowatt' [26]. This would represent a convergence of both high-peak and high-average laser power; dual requisites for LPA-based sources with application-rated radiation fluxes. Near-term scientific and industrial availability of such high-repetition drivers establishes a demand signal for suitable plasma target systems. To date, this has proved technically daunting for a multitude of reasons.

1.4 Current limitations of repetition-rated high energy density science

Obstacles to fielding kHz rep-rated laser targets for high energy density science (HEDS) applications have been compiled in several recent review works and strategic working groups [37, 38]. These works primarily focus on target systems for PW-scale 1-10 Hz Ti:Sa lasers installed at the European Extreme Light Infrastructure (ELI), Berkeley National Laboratory (BELLA), Gemini Laser Facility (UK), Apollon (France), and many others. To frame the complexity of the targetry problem, consider that using these systems as a representative lower bound, 3,600-36,000 targets would need to be synthesized, characterized, aligned, and shot per a single hour of experimentation. Now consider, a 3FST USPL driver system operating at 1-10 kHz, this would further increase on-target shot rates by a factor of 10^{2-3}, indeed a technically rigorous demand on vacuum systems, target positioning, online diagnostics data acquisition, and mean-time-to-failure (MTTF) of target generation systems. Target needs are predominantly dictated by the physics under investigation and fall into three broad categories : (1) targets for dynamic compression physics, (2) targets for electron transport

and isochoric heating studies, and (3) targets for laser-driven particle and secondary radiation sources [37]. kHz-repetition deuterated targets for tabletop, laser-driven neutron source (LDNS) applications were the primary focus of this thesis work, and a brief motivation for their development is now discussed.

With rare exception [39, 40], intense laser-plasma interaction experiments are usually conducted under vacuum conditions. As discussed further in Chapter 1, intensity-induced beam self-focusing can lead to catastrophic wavefront distortion or beam collapse when TW-class ultrashort pulses are propagated at atmospheric conditions. Additionally, many diagnostics contain high voltage elements necessary for electrostatic particle deflection, and pressure-induced electrostatic breakdown along with particle transport concerns further constrain acceptable target chamber pressure levels. Together these considerations necessitate the execution of experiments in technical vacuum ($\leq 10^{-3}$ mBar) environments. Therefore, the vapor pressure and atomic/molecular content of fielded target materials are highly scrutinized at most experimental facilities. Practically, non-volatile metallic (LiD) [41, 42] and plastic thin films ($C_xD_xO_x$) are a natural choice for ion acceleration via the target normal sheath acceleration (TNSA) mechanism [43–46], and super-cooled deuterated (D_2, CD_4) gas clusters or cryogenic ribbons have been fielded for thermonuclear neutron yield via Coulomb explosion [47–50].

While gas target systems are capable of delivering high-purity species for laser acceleration, the added pumping load can be extreme. Most setups are limited to <5 Hz and require turbomolecular or LN_2 cold-trap systems with $> 10^4$ L/s pumping speeds in the molecular flow regime. This auxiliary system requirement all but eliminates the likelihood of developing a field portable LDNS based on this target generation mechanism. Solid phase targets consisting of foils, foams, nanoarrays, and bulk discs do not outgas at appreciable levels and generate minimal vacuum load when irradiated. Repetition-rated versions of these targets include rotating platter/disc targets [51], tape drives [52, 53] and multi-cell arrays [54]. The full-width half-maximum (FWHM) beam diameters necessary to achieve $\geq 10^{18}$ W/cm^2 in-

tensities associated with relativistic plasma dynamics are a few μm for most advanced 2FST USPL systems, with corresponding Rayleigh ranges of the same spatial order-of-magnitude. Therefore, the mechanical latency of successive target positioning and the alignment tolerance of target surfaces to the incident driver beam dominate the limiting factors for kHz scaling of repetition-rated solid targets. To maintain acceptable positioning error, X-Y arrays of targets coupled with advanced stepper motors have not been demonstrated above 1 Hz [54], Gatling-style targets are limited to 0.2 Hz [51], and tape drives 100 Hz [53]. Rotating disc targets have seen success when used in kHz generation of bremsstrahlung and K_α X-ray sources but their lifetime is relatively short. In most cases, the fresh target material is exhausted in $\sim 10^4$ seconds [55]. For proposed 3FST systems with laser energies in excess of 1J, target fratricide, and debris generation must also be considered [37]. None of the aforementioned targetry schemes provide a useful means of addressing nearby target damage or contamination from preceding shots without reducing the shot repetition rate or increasing spatial offset from the previous target volume. The summed penalty of these actions yields reduced average source flux in neutron generation applications and reduced effective target lifetime. In this context, an effective target lifetime is the elapsed time before the vacuum regime must be broken and the target assembly and material replaced in its entirety.

Liquid phase targets provide a unique solution to many of the above challenges and, to this author's knowledge are the only target system thus far experimentally implemented for kHz repetition ion acceleration and neutron production under continuous operation ($\geq$ 3600 s). Liquid targets include droplets, jets, leaves/sheets, vapors, and liquid crystal films. At present, all but the last two paradigms have been successfully demonstrated at kHz-capable repetition rates. When considering the vapor load imparted by liquids, a judicious selection of the liquid composition (glycerine, glycol, hydrocarbon oils) can ensure excellent vacuum compatibility with simple deferentially-pumped recovery wells. In terms of positional reliability, sub-micron jitter was reported for piezo-emitted droplets [56] and liquid leaf targets formed by impinging two high-velocity streams [57]. Targets made of liquid are consumable

and when ejected with the proper velocity ∼10-20 m/s are resilient to fratricide. As an added benefit of the fluid state, the collection of unused target material through condensation or pooling allows unused material to be recovered and recirculated. Fine mist targets (0.1-5 μm) and droplet targets (5-10 μm) also fall into a unique class of mass-limited targets. Lack of electron distribution coupling to the adjacent target material, stalks, or holders means that efficient laser energy deposition into these targets can result in highly efficient volumetric heating mechanisms. Enhancement of the fusion cross section from such bulk heating was originally shown with particle-in-cell (PIC) computational simulations and later confirmed in real-life experiments [58]. Further, fast neutron generation at moderate fluxes has been shown from ultrashort laser irradiation of droplets [56, 59] and free-flowing jets [40] consisting of liquid deuterium oxide. Recently multi-MeV deuteron acceleration from D_2O sheets was shown with the addition of a suitable Be or Li converter to deliver up to an estimated 1×10^{11} n/cm^2/s [60].

1.5 Tabletop neutron sources based on laser-irradiated microscale liquid targets

As a tabletop-scale source of fast neutrons (epithermal or thermal when used in conjunction with a correctly designed moderator), laser-driven neutron sources (LDNS) exhibit the following advantageous characteristics: (1) sub-ns pulse duration with excellent timing fidelity, (2) sub-mm source size, (3) time-averaged fluxes rivaling accelerator and spallation facilities, (4) on-demand yield, and (5) and intrinsic proliferation safety. Such sources have already proven useful in prompt gamma neutron activation analysis (PGNAA) [54, 61] and with increased time-averaged flux could revolutionize radiographic nondestructive testing (NDT) of low-Z materials. Neutron imaging and tomography are highly sought after for the characterization of advanced high-density composite batteries, hydrogen fuel cells, and aerospace additive manufacturing. Figure 1.3 exemplifies how such imaging techniques could serve as

an excellent complement to commercially mature gamma and x-ray imaging.

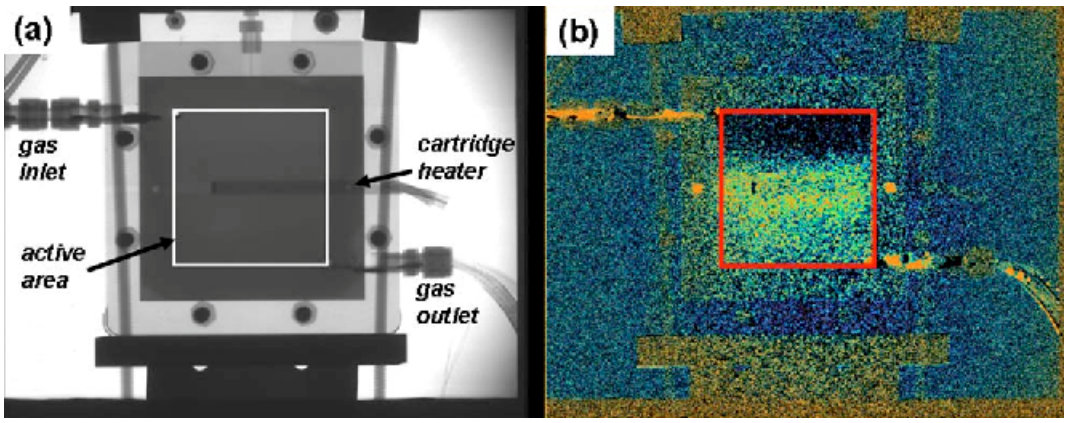

Figure 1.3: Neutron radiographs of a proton exchange membrane fuel cell under active operation showing (a) high contrast grayscale image of the device layout and subcomponents, and (b) colorized thermal neutron absorption corresponding to increased (yellow-orange) presence of liquid water on the membrane electrode assembly. Figure from Ref. [3] used with permission.

Irradiation of microscale liquid jets at 0.480 kHz by Hah *et al.* [40] was previously shown to deliver 2×10^5 n/sec/sr from D-D fusion. Similar work at the Air Force Research Laboratory utilizing free-flowing micron sheets by Morrison *et al.* [57] demonstrated acceleration to >2 MeV per nucleon ion energies at 1 kHz in the readily obtainable rough-vacuum (0.035-8 torr) regime. These and similar work by various other high-field science researchers have shown the powerful scalability of microfluidic targets for laser plasma ion acceleration and by extension, neutron generation.

Continued advances in 3FST photonic sources will soon realize compact (room-sized) systems capable of delivering relativistic laser pulses with unprecedented intensity and average power. Harnessing these photonic drivers to create efficient secondary radiation sources would truly represent a technological paradigm shift but comes with significant challenges. Historically fielded thin foil target systems for LDNS applications are ill-suited to scale to the kHz repetition regime.

The experimental work performed during this thesis work serves to further bridge the divide between emerging advanced 2FST and 3FST drivers and repetition-rated targets.

Investigation of novel target extraction methods, irradiation dynamics, and driver coupling was undertaken with the primary goal of scaling TW-class LDNS isotropic flux by an order of magnitude to $\sim 1 \times 10^6$ n/sec/sr. Successful integration of a 3FST photonic driver with the kHz-repetition microscale liquid targets developed throughout this work would provide a viable pathway toward further source scaling by an estimated factor of 10^{2-3}. The practical realization of a tabletop ultrashort pulsed laser-driven high-brightness and high-average flux neutron source rivaling capabilities of a sealed tube D-T generator would have far-reaching commercial, industrial, scientific, and national security implications.

1.6 Dissertation outline

This thesis details the design, engineering, and experimental testing of various advanced high-repetition liquid target modalities suitable for laser-based generation of scalable, pulsed fluxes of fast neutrons at tabletop scales. The target schemes described herein were tested on multi-mJ 0.48 kHz 2-10 kHz laser systems based on Ti:Sapphire and Yb-doped glass fiber gain media, respectively. The content of this dissertation is organized as follows:

- Chapter II provides a theoretical groundwork for the ultrashort laser physics, nonlinear optics, and plasma physics that were integral to this thesis work. Schemes for generating intense femtosecond laser pulses are discussed, this is followed by a succinct primer for mechanisms by which these intense pulses may initiate and subsequently heat plasmas. Lastly, various laser ion acceleration mechanisms are introduced and their relevance to ion acceleration and nuclear fusion is explored.

- Chapter III details the laser systems used during the experimental campaigns of this thesis work and methods for controlling and characterizing their femtosecond output pulses. This chapter also delves into the suite of radiation diagnostics which were utilized to measure neutron, x-ray, and γ-rays generated from the laser-plasma interactions. Chap. III also discusses adaptive optics and associated optimization algorithms.

- Chapter IV describes the iterative development of a mass-limited, spatiotemporally synchronized, electrohydrodynamic liquid microjet target. Proof-of-concept relativistic irradiation of mixtures containing D_2O and deuterated ethylene glycol resulted in a quasi-monoenergetic D-D neutron characterized via neutron time-of-flight. Flux scaling with pulse energies and maximum target repetition rate are analyzed.

- Chapter V covers experiments performed with near-relativistic optical vortex beams incident at grazing versus incidence on microscale free-flowing D_2O jets. Marked enhancement of fast neutron yield is shown for tuning of the transverse beam position. Methods of optimizing OAM beams used in tight-focusing geometries are covered and the basic theory for OAM-enhanced target heating is extrapolated from empirical data and computational simulations.

- Chapter VI captures all work pertaining to a collaborative experimental campaign where liquid targets were used to generate the first laser-based fusion reactions with a high-intensity kHz-repetition rate ultrashort fiber drive laser. Parallel work with a nonlinear fiber system resulting in a synchronous off-color ultrashort plasma backlighter is presented. Operation of the backlighting system is demonstrated through proof-of-principle time-resolved imaging of hydrodynamic shocks.

- Chapter VII summarizes the key results from the novel work performed during this thesis work and provides insight on how future work could incorporate elements from each thesis chapter to realize a tabletop high-brightness fast neutron source capable of sustained $>10^7$ n/s/sr isotropic flux.

CHAPTER 2

Theoretical Background

2.1 Ultrashort laser physics

As previously mentioned, CPA and OPCPA photonic architectures are a fundamental prerequisite for realizing the high-intensity pulsed laser drivers used in plasma-based acceleration schemes. It is essential to buttress the importance of these technologies by now introducing relevant nonlinear optical theory. The detrimental effects of non-linear phase accumulation and self-focusing formulate the design basis for amplifying optical pulses without causing catastrophic damage to laser gain material, as was typical prior to the application of optical chirping [22].

2.1.1 Nonlinear Optics

Ultrashort pulsed laser light is a form of electromagnetic radiation. It is useful to therefore to briefly review Maxwell's equations, as this concise set of relationships completely characterizes the interplay between the electric field **E** and magnetic field **H**:

$$\nabla \cdot \mathbf{D} = \rho \tag{2.1}$$

$$\nabla \cdot \mathbf{B} = 0 \tag{2.2}$$

$$\nabla \times \mathbf{E} = -\frac{\partial \mathbf{B}}{\partial t} \tag{2.3}$$

$$\nabla \times \mathbf{H} = \mathbf{J} + \frac{\partial \mathbf{D}}{\partial t} \tag{2.4}$$

where ρ is charge density, $\mathbf{J}$ is current density, and the constants ϵ_0 and μ_0 are the permittivity and permeability of free space respectively. The displacement field $\mathbf{D}$ is defined as:

$$\mathbf{D} = \epsilon_0 \mathbf{E} + \mathbf{P} \tag{2.5}$$

and the magnetic field $\mathbf{B}$ is defined as:

$$\mathbf{B} = \mu_0(\mathbf{H} + \mathbf{M}) \tag{2.6}$$

with polarization field $\mathbf{P}$ and magnetization field $\mathbf{M}$ in their usual form. The wave equation for light is derived by taking the curl of the Maxwell-Faraday equation (Eq. 2.3, invoking Ampere's law (Eq. 2.4 and simultaneously applying the below vector identity:

$$\nabla \times \nabla \times \mathbf{E} = \nabla(\nabla \cdot \mathbf{E}) - \nabla^2 \mathbf{E} = -\mu_0 \epsilon_0 \frac{\partial^2 \mathbf{E}}{\partial t^2} \tag{2.7}$$

Considering the source free case ($\rho = 0$) we arrive at the free space wave equation presented in its usual form:

$$-\nabla^2 \mathbf{E} + \mu_0 \frac{\partial^2 \mathbf{D}}{\partial t^2} = 0 \tag{2.8}$$

In a dielectric medium, the presence of a propagating EM wave will result in a modification to the local dipole moment. Considering an isotropic and source-free medium, the relationship between polarization density and the electric field is $\mathbf{P} = \epsilon_0 \chi \mathbf{E}$, where χ is the

electric susceptibility. Typical light-matter in the linear regime exhibits polarization which is directly proportional to the applied field and the resulting electronic response follows closely that of a harmonic oscillator model. Highly focused continuous wave (CW) or pulsed laser light generates optical intensities where the effects of higher-order susceptibilities may no longer be ignored. Through Taylor expansion, the polarization field can be re-written

$$\mathbf{P} = \epsilon_0[\chi^{(1)}\mathbf{E} + \chi^{(2)}\mathbf{E}^2 + \chi^{(3)}\mathbf{E}^3 + \dots] \tag{2.9}$$

The appearance of $\chi^{(n)}$ terms are referred to as n-th order susceptibilities and are associated with a wide range of nonlinear optical phenomena. Regularly $\chi^{(1)} \gg \chi^{(2)} \gg \chi^{(3)}$ and accordingly the higher order effects will be negligibly expressed unless the optical field strength is very high. As in [62], basic expansion of the polarization gives a linear and nonlinear component, with the latter added as a source term to the generalized wave equation (Eq. 2.8) to yield:

$$\nabla^2\mathbf{E} - \mu_0\epsilon_{(1)}\frac{\partial^2\mathbf{E}}{\partial t^2} = \mu_0\frac{\partial^2\mathbf{P}_{\mathrm{NL}}}{\partial t^2} \tag{2.10}$$

Thus the nonlinear polarization density can be treated as a source term for wave mixing within linear media with refractive index n, with relation $n^2 = 1 + \chi$ and $c = 1/(\epsilon_0\mu_0)^{1/2}$.

Second harmonic generation (SHG) is a $\chi^{(2)}$ effect which was particularly important to many aspects of this work. This special case of three-wave mixing occurs when $\omega = \omega_1 = \omega_2$ and $\omega_3 = 2\omega$ in non-isotropic media. Considering an applied electric field $E = E_0\sin(\omega t)$ the induced polarization takes the form:

$$\mathbf{P} = \epsilon_0[\chi^{(1)}\mathbf{E}\sin(\omega t) + \chi^{(2)}\mathbf{E}^2\sin^2(\omega t) + \dots], \tag{2.11}$$

which using trigonometric identities may be rewritten as

$$\mathbf{P} = \epsilon_0[\chi^{(1)}\mathbf{E}\sin(\omega t) + \frac{1}{2}\chi^{(2)}\mathbf{E}^2(1 - \cos 2\omega t) + \dots], \tag{2.12}$$

where in the second term we see a wave oscillating at twice frequency of the fundamental laser field. Pulsed SHG processes are integral to the operation of frequency doubled Nd:YLF and Nd:YAG lasers which are the primary pump sources for Ti:Sa power amplifiers. Additionally, SHG plays an important role in ultrashort optical pulse measurement via autocorrelation or frequency resolved optical gating, both covered in the methods section of this thesis.

The optical Kerr effect is a third-order $\chi^{(3)}$ nonlinearity that drives an intensity-dependent refractive index in dielectric materials. In the standard four wave picture, where $\omega_4 = \omega_3 + \omega_2 + \omega_1$ we consider the case where $\omega_2 = -\omega_1$. Once again expanding the induced polarization it can be shown that

$$\mathbf{P} = [\chi^{(3)}\mathbf{E}^{\mathbf{2}}_{\text{avg}}]\mathbf{E}(\omega), \tag{2.13}$$

where $\mathbf{E}_{\text{avg}}$ is the average electric field strength, and $\chi^{(3)}$ is a rank-four tensor describing the effect of intensity on beam propagation through the optical medium. Taylor expanding the effective refractive index, we obtain $n \approx n_0 + n_2 \cdot I$. From Eq. 2.13, in the limit that $\chi^{(3)}\mathbf{E}^{\mathbf{2}}_{\text{avg}} \ll \chi^{(1)}$, we obtain the relationship between the nonlinear index of refraction n_2 and the nonlinear susceptibility

$$n_2 = \frac{1}{2}\frac{\chi^{(3)}}{n_0^2}\sqrt{\frac{\mu_0}{\epsilon_0}} \tag{2.14}$$

This intensity-dependent refractive index is responsible for self-phase modulation and self-focusing in high-power laser beams. Applied under appropriate conditions, these effects can be beneficial - such is the case in femtosecond Kerr-lens mode locked oscillators. Experimentally, more often these effects correspond to aberrated beam focusing due to spontaneous beam collapse prior to the geometric focus or bulk optical material damage by filament-induced avalanche breakdown.

2.1.2 Nonlinear phase accumulation

Total nonlinear phase accumulation across all passive and active optical media in high-power ultrashort lasers is a fundamental system parameter that ultimately limits output compressibility and total power extracted from amplification stages. In the previous subsection, we showed that third-order susceptibility is linked to changes in the refractive index along the propagation path of an intense beam. Two nonlinear optical terms are used interchangeably in the literature, and the conversion between n_2 and γ is:

$$\gamma[\mathrm{cm}^2/\mathrm{W}] = 4.19 \times 10^{-3} \frac{n_2}{n_0} \qquad [\mathrm{esu}] \quad (2.15)$$

Small-scale self-focusing within a USPL beam grows exponentially with propagation distance. Estimation of maximal ripple growth in a non-uniform beam profile from total nonlinear phase accumulation along the beam path is approximated by the "B-integral":

$$B = \frac{2\pi}{\lambda_0} \int \gamma I(z) dz \quad (2.16)$$

For a typical laser amplifier stage, empirical best practice dictates that $B \leq 2$ ensures control of unacceptable noise ripple growth within the beam spatial profile [62]. Further suppression of self-focusing is achieved by injection seeding with single longitudinal mode oscillators, incorporation of inter-stage vacuum spatial filters, and reduction of peak power in femtosecond systems by application of chirped pulse amplification [63].

2.1.3 Chirped pulse amplification

By the mid-1980s, broadband organic dye lasers were routinely generating trains of sub-100 femtosecond duration laser pulses via colliding pulse mode locking. Attempts at further amplifying pulses sourced from these oscillators proved unsuccessful because the beam intensities generated during power amplification were sufficient for self-focusing resulting in catastrophic damage to the gain media. To overcome this obstacle, a technique referred to

as pulse *chirping* was extended from the microwave to the optical frequency domain. By definition, chirp refers to the time dependence of the instantaneous frequency within a pulse envelope. In practical terms, the spectral content of the light is chromatically dispersed in time, when redder light precedes the blue - the pulse is said to be *positively chirped* or up-chirped. It follows that the reverse case applies for *negatively chirped* or down-chirped pulses. The shortest possible pulses for a given pulse spectrum are realized in the "no-chirp" or Fourier transform-limited case:

$$\Delta\omega \cdot \tau_{\text{pulse}} \geq 2\pi C_B \tag{2.17}$$

where $\Delta\omega$ is spectral bandwidth, τ_{pulse} is the pulse duration, and C_B is a proportionality constant associated with the pulse's temporal shape - 0.441 for the typical Gaussian pulse. Thus far, it has been stated that broadband pulses are required for femtosecond pulse generation and the implications of this nuance are clear from Eq. 2.17.

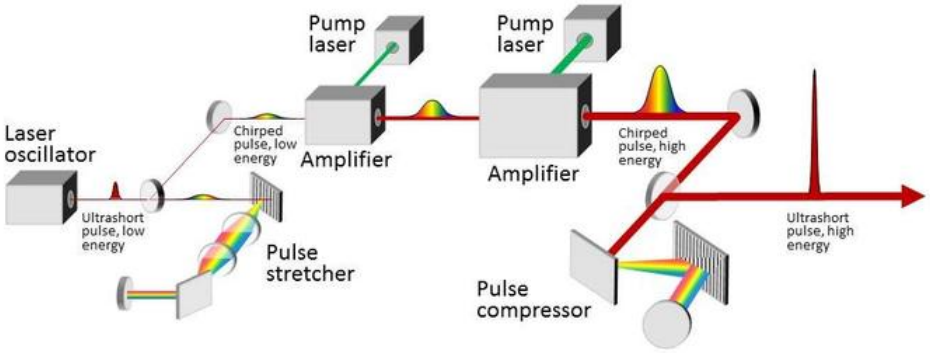

Figure 2.1: A typical schematic for solid-state CPA laser system including a master oscillator and power amplifier configuration. Figure from [4] used with permission.

As shown in Figure 2.1, a typical CPA system is comprised of: (1) a mode locked ultrashort laser oscillator, (2) a dispersive pulse stretcher, (3) laser amplifiers, and (4) a dispersive pulse compressor. Not pictured in this rudimentary system diagram but instrumental in modern system design are pulse-picking elements, active or passive spectral filters, and beam-shaping optics (i.e., collimators and telescopes).

Broadband seed pulses for a CPA laser are generated in a mode-locked laser oscillator. Cavity repetition rates usually span from 10-1000 MHz and result in a train of ∼nJ pulses with broadband spectral content. In both solid-state and fiber gain media, the shortest pulse durations are achieved by passive mode locking mechanisms which initiate self-sustaining Kerr-lensing [24] in dispersion-compensated cavities. Front-end oscillators are also tasked with synthesizing low-jitter electronic timing signals that play a key role in injection seeding, pulse dumping, pump laser Q-switching, and subsequent electronic triggering of experimental diagnostics.

Key to the CPA technique, and prior to subsequent high-power amplification, ultrashort seed pulses must pass through a dispersive stretcher. To obtain 10^3 - 10^5 pulse broadening necessary for TW-class USPLs, a diffraction grating pair is generally employed in an Offner or Martinez stretcher configuration [64, 65]. By tuning the separation and incidence angle of the grating(s), an engineered second and third-order phase is applied to the frequency components of the pulse spectrum - temporally this results in chromatic dispersion. Temporal broadening tied to this dispersion substantially reduces the peak power of stretched laser pulses and allows for subsequent amplification below the nonlinear damage threshold of high-power laser amplifiers. Within integrated photonic fiber systems, specifically tailored chirped volume Bragg gratings may also be used in lieu of free-space gratings, further enhancing system environmental stability [66].

Amplifier designs incorporated into CPA laser systems are often characterized by their optical geometry and the number of passes required for the stretched pulse to achieve the desired gain. Single-pass power amplifiers are common in RE-doped fiber systems because highly efficient gain can be achieved over active fiber lengths of only a few meters. Typical RE active ions used in such amplifiers are efficiently CW pumped with NIR diodes and direct fiber integration of pump sources is commonplace. Large mode area active fiber amplifiers routinely exhibit small-signal gain of $\geq$ 30-40 dB, are compact when wound on a mandrel, and are capable of multi-mJ pulse energies. The long interaction length and small mode

field associated with fiber geometries favor the onset of detrimental nonlinear phenomena for modest pulse energies compared to solid-state gain media. Divided pulse amplification [67], spatial and spectral beam combining [68], and pulse stacking amplification [69,70] techniques have been applied with some success to multiplex fiber systems and scale toward LPA relevant intensities with high average power.

Thermal, mechanical, and growth considerations place fundamental limits on the longitudinal and transverse size of optical-grade solid-state gain media. Spatial constraints imposed by these smaller rod, slab or thin-disk geometries dictate that stretched pulses must traverse the pumped area of amplifier media many times for proper extraction of the saturated energy. Such a multi-pass amplifier design is shown in Figure 2.2:

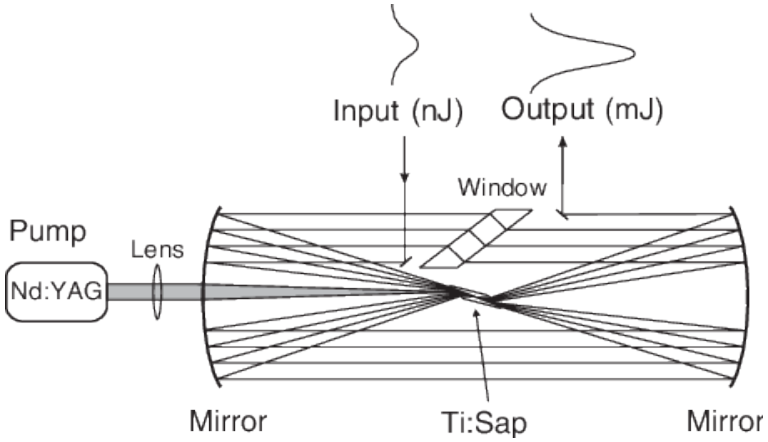

Figure 2.2: Schematic of a concentric ring style Ti:Sa multipass amplifier. Diagram from Ref. [5] used with permission.

Each pass through the saturated region of the amplifying medium is geometrically offset in a multipass configuration, a factor that limits the total achievable number of gain passes to 2-10 [71]. For this reason, multipass amplifiers are best suited for cases where input pulse energies are comparable to the saturation fluence of the gain media, especially in PW-class CPA systems. The use of slightly diverging beams within the pass geometry can aid in mitigating thermal lensing effects seen at high-average pump powers expected in kHz repetition systems. Additional benefits of this amplifier layout include reduced group velocity

dispersion (GVD) compared to regenerative amplifiers and superior pulse pedestal contrast due to suppression of amplified spontaneous emission (ASE) within the pulse pedestal.

A regenerative amplifier or "regen", is a special type of multi-pass amplifier where polarization gating is used to trap pulses within a ring-type resonator cavity. Figure 2.3 details a widely employed Ti:Sa regen design utilizing an electro-optic element known as a Pockels cell (PC).

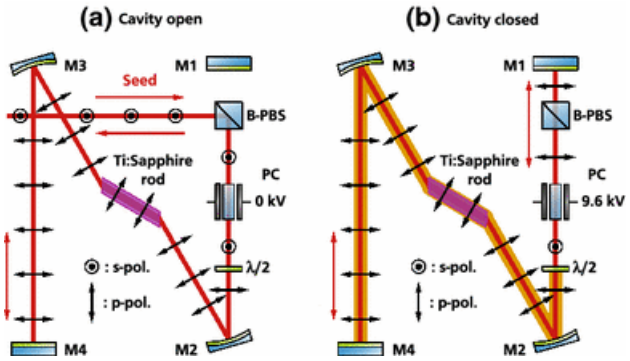

Figure 2.3: A Ti:Sa regenerative amplifier in the (a) cavity open configuration - used for seed injection and amplified pulse dumping; (b) cavity closed configuration - pulses are amplified continuously on every cavity round-trip. Figure adapted from Ref. [6] with permission.

S-polarized seed pulses are injected into the cavity by means of a properly configured thin film polarizer or polarizing beam-splitting prism. If deactivated, the pulse passes unchanged through the PC, and the remaining cavity elements ultimately arriving at the injection optic with their original polarization and is dumped. When coupled with an intracavity quarter-wave plate (QWP) or half-wave plate (HWP) the high-voltage biased PC negates polarization rotation imparted by the wave plates and P-polarized pulses become within the amplifying cavity. In this way, pulses undergo multiple round-trips within the regen, usually resulting in 50-60 dB signal gain. Upon saturation of the amplifier's gain, the PC's high-voltage is quickly switched to effectively dump the amplified pulse from the cavity. Regen cavities are usually employed as the primary amplifiers within most mJ level Ti:Sa systems commercially available because their cavity design accommodates simplified alignment through free-lasing and moderate contrast. Notable drawbacks of regenerative amplifiers include significant

higher-order dispersion accumulation due to cavity optical elements and spectral narrowing from multiple gain passes in tandem with limited broadband coatings on polarizing elements.

In order to generate high-intensity output pulses for laser-plasma acceleration applications, the temporally stretched and now amplified laser pulses must now be sent through an optical compressor. These devices are engineered to remove the spectral phase imparted by the system's stretcher along with all phase accumulated from material dispersion from cavity optics and active photonic elements. Routinely this is tasked to a set of wide aperture diffraction gratings which are identical in blaze and groove depth to those located in the CPA stretcher. Treacy compressor designs utilizing a grating pair and elevation manipulating periscope are commonly used in systems where the compressed pulse energy is $\leq$ 200mJ [65]. B-integral accumulation is non-negligible for CPA systems capable of relativistic intensity and housing of the entire compressor configuration in evacuated vacuum chambers is mandatory to prevent output self-focusing.

2.2 Laser ionization mechanisms

As a preface to reviewing mechanisms by which laser electromagnetic field can couple energy into, and further heat the plasma to conditions necessary for fusion, let us first review the initial process by which a neutral atomic target may be ionized. Given its simple electronic structure, the hydrogen atom is an exemplary case for introducing meaningful plasma parameters. Within the framework of laser-matter interactions, it is helpful to establish a relative parity between the atomic electrostatic potential and that of the intense electric field generally associated with laser light. Starting from the Bohr radius:

$$a_B = \frac{\hbar^2}{me^2} = 5.3 \times 10^{-11} \quad \text{[m]} \quad (2.18)$$

Using Coulomb's Law this scale length can be used to determine the approximate electric field acting upon the sole bound electron in the hydrogen 1s-orbital.

$$E_a = \frac{e}{4\pi\epsilon_0 a_B^2} = 5.1 \times 10^9 \qquad [\mathrm{V/m}] \quad (2.19)$$

Substituting into Equation 2.20 we obtain an expression for the *atomic intensity* [72] - corresponding to an optical field intensity at which the laser field is at parity with binding strength of the hydrogen nucleus.

$$I_a = \frac{\epsilon_0 c E_a^2}{2} \simeq 3.5 \times 10^{16} \qquad [\mathrm{W/cm^2}] \quad (2.20)$$

It is readily apparent from the previous section that optical field intensities present in the focused output of the state-of-the-art CPA laser systems easily exceed that of the Bohr potential. For laser intensities in excess of the I_a, matter is directly ionized but as a consequence of the quantum nature of light, target ionization is possible under this threshold (as explained in the following sections). Considering the finite pre-pulse contrast associated with CPA architectures, such ionization processes can have serious implications for pre-plasma generation.

2.2.1 Photo-ionization

Photo-ionization occurs when the energy of individual photons incident on a specific atom exceeds the ionization potential of the bound electrons. In direct ionization, the photon transfers its energy to the electrons and they are ejected into the continuum leaving the atom in an excited state. Commonly known as the photoelectric effect, this process is important to the operation of photomultiplier tubes (PMT) and photodiodes (PD) utilized during this work but is generally an ionization mechanism associated with NIR CPA systems. The lasers used within this thesis work have broadband spectral content with center wavelengths of $\lambda_{\mathrm{Ti:Sa}} = 800$ nm and $\lambda_{\mathrm{YDFL}} = 1035$ nm respectively. Even when considering the case of the Ti:Sa system with $\hbar\omega = 1.55$ eV photons, we find that these photons are nearly an order of magnitude below the 13.6 eV ground state of hydrogen.

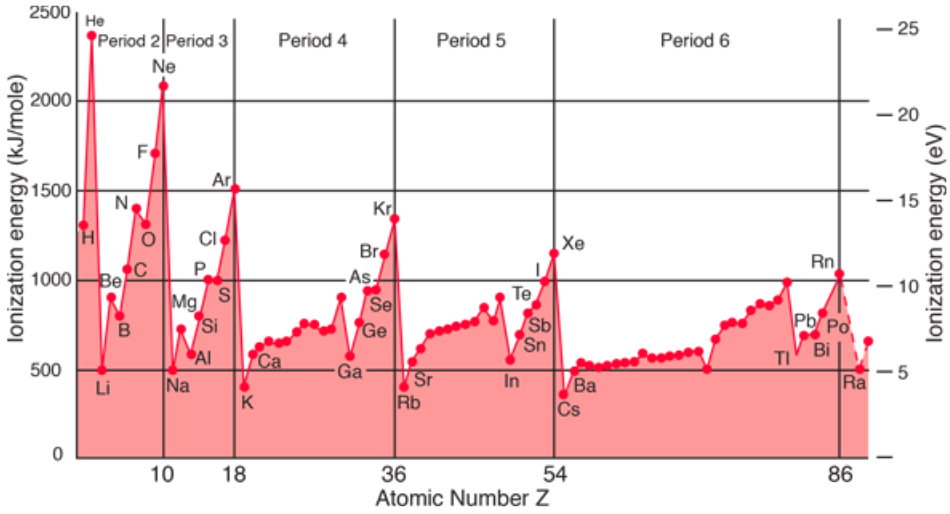

Figure 2.4: First electron ionization energies of various atomic species. In every period it can be seen that alkali metals exhibit the lowest relative ionization energy due to their single surplus electron outside of the closed electronic configuration corresponding with the highest ionization energies associated with preceding noble gases. From the public domain.

Especially pertinent laser-induced damage thresholds of optical surfaces, multiphoton ionization (MPI) is possible in cases where the high photonic density associated with pulsed lasers results in simultaneous absorption of n-photons. Rates for MPI processes can be estimated from perturbation theory as:

$$\Gamma_n = \sigma_n I_L^n \tag{2.21}$$

The cross-section σ_n for this process decreases with increasing photon number but the intensity dependence I_L^n supports the likelihood of the nth-order ionization event. It follows that the summed total of energy quanta from all incident photons must exceed the associated electron binding energy. For sufficiently intense fields, electrons can even absorb more energy than is specifically required to enter the continuum. Such above-threshold ionization (ATI) was first confirmed experimentally in the late 1970s and the final kinetic energy of the liberated electrons is provided by a modified version of Einstein's formula:

$$E_f = (n+s)\hbar\omega - E_{\text{ion}} \tag{2.22}$$

where n is the number of photons needed for MPI; s is the number of excess photons absorbed; E_{ion} the ionization potential and E_f the resulting kinetic energy of the liberated electron. It is worth noting that MPI and ATI processes dominate below incident optical intensities of $I_L \leq 10^{14}\ \frac{W}{cm^2}$.

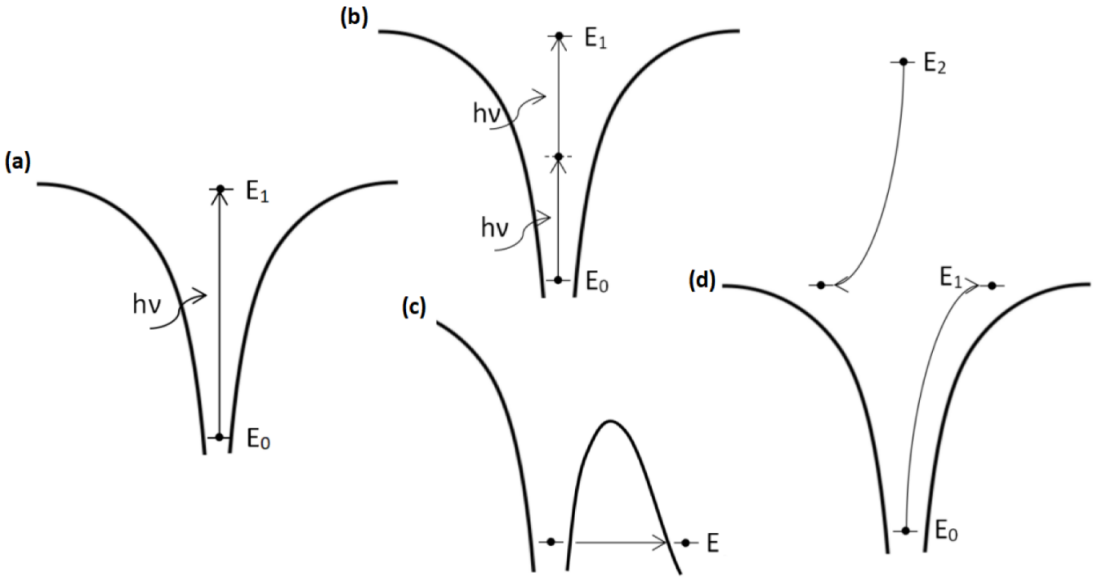

Figure 2.5: The atomic Coulomb potential in the presence of an intense laser pulse. In (a) the potential barrier is unperturbed in a field-free configuration, (b) shows electron excursion from the well via multiphoton ionization, (c) significant distortion of the barrier leading to tunneling ionization, and (d) avalanche ionization. Figure adapted from Ref. [7] with permission.

2.2.2 Tunnel ionization

For incident optical intensities above $I_L > 10^{14}\ \frac{W}{cm^2}$, we can no longer reasonably assume a regime of perturbative MPI where the laser field is not distorting the atomic binding potential. Strong distortions of the Coulombic field result in an increased probability that the electron wave packet will undergo quantum mechanical tunneling through the walls of the potential well. It is useful to introduce the Keldysh parameter (γ_K) [73]:

$$\gamma_K = \omega_L \sqrt{\frac{2E_{\text{ion}}}{I_L}} \sim \sqrt{\frac{E_{\text{ion}}}{\Phi_{\text{pond}}}} = \frac{\text{Tunneling time}}{\text{Laser period}} \tag{2.23}$$

which relates the relative strength of the ponderomotive potential, introduced in Eq. 2.42, to the binding potential of ground-state electrons. Intuitively we can see that for $\gamma_K > 1$ ionization favors the quadratic intensity and wavelength scaling associated with the ponderomotive potential (i.e., tunneling dominates); similarly, for $\gamma_K < 1$, the MPI regime is preferential (i.e., the electron doesn't have time to tunnel out before the field changes sign).

2.2.3 Barrier suppression ionization

In sufficiently intense laser fields, the superposition of the light field and barrier potential can result in direct field ionization. Also referred to as barrier suppression ionization (BSI), in this regime the effective binding potential falls below E_{ion} and the electron will simply escape the atom. Practically we may then express this as an *appearance intensity* for ions of charge Z by first taking the case of laser (E_L) acting upon a Coulomb potential $V(x)$:

$$V(x) = -\frac{Ze^2}{x} - eE_L x \tag{2.24}$$

as illustrated in Figure 2.5, we can see that past a local maximum in the binding field - the Coulomb barrier is effectively suppressed. By differentiation, we can determine the $x_{\max}$ position of the boundary in the case where $\frac{dV(x)}{dx} = 0$. Equating the potential at $V(x_{\max})$ to the binding potential we solve for an optical field strength denoting the onset of BSI:

$$E_L = \frac{E_{\text{ion}}^2}{4Ze^3} \tag{2.25}$$

This leads to the *appearance intensity* as was performed in Eq. 2.20:

$$I_{\text{app}} = \frac{c}{8\pi}E_L^2 = \frac{cE_{\text{ion}}^4}{128\pi Z^2 e^6} \simeq 4\times 10^9 (\frac{E_{\text{ion}}^4(\text{eV})}{Z^2}) \qquad [\text{W/cm}^2] \quad (2.26)$$

Assuming an USPL Yb-fiber laser centered at $\lambda = 1.035$ μm, and a ground state deuteron with $E_{\text{ion}} = 13.603$ eV, we calculate an $I_{\text{app}} = 1.37\times 10^{14}$ W/cm^2 which is approximately two orders of magnitude lower than the Bohr intensity for the same electronic configuration. This example highlights the importance of system pulse contrast as even modest $\sim \mu$J energies in a millijoule or joule class femtosecond laser can readily approach 10^{14-15} W/cm^2 when tightly focused - a common practice used throughout this thesis.

2.2.4 Collisional ionization

Electrons liberated during any of the previously described processes can lead to secondary electron cascades during collisions with neutral or unstripped ions still present in the target material. The resulting population of free electrons with kinetic energy in excess of local E_{ion} will cause additional cascades resulting in an avalanche effect. This process is described by

$$e^- + A^{Z+} \rightarrow 2e^- + A^{(Z+1)+} \quad (2.27)$$

where Z^+ specifies the ionic charge of an atomic species with the atomic mass number A. This avalanche process is especially important for long-pulse ($\sim$1-10 ps) interactions or laser interaction with solid-density targets. Effective collision rate scales with electron population density and usually dominates in sub-relativistic intensity regimes of $I_L \leq 10^{15}$ W/cm^2.

2.3 Laser absorption mechanisms

The previous section explored various modes by which a laser field can ionize target material and initiate the formation of a plasma. In this section, we review the absorption mechanisms

that ultimately couple laser energy into the plasma and result in further particle heating. Electromagnetic wave propagation through a plasma is governed by the plasma density and is described by the mathematical expression referred to as the *dispersion relation*. In the basic case of a cold, unmagnetized, and collisionless plasma where we consider only the relative motion of the electrons we obtain the dispersion relation for laser light:

$$\omega_L^2 = \omega_{pe}^2 + (k_0 c)^2 \tag{2.28}$$

where ω_L is the center frequency of the laser light, $\omega_{pe} = \sqrt{n_e e^2/\epsilon_0 m_e}$ is the electron plasma frequency, and k_0 is the wavenumber. By inspection we see that optical opacity occurs when the plasma frequency and laser frequency exactly match, this is occurs at critical density, given by the expression

$$n_{\text{crit}} = \frac{m_e \epsilon_0 \omega_L^2}{e^2}, \tag{2.29}$$

further expressed in practical units $n_{\text{crit}} \simeq 1.1 \times 10^{21} (\lambda/\mu\text{m})\ \text{cm}^{-3}$. Typical lexicon regards plasmas with density lower than, namely ($n_e < n_{\text{crit}}$), as *underdense* while those with ($n_e > n_{\text{crit}}$) as *overdense*. With the specific exception of relativistic transparency [74], an overdense plasma will reflect incident laser light at its critical surface. Given this mirror-like behavior, it would seem impossible to couple high-intensity laser light into a solid target. This section will explore how in practice the characteristics of the plasma density scale length can successfully circumvent this obstacle and lead to plasma heating via resonance absorption, vacuum heating, and $\mathbf{j} \times \mathbf{B}$ heating.

2.3.1 Resonance absorption

An extended plasma scale length up to the critical surface of an overdense target can lead to highly efficient laser-matter coupling through a collisionless energy transfer process referred to as resonance absorption. Various mechanisms can lead to the necessary plasma gradient

but typical experimental conditions include: ns-to-ps laser pulse pedestal initiating a blow-off plume prior to the arrival of the main intense pulse and underdense background gas fill from technical limitations of chamber vacuum pumping or use of high vapor pressure target materials. The driving mechanism of resonance absorption can best be understood by considering the evanescent wave solution of the P-polarized laser pulse incident on a solid target. Although the laser pulse will reflect at an angularly dependent turning point up to n_{crit}, the tunneling of the evanescent field resonantly excites a plasma wave because the laser frequency perfectly matches the plasma frequency ($\omega_L = \omega_{pe}$) at the boundary condition. Plasma heating is achieved when the Langmuir wave is subsequently damped through inter-particle collisions or wave breaking and particle trapping in high-intensity cases.

If we consider P-polarized light at an oblique incidence angle (θ), then the approximate fraction of laser light coupled to a plasma wave during the resonance condition is:

$$f_{\text{ra}} = \frac{1}{2}\Phi(\tau)^2, \tag{2.30}$$

where $\tau = (kL_s)^{1/3}\sin(\theta)$, the parameter $\Phi(\tau) \simeq 2.3\tau\exp(-2\tau^3/3)$ $k = 2\pi/\lambda$ is the laser's wave vector and L_s is the plasma density scale length [75]. Absorption for a particular laser frequency and density scale length may be maximized by using an optimum incidence angle given by

$$\theta_{\text{max}} \approx \arcsin[0.8(kL_s)^{-1/3}]. \tag{2.31}$$

2.3.2 Vacuum heating

Steep density gradients in the plasma profile will serve to dampen the excitation of plasma waves by resonance absorption, but this new transitional boundary condition will support vacuum heating, otherwise known as Brunel heating. Consider the interaction of an intense laser pulse on a sharp plasma density profile. The amplitude of the electrons oscillating

on the surface can be approximated as v_{osc}/ω and if this exceeds the scale length L_s, then the quiver motion of thermal electrons will result in excursions across the vacuum-plasma boundary. Once the incident field reverses direction, this electron will be driven towards the plasma volume but unlike the laser field which can at most penetrate to the skin depth $\sim c/\omega_p$, the electron traverses well inside the target. From here, stochastic collisions with ions or neutrals effectively transfer the kinetic energy of the electron population into the heating of the bulk plasma.

2.3.3 $\mathbf{j} \times \mathbf{B}$ heating

High-intensity ultrashort laser pulses exhibit a non-negligible magnetic field component that will accelerate electrons through the critical surface at twice the laser frequency. Electron motion in this manner is induced via the Lorentz force, and can be understood as the $\mathbf{j} \times \mathbf{B}$ term in Eq. 2.33. Generation of a longitudinal force f_x can be shown in the case of a linearly polarized light wave with $E = E_0(x)\hat{y}\sin(\omega t)$ [72]:

$$f_p = -\frac{m_e}{4}\frac{\partial v_{osc}^2(x)}{\partial x}[1 - \cos(2\omega t)] \tag{2.32}$$

The RHS of Eq. 2.32 includes both the DC ponderomotive force - responsible for perturbing the electron density profile into the target, and a second high-frequency component that gives rise to the 'twice per cycle' heating effect mentioned above. Plasma heating via this mechanism is especially relevant when normal incidence solid target geometries are employed, works for any field polarization case except circularly polarized, and plays a notable role in target heating for relativistic quiver velocities [72].

2.4 Strong field interactions

When manipulated in a tight-focusing geometry, the peak vacuum intensity achievable with many kHz repetition-rate USPLs easily exceeds the *relativistic intensity*. Regardless of the

ionization mechanism, electrons contributing to the resulting plasma are subject to these strong spatial-temporal EM perturbations in a variety of manners. Through a heuristic approach, we will first consider the null case for single electron motion in a uniform plane wave and then contrast this with particle motion resulting from inhomogeneous (spatially varying) optical fields.

2.4.1 Single electron motion in an EM plane wave

In the cold fluid limit, the equation of motion for a single electron of charge $-e$ and mass m_e in laser fields $\mathbf{E}$ and $\mathbf{B}$ is given by the Lorentz equation:

$$\frac{d\mathbf{p}}{dt} = -e(\mathbf{E} + \mathbf{v} \times \mathbf{B}) \tag{2.33}$$

where $\mathbf{p} = \gamma m_e \mathbf{v}$ is the electron's momentum, $\beta = v/c$ is the normalized velocity, and $\gamma = \frac{1}{\sqrt{(1-\beta^2)}}$ is the Lorentz factor. Conveniently, we recast the electric and magnetic field in terms of the vector potential for a wave $\mathbf{A}$ giving:

$$\mathbf{E} = -\frac{\partial \mathbf{A}}{\partial t} \tag{2.34}$$

and

$$\mathbf{B} = \nabla \times \mathbf{A} \tag{2.35}$$

It is convenient to introduce a peak normalized vector potential $a_0 = eA_0/(m_e c) = eE_L/(m_e c\omega_0)$, usually referred to as the laser relativistic strength parameter. Simple manipulation of this expression yields a practical expression for a_0 in terms of laser intensity I_L, and the center wavelength of the laser spectrum λ:

$$a_0 = \left[\frac{I_L \lambda^2}{1.37 \times 10^{18} \mathrm{W/cm^2 \cdot \mu m^2}}\right]^{1/2} \tag{2.36}$$

For simplicity, we assume a linearly polarized plane wave traveling in the $\hat{z}$ direction.

Vector potential in this case is expressed:

$$\mathbf{A}(z,t) = A_0 \sin(kz - \omega t)\hat{x} \tag{2.37}$$

where $A_0 = E_L/\omega_0$ is normalized amplitude. In the non-relativistic case when $\beta \ll 1$, and considering $|\mathbf{B}| = |\mathbf{E}|/c$, then the RHS of Eq. 2.33 may be ignored yielding

$$\frac{d\mathbf{p}}{dt} = -e\mathbf{E} = e\frac{\partial \mathbf{A}}{\partial t}. \tag{2.38}$$

Through simple integration, we find that the electron which was originally at rest $z = 0$, oscillates in the direction of the electric field with a corresponding *quiver* velocity of:

$$\beta = -\frac{eA_0}{m_e c}\sin(\omega_0 t) \triangleq -a_0 \sin(\omega_0 t) \tag{2.39}$$

Eq. 2.39 clearly shows that to first order, the electron will merely oscillate at in the applied field but is not subject to net energy gain. This picture fundamentally changes in cases where the incident field is no longer spatially homogeneous or exhibits slow temporal variation, effects which both give rise to *ponderomotive force* [76].

2.4.2 The ponderomotive force

CPA laser systems achieve high peak power by compressing energy in ultrashort durations of time, further geometric focusing allows further enhancement of field intensity by compressing the same pulse energy in space. We now consider the effects of these spatiotemporal electric field gradients and will examine how they can lead to an intensity-dependent force exerted on electrons within a plasma - this force is known as the ponderomotive force. Starting again from Eq. 2.33, and considering a second-order perturbation $\mathbf{p} = \mathbf{p}_q + \delta\mathbf{p}$ with the first-order motion given as $\mathbf{p}_q = m_e c\mathbf{a}$. We find that the second-order momentum is,

$$\begin{aligned}\frac{d\delta\mathbf{p}}{dt} &= -\left(\frac{\mathbf{p}_q}{m_e}\cdot\nabla\right)\delta\mathbf{p} - \mathbf{p}_q \times (c\nabla\times\mathbf{a}) \\ &= -m_e c^2 \nabla(a^2/2)\end{aligned} \tag{2.40}$$

and by time averaging one obtains the mathematical equation for the ponderomotive force

$$\mathbf{F}_p = -m_e c^2 \left\langle \nabla(\gamma - 1) \right\rangle . \tag{2.41}$$

The brackets on the RHS of Eq. 2.41 denote averaging performed over the period of the laser pulse. In the relativistic case, we must modify the previous equation to capture the "effective mass" of the electron which gives

$$\mathbf{F}_p = -\frac{m_e c^2}{\bar{\gamma}} \nabla \left\langle \frac{a^2}{2} \right\rangle \tag{2.42}$$

where $\bar{\gamma} = \sqrt{(1 + < p^2 > /m_e^2 c^2 + < a^2 >)}$ is the time averaged relativistic Lorentz factor. From Eq. 2.41 it is clear that the ponderomotive force is proportional to the strength of the laser's spatiotemporal intensity gradient ($\mathbf{F}_p \propto -\nabla I_L$), and over successive light cycles this longitudinal force will act to expel particles from the beam focus towards lower intensity.

2.4.3 Laser ion acceleration

Thus far the theoretical discussion presented has focused on the various methods through which intense laser light will ionize and further transfer its energy into solids, liquids, and gases to form energetic plasmas. A deliberate focus was placed on the interaction of the electric field with the electron population because the charge-to-mass ratio of electrons to protons is $m_e : m_p \simeq 1{:}1836$. Within the current limits of laser technology direct ponderomotive ion acceleration to relativistic intensity is unfeasible and as a direct consequence of their mass, ion motion is generally ignored on ultrashort temporal scales. On longer time

scales, intense field gradients established by perturbation of the electron population indeed play a critical role in accelerating ions from the target. This section will summarize various laser ion acceleration methods with specific emphasis on target normal sheath acceleration and Coulomb explosion as they relate to fusion favorable kinetics. The evolution of electron-ion dynamics during intense laser interaction is complex and in experiments conducted in the relativistic regime $I_L \simeq 10^{18}$ W/cm^2, multiple ion acceleration mechanisms compete. Ultimately, the dynamics that dominate are a function of laser intensity, target geometry, pre-pulse contrast, and atomic mass makeup of the ion species undergoing acceleration. Ultrashort laser acceleration of high-quality >MeV ion beams was first achieved in 2000 and in the past two decades, the field has experienced rapid advances in both theoretical understanding and experimental demonstration of a wide array of ion acceleration mechanisms with prospects for industrial, scientific, and medical applications.

Target Normal Sheath Acceleration (TNSA) [77] was first demonstrated in 2001 and has been extensively characterized analytically and experimentally across a range of drive lasers and target types [43, 44, 46, 78]. In TNSA an intense laser pulse rapidly heats electrons at the critical surface through ponderomotive interactions. If a "thin" solid target of 0.01-20 μm thickness is employed, the energetic electrons will penetrate through the target and establish a Debye sheath field at the target rear. Blow-off electrons in the interaction volume simultaneously establish an identical sheath at the target front surface. These virtual cathodes are accompanied by an intense electrostatic field of up to $E_f = 100$ GV/cm which further ionizes contaminant layers (H, D, C) layers present on target surfaces [79]. Surface ions and those created during collisional ionization from hot electron scattering are then accelerated toward the sheath region in a low angular divergence beam. TNSA typically creates quasi-Maxwellian ion populations with laser-ion acceleration efficiencies of a few percent [46, 78]. To date, protons, deuterons, and helium ions have been accelerated to ≥ 90 MeV by multiple facilities with multi-TW drive beams [80]. The overall quality of the TNSA ion beam is governed by the laser pulse contrast and target thickness, with superlative results, attained

typically with picosecond pedestal contrast of $< 10^{-10}$ and 10-1000 nm thin foils. For campaigns where upper ion cut-off energy is not the primary optimization parameter, such as in the generation of neutrons from liquid targets, the TNSA mechanism is robust and tolerable of lower laser contrast when paired with microscale liquid jets, sheets, and droplets.

Ion acceleration from mass-limited droplets ($\sim$1 μm^3) and gas cluster targets typically favors ion acceleration by means of the Coulomb explosion mechanism. Cryogenic cooling or sub-cooled expansion of a high-pressure gas into a vacuum environment will result in the rapid formation of molecular clusters weakly bound by van der Waals forces. An intense femtosecond laser pulse incident on a homonuclear or heteronuclear gas cluster can result in the complete stripping of the electron population in the irradiated volume. The remaining stripped ions will then experience intense thermal pressure and Coulomb repulsion from their ensemble of positive nuclear charge. For large Z nuclei, this effect can be quite marked as was demonstrated in $>$ MeV Xe ions by Ditmire *et al.* [81]. The large corresponding release of multi-keV kinetic energy from this superheated microplasma can drive D-D fusion generation through thermonuclear and beam-target fusion processes. Seminal work by Zweiback *et al.* showed $\sim 10^3$ n/shot yield for cryogenic D_2 clusters of up to 100 angstroms irradiated with $I_L = 5 \times 10^{17}$ W/cm^2 [48]. This work has been successfully extended to include irradiation of heteronuclear molecules (CD_4) [49]. Computational experiments have shown similar explosion dynamics will prevail in superheated microdroplets although experimental confirmation has not yet been demonstrated.

The TNSA mechanism and Coulomb explosion dominate ion acceleration in the near relativistic intensity regimes ($I_L \simeq 10^{16} - 10^{18}$ W/cm^2) utilized throughout this work. For sufficiently thin nanometer targets and when on-target pulse intensities exceed 10^{19} W/cm^2, radiation pressure acceleration (RPA), light sail acceleration (LSA), collisionless shock acceleration (CSA) and breakout afterburner acceleration (BOA) of ion species begin to compete with TNSA. The physics associated with these mechanisms are succinctly reviewed in Ref. [79, 82].

2.5 Types of neutron sources

Encapsulated radionuclide sources are most often realized from isotopes that naturally undergo spontaneous fission (Cf-252, Cm-250) or utilize α-stripping reactions (AmBe, AmLi, RaBe, PuBe) on light nuclei such as C, Be, and Li. In either case, a mixed spectrum of fast neutrons is emitted with total isotropic fluxes generally ranging from $\sim 10^{5-9}$ n/s [83]. Owing to their small size (a few cm^3) and their ease of transport, sealed sources are ideally suited for laboratory use in detector and instrument calibration as well as limited field applications including soil densitometry or well-logging. (α,n) conversion and spontaneous fission sources alike are controlled by specific nuclear regulatory commission (NRC) radioactive material licenses and must be shielded when not in use - an intrinsic restriction attributed to their strong mixed neutron and γ-field emission which can pose a significant dose hazard in close proximity. Furthermore, the small size of the source capsule and neutron emission of these radionuclides makes such sources a proliferation risk in the context of improvised radiological dispersal devices.

For situations requiring moderate isotropic flux of $\sim 10^{6-11}$ n/s accelerator tube neutron generators based on beam-target fusion reactions represent an attractive solution. Principal designs incorporate RF-driven ion acceleration to initiate D-D or D-T fusion reactions producing 2.45 MeV and 14.1 MeV fast neutron pulses respectively. Commercially available neutron tube generators are $\sim$ 1m in length and can easily fit on a tabletop. Power requirements for the accelerator electronics and source/target cooling systems are usually no more than a few kW and certain high-efficiency designs are now passively cooled and can be powered by compact battery supplies. Primary uses of these devices include prompt gamma neutron activation analysis, isotopic activation experiments, radiation hardening, nuclear material active interrogation, geological dating, and petrochemical logging. NRC permitting is required for the operation and a special licensure is needed for tritium-loaded modules. Tube generator technology is very mature and hermetically sealed units are often fielded in extreme environments due to their robust design. Disadvantages of accelerator-tube sources

include finite fill gas and target lifetime in sealed tube units, long (μs) pulse duration when used for coincidence detection, and ∼mm source sizes which limit usefulness in imaging applications.

Accelerator-driven spallation sources and conventional fission reactor facilities are superlative in terms of spatial size, available neutron fluence, and cost. At specially designed reactors, such as the high flux isotope reactor at Oak Ridge National Lab, highly enriched U-235 is configured into annular core geometries that result in 'trapped' thermal fluxes when the reactor is under operation. Under full-load conditions, in-core reactor fluxes routinely hit $\sim 10^{12-15}$ n/s/sr. More impressively, the unmoderated target flux at ∼GeV class spallation beamlines can exceed $>10^{17}$ n/s. Beam ports derived from these intense neutron fluxes are suitable for technically rigorous applications including neutron diffractometry and scattering measurements, 3D tomography, radioisotope breeding, and fissile material assay.

2.5.1 Nuclear fusion reactions

The physics that govern thermonuclear fusion reactions are exceedingly complex but ultimately they can be diluted at the simplest level back to Einstein's famous equation for energy-mass conservation:

$$E = \sqrt{m_0^2 c^4 + p^2 c^2} = \gamma m_0 c^2 = mc^2 \tag{2.43}$$

where E is energy, m_0 is the particle or nucleon rest mass, p momentum, and c the speed of light in vacuum. Fusion like its sister process nuclear fission involves the release of tremendous amounts of energy from the conversion of excess mass to energy. Behind either process is the action of the strong nuclear force, which acts on 1-3 fm spatial scales to confine quarks and form hadrons. By extension, this strong force also binds the protons and neutrons in the atomic nucleus. For all known elements, a binding energy curve may be constructed by dividing the total nuclear binding energy of an atom by its number of

constituent nucleons, see Fig. 2.6.

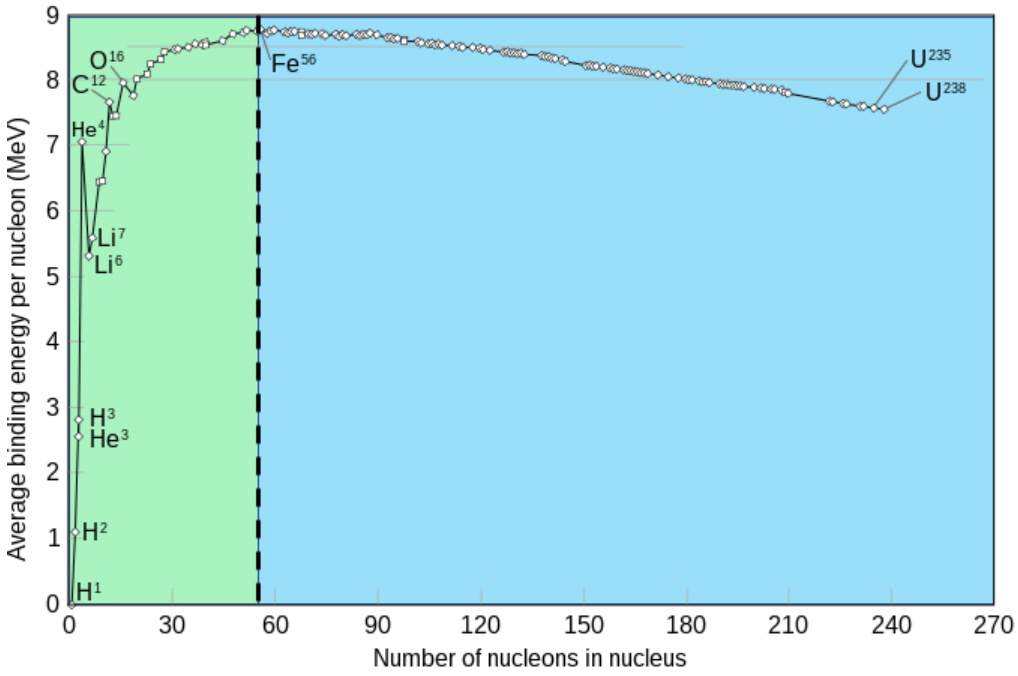

Figure 2.6: Plot of the average binding energy per nucleon for elements with mass A $\leq$ 238. The mass defect can be released as energy by nuclear fusion of light nuclei (green) and nuclear fission of heavy nuclei (blue). Image released to the public domain.

At the apex of this curve are "iron group" isotopes which are the most tightly bound and, therefore, atomically stable. Reactions involving elements on either side of $^{62}_{28}$Ni will result in an associated release of energy from the mass defect. In the case of fission, heavier elements (U-235, P-239) are broken apart, resulting in fission fragments with less total mass than the original fissile species. The fusion process proceeds from the other end of the curve, wherein two light nuclei (H, He, D) are joined to form an element with a more stable nuclear configuration, and the stored binding energy is released as kinetic energy in the product particles or bursts of radiation. This release of energy is immense (MeV) and is typically $\sim 10^{5-7}$ times larger than the ionization energies (eV-keV) associated with tightly bound inner-shell electrons.

Terrestrial control of fission reactions was first demonstrated at the Chicago pile experiment in 1939 and has been refined into an industrial tour de force for global electrical energy

production since. The relative ease with which fission reactions occur can be understood by considering that simple thermal neutron capture by a target U-235 nucleus instantly creates a condition where the binding energy of the excited nucleus exceeds the critical energy necessary for fission. At ambient conditions, U-235 and other fissile materials exhibit high thermal capture cross sections, and fragmentation results in neutron multiplicity that under proper conditions can trigger subsequent fission reactions that propagate exponentially. Nuclear fusion was first demonstrated by Cockcroft and Walton when electrostatically accelerated protons bombarded a lithium target driving the $^{7}\mathrm{Li(p,}\alpha)^{4}_{2}\mathrm{He}$ fusion reaction. Recently, a net Q fusion reaction was realized at the U.S. National Ignition Facility [84] and numerous electrostatic, inertial, and magnetic devices are actively pursuing sustained reactions. In order to obtain a better understanding of the challenges associated with initiating nuclear fusion and to understand the role intense laser-plasma interactions play in driving fusion-based neutron sources, we now will consider specific nuclear fusion reactions and the conditions under which they occur.

The potential well describing the boundary between the strong nuclear force and the electrostatic force acting upon the protons in the nucleus has a sharp transitional region at only a few fm of distance. In the classical electrostatic framework, an ion approaching a target nucleus will feel an exponential repulsion proportional to its proximity to the Coulomb barrier. The magnitude of this electrostatic force between two charges q_a and q_b spatially separated by a distance r in a vacuum is given by Coulomb's law:

$$\mathbf{F}_{\mathrm{Coulomb}} = \frac{1}{4\pi\epsilon_0}\frac{q_a q_b}{r^3}\mathbf{r} \tag{2.44}$$

As an illustrative example, we will now consider the neutronic D(d,n)T half-reaction which was extensively used throughout this work. To estimate the energy necessary to place fusion nuclei at the edge of the barrier and precipitate favorable conditions for a subsequent reaction, let us consider the electrostatic field to be conservative in nature and take the work moving two stripped deuterons q_{d1} and q_{d2} from a sufficient distance to local proximity r.

As in Harms [85], the potential energy $U = F \cdot x$ necessary to establish this configuration is given as

$$\begin{aligned} U(r) &= \int_{\infty}^{r} \mathbf{F}_{\mathrm{c,a}}(\mathbf{r}')d\mathbf{r}' \\ &= \int_{\infty}^{r} \frac{1}{4\pi\epsilon_0}\frac{q_a q_b}{(r')^3}\mathbf{r}\cdot d\mathbf{r}' \\ &= \int_{r}^{\infty} \frac{1}{4\pi\epsilon_0}\frac{q_a q_b}{(r')^3}(-r dr') \\ &= \frac{1}{4\pi\epsilon_0}\frac{q_a q_b}{r} \end{aligned} \tag{2.45}$$

This approximation is valid if the deuteron separation distance is larger than the combined radii of the deuteron nuclei, namely $r \geq \mathrm{R}_{d1}+\mathrm{R}_{d2}$. By inspection of Eq. 2.45, the potential energy at the point of closest approach between deuterons is that of the Coulomb barrier and slight modification of Eq. 2.44 gives

$$U(r) = \frac{1}{4\pi\epsilon_0}\frac{q_a q_b}{(R_{d1}+R_{d2})} \tag{2.46}$$

where as before R_{d1} and R_{d2} are the deuteron radii. Using the established value for this charge radius R_d = deuteron radius = 2.172×10^{-15} m, it is possible to estimate the minimum kinetic energy required in the center of mass frame to move the two deuterons close enough to overcome this repulsive barrier and allow the action of the strong nuclear force to dominate. Simple classical approximation gives $U(r = \mathrm{R}_{d1}+\mathrm{R}_{d2}) \simeq 331$ keV, which is 3.84×10^9 K and roughly two hundred and forty-five times hotter than the core of our sun. At first glance the strength of this repulsive field would seem to make D-D fusion all but intractable with known technologies, fortunately, quantum mechanical tunneling reduces this limit significantly. The inability to define the absolute spatial scale of the deuteron wave packet leads to a probability distribution for ion tunneling through the Coulomb barrier. The likelihood of tunneling scales exponentially with relative speed v_r of the two fusion species

and varies as [85]

$$P(\text{tunnel}) \propto \frac{1}{\mathrm{v}_r} \exp\left(-\gamma \frac{q_a q_b}{\mathrm{v}_r}\right) \tag{2.47}$$

where γ is a constant of proportionality. This reduces the otherwise extreme kinetic energy requirements for fusion and also leads to non-negligible chances of fusion at even ambient conditions, in practice this finite probability is vanishingly small. Further, this v_r scaling highlights the usefulness of ion acceleration by relativistic laser-matter interactions where locally non-Maxwellian ion populations can exceed $\sim$1 MeV, easily exceeding the Coulombic potential for modest pulse energies.

To simplify calculations of thermonuclear reaction densities, we now consider a plasma in thermodynamic equilibrium and in the absence of external fields. Particles in this plasma exhibit a Maxwell-Boltzmann velocity distribution function given by

$$f(\mathbf{v}) = \left(\frac{m}{2\pi kT}\right)^{3/2} \exp\left(\frac{-\frac{1}{2}mv^2}{kT}\right) \tag{2.48}$$

where m is particle mass, T is absolute temperature, and k is the Boltzmann constant. The particles in this ensemble will possess a wide range of velocities, speeds, and energies but the temperature T of the plasma accurately describes the distribution function and is assumed to be fixed for a given thermal state [85].

Considering the implications of Eq. 2.47, then the general reaction rate R_{fu} for beams of two types of monoenergetic particles N_a and N_b with relative velocity v_r is given by the proportional relationship $\rightarrow R_{fu} \propto N_a N_b \mathrm{v}_r$. This idealized equation reasonably assumes binary fusion reaction events, as is typical for most non-solar kinetic systems, but ignores situations where particles may have varying energy and direction of motion as well as interactions with neutral or partially ionized species. Through the process of velocity distribution normalization and the assumption that particle densities are distributions in the velocity phase space the general reaction rate can be expressed as a system of integrals over all three velocity

components. The relative speed of the binary reactants at the point of interaction is given by $\mathrm{v}_r = |\mathrm{v}_\mathbf{a} - \mathrm{v}_\mathbf{b}|$. Taken together over all velocity space, it can be shown that the general fusion rate density expression for a binary reaction is [85]:

$$\begin{aligned} R_{fu} &= \int_{\mathbf{v}_a} \int_{\mathbf{v}_b} \sigma_{fu}\left(|\mathbf{v}_a - \mathbf{v}_b|\right) |\mathbf{v}_a - \mathbf{v}_b| \, N_a F_a(\mathbf{v}_a) N_b F_b(\mathbf{v}_b) d^3 v_a d^3 v_b \\ &= N_a N_b \int_{\mathbf{v}_a} \int_{\mathbf{v}_b} \sigma_{fu}\left(|\mathbf{v}_a - \mathbf{v}_b|\right) |\mathbf{v}_a - \mathbf{v}_b| \, F_a(\mathbf{v}_a) F_b(\mathbf{v}_b) d^3 v_a d^3 v_b \end{aligned} \tag{2.49}$$

The proportionality associated with tunneling and particle scattering is now expressed by σ_{fu} and is typically referenced against empirical lookup tables. Similarly, analytic execution of Eq. 2.49 requires explicit knowledge of the particle distribution functions $\mathrm{F}_i(\mathbf{v}_i)$. In practice, Eq. 2.49 is simplified by averaging the cross-sectional velocity product by normalization of the velocity components $\mathbf{v}_a$ and $\mathbf{v}_b$ and invoking the assumption of a Maxwell-Boltzmann thermal distribution described by Eq. 2.48. Averaging in this manner yields

$$\langle \sigma v \rangle_{ab} = \int_{\mathbf{v}_a} \int_{\mathbf{v}_b} \sigma_{fu}\left(|\mathbf{v}_a - \mathbf{v}_b|\right) |\mathbf{v}_a - \mathbf{v}_b| \, F_a(\mathbf{v}_a) F_b(\mathbf{v}_b) d^3 v_a d^3 v_b \tag{2.50}$$

where $\langle \sigma v \rangle_{ab}$, commonly pronounced "sigma-vee", is taken to be the reaction rate parameter. Conveniently then, binary fusion reaction rates with known interaction cross-sections and Maxwellian distributions may be calculated with

$$R_{fu} = N_a N_b \langle \sigma v \rangle_{ab} \tag{2.51}$$

because sigma-v is now uniquely specified as a function of the plasma temperature kT. Note R_{fu} is expressed in units of fusion reactions$\cdot\mathrm{m}^{-3}\cdot\mathrm{s}^{-1}$.

Fusion power density P_{fu} is calculated as the product of the rate density R_fu and the binding energy released per reaction Q_{fu}. Integrating over a time interval τ and for a known volume V gives the total energy released per fusion event:

$$E_{fu}^{*} = V \int_{0}^{\tau} P_{fu} dt \tag{2.52}$$

Straightforward estimates of fast neutron yield for pulsed fusion events (as in the case of laser-driven fusion) are obtained by dividing the E_{fu}^{*} by the fractional energy associated with the fast neutron and scaling by the reaction probability of the associated reaction channel if more than one exists. A plot of terrestrially relevant binary fusion cross-sections for a range of reactant kinetic energies is shown in Figure 2.7.

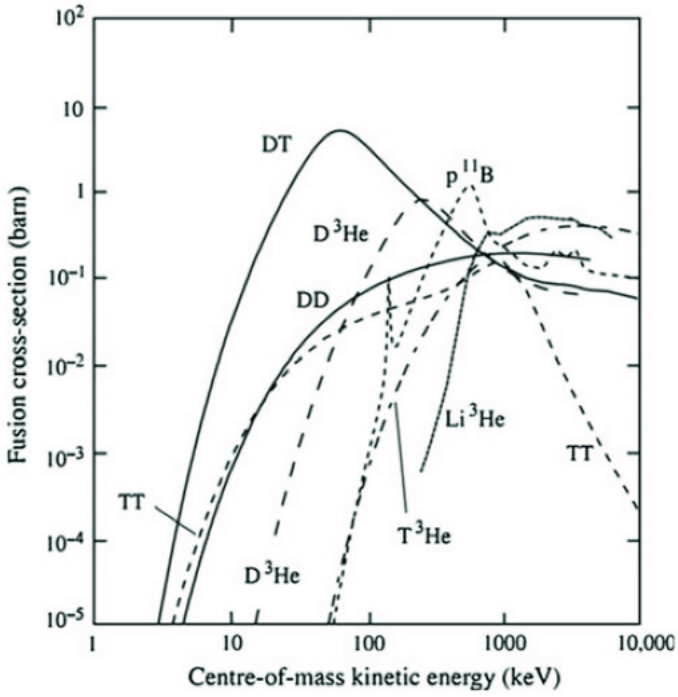

Figure 2.7: The nuclear fusion cross-section in units of barns for various binary fusion reactions with various center-of-mass kinetic energies. Figure from Ref. [8] used with permission.

Laser-driven neutron sources are typically modeled as thermonuclear reactions, beam-target fusion reactions, or a complex hybrid of both processes. Two common cases considered include (1) mass-limited targets with complete target ionization or for bulk thermonuclear heating from Coulomb explosion, where a Maxwellian population is assumed and appropriate values of $\langle \sigma v \rangle_{ab}$ are directly substituted; (2) ion-acceleration mechanisms resulting in beam-

like (delta distribution function) ions impinging on a catcher target, wherein $\langle \sigma v \rangle_{ab}^{b}$ tables are invoked. These modified sigma-v values allow for idealized averaging cases considering a monoenergetic beam incident on a Maxwellian plasma of various temperatures ranging from $T = 0 \rightarrow kT_{ion}$. In either case, empirical (Thomson parabola, track detectors, Faraday cup) or computational diagnostics (particle-in-cell) are required to properly fit the $\langle \sigma v \rangle$ parameter for the appropriate particle velocity distributions or approximate temperature of the ion Maxwellian. For ultrashort-laser matter interactions, τ is generally estimated as the time it takes for the fusion reactants to diffuse out of the plasma volume assuming their worst-case drift velocity, typically on the order of 1-100 ps.

2.5.2 Ultrashort laser-driven neutron sources

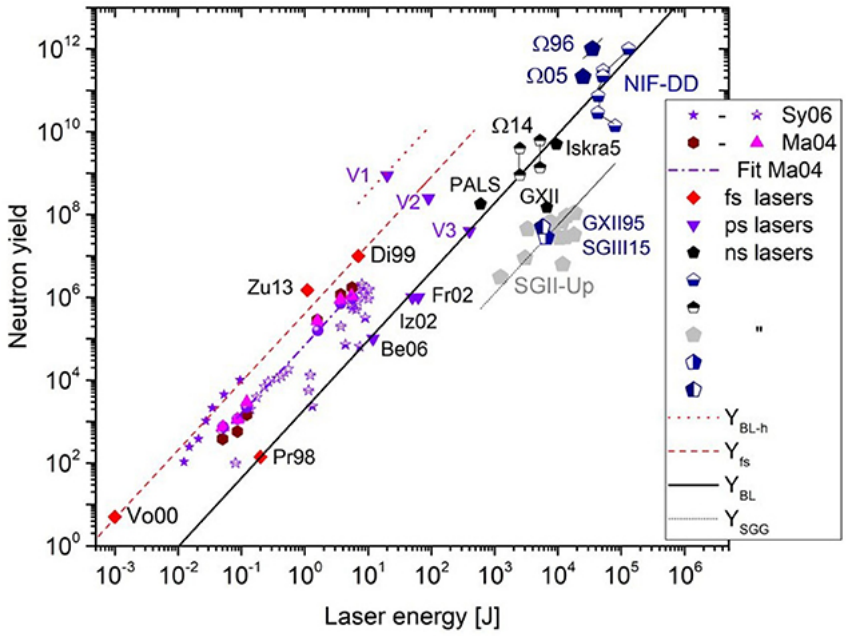

Figure 2.8: A plot showing the DD fusion neutron yield versus laser pulse energy across a variety of experimental campaigns. Power law scaling of yield with $Q_{SGG} = 14$, $Q_{BL} = 2000$ and $Q_{BL} = 4.1{\times}10^4$, and $Q_{BL} = 7.5{\times}10^6$ is reflected for various pulse energies. Figure and data compiled in Ref. [9] used with permission.

Figure 2.8 shows the approximate $\mathrm{Y} = Q \cdot E^{1.65}$ scaling for DD fusion neutron yield achieved across a variety of target types and lasers with pulse durations ranging from fs

to ns duration [9]. The spatiotemporal focusing of laser energy provides a useful mechanism to achieve particle kinetic energies necessary to initiate nuclear reactions resulting in short bursts (sub-nanosecond) of secondary radiation. Relevant to the tabletop experiments performed in this thesis work, ultrashort laser-plasma interactions can initiate fast neutron generation via binary fusion reactions, stripping reactions, and photoneutron conversion reactions. The following reactions represent some of the most extensively studied reaction mechanisms for laser-driven fast neutron yield:

$$\mathrm{D} + \mathrm{D} \rightarrow {}^{3}\mathrm{He} + \mathrm{n}(2.45\ \mathrm{MeV}), \mathrm{Q} = 3.27\ \mathrm{MeV} \tag{2.53}$$

$$\mathrm{D} + \mathrm{T} \rightarrow {}^{4}\mathrm{He} + \mathrm{n}(14.1\ \mathrm{MeV}), \mathrm{Q} = 17.59\ \mathrm{MeV} \tag{2.54}$$

$$\mathrm{D} + \mathrm{Li} \rightarrow {}^{8}\mathrm{Be} + \mathrm{n}(13.36\ \mathrm{MeV}), \mathrm{Q} = 15.03\ \mathrm{MeV} \tag{2.55}$$

In the case of binary fusion, the D(d,n)^{3}He (E_n = 2.45 MeV) and the D(t,n)^{4}He (E_n = 14.1 MeV) reactions are commonly employed. As shown in Figure 2.7, these hydrogen isotopes exhibit the highest cross-section for thermonuclear yield and beam-target reactions generally below the ∼1 MeV threshold. Owing to its intrinsic radioactivity and proliferation risk, tritium handling requires specific precautions, and therefore DT experiments are typically reserved for execution at appropriately equipped national laboratories [86]. High-purity deuterium gas, deuterium oxide, and deuterated hydrocarbons have been widely fielded as the target material during LDNS experimental campaigns. When irradiated below the relativistic threshold, researchers have shown that preferential Coulomb explosion of deuterated cryogenic gas clusters can generate significant neutron yield through both thermonuclear and beam-target interactions [47–49, 87]. Similarly, ponderomotive evacuation of the electrons in a near-critical density deuterium plasma can result in a Coulomb explosion of the highly charged ion channel trailing behind the laser pulse [50].

Fast neutron production via stripping reactions is a two-step process. First, a relativistic laser pulse is focused on a thin target consisting of a pure metal (Ti, Au, Cu) coated with a deuterated contaminant layer or a pure CD plastic. The purity of this contaminant layer plays an important role in the peak ion energy and species accelerated from the target and various experiments have explored deuterium conditioning through ion sputter guns [88], target heating [89] and cryogenic ice films [90]. For kHz repetition relevant intensities of $10^{18} - 10^{19}$ W/cm^2, TNSA then accelerates a diverging beam of protons or deuterons into a secondary target consisting of CD, ^{7}Li or ^{9}Be [91–93]. During this so-called 'pitcher-catcher' (P-C) interaction, beam-target fusion or stripping is initiated resulting in fast neutrons with characteristic energies shown Eq. 2.53-2.55 LDNS based on P-C schemes have resulted in some of the highest report single shot neutron yields of $\geqslant 10^{10}$ n/shot/sr [74,94]. Multi-MeV ion beams generated during the acceleration phase also can contribute to significant beam anisotropy that could favor medical dose applications or nuclear physics studies related to fundamental S-process and R-process capture dynamics [95]. P-C based fast neutron sources are an active field of study for PW-class lasers with sustained target repetition rates posing a bottleneck to further average flux scaling [60].

Photoneutron sources are commonly encountered in facilities with existing advanced particle accelerator systems. The application of laser wakefield acceleration of electrons to multi-MeV energies has recently opened a new pathway toward non-fusion ultrashort fast neutron sources. In this scheme, an intense USPL is focused into an underdense gas jet or gas cell, and plasma wave breaking traps and accelerates ∼pC bunches of electrons to relativistic kinetic energies. The electron beam is then dumped into a high-Z converter (W, U) and subsequent bremsstrahlung-induced and photoneutron reactions result in the generation of a fast neutron pulse. Using this method, Jiao *et al.* [87] recently demonstrated 2.4×10^6 n/shot from irradiation of a tungsten converter with ∼37 MeV electrons accelerated in a 90:10 He:N_2 gas mixture. Computational simulation has shown that 3FST drivers could further extend this compact source to flux levels necessary for ^{99m}Tc breeding and neutron

holography [96].

Neutron fluxes derived from intense laser-matter interactions possess many characteristics that set them apart from non-laser sources discussed in section 2.5. Significant advantages of LDNS include: (1) short-pulse duration, typically on the order of $\sim 10^{-12}$ seconds, (2) sub-millimeter source size resulting in high neutron fluence, (3) ability to generate characteristic monoenergetic and accelerator-quality neutron kinetic energies, and (4) high timing fidelity for coincidence applications.

This experimental thesis further expands on the use of high repetition rate liquid targets [40, 56, 57] for fast neutron generation applications. Chapter 4 investigates the use of electrohydrodynamic forces to extract mass-limited fluid jets under technical vacuum conditions supporting extreme matter interaction campaigns involving coupled interactions of XFEL or relativistic particle beams with TW-class lasers. The use of free-flowing D_2O liquid jets is further explored in Chapter 5 to show an order of magnitude enhancement of D-D fusion neutron generation with intense relativistic structured light beams. Chapter 6 then demonstrates the proof-of-principle extension of USPL-driven neutron generation to multi-kHz repetition rates enabled by novel ultrashort fiber optics.

CHAPTER 3

Methods and Capabilities

3.1 Laser systems and diagnostics

3.1.1 The relativistic lambda cubed laser system

High-repetition microscale liquid target experiments discussed in Chapter 4 and Chapter 5 were conducted using the Relativistic Lambda Cubed (λ^3) laser laboratory located in the Center for Ultrafast Optical Science at the University of Michigan. The λ^3 system is an ultrashort CPA Ti:Sapphire laser leveraging cryogenically cooled amplification stages. The namesake of this USPL is credited to legacy generations of this system that were designed to focus few-cycle pulses ($\sim c/\lambda$) synthesized via nonlinear compression to a near-diffraction-limited spot ($\sim \lambda^2$) in order to obtain relativistic on-target laser intensities ($I_L \approx c/\lambda$) [97]. Presently, at design pump fluence and with a properly shaped spectral hole, the system is capable of delivering ∼18 mJ, 35 fs pulses at a nominal 480 Hz pulse repetition rate. Figure 3.1 details the current system architecture and is included for reference.

Initial $\lambda_{\text{center}} = 800$ nm ultrashort seed pulses for the λ^3 laser are generated by a Kerr-lens mode-locked Ti:Sa oscillator (Coherent Micra-5) pumped by a ∼5W CW Nd:YVO_4 (Coherent Verdi). Intra-cavity dispersion compensating prisms allow for stable output of $\Delta\lambda = 120$ nm floor-to-floor bandwidth pules with sub-15 fs pulse duration at $f_{\text{rep}} = 80$ MHz. During daily operation, the oscillator is auto mode-locked via an internal voice coil-mounted mirror and two-axis PZT feedback loop. To ensure proper spectral content and central wavelength,

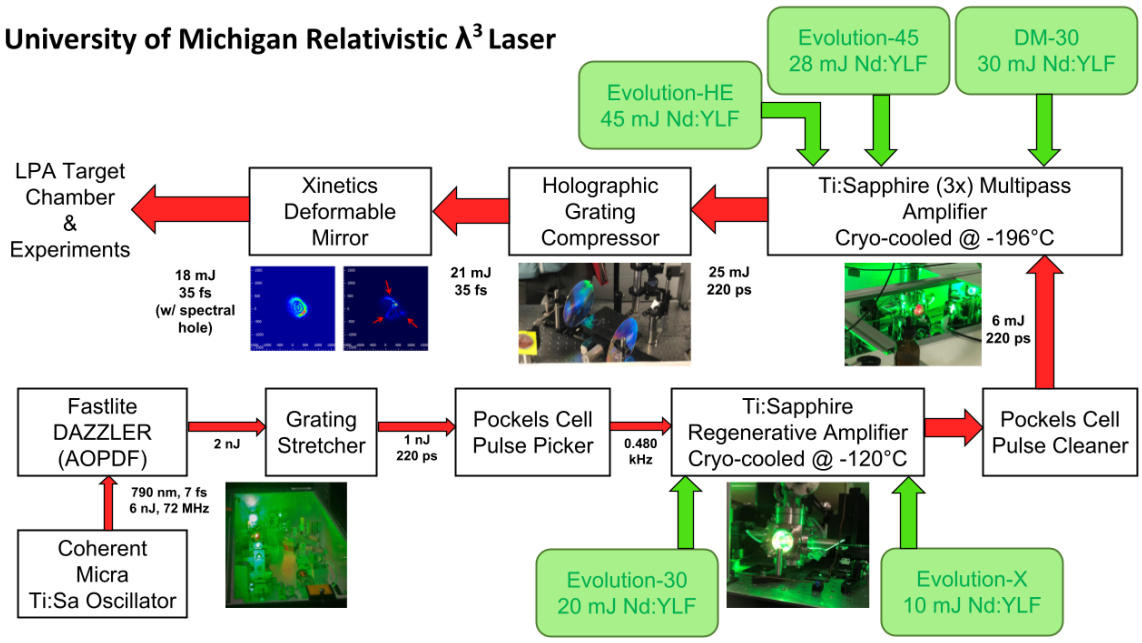

Figure 3.1: The University of Michigan's relativistic λ^3 high repetition Ti:Sapphire laser facility.

the oscillator output is monitored via a compact Czerny-turner spectrometer (OceanOptics USB400) connected to a desktop computer. Prior to arriving at the first pulse-picker, the amplitude and phase of the seed pulse is shaped with an acousto-optic programmable dispersive filter (AOPDF). This device, herein referred to as a DAZZLER (Fastlite), utilizes the interaction of RF-synthesized polychromatic acoustic waves to manipulate the spectral shape and phase of the broadband optical seed. During standard operation, a spectral hole is "drilled" into the seed around 790-810 nm to pre-compensate gain narrowing effects of the upstream regenerative amplifier. Additionally, the first to fourth-order spectral phase may be arbitrarily adjusted within the tuning range of the DAZZLER to perform online pulse profile shaping or perform chirp scans without physical manipulation of the compressor gratings.

The first of two Pockels cell pulse pickers is located directly after the DAZZLER. This module passes individual pulses at 0.480 kHz to set the down-counted system repetition rate and provide $\sim 10^4$ contrast to pulses injected into the regenerative amplifier. Pulses are then expanded with a telescope and passed through a two-grating stretcher where they are

broadened to approximately 220 ps duration. First-stage amplification is achieved in a mixed-refrigerant cryo-cooled regenerative Ti:Sa amplifier that is end-pumped with nominally 30 mJ of 527 nm light from two frequency-doubled Nd:YLF DPSSLs. Electronically synchronized polarization gating allows for $\sim 10^7$ optical gain during 10-12 cavity round trips. If <40 fs pulses are required, an additional round trip is added to the timing system to achieve proper amplifier saturation with DAZZLER-shaped spectral profiles. Once amplified to ∼6 mJ, pulses are dumped from the regen and pass through a second pulse picker for polarization cleaning and an additional 10^3 contrast enhancement. Stretched and amplified pulses are now sent through a three-pass rod Ti:Sa amplifier pumped again by Nd:YLF DPSSLs with up to 100 mJ. When under load, this amplifier is cyro-cooled to LN_2 temperatures with a closed-loop helium pulse tube cryohead. A saturated per pass gain of approximately 1.5 delivers pre-compressor pulses with a total energy of $\sim$ 25 mJ.

Amplified and positively chirped pulses are expanded to a 25 mm Gaussian beam diameter and subsequently compressed with 85% efficiency in a dual holographic transmission grating Treacy compressor. To reduce the total B-integral accumulated from relaying the compressed beam to experimental target chambers the beam is further expanded in a 1:2 telescope and apertured on the face of a deformable mirror to an approximately 47 mm $1/e^2$ beam diameter. At design specifications, the λ^3 laser provides 0.51 TW of peak laser power at a repetition rate of 0.480 kHz for relativistic laser-plasma experiments.

3.1.2 Ultrashort Yb-Fiber Laser System

In Chapter 6, the >1 kHz repetition-rate scaling capability of microscale liquid targets was validated with a novel fiber optic ultrashort pulse laser. This system represents the functional culmination of two systematic experiments aimed at simultaneously increasing the average and peak power delivered by Yb-doped fiber lasers (YDFL). In this unique system, high average power is realized through coherent beam combining (CBC) of four chirally coupled core (CCC) fiber power amplifiers. Likewise, peak power enhancement is derived through

coherent pulse stacking amplification (CPSA) wherein a burst train of 81 individual pulses is stacked into nominally one large output pulse by active phase compensated Gires-Tournois interferometer (GTI) cavities. Figure 3.2, shows a high-level system schematic for the scheme of laser operation.

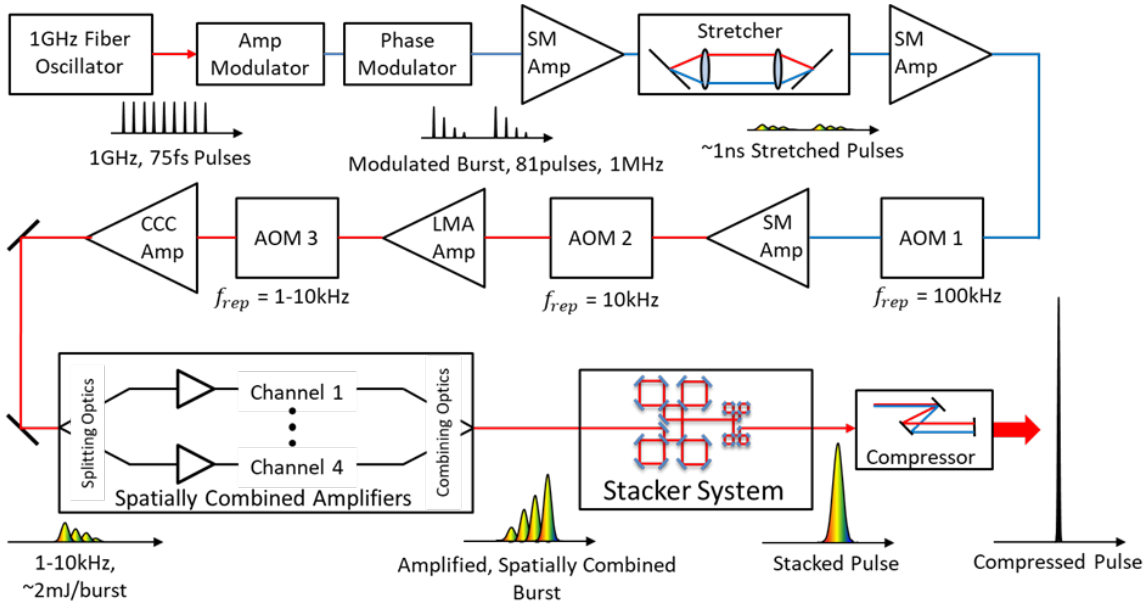

Figure 3.2: The experimental setup for a high-repetition ultrashort pulse laser system based on coherent beam combining and coherent pulse stacking amplification in Yb-doped fibers. Figure courtesy of Alex Rainville.

The spectrally broadband and ultrashort seed for this novel CPA system are delivered by a nonlinear polarization rotation modelocked oscillator operating at ∼1 GHz. A high-fidelity electro-optic (EO) timing signal derived from this module provides the asynchronous master clock to a system of high-speed field programmable gate arrays (FPGAs) that control all major system parameters. Prior to injection into the dispersive grating stretchers, a pair of EO phase and amplitude modulators window and shape stacking bursts of 81 pulses at a rate of f_{burst} =1 MHz. This burst pre-shaping compensates for gain saturation effects of the later amplification stages and imparts all-important initial phase control of the individual pulses. Loss incurred in the shaping stage is then recovered by passing the burst through a single-mode (SM) booster amplifier. Pulses are then stretched to approximately 1 ns in

duration in a grating stretcher. An alternating series of acousto-optic modulators (AOM) and successive amplifiers perform two tasks: (1) the burst is down counted to a frequency of f_{rep} 1-10 kHz to ensure proper saturation dynamics within the CCC amplifiers and (2) the mode field diameter (MFD) is iteratively increased to match the acceptance mode of the CBC amplifiers and mitigate unwanted nonlinear phase accumulation.

The pulse burst now passes through a chicane of symmetric 50/50 beamsplitters and is injected with equal amplitude into each CCC fiber amplifier. A series of FPGA-controlled PZT mirror mounts dynamically phase the burst sequence entering each spatial channel to ensure optimized coherent combining following power amplification. Up to 7 mJ of energy is extracted in each amplifier to provide a nominally combined output energy of $\sim$20 mJ at the input of the GTI stacker cavities. At the CBC output, the parallel channels are again combined via 50/50 beamsplitters, and the output is split between feedback diagnostics running the combining algorithm and the input of the GTI stackers. The stackers consist of a serial N+1 cavity configuration [27], where the burst phase is actively controlled using PZT actuators to manipulate tip, tilt, and piston motion of a single high reflector (HR) mirror within each cavity. Upon exiting the stacker cavities, the optical energy of each pulse in the burst has now been temporally stacked into the 81st pulse of the burst train. A stochastic gradient descent (SGD) machine-learning algorithm optimizes the burst stacking by monitoring SHG conversion in a multi-GHz fast photodiode located post-compressor. The system's compressor is of a folded Treacy design and features a half-wave plate and thin-film polarizer attenuator. Under experimental operation, the CBC + CPSA delivers up to 21 GW of peak power at a scalable repetition rate of 2-10 kHz.

3.2 Ultrashort pulse characterization

The efficiency of ion acceleration and by extension laser-driven fusion neutron yield is sensitive to the peak on-target intensity delivered by a tightly focused ultrashort laser. Temporal

optimization of the pulse compression is achieved by self-referencing optical measurement of the pulse duration and iterative adjustment of the system stretcher and compressor to remove residual chirp. Analogously then, spatial optimization of the focused beam requires magnified imaging diagnostics to characterize axial symmetry and intensity.

3.2.1 Pulse duration measurement

Ultrafast laser pulses have the shortest duration of any temporal events ever technologically synthesized by humans. Accordingly, measurement and characterization of optical pulses is non-trivial as all currently available "high speed" photodetectors and large bandwidth oscilloscopes are still 100-1000 times slower than pulses generated by modern CPA lasers. For this reason, ultrashort pulse measurement is cleverly obtained using the pulse itself as the reference. Two well-established techniques for this purpose are intensity autocorrelation and second harmonic generation frequency-resolved gating (SHG-FROG), both were diagnostically fielded during shot campaigns of this work.

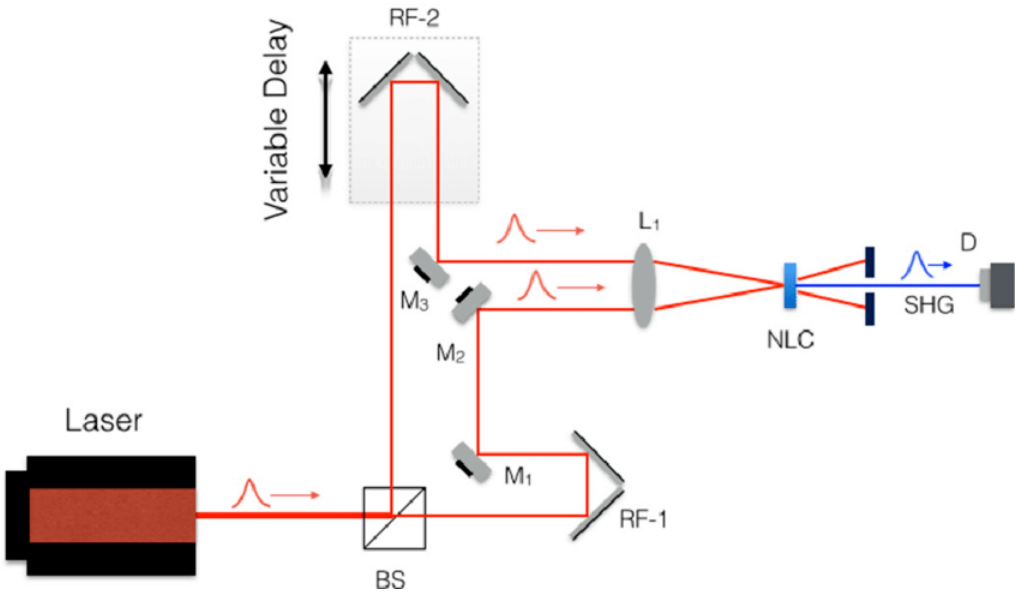

Figure 3.3: A common non-collinear intensity autocorrelator optical setup. Optomechanical component abbreviations - BS: beam splitter, M: mirror, NLC: nonlinear crystal, RF: retroreflector, D: detector, L: lens. Figure from Ref. [10] used with permission.

Due to its narrower gain bandwidth, transform-limited pulses of >300 fs duration were typical of the CPSA fiber system used in Chapter 6. Compressed pulses from the primary laser driver and the diagnostic backlight probe were measured and optimized using the intensity autocorrelation method. The operating principle of this system requires dividing the input laser pulse into two copies, typically with a thin beam-splitting optic. In one arm of the device, the replicated pulse is delayed by electromechanical means and is then focused to overlap with the reference pulse in a nonlinear crystal. Due to their high intensity, the superimposed beams will generate a bisecting SHG signal that is a function of the lag between the two pulses. Successive symmetric scans of this delay generate a pulse shape which can then be fitted to the delay calibration. The second-order correlation function is given by:

$$A_c(\tau) = \int_{-\infty}^{\infty} I(t)I(t-\tau)dt \tag{3.1}$$

where $I(t)$ is the pulse intensity in the reference arm and $I(t-\tau)$ is the pulse intensity in the delayed arm, t is time, and τ is the variable time delay between the two pulses. The resulting signal $A_c(\tau)$ is integrated by a slow detector, such as an avalanche photodiode. In the case of an ideal wing-free pulse, the temporal width of the pulse is obtained by dividing the measured correlation function signal by known fitting factors - 1.543 and 1.414 for the sech^2 and Gaussian fit respectively.

Figure 3.3 shows a representative layout of the non-collinear geometry. In our system, the calibrated delay is scanned via a computer-controlled voice coil module, the nonlinear crystal is a $\sim$100 μm β-barium borate (BBO) crystal, and the envelope detector consists of an appropriately biased photomultiplier tube (PMT) with high quantum efficiency for the 515 nm SHG signal. Prior to entering the PMT photocathode, the SHG signal is passed via a blue-green filter to reject fundamental laser light at 1035 nm. Voltages from the PMT are cleaned with an RF low-pass filter and read out on a 2 GHz oscilloscope at 10 GSa/s (Agilent).

Field autocorrelation is a simple and robust method for quantitatively characterizing the duration of an ultrashort pulse but because it lacks any information regarding the pulse's spectral phase it is unable to recover any information regarding residual chirp. One key take-away from this fact is that an intensity autocorrelation cannot distinguish between a narrow-band transform-limited pulse and a broadband laser pulse that has been poorly compressed. Consequently, experimental manipulation of the pulse duration by DAZZLER applied phase or compressor grating adjustment benefits from the application of the SHG-FROG technique. During λ^3 experiments in Chapters 4-5 a commercial PC-controlled FROG device (SwampOptics Model 8-9-USB) was used to *completely* characterize the CPA output pulse train.

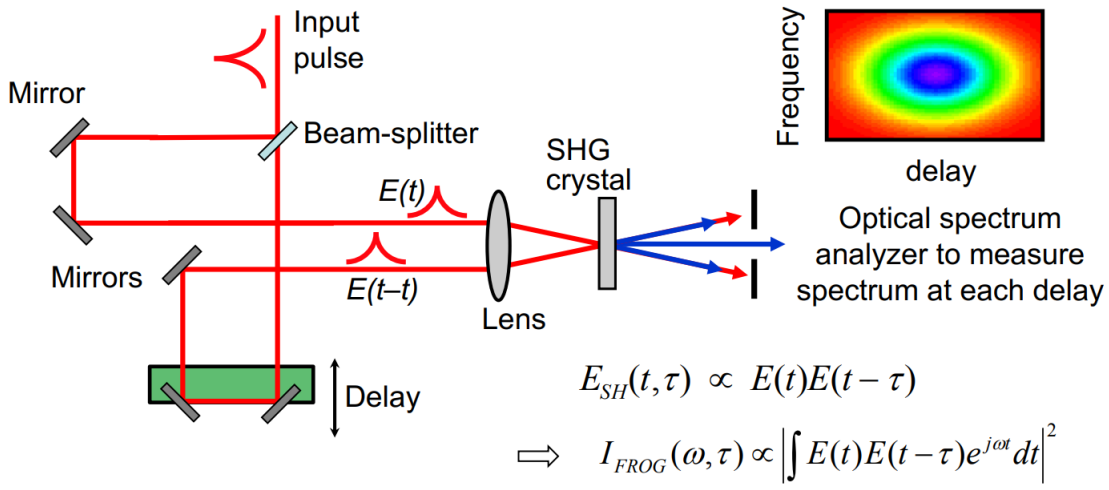

Figure 3.4: Schematic of a non-collinear SHG-FROG for ultrashort pulse characterization. From the public domain.

Frequency-resolved optical gating captures both the time-dependent intensity and spectral phase of an ultrashort pulse. As shown in Figure 3.4, the rough optical layout of a FROG is nearly identical to that of an autocorrelator but with the critical addition of an optical spectrometer. This adaption was first demonstrated in [98] and allows for iterative reconstruction of the time-dependent electric field of an ultrashort laser pulse. Convention-

ally the two-dimensional spectrogram trace generated by an SHG-FROG system is referred to as a FROG trace and is analytically described by

$$I_{\mathrm{SHG-FROG}}(\omega,\tau) = \left| \int_{-\infty}^{\infty} E(t)E(t-\tau)\exp[-i\omega t]dt \right|^2 . \tag{3.2}$$

Reconstruction of the laser pulse's electric field is achieved by a computer algorithm with minimal computational overhead. Time ambiguity of the trace is a notable drawback of the SHG-FROG technique as the trace always exhibits symmetry about the time axis. Familiarity with spectrogram features allows an experimenter to heuristically add or remove dispersion to lengthen a pulse and proves beneficial in removing phase errors imparted by poor compressor grating alignment. Shown in Figure 3.5 below, spectral hole drilling and dispersion pre-compensation with a DAZZLER results in nearly transform-limited pulses from the relativistic λ^3 USPL system.

3.2.2 Spot size measurement

Under experimental conditions, tight focusing ($< f/2$) geometries are used to deliver the highest possible beam intensities on target. To prevent beam self-focusing or phase distortion of the compressed pulses, transmissive lenses generally cannot be used above a few GW peak power. To avoid imparting spherical aberration, throughout this work d = 50.8 mm low dispersion metallic (Ag or Au) [Chapter 4 & 5] or dielectric coated [Chapter 6] off-axis parabolic (OAP) mirrors were used as final focusing optics. Technical limitations in the surface flatness of OAPs result in reflected wavefront error of $\lambda/4$ RMS or larger and will lead to non-negligible focusing error in the far-field beam profile.

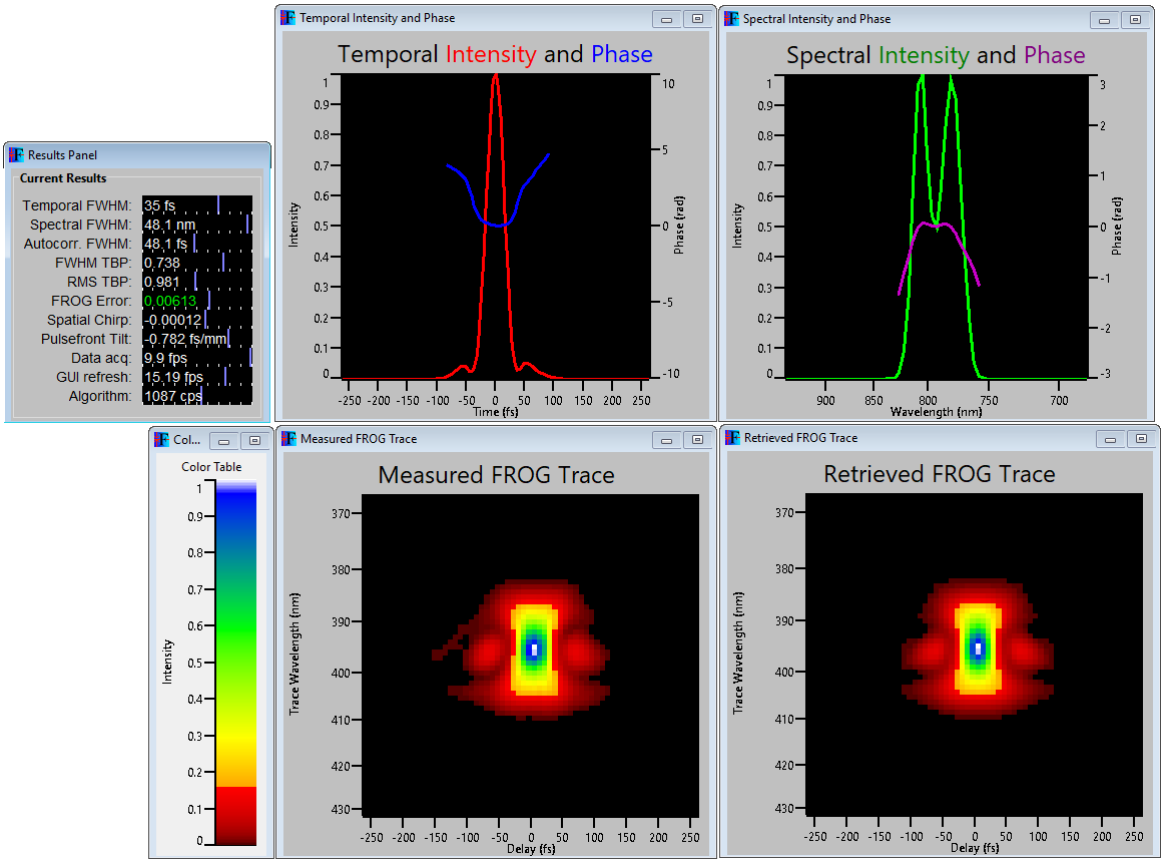

Figure 3.5: A $\tau = 35$ fs pulse experimentally measured during this thesis work by the SHG-FROG technique.

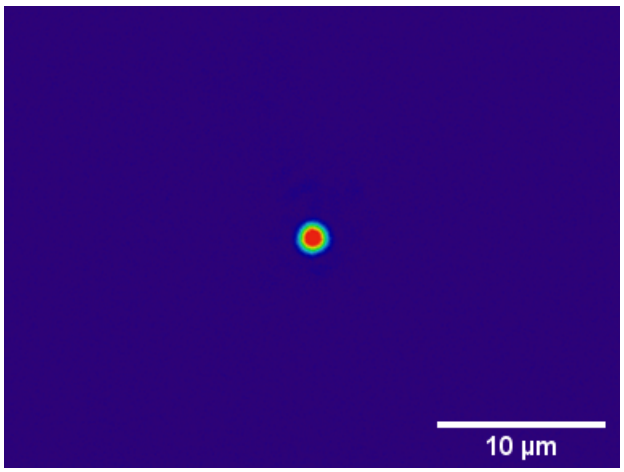

Figure 3.6: A 2.86 μm $1/e^2$ focal spot imaged with a 50x NIR apochromatic microscope objective and CCD during characterization of the EHD experiment.

Rough manual optimization of an initially astigmatic focus was performed by focusing

$\sim$ 1 mJ at the best system compression point at atmospheric conditions and optimizing the spatial convergence of the laser-induced plasma discharge. Fine optimization and measurement of the beam profile at the focus was performed by significantly attenuating the laser output power below the air breakdown threshold and imaging the focal plane onto a CCD with a long working distance microscope objective. θ_x and θ_y adjustments were then incrementally performed until the beam's best focus was obtained. Absolute spatial calibration was then obtained by imaging a back-lit USAF 1951 resolution test plate or x-ray test grid with known bar sizes. An empirical methodology to recover a near-diffraction-limited Gaussian profile using adaptive optics will be discussed further in the following section.

3.3 Radiation diagnostics

Various radiation detection instruments were utilized as plasma and fusion diagnostics throughout this thesis work. Gaseous discharge and semiconductor photon detectors were used to characterize and optimize X-ray emission from interactions of focused ultrashort laser pulses with near-solid density targets. Simultaneously, a suite of thermal and fast neutron detectors was fielded to monitor both the average and instantaneous shot-to-shot flux during LDNS experiments employing high repetition liquid targets.

3.3.1 Geiger-Müller detector

Ionizing radiation detectors operating in the Geiger-Müller (GM or G-M) discharge regime are commonplace in radiation detection applications. First invented by Geiger and Müller in 1928 [99], these devices comprise one of three generalized categories of gas-filled detectors, with ion chambers and proportional counters defining the remaining two. Similar to proportional detectors, G-M detectors harness gas multiplication to enhance the charge associated with ion-pair (IP) generation along the track of ionizing radiation passing through the detector body. The fundamental similarity ends here because the increased bias voltage

applied in G-M regime creates substantially higher electric fields than those of a proportional counter. As a result, IP-seeded avalanche events proceed as a self-propagating chain with exponential pulse buildup occurring over only a few microseconds. Collective charge effects ultimately terminate charge accumulation but this limiting point is usually associated with the same number of avalanche events regardless of the incident radiation energy. It follows that all pulse events initiated from a GM tube are approximately the same amplitude and detector functionality is suited only for counting or survey applications [100].

During all high-repetition liquid targetry shot runs, a halogen-quenched end-window GM tube (Ludlum 44-7) matched with an analog dose survey meter (Ludlum Model 15) was fielded in close proximity of the target focus. In all instances, the tube's mica window was oriented with a line of sight to the laser-target focus to provide a basic radiation safety survey and for optimized target positioning following chamber evacuation.

3.3.2 Helium-3 proportional detectors

In-situ detection of fusion neutrons emitted from intense laser-plasma-initiated nuclear reactions remains a technically challenging effort. Neutrons are neutral particles and therefore cannot directly trigger ionizing events along their flight paths through matter. Additionally, energetic neutrons above ∼300 eV do not exhibit strong capture or resonance reactions and necessitate detection by elastic scattering interactions in hydrocarbon materials with scintillation properties. Thermalization of neutron fields with low Z materials (water, plastic, graphite) can however allow for feasible detection via inelastic capture reactions in materials with high absorption cross sections. At the cost of eliminating virtually if not all spectroscopic and timing data imprinted on the neutron during its emission, thermal detection allows for a robust survey and online counting with gas proportional tubes.

Helium-3 along with Boron-10, Gadolinium-157, and Lithium-6 fall into a unique category of isotopes for which the interaction probability of thermal neutrons with the atomic nucleus is "large". He-3 is an inert gaseous daughter product of tritium decay and is terrestrially

scarce. With a capture cross-section of 5330 b (1 barn = 10^{-24} cm^2) for the reaction given in Equation 3.3, He-3 is considered a gold standard for thermal neutron detection.

$$ {}^{1}_{0}\mathrm{n} + {}^{3}_{2}\mathrm{He} \rightarrow {}^{3}_{1}\mathrm{H} + {}^{1}_{1}\mathrm{H} + 0.764 \text{ MeV} \tag{3.3} $$

Thermal neutron proportional detectors filled with ^{3}He or BF_3 operate with an applied anode bias that generally falls between that applied to ion-chambers and GM tubes. During inelastic reactions with the fill gas, thermal neutrons will release kinetically energetic daughter ions that cause follow-on pair generation as they recoil in the tube. Avalanche dynamics due to the 1/R field near the wire electrode in the tube are directly proportional to the kinematic energy deposited by ion Bragg stopping in the detector volume. Specific care must be taken in biasing this tube such that it remains in the quasi-linear response region of the detector operation curve. From the conservation of momentum and appropriate scaling with their rest mass, the proton and triton liberated from a He-3 capture are ejected with 573 keV and 191 keV respectively. Amplified pulse height measured from a proportional detector corresponds with the deposited energy and contributes to the excellent gamma rejection exhibited by detectors of this type. Below the thermal peak of 764 keV, two plateau regions in the pulse height spectrum are prevalent and can be understood as *wall effects* [100]. These areas of incomplete energy deposition correspond to loss of the proton or triton through tube cathode wall. Multiplication in proportional tubes is limited and the ∼mV output pulses require gain in low noise charge sensitive preamplifiers prior to processing by upstream nuclear electronics modules.

Two separate proportional detectors were utilized as online diagnostics for neutron generation during the microscale liquid target laser-plasma experiments carried out in Chapters 4-6. The first instrument (Ludlum Model 42-31H) was a polyethylene-moderated and cadmium-loaded sphere containing a tube detector with a 2 atm ^{3}He fill. The detector was paired with a digital counter and ratemeter (Ludlum Model 3001) and was commercially calibrated against a NIST traceable source. Designed as a rem-responding detector, this

system exhibits flat energy response (100 cpm per mRem/hr) across the thermal (0.025 eV) to fast ($\leq$12 MeV) neutron range. During high-intensity laser-liquid target irradiation this detector was primarily engaged in radiation safety dose monitoring and for basic spatial survey purposes.

A second He-3 detector with a significantly larger active volume was configured as a sensitive neutron counter for rudimentary optimization of the laser-plasma interactions. The detector element (GE Reuter Stokes RS-P4-808-214) contains a 4 atm charge of He-3 and is moderated within the annulus of a parallel-piped high-density polyethylene (HDPE) block. The system consists of a pre-amplifier, shaping amplifier, and timing single channel analyzer (SCA). Detector bias was set to -1750 V and by calibrating the system pulse response to a commercial D-D neutron generation (Thermo Fisher MP320) and then optimizing for gamma rejection against a 10 μCi Cesium-137 disc source. Total coarse and fine gain applied were G = 200 with 2 μs and 1 μs pulse peaking time and shaping time respectively. Pulse height discrimination of thermal neutron events was obtained by operating the SCA in the "normal" operational mode with the lower-level discriminator set for $V_{\mathrm{LLD}} = 1.3$ V and the upper-level discriminator set to its max value of V_{ULD}ULD = 10.0 V. Positive pulses corresponding to detection events were counted with a standard NIM timer/counter module and averaged by an analog rate meter. During experiments, the detector was mounted between 30-60 cm from the target focus to obtain reasonable counting rates ($\leq$1000 cpm) and avoid pile-up from plasma-induced electromagnetic pulse (EMP) interference. Background count for cosmogenic neutron events was typically 5.2$\pm$0.5 cpm as measured over statistically significant ($\gg$180 minute) periods. Intrinsic thermal detector sensitivity as reported by the manufacturer was for 26$\pm$2.6 cps/nv this proportional counter.

3.3.3 Microstructured semiconductor neutron detector

In addition to the proportional counters, the application of a solid-state thermal detector was explored for applications to optimization of the laser-driven neutron source. The growing

scarcity of Helium-3 supplies following the rapid deployment of portal detectors over the last two decades has spurned considerable interest in other neutron detectors with comparable sensitivity. Microstructured semiconductor neutron detectors (MSND) are a relatively new class of thermal neutron detector based on capture reactions in Lithium-6 or Boron-10 doped P-N diodes. A key improvement of MSNDs over similar planar diode technology is an engineered etch process that creates features inside the semiconductor substrate that is subsequently back-filled with neutron reactive coatings. This enhancement increases the total volume of capture-sensitive material leading to higher neutron absorption efficiency and also increases the effective surface area in contact between the device's active region and the reactive film where reaction products are ejected during a thermal capture. Commercially available MSNDs are compact, γ-radiation hard, draw minimal low-voltage power, and have thermal detection efficiencies of $\varepsilon > 30\%$ for single-sided devices and $\varepsilon \leq 70\%$ for dual-stacked designs [101].

$$ {}^{1}_{0}\mathrm{n} + {}^{6}_{3}\mathrm{Li} \rightarrow {}^{4}_{2}\mathrm{He} + {}^{3}_{1}\mathrm{H} + 4.79 \text{ MeV} \tag{3.4} $$

The detection system used during LDNS experiments consisted of two 1-D tiled Domino® MSND modules coupled to an SMA-terminated electronic driver board. To moderate fast D-D neutrons generated from intense laser-plasma interactions, the entire 8 cm^2 detector area was placed at 2.5 cm depth inside of an appropriately designed HDPE block. TTL pulses from neutron detection events were recorded with a 50 Ω terminated NIM counter/timer module. Summed background and dark count event rate was measured to be 0.56±0.05 cpm as measured over statistically significant ($\gg$120 minute) periods. Intrinsic thermal neutron sensitivity for the tiled detector array is 2.4±0.8 cps/nv which empirically scaled to an approximately 1:10 counting ratio reported by the 4 atm He-3 proportional counter. The compact size of this detector allowed for close placement to the target chamber center and

3.3.4 Scintillation detectors and neutron time-of-flight

The thermal neutron detectors introduced thus far provide a great diagnostic capability for the survey and counting of moderated neutrons exiting an ultrashort laser-driven neutron source. One primary drawback in the use of these detectors is that spectroscopic data is lost in the process of achieving inelastic neutron interactions which are fundamental to the operation of capture-based detectors. Detection of fast neutrons and spectroscopic characterization of their associated energies is possible by using kinematic neutron interactions of an elastic nature. The solution of the basic momentum transfer equations shows that the maximum energy transferred to the recoil ion (E_{recoil}) is given by

$$E_{\text{recoil}} = \frac{4A}{(1+A)^2} E_n \tag{3.5}$$

where E_n is the incident neutron kinetic energy and A is the atomic mass of the recoiling ion. In a scintillation detector, neutron scattering off of light hydrocarbon materials can eject a recoil particle that will subsequently deposit its energy to the scattering medium emitting a scintillation light pulse. Recoil protons have high linear energy transfer (LET) and as they are slowed in the detector volume, Bragg effects result in almost full deposition of the energy for energy ranges pertinent to this thesis work. In specially designed liquid scintillators such as those used in this thesis work (Eljen Technologies, EJ-309), scintillation emission is well characterized [11, 102]. In properly calibrated detectors, the intensity of the light output can provide spectroscopic insight regarding the incident neutron field while the temporal shape of the scintillation pulse can enable discrimination between energetic neutron and photon radiation incident on the detector volume.

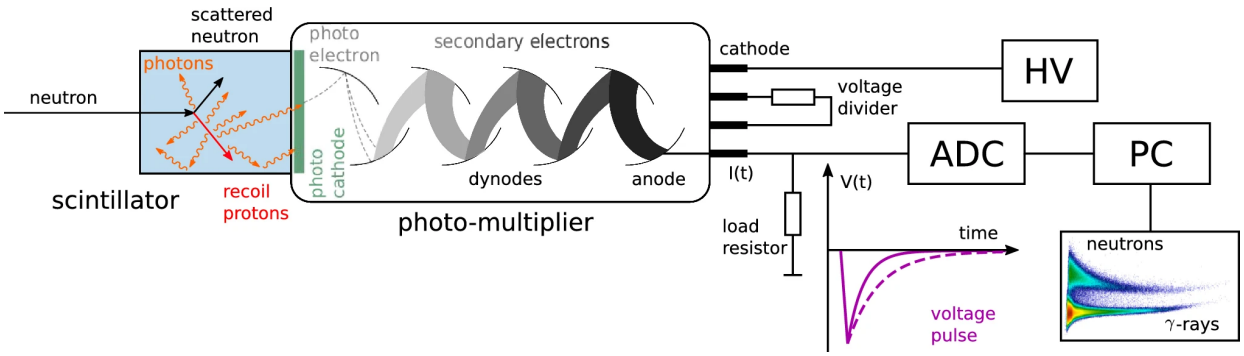

Figure 3.7: A diagram showing the operating principles of the scintillator configured for fast neutron interrogation via proton recoil. Image from Ref. [11] used with permission.

The typical configuration of a scintillation detector for neutron detection is shown in Figure 3.7. Fast neutrons incident on the scintillator element of the detector first generate recoil protons resulting in a fast (ns duration) scintillation pulse. Light emitted during ion-pair recombination is generally in the UV to blue range of the optical spectrum. Scintillation photons are coupled out of the detector volume and into a photocathode by means of refractive index matching grease and light-guide/light-pipe assemblies which further concentrate the photonic flux. The relatively weak scintillation signal is then amplified by a photomultiplier tube (PMT) that exhibits good quantum efficiency for light-to-photoelectron production for the scintillation spectral peak of interest. Amplification in the dynode stages of the PMT results in a signal gain of 50-60 dB. Electrons traversing the PMT generate a charge pulse resulting in a time-varying voltage that is read out of the anode. Pulse waveforms are read by a fast analog-to-digital converter (ADC) and data processing is performed with a PC.

To reduce detector noise induced by the high voltage electromagnetic pulse (EMP) and prompt γ-flash associated with placing scintillation detectors in close proximity of the laser-liquid target interactions, pulse shape discrimination (PSD) filtering was used for online processing of the pulse signals from the liquid scintillation detectors. Using the difference in the long-lived fluorescence decay in EJ-309 between photon-induced electron recoil scintillation (short) and neutron-induced proton recoil scintillation (long), photon and neutron signals may be discriminated via the definition of a pulse shape parameter (PSP) which

serves as a surrogate for the relative length of the pulse.

$$PSP = \frac{Q_{total} - Q_{short}}{Q_{total}} = \frac{Q_{long}}{Q_{total}} \tag{3.6}$$

Calculation of the PSP is shown in Eq. 3.6, wherein Q_{total} is the entire integrated charge for a single scintillation pulse, Q_{short} is the integrated charge in the fast decay component and Q_{long} total integrated charge in the pulse tail [103]. In our experiment, these parameters were configured in the CAEN CoMPASS software suite with specified gate, short gate, and pre-gate values of 400 ns, 48 ns, and 24 ns respectively. Q_{total} is the integrated charge beginning with the pre-gate and accumulated to the gate time where the integration windows are defined relative to the time of trigger. Q_{long} is all charge integrated within the time window between the short gate and the gate. The light output of each liquid scintillator was independently calibrated using the Compton edge of a ^{137}Cs gamma source. Fast neutron energy vs. PSP binning parameters were calibrated using a sealed tube D-D neutron generator with an approximate isotropic flux of 1-2$\times 10^6$ n/sec (ThermoFisher MP320). Figure 3.8 shows this calibration setup.

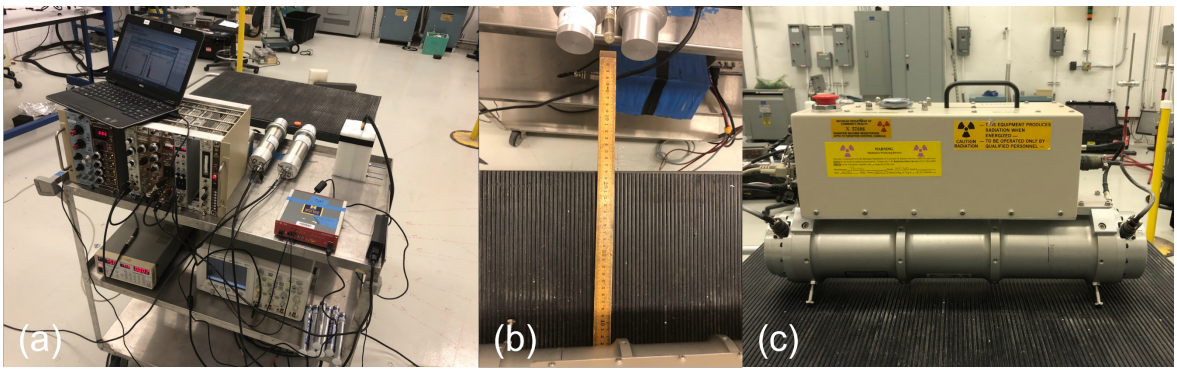

Figure 3.8: Liquid scintillator neutron response calibration performed in the University of Michigan Neutron Science Laboratory. (a) EJ-309 scintillators and other neutron detectors were used during experimental campaigns. Detector standoff measured (b) measured to the target axis (c) of a commercial D-D sealed tube neutron source.

Neutron time-of-flight (nTOF) is a powerful spectral diagnostic for characterizing the kinetics of fast neutron fluxes. Employment of this technique requires a well-characterized

flight distance L_{flight} between a neutron source as well as the neutron's flight time Δt as measured with a time-gated fast recoil detector. These two values can be used to calculate the particle velocity and therefore its kinetic energy at the time of creation. The relativistic kinetic energy of a neutron is given by

$$E_n = (\gamma - 1)m_n c^2 \tag{3.7}$$

where m_n is the neutron mass, γ the relativistic Lorentz factor, and c the vacuum speed of light. The energy of the characteristic neutron expected from D(d,n)^{3}He thermonuclear fusion reaction has a well-known value of $E_n = 2.45$ MeV. A maximum normalized vector potential of $a_0 \simeq 2$ was expected during deuterated liquid target experiments carried out in this work and the resulting peak ion temperatures were not expected to exceed 3 MeV based on similar campaigns carried out in Ref. [40, 45, 104]. The neutron has a rest mass energy of 939.37 MeV and we can therefore reasonably conclude that fast neutrons expected during LDNS experiments of the thesis are non-relativistic. Simple binomial expansion then gives us the classical kinetic energy

$$E_n = \left[(1 + \frac{v_n^2}{2c^2}) - 1\right] m_n c^2 = \frac{m_n v_n^2}{2} \tag{3.8}$$

further substitution of the particle flight length and flight time coupled with simple algebraic manipulation gives the following expression for the detected neutron's energy

$$E_n = \frac{m_n (\frac{L_{\text{Flight}}}{\Delta t})^2}{2 \cdot 1.602177 \times 10^{-19} (\text{J/eV})} \quad [\text{MeV}] \tag{3.9}$$

A combination PSD/nTOF fast neutron system was fielded as a primary particle detection diagnostic during all laser-driven neutron experiments. A minimum of two cylindrical 50x50 mm liquid scintillators (Eljen Technologies, EJ-309 510-20x20-11/309) coupled to fast PMTs (Hamamatsu, R7724) were used at calibrated distances from the target chamber center (TCC). PMT bias was applied with a computer-controlled desktop high voltage

supply (CAEN Electronics, DT5533E). Pulse waveforms from each detector were captured on CH2/CH3 respectively of a 500 MSa/s digitizer loaded with pulse shape discrimination (PSD) firmware (CAEN Electronics, DT5730S DPP-PSD). Hardware triggering of the $\tau_{\text{coincidence}} = 512$ ns window was initiated utilizing a high-fidelity femtosecond oscillator-derived TTL timing signal provided to CH0/CH1 buffers of the digitizer and zeroed using a 1 ns rise time Si photodiode (Thorlabs, DET10A) monitoring ultrashort driver pulses entering the target chamber sourced to digitizer CH4. Particle flight time Δt was calculated through post-processing FPGA time-stamped, binned, fast neutron events and subtraction of the summed pulse delay from: (1) pulse transit time in 50 Ω terminated RG-58/U coaxial cables, (2) PMT electron transit time, (3) PMT pulse transit time spread, and (4) photodiode rise time. Experimental fast neutron energy spectra were deconvolved in MATLAB using Eq. 3.9.

3.3.5 Neutron bubble detectors

Absolute measurement of the shot-to-shot flux delivered from laser-driven neutron sources is technically rigorous for the following reasons: 1) intense laser-plasma interactions generate significant bremsstrahlung that can trigger false detection in virtually all pulse-based detection methods due to finite gamma rejection properties, 2) high-Z shielding required to minimize the impact of mixed field presence ultimately places detectors further from the source leading to diminished fluence at the detector position, 3) the intrinsic pulsed nature of the source increases the probability of under-counting caused by detector pile-up, 4) direct fast neutron detection through elastic recoil is inefficient and required moderation leads to ms scale response times in more sensitive thermal counting modes. In legacy experiments on 0.001-0.1 Hz petawatt-class USPL drivers, some of these factors were mitigated by long recovery periods between each laser shot and the large $\gg 10^7$ n/sr/shot yields generated [105]. For kHz repetition-rate experiments, time-averaging of the neuron dose is an accepted measurement for approximating isotropic source flux. The use of superheated droplet recoil

detectors (bubble detectors) has been a universally accepted metrology to this end since their introduction to the dosimetry field in 1979 [106].

As their name suggests, bubble detectors operate continuously on the principle of particle radiation-driven nucleation. The detector volume consists of overexpanded (superheated) hydrocarbon or halocarbon emulsions [107, 108]. These metastable droplets vaporize when they are irreversibly nucleated during recoil interactions caused by charged particle recoils. Macroscopic bubble generation occurs when recoil events generate a trail of sub-microscopic vapor cavities which exceed the critical radius for bubble formation [107]. Bubble detectors provide direct fast neutron dose monitoring and exhibit flat response across neutron energies ranging from 0.2-15 MeV. The dosimeter itself is a completely passive detector and the accumulated dose can be read by manual inspection or in cases of large doses, read out via a computer. Following dose exposure, the bubble detectors are reset by rethreading the compression piston into the detector body and waiting 25-30 minutes. A large LET is required to generate macroscopic bubbles and as a superlative consequence, bubble detectors are x-ray and gamma blind and may be fielded in close proximity to intense mixed field sources. To deconvolve the neutron flux to which the detector was exposed, the bubble count must be first converted back to dose as per NCRP38 and ICRU66 standards, then, the dose is scaled using neutron energy range estimates found in Table 1004(B).2 in 10 CFR 20. Calibrated model PD-BND personal bubble dosimeters (Bubble Tech Industries) with a responsivity of ≥ 20 b/mrem were used directly during Chapters 4 and 5, and for coincidence detector response calibration in Chapter 6.

3.3.6 Semiconductor photon detectors

Basic radiation detection and counting performed by a standard GM tube lacks any information regarding the type of incident ionizing radiation and its spectral energy content. All on-target focused intensities realized during experiments with the USPL systems described in this work will result in significant hard X-ray and possibly γ-ray emission. Spectroscopic

characterization of these emitted photons provides critical insight into the approximate temperature thermal temperature of the plasma electrons (T_e), and in turn, can be used as a metric for the efficiency of laser-plasma energy coupling. ponderomotive scaling for relativistic intensities empirically derived as $T_h = 215(I^{18}\lambda^2)^{1/3}$ keV in [109] predicts that the hot electron temperature encountered during liquid target experiments will exhibit a cutoff of $\sim$ 140 keV. This upper energy limit for bremsstrahlung radiation is well suited for measurement by solid-state CdTe single photon detectors. With active areas composed of cadmium (Z = 48) and tellurium (Z = 52), diodes in these detectors operate in a photoelectric effect-dominated regime and as such are highly sensitive lower energy photons. CdTe also has a band gap energy of 1.52 eV and is less susceptible to thermal noise that necessitates cryo-cooling of high-purity germanium (HPGe) detectors. A thermoelectric-cooled CdTe detector with a 25 mm^2 active area and 100 μm Be entrance window (Amptek XR-100) was paired with integrated shaping electronics to provide real-time spectroscopy of radiation emitted from laser-target interactions.

Polynomial calibration of the ADC channel bins to photon energy in keV was accomplished by 180-second live time measurements of a $\sim$1 μCi Americium-241 placed in line-of-sight to the detector's entrance window. Well-defined x-ray and γ-ray peaks at 13.95 keV and 59.54 keV were used for fitting. Device gain was set to G = 2.0 with a 3.2 μs shaping time, while channel 24 was set as the LLD threshold to prevent spurious pile-up from EMP. Prior to any experimental measurement the detector was allowed to stabilize for 10 minutes following device cooling to 232 K and application of the 1000 V bias.

3.4 Adaptive Optics

Significant distortions to the optical wavefront of a laser beam will result in poor ability to focus the beam. In the high-power laser systems used in this thesis work, such distortions are a consequence of finite optical diffraction, thermal deformation of optical components at high

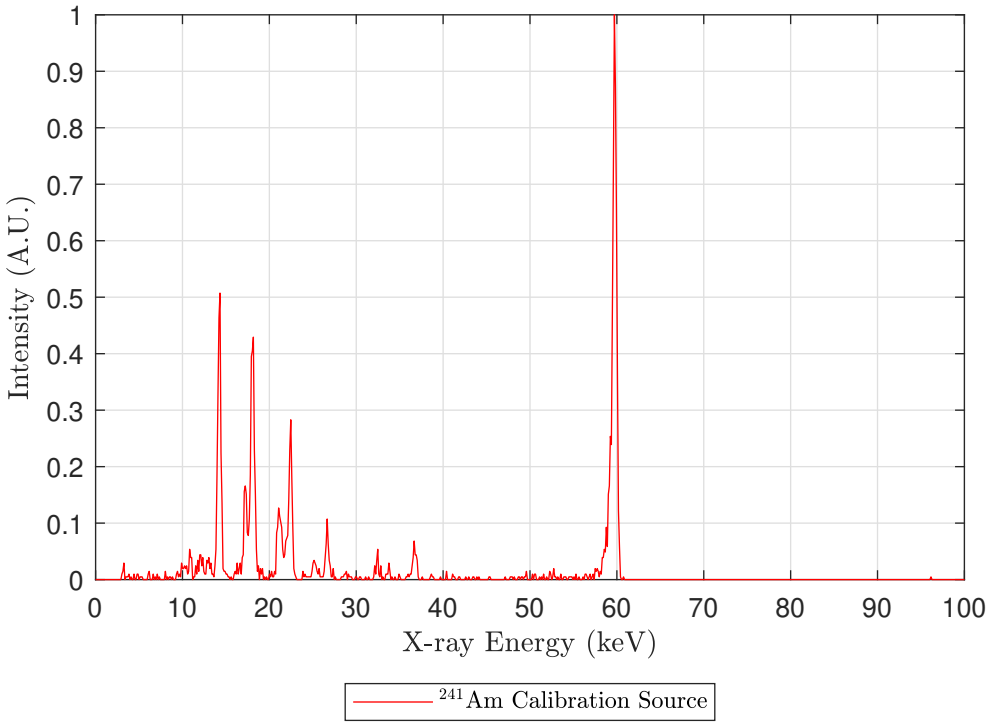

Figure 3.9: A channel-to-energy calibration spectra recorded from a 180s live time measurement of an ^{241}Am check source.

average power, mounting stress on large aperture optics, and imperfect alignment of telescope systems used to manipulate the beam size. Ultrashort laser-matter interactions are very sensitive to the peak intensity of the driving laser pulse and uncorrected beam aberrations cause two major problems: (1) the focused intensity of the beam is far lower than that predicted by using a diffraction-limited focus, and (2) geometric deformation of the focused beam and the resulting energy spread out of the center of the focus is unpredictable on a shot-to-shot basis which leads to poor ability to exactly recreate experimental conditions. Adaptive optics (AO) were originally developed for astronomical [110] and military [111] applications to correct beam degradation due to atmospheric propagation. AO utilizes a closed-loop feedback-based system of optimization where the wavefront is first measured, error from ideal propagation is calculated and then an active mirror element is actuated to

compensate for the measured error. Within well-characterized optical systems, this can be achieved on a single-shot basis but typically multiple iterations are required.

Recent work has focused on applying this powerful technique to optimize the wavefront quality of high-power femtosecond lasers. Experimental demonstrations reported in [112] have resulted in record-focused intensities through the recovery of near diffraction limited focal spots and reduction in compressed pulse duration. Deformable mirrors (DM) are one of the enabling technologies for this effort and consist of a flexible mirror substrate that is physically bonded to addressable piezoelectric or micro-electromechanical (MEMS) actuators. Feedback from wavefront or intensity sampling is then used to manipulate the actuators resulting in corrective deformations of the mirror surface. Optimization of the focused beam profile and resulting on-target peak intensity of the Lambda Cubed USPL was instrumental in laser-driven neutron campaigns discussed in Chapters 4 and 5 of this thesis work. This section will provide details on the deformable mirror's characteristics and the use of an evolutionary algorithm (from here forward called a genetic algorithm or GA) to optimize beam parameters according to a quantitative Figure-of-Merit (FOM).

3.4.1 Deformable mirror

The NIR compressed output beam of the λ^3 USPL is first expanded in a 2:1 off-axis Cassegrain telescope to an approximately 50 mm $1/e^2$ Gaussian beam diameter. Prior to routing to the various laser plasma experimental chambers, this beam is reflected off a protective silver-coated surface normal deformable mirror (Northrop Grumman AOA Xinetics DM37PMNS4). This mirror consists of 37 individual electrostrictive actuator channels, each with up to 4μm of available stroke. High voltage bias is applied to the DM by a custom AOA serial-to-ADC which is controlled by NI LabView modules controlled by a custom Python GUI. Application of a 40 V drive signal to all actuators results in a "neutral" mirror shape with corresponding $\lambda/4$ surface figure. During experiments, the applied bias voltage is restricted to $V_{mirror} = 40 \pm 30$ Volts to reduce actuator stress and prolong DM lifetime. The

clear aperture of the DM truncates the final usable beam diameter to approximately ∼47 mm and is usually associated with a nominal 10-12% reduction in pulse energy to scattering.

3.4.2 Genetic algorithm

The nonlinear dynamics associated with laser plasmas interactions represent a complex multi-dimensional parameter space. Machine learning (ML), artificial intelligence (AI), and evolutionary algorithms are well suited to optimize particular experimental parameters such as electron beam emittance, LWFA bunch charge, and peak laser intensity. Previous work by Albert *et al.* led to the development and implementation of an adaptable genetic algorithm code widely used within the University of Michigan High-Field Science cohort [113]. This genetic algorithm (GA) is a representative subset of evolutionary algorithms wherein optimization is based on the concept of survival of the fittest. Solution space parameters colloquially known as chromosomes are made up of strings of integers that represent parameters to be optimized. Integer values within the strings are known as genes and as in nature, the algorithm progresses toward an optimal solution by retaining the best genes from previous generations while discarding those which do not yield improvement to the fitness function. Iterative operation of the GA results in stochastic optimization of a fitness function usually referred to as a Figure-of-Merit (FOM).

A flow chart illustrating the basic looping operation of a GA is shown in Figure 3.10. An initial population of *parents* with corresponding genes can be initialized randomly or from a previously optimized solution set. Possible parameter space solutions corresponding with this initial population is then tested by the user-specified FOM and quantitatively ranked for fitness. During the process of *reproduction*, a percentage (in practice 10-20 %) of the highly-ranked parents are retained to ensure the next trial generation at worst performs as well as the previous generation. From this set of parents a new population of *children* are created through processes of *crossover* and *mutation*, heuristically shown in Figure 3.11. During the crossover, the genes of two selected parents are blended to create a hybrid offspring.

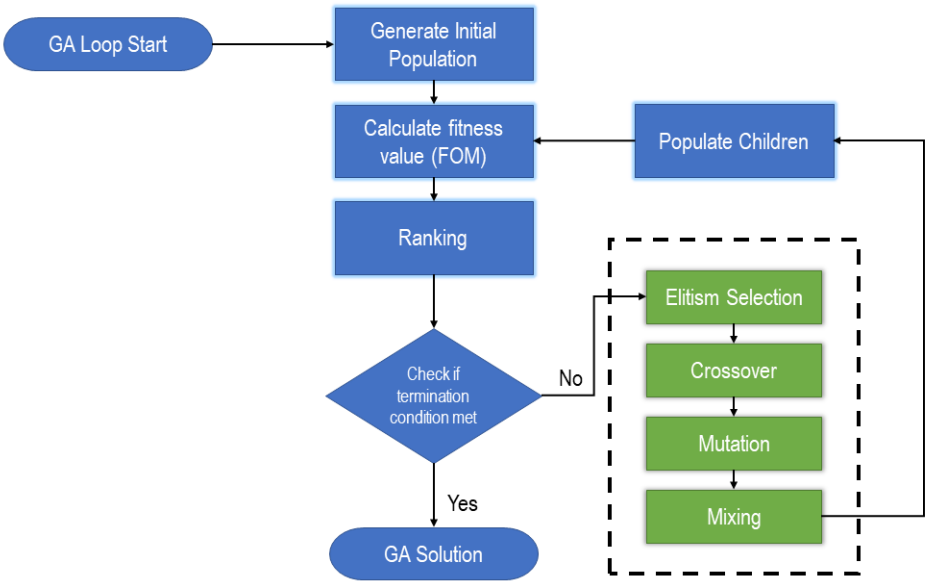

Figure 3.10: The working principle of a genetic algorithm.

Next, a certain percentage of children are then selected on a random basis, and random alterations are performed to their genes. This randomization step is critical to ensuring that the global parameter search space traversed by the GA does not arbitrarily converge on a local maximum. At this point, the algorithm now evaluates all hereditary population members relative to the FOM. In instances where all children are found to be quantitatively inferior to the previous generation, a certain number of the highly-ranked parents are stored and mixed with the children to form the next test generation. The GA loop progresses in this manner until a specified termination condition is reached.

In this thesis work, the second-order moment of the intensity registered on the pixels of a CCD camera was used as the FOM. In this system, an objective was used to magnify and image the heavily attenuated beam profile of the λ^3 beam at focus. Data from this image was parsed by a Python-based GA whose genes represented bias voltages applied to the 37 electrostrictive actuators of the DM. During optimization, a wavefront-correcting "best mirror" resulting in the highest intensity at the focus was obtained after 40-70 iterations of

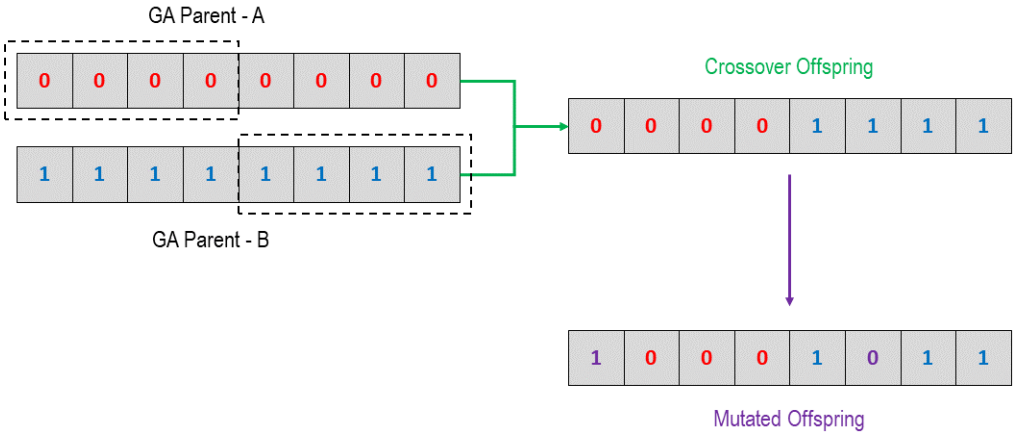

Figure 3.11: A simple example of the crossover (*green*) and mutation processes (*purple*) applied to sets of chromosomes. The crossover process uses a single-point operator identified by the dashed rectangle overlaid on the parents.

the GA. The algorithm's first generation was seeded with small mutations to an initially flat DM with all actuators set to the middle of their stroke (40 V applied bias). Application of this AO technique resulted in optimized relativistic on-target intensity used to generate neutrons from the EHD jet target in Chapter 4 and quasi-Gaussian beam profiles required for the synthesis of symmetric Laguerre-Gaussian beam modes explored in Chapter 5.

CHAPTER 4

Electrohydrodynamic Microjet Target

4.1 Introduction

Target synthesis at >1 kHz repetition rates remains a technical challenge for laser ion acceleration schemes. Tape drives [114], rotating target platters [115], Gatling gun [51] style mechanisms, and thin-film swipers [116] have enabled fresh target replacement per shot but generally suffer from mechanical alignment hysteresis and target depletion within thousands of shot cycles. Similarly, while producing highly efficient neutron yields through Coulomb explosion, molecular cluster gas jets [50, 117] and cryogenic nozzles [118, 119] often require complex helium cooling systems and impart significant differential pumping demand ($\geq$1000 L/s) on target chambers. Therefore, liquid targets based on droplets, streams, and leaves constitute the only technically feasible path for scaling towards multi-kHz acceleration regimes [40, 45, 56, 59, 104, 120]. Recently, there has been considerable interest in developing so-called "mass limited" targets, which benefit from enhanced ion acceleration due to target volume scales which are efficiently matched to the focused Gaussian beam diameter of the driving laser. Consequently, reduced target mass achieves increased plasma heating through electron recirculation [121] and the isolation of the target volume yields increased thermonuclear fusion interaction cross sections through bulk thermal heating and Coulomb explosion [59]. Recent advances in photonic architectures and nonlinear compression systems have developed a path toward relativistic ultrashort drivers with repetition rates ranging from

0.001-1 MHz. Such systems when coupled with suitably engineered high repetition solid density targets could realize high-brightness tabletop radiation sources with the capability of continuous operation.

Electrohydrodynamic (EHD) pulsating liquid jets have been explored for a wide variety of additive printing applications [122–127]. As a microjet and droplet generation mechanism, EHD jetting is considered one of the few fluid extraction mechanisms that can generate microfluidic features with dimensions an order of magnitude smaller than the inner diameter of the emitting nozzle [127]. This remarkable feature of the EHD fluid extraction mechanism leads to sub-micrometer printing resolution with viscous colloidal or entrained solutions that would otherwise irreversibly clog ultrafine piezo jet printing nozzles. Our work adapts this printing technology and extends its application to high repetition, mass-limited target synthesis, for ultrashort laser-driven fusion neutron sources. The tight focusing geometries used to create near diffraction-limited relativistic on-target intensities usually are accompanied by beam waists and a depth of focus (defined as two times the Rayleigh range z_R) that are only a few microns in spatial extent. Using pulsed EHD cone jetting, we were able to synchronously generate deuterated liquid targets of similar scale that optimize absorption of laser energy resulting in favorable ion kinetics for D-D fusion at tabletop scales. Microscale EHD fluid targets exhibit many advantages over free-flowing liquid jets [40, 45] and piezoelectric droplet generators [56, 104], namely: (1) reduced target fluid consumption due to single nL/min-μL/min operational flow rates, (2) < 5 μm feature sizes, (3) the capability of operating in accelerator beamline vacuum conditions, (4) repetition rate scaling above 8.4 kHz, and (5) pulsed target generation "on demand."

This chapter covers the design, development, and testing of an electrohydrodynamic jet target for mass-limited laser plasma particle acceleration applications. Experiments performed with a kHz-class relativistic driver confirm the capability of the target system to operate over millions of shot cycles and demonstrate for the first time, D(d,n)^{3}He fusion neutron production from colliding relativistic femtosecond pulses with electronically syn-

chronized microscale jet targets. Various regimes of EHD target operation are characterized and optimized target synthesis parameters are reported.

4.2 Electrohydrodynamic (EHD) target system

4.2.1 Theory of operation

The dynamic behavior of liquids in the presence of strong applied electric fields has been investigated for over a century for its many applications to aerosol science, materials science, biomedicine, and materials processing. Electrohydrodynamic atomization (EHDA) is a categorical label given to the generation of aerosols, jets, and fine droplets by active perturbation of liquids or suspensions by an applied voltage [128]. Pioneering theoretical work by Sir Geoffrey Taylor in 1964 led to a comprehensive mathematical model for the surface stress imparted on the meniscus of a liquid droplet under applied electrostatic stress [129].

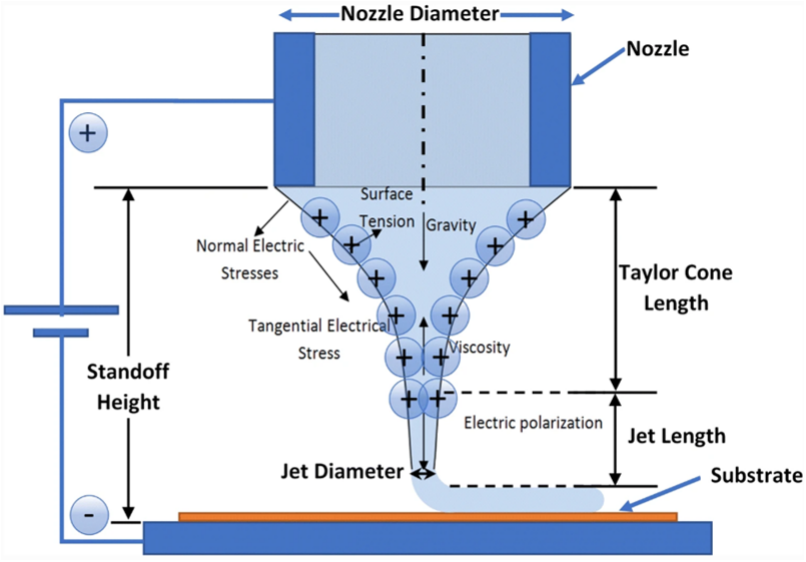

Figure 4.1: Forces acting upon the fluid during stabilized electrohydrodynamic cone jetting. Figure from [12] used with permission.

The fundamental dynamics of EHD jet nozzles (see Figure 4.1) in additive microscale printing processes have been extensively reported by various groups [124, 125, 127]. In the

typical configuration, a conductive nozzle backed by a pressurized fluid source is mounted at a stand-off distance of 100-1000 μm from a grounded extraction plane. Fluid pumped through the nozzle will form a spherical meniscus with a diameter that is approximately equal to the inner diameter of the nozzle. Stabilized jetting of the EHD nozzle is accomplished by transiently electrostatically biasing the nozzle and therefore target fluid via transient high voltage pulses. Application of this external electric field results in the migration of mobile ionic species within the fluid to the outer surface of the meniscus [122]. This accumulation of surface charge causes Coulombic repulsion which deforms the meniscus via tangentially applied stress. Further increases to the applied field cause prolate deformation of the meniscus, and upon application of a critical potential Φ_0, the meniscus will suddenly transition to a cone-like shape. The resulting Taylor cone [129] exhibits a characteristic half opening angle of $\theta_{\text{Taylor}} = 49.3^\circ$ [130]. Additional bias in excess of the Φ_0 yields an EHD boundary transition between macroscopic charged droplet ejection and microscale jetting from the apex of the cone structure. The fluid neck-down during this process can result in jet features with up to 25:1, as in our experiment, reductions in diameter relative to the inner diameter of the conductive nozzle. In the Rayleigh limit, this filamentary fluid extension then goes on to break up into fine droplets. During the application of a continuous DC bias, droplet ejection results in a transitory charge-depleted fluid that subsequently retracts to form an unperturbed meniscus at the nozzle output. A stochastic, oscillatory, EHD cone jet cycle will proceed in this manner as the charge repetitively accumulates and is depleted from the fluid surface.

In our experiment, spatiotemporally synchronized jetting was accomplished by biasing the EHD nozzle with multi-kHz repetition high voltage pulses. Stabilized, deterministic operation of our nozzle in the cone jet regime was accomplished by triggering jet operation at integer multiples (10-20x) of the λ^3 laser's repetition rate $f = 480.374$ Hz. By electronically matching the duty cycle of the bias pulse to the temporal duration of a single jet cycle (operating under DC bias potential of the same peak magnitude) one obtains pulse "on demand"

operation of the EHD cone jet. During our experiment, microscale liquid target generation in this manner was further empirically optimized through the application of a superimposed offset voltage on the extraction pulse shape. In this scheme, the fluid meniscus does not completely relax, and the onset of jetting corresponds with the next applied transient bias. Our nozzle operates within this pulsed cone-jetting mode as a consequence of applied fluid backing pressure, absence of drag forces under technical vacuum, and applied offset voltage.

4.2.2 Additive manufacturing of vacuum chambers

As part of this experimental work, advanced additive manufacturing was explored to rapidly prototype target chambers and test assemblies. Stereolithography (SLA) 3D printing was developed in 1986 and has quickly scaled in fundamental capabilities related to printing material, print speed and print spatial resolution. When paired with modern computer-aided design (CAD) software, SLA printing provides a powerful tool to synthesize complex spatial geometries that would otherwise prove intractable to machine with computer numerical control (CNC) techniques. Recently, $\lambda = 405$ nm (near UV) curable polymer resins have been developed that provide highly stable finished workpieces with virtually no residual volatile organic compounds that result in long-term out-gassing. The use of SLA-printed vacuum target chambers for these experiments accomplished three goals: (1) adaptable design allowed for the operation of optical diagnostics at atmospheric conditions, (2) modular chamber geometry reduced dead space and stand-off distance required for secondary radiation detectors, and (3) an overall reduction in the iteration time between EHD nozzle testing, revision, and manufacturing.

Computer 3D models were built in TrueSpace 7.6 software and rendered as 3D objects in the .stl format. Appropriately scaled models were then uploaded into print preprocessing software (CHITUBOX 64) and the required supports and raft were added to aid in physical printing. Slicing was performed in 50 μm vertical layers with 10-12 layers in the bottom layer count. Optimal bottom and layer exposure times of 60 and 12 seconds respectively

were empirically determined to deliver the strongest prints and lowest associated feature defect rate. A standard desktop SLA printer (ELEGOO Mars 2K) was used to print parts which were subsequently cured and washed in a separate post-processing machine (ELEGOO Mercury Plus). An agitated bath of $> 91\%$ isopropyl alcohol was used during washing cycles of 90-120 seconds duration. Typical part curing cycles lasted 30-60 seconds depending on geometry and part complexity.

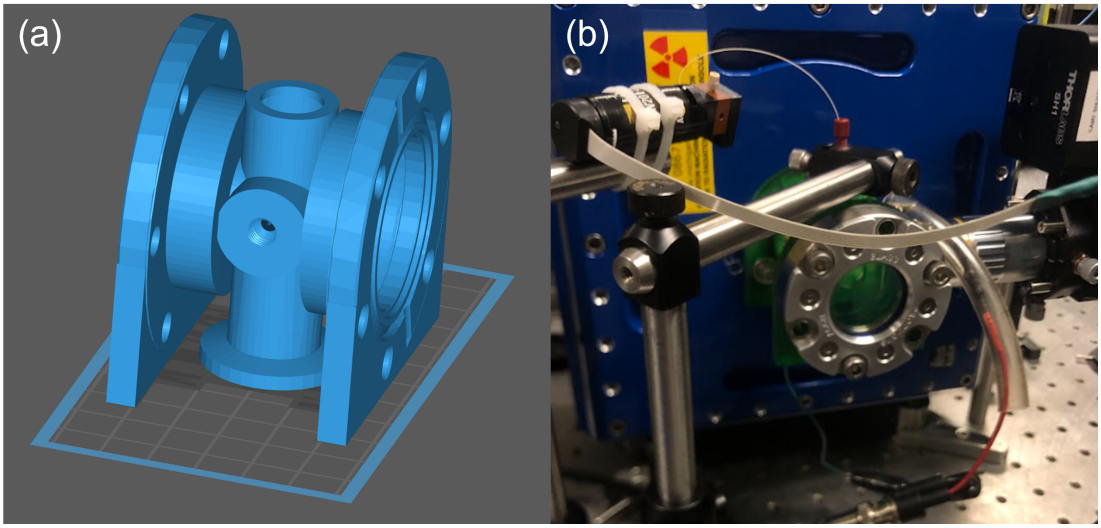

Figure 4.2: An image of the 3D vacuum chamber (a) as a sliced pre-print CAD rendering and (b) SLA printed in a photopolymer resin.

When used as part of the completed target chamber, printed vacuum components were coupled to existing commercial hardware with inert Viton gaskets. 3D-printed flanged surfaces were coated with low vapor pressure vacuum grease (Apiezon M) to ensure microscopic leak tightness. Optical grade surfaces supporting the transverse diagnostic probe were mounted with ultrahigh vacuum (UHV) grade epoxy (Hysol 1C) and allowed to cure for at least 24 hours prior to testing. A similar process was used to mount the conductive feedthrough for the EHD ground plane electrode. Extensive print testing performed throughout experimental shot campaigns performed as part of this chapter has demonstrated the capability of 3D printed parts to achieve a base pressure of $\leq 1 \times 10^{-6}$ Torr.

4.2.3 Electronic systems design and operation

Intrinsic coupling between the fluid motion response and the applied electrostatic field is one of the fundamental characteristics of electrohydrodynamic jetting. As detailed in subsection 4.2.1, Taylor cone formation is possible with applied either DC, AC, or pulsed biases. The jetting cycle will progress so long as the induced stress forces resulting from the peak field strength are in excess of the fluid surface tension and environmental forces acting upon the liquid. One notable drawback of using fluids as targets in LPA experiments is their associated alignment jitter. Specific to the EHD mechanism, this jitter can result from natural fluid dynamics, abnormalities in the local electric field, and timing errors in the application of the extraction bias. In our experiments, we determined that correctly synchronized target presentation to the focused driver pulse is of utmost importance for high-brightness secondary radiation sources. Consequently, control and minimization of timing jitter is a key system design parameter.

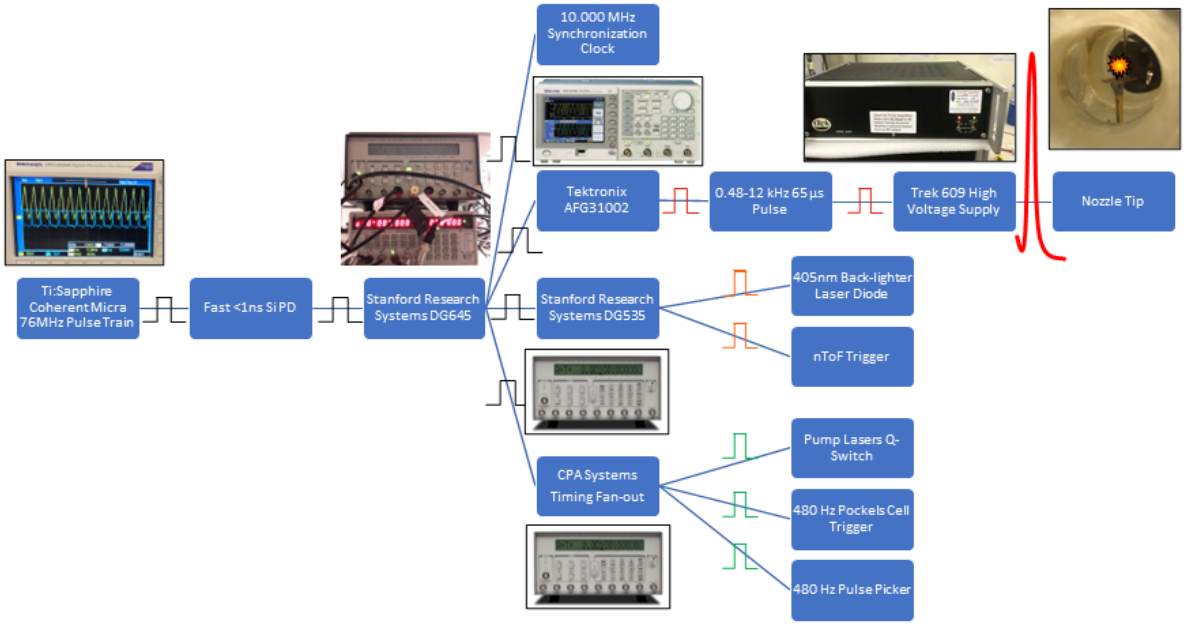

Figure 4.3: A schematic of the electronic timing and pulse synthesis change.

Arbitrary Waveform Generator Parameters	
Mode:	Triggered N-Cycle Burst
Cycles:	48
Frequency:	4.8040000 kHz
Lead Delay:	0.00 ns
Pulse High Level:	1.280 V
Pulse Low Level:	0.780 V
Pulse Width:	65.000 μs
Leading Edge:	25.00 μs
Trailing Edge:	4.000 ns
Idle State:	Start Point
Trigger Delay:	2.0076 ms

Table 4.1: AWG experimental pulse parameters for stabilized EHD operation.

To ensure deterministic target interactions, we chose to operate our target system with a pulsed high-voltage bias superimposed over a DC offset. High-fidelity timing of the extraction pulses was accomplished by triggering the extraction pulse generation with synchronous timing tied to the laser oscillator. Figure 4.3 shows a diagram detailing the electronic timing and pulse fan out for the EHD nozzle. A synchronous electronic clock reference is derived by sampling the mode-locked oscillator beam with an intracavity photodiode. f_{rep} = 76 MHz pulses were then down-counted by a timing and delay generator (Stanford Research Systems DG645). In the λ^3 laser chain, this master timing box synthesizes all triggers/delays for the EO pulse pickers, regenerative amplifier Pockels cell, and Q-switching of the Nd:YLF pump lasers. From this module, a 10.00±0.01 MHz external synchronization reference and TTL trigger signals were generated and fed to an arbitrary waveform generator (Tektronix AFG31002). This AWG was used to synthesize initially small-signal pulses with a linear ramp-to-square profile.

Table 4.1 details the pulse and delay parameters used throughout experimental campaigns to drive microscale EHD jetting at frequencies ranging from f_{rep} = 0.480-12 kHz. Unless otherwise noted, the parameters listed in this table were used during LDNS shot campaigns.

These extraction waveforms were then amplified at G = 1000 V/V by means of a fast slew

rate bipolar amplifier (Trek Inc. 609D-6). The high voltage pulses at the amplified output of this unit were then passed through two series 10 MΩ ballast resistors and connected to the EHD nozzle and ground plane. To prevent spurious ground loops and signal ringing in the system, the vacuum chamber, target extraction plane, and all optomechanics were bonded in a hub-spoke configuration to the earth ground terminal of the amplifier casing. Electromagnetic pulse (EMP) generation during the experiment was severe at times and clamp-on ferrite chokes were used on all serial communication and RF coaxial cables.

4.2.4 Microfluidic system design and operation

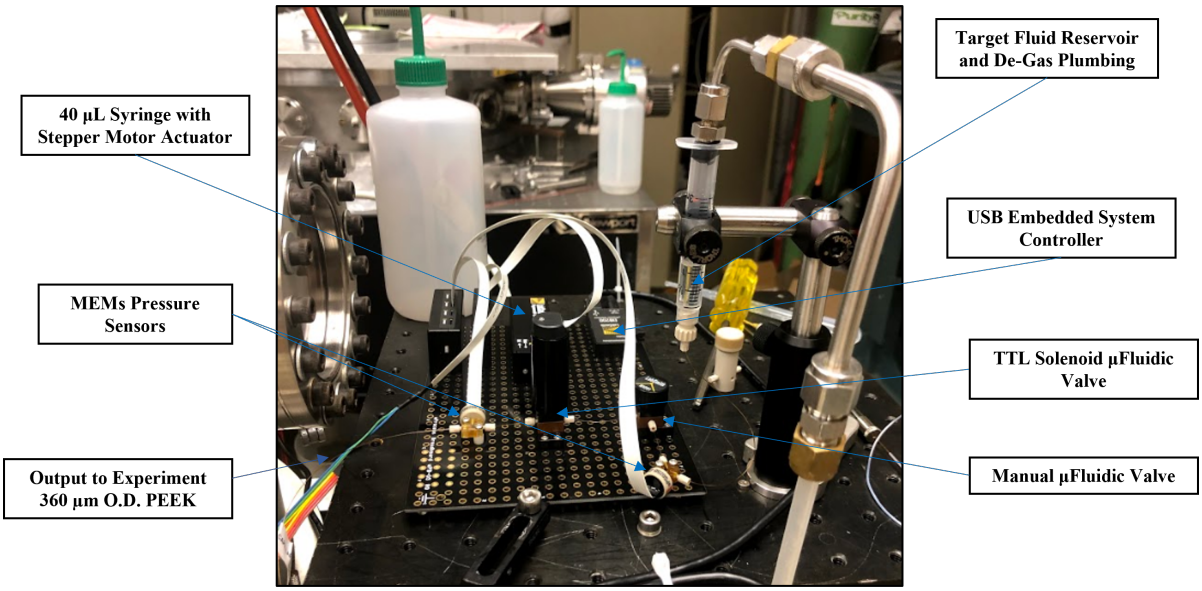

Figure 4.4: A diagram of the microfluidic components used during operation of the EHD jet target.

Stable operation of the EHD target system requires precise control of the flow rate of target fluid supplied to the syringe tip for pulsed extraction. For this purpose, a custom microfluidic handling system was constructed using commercial-off-the-shelf components. As shown in Figure 4.4, the complete system is computer controlled and allows for remote sequencing of individual devices. During operation, this system performs the following functions: (1) storage of spare target material, (2) de-gassing of the material prior to injection into the

target generator, (3) precision metering of fluid to the nozzle, and (4) isolation of the liquid-vacuum systems.

De-gassing of low-vapor pressure liquids entering a technical vacuum environment is critical to prevent the spontaneous formation of bubbles. Dissolved atmospheric gases can form expanding vapor pockets that effectively 'pump' material through from the finite dead volumes present between the final isolation valve and tip-vacuum interface of EHD nozzle. Furthermore, coalescing macroscopic bubbles prevent the stable formation of a fluid meniscus at the nozzle output. To address this problem, our system design incorporates the reservoir shown in Figure 4.4. This 3.0 cc luer lock syringe is the primary storage vessel for excess target fluid and is connected to a pneumatic manifold which allows for vacuum evacuation or venting to atmospheric pressure. A hard vacuum is pulled by means of a two-stage rotary vacuum pump on one arm of the manifold. Pressure is monitored with a standard digital vacuum gauge and is adjusted by manipulating a fine needle metering valve connecting the manifold to the atmosphere. Prior to experiments, fluids in the reservoir were de-gassed at $\sim$10 mTorrr for approximately 90 minutes.

Once de-gassed, target fluid is pulled from this reservoir and flows through an automated selector valve (LabSmith AV201) to be temporarily stored in the retracted volume of a programmable stepper-actuated syringe pump (LabSmith SPS01). During normal operation of the EHD nozzle or to initially purge the microfluidic system of trapped gas volume, the multi-port valve rotates and fluid is pumped into the back end of the target system. Connections between individual system elements are made with 300 μm O.D 150 μm I.D PEEK tubing and CapTite fittings. Prior to entering the Nanofil syringe and barrel assembly comprising the physical nozzle, the fluid stream must again pass through an automated isolation valve (AV201). This valve de-couples the microfluidic system from UHV during the initial target chamber pump down, periods of troubleshooting or during target fluid refill. Real-time sequencing of the individual microfluidic system components was controlled over USB by the uProcess software suite (LabSmith uProcess).

4.3 Target system characterization

4.3.1 Synchronized optical backlighting

The fluid dispensed during the normal operation of the pulsed EHD nozzle is not visible to the naked eye because of the microscopic spatial scales involved. Furthermore, jetting action and subsequent droplet formation occurs at speeds that are approximately two orders of magnitude faster than the response time of human visual perception. To facilitate complete spatiotemporal characterization of the jetting cycle, photomicroscopy, and pulsed shadowgraphy were implemented in tandem as part of an online experimental optical diagnostic.

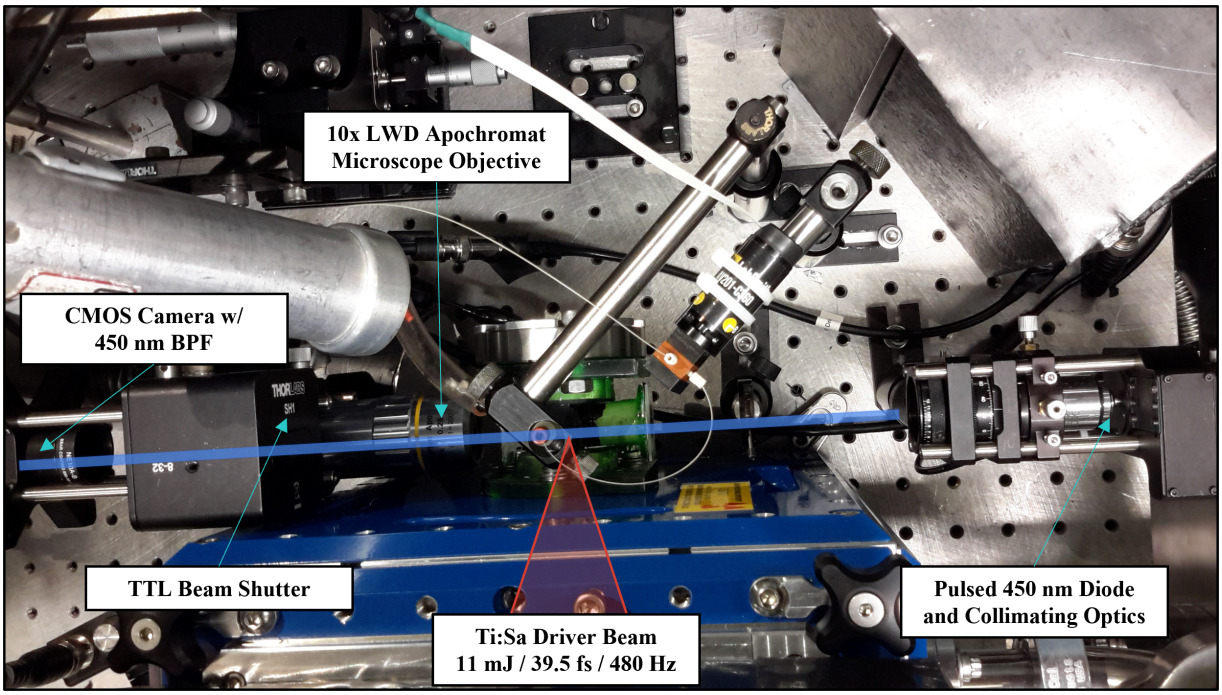

Figure 4.5: A schematic of the transverse optical backlighter.

Figure 4.5 shows the physical layout of this system. Optical micrographs of the EHD jet and target interactions are obtained by magnification and relay imaging performed with an infinity-corrected long working distance 10x microscope objective. The objective is mounted to an X-Y tip-tilt adapter set in a 30 mm cage system. Directly behind the objectives

Back-lighting was obtained through 20-50 ns pulsed operation of a P = 25 mW, $\lambda = 405$

nm InGaN laser diode. The laser diode was mounted on the center axis of a cage mount assembly with XY manipulators. A 20x microscope objective was used to both collimate and focus the elliptical spatial mode emitted by the bare diode face. To protect the laser diode from scattered femtosecond light or plasma harmonic emission a 4.0 OD hard edge band-pass filter was placed at the output of the objective facing the target volume.

4.4 High repetition relativistic laser experiment

4.4.1 Experimental setup

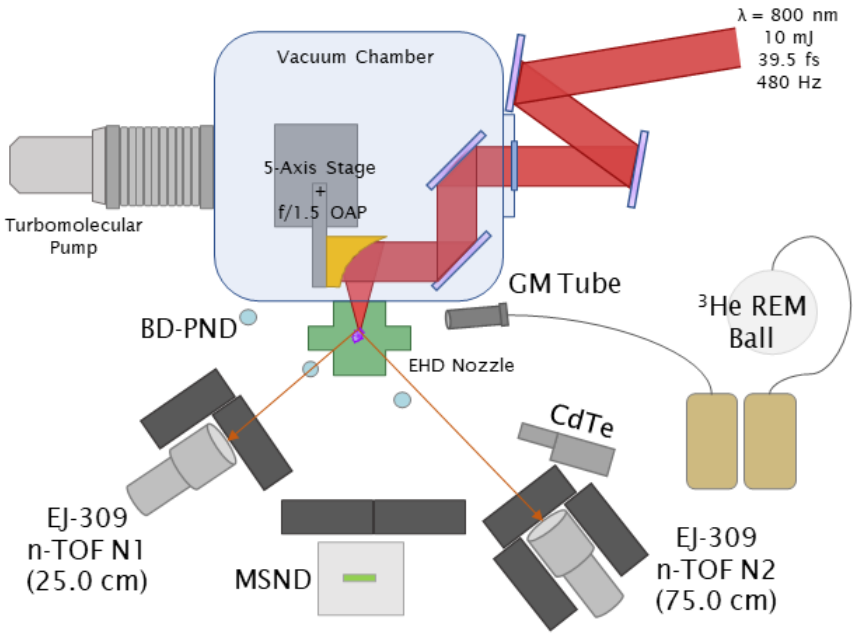

Figure 4.6: A top-down overview of the EHD neutron source experimental setup. All secondary radiation detectors are shown in their approximate position relative to the target chamber center.

Fusion neutron experiments conducted using the EHD liquid jet target were performed using the λ^3 laser facility at the University of Michigan. The basic experimental setup is shown in Figure 4.6. Although the system provides up to ~18 mJ of energy in the compressed NIR output, relay and reflection losses resulted in maximum focused on-target energy of 10.6 mJ

during this campaign. Losses were a net result of: (1) aperturing the nominally 50.8 mm Gaussian beam down to 44 mm at the AR-coated vacuum entrance window, (2) operating 0° AOI mirrors at geometrically practical folding angles (∼12-15° AOI), (3) and standard Fresnel loss on the protected gold OAP. To facilitate the compact footprint shown the Fig. 4.6 a 90° f / 1.5 off-axis parabolic (OAP) mirror was employed as the final focusing optic. Using the GA + DM optimized focal spot of 2.7 μm FWHM, a relativistic peak on-target intensity of 6.7×10^{18} W/cm^2 was used to irradiate the microscale liquid targets.

The experimental vacuum system consisted of two chambers. The primary chamber consisted of a 9" x 9" x 9" modular commercial vacuum chamber that housed the final folding optics and the OAP with its micro-positioning stage. This chamber also incorporated feed-throughs for picomotor power and control connections, pneumatic control required for venting, and large-diameter connections for pumping. Prior to shot campaigns, the chamber was evacuated at 170 L/s using two turbomolecular pumps (TMP) to a base pressure of $< 5 \times 10^{-6}$ Torr. Roughing pressure of 20 mTorr was first attained using a 7.5 CFM scroll pump (Edwards nXDS10i) and a 22.3 CFM two-stage rotary vane pump (Edwards E2M28). Chamber pressure in the molecular flow regime was monitored with a calibrated Bayard-Alpert Pirani combination gauge (Inficon BPG400) paired with a digital gauge controller (Terranova Model 970). Coupled with the primary vacuum chamber via Conflat were a 3D-printed chamber that housed the EHD jet electrodes, transverse optical viewports for the back-lighting diagnostic, and a detachable B-coated laser-grade viewport mounted in the target forward direction.

Target fluid consisted of a 40:60 ratio mixture of 98% purity deuterated ethylene glycol (DEG) (Sigma-Aldrich, CAS:15054-86-1) mixed with 99.8% purity deuterium oxide (Sigma-Aldrich, CAS:7789-20-0). DEG was selected over propylene glycol for its superior vapor pressure performance ($\leq 6 \times 10^{-2}$ Torr at 20°C). The ratio was empirically determined to maximize the D:C ratio and prevent freezing of the jet under base pressure. Volumetric flow rates commanded to the microfluidic syringe pump ranged from 2.00-4.50 μL/min and

a corresponding maximum pressure excursion to $< 5 \times 10^{-4}$ Torr in the target chamber during laser shots. For mixture ratios favoring higher volumetric fractions of D_2O, empirical testing resulted in pressure excursions above 1 mTorr which caused jetting instability due to capacitively-coupled RF discharge. Operation of the TMPs in the choked-flow regime validated that plasma discharge between the anode and cathode comprising the EHD jet nozzle was continuous at local chamber pressures in excess of 15 mTorr. This is best explained by considering the detrimental consequences of operating with a sub-mm electrode gap at an approximate minimum of the Paschen discharge (P·d) curve for a mixed volume of hydrogen and oxygen gas [131].

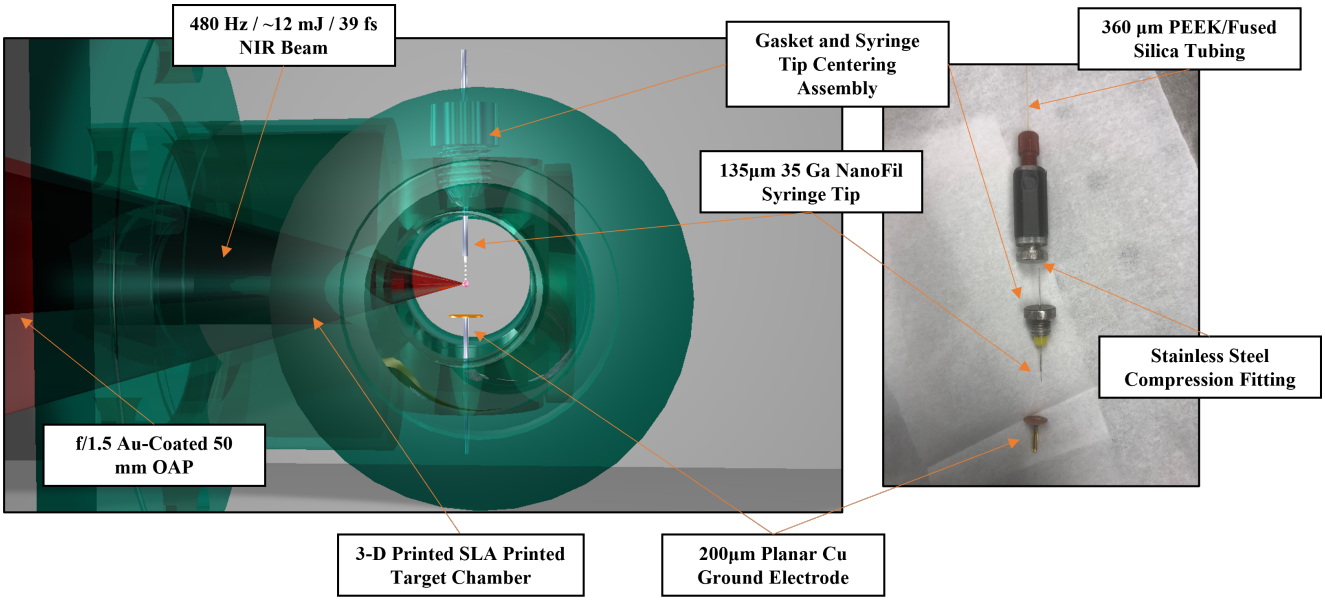

Figure 4.7: (*Left*) A CAD rendering of the 3D-printed vacuum chamber showing the mounting configuration for the EHD jet nozzle and extraction electrode. (*Right*) A photograph showing the individual unmounted microfluidic jet components.

An exploded diagrammatic view of the experimental EHD jet nozzle is shown in Figure 4.7. During laser-fusion experiments, a stainless steel 35 gauge (135/55 μm O.D./I.D) blunt syringe tip was used as the jet's output nozzle. The nozzle was mounted with an adjustable standoff above a circular copper extraction electrode. This planar electrode was formed by punching 2.5 mm diameter discs from 200 μm thick copper sheet. Mounting of the

disc to a gold-plated stalk was achieved by silver soldering at 450F. High-voltage bias was applied to the otherwise insulated nozzle by a custom ring electrode that sat between the stainless steel upper and lower annular compression fittings. Conversely, the ground plane was friction bonded over a 24 AWG copper wire penetrating the bottom of the modular vacuum chamber. The ring electrode and ground wire were then terminated into the SHV cable relaying high-voltage pulses from the output stage of the signal amplifier.

4.4.2 Focal spot optimization

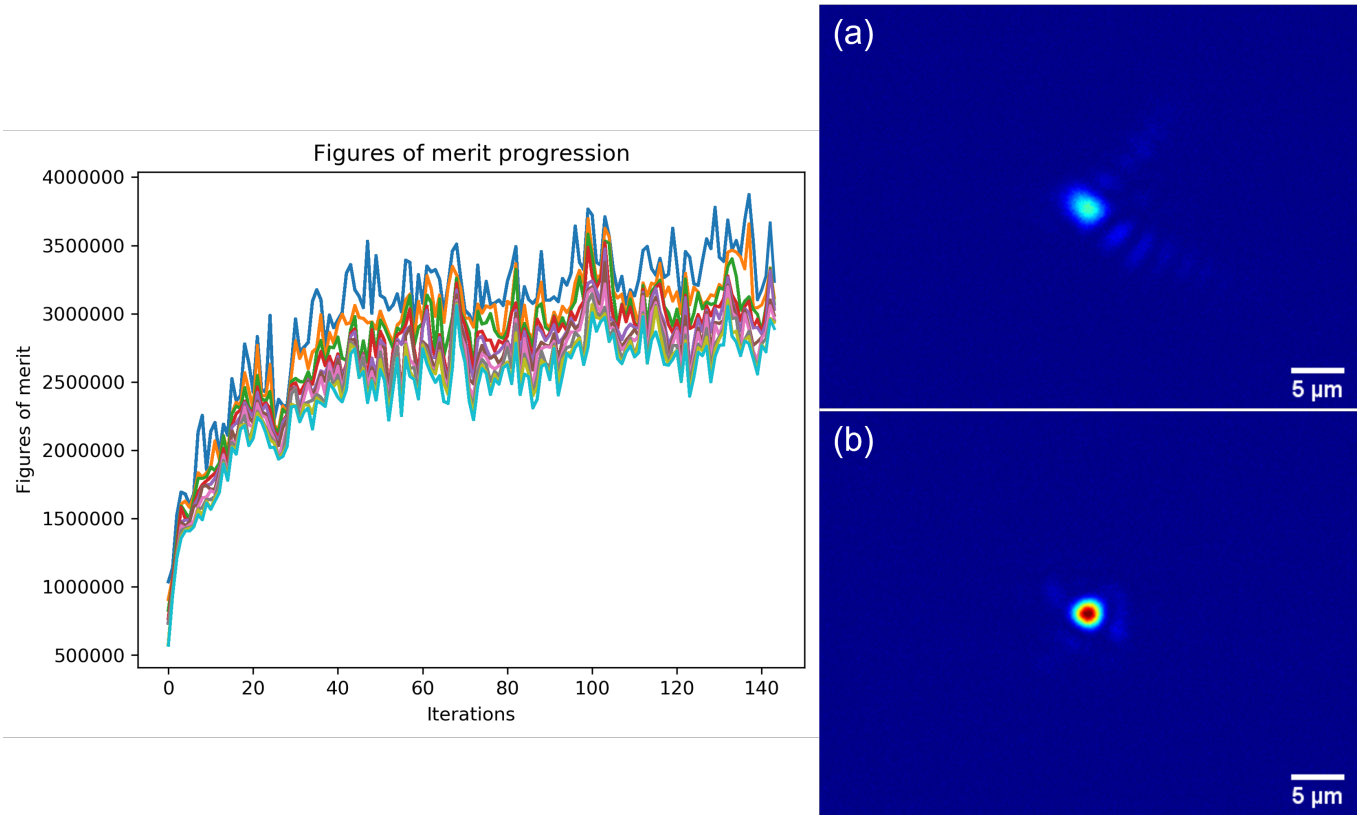

Figure 4.8: The λ^3 laser beam profile at focus (a) before GA with aberrations, and (b) after GA as a quasi-Gaussian. The left plot shows the fitness of the 10 elite parents from each successive generation as the algorithm progresses toward the optimized solution.

Focal spot optimization was used throughout the LDNS campaigns fielding the EHD target system on the λ^3 laser. Prior to evacuating the target chamber, a 50X infinity-corrected NIR objective and CCD were used to image the attenuated laser at best focus. Initial focusing

was performed by manually optimizing the OAP tip-tilt adjustment while focusing 2-3 mJ of the laser's compressed output at atmospheric conditions. When roughly aligned, the OAP focus would generate an air plasma in two locations corresponding with the astigmatic line foci of the sagittal and tangential planes. Continued adjustment of the OAP focusing in all dimensions would result in convergence of the plasma into a singular discharge and enhancement in SPM-driven conical white light generation as viewed after focus. At this point, the laser energy was reduced to a few hundred μJ using an achromatic first-order half-wave plate and thin film polarizer. Prior to viewing the magnified focus on a computer-connected CCD the beam was then further attenuated with 7 O.D. neutral density filters. Figure 4.8a shows a typical focal spot obtained using this procedure and the deformable mirror set to a uniform flat surface when biased at 40 V on all actuators. The FOM for the GA was set as the second-order moment of the intensity as measured by the individual pixels of a monochrome CCD (Imaging Source 31BU03). Elapsed time for a single evolutionary iteration of the GA was typically 60-62 seconds, with full convergence realized in 30-45 minutes. FOM enhancement was typically 5.5-7 times the initial value and resulted in the quasi-Gaussian 3.2 μm ($1/e^2$ diameter) focus shown in Fig. 4.8b.

4.4.3 Target positioning and alignment

Ensuring precise alignment of the EHD nozzle to the focused driver beam is one of the primary operational challenges encountered during high-intensity experiments. The nozzle was held rigidly in position and the focus of the UPSL beam was manipulated by closed-loop adjustment of the OAP stage. As part of the modular target chamber design, NanoFil syringe needles comprising the conductive portion of the nozzle physically penetrated the top of the chamber through a $\sim$400 μm orifice. Rough centering of the needle was accomplished by incorporation of a commercial tapered silicone gasket adapted from an ophthalmic injection system which was held in place by compression applied with an external annular retainer fitting machined from stainless steel. Height above the ground plane was set by sliding

the needle position up or down prior to tightening the compression fitting. A second non-conductive cylindrical mount was used to hold the NanoFil injection holder (World Precision Instruments, NanoFil) at calibrated height and perpendicularity above the top of the 3D-printed target chamber.

During experiments, the final focusing optic (OAP) was mounted on a 5-axis (XYZ, θ_x, θ_y) kinematic stage. Beam-based scanning was previously used during free-flowing liquid experiments in our group but open-loop actuation resulted in poor position reproducibility. Here, movement of the beam focus in the cardinal directions was obtained by closed-loop scanning with compact Picomotor actuators (Newport, Model 8311) driven by a computer-controlled closed-loop driver (Newport, Model 8734-CL). Minimum resolvable steps were $\Delta_{\text{step}} = 49.6$ nm with a full range bi-directional error of ± 1 μm. Full range homing of the CL Picomotors performed during the initial installation of the stage and relative starting position was recorded during experimental runs.

Prior to evacuating the target chamber to experimental conditions and following the optimization of the attenuated focal spot, the alignment of the target system was further optimized by steering in XYZ. To determine the precise location of the geometric focus, a visible discharge plasma was generated by focusing 500-1500 μJ of the compressed laser in air. N_2 emission spanning the visible range was imaged using the transverse optical diagnostic described in subsection 4.3.1. During alignment, the position of the discharge was centered longitudinally under the syringe tip and brought into the objective's depth of focus showing the resolved outer diameter of the tip. Figure 4.9 shows an example result of this preliminary alignment procedure.

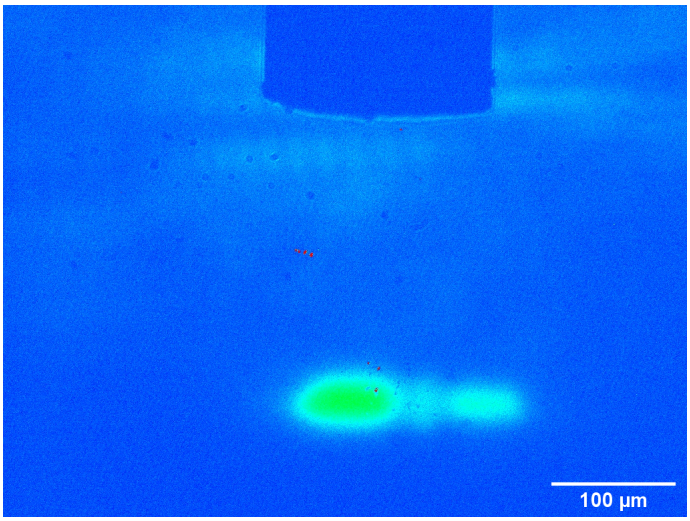

Figure 4.9: Target pre-alignment using an atmospheric breakdown plasma below a 34 Ga. syringe tip initiated with 37.8 fs, 580 μJ pulses.

To compensate for small drifts in the absolute positioning of the EHD jet nozzle during chamber evacuation, the position of the longitudinal discharge plasma was minutely adjusted to remain centered below the syringe tip. Similar adjustments were made to the transverse position of the discharge to keep the plasma channel in focus as viewed by the micrography setup. Typical adjustments were on order of < 10 μm in either direction.

Final microscale target alignment prior to full-power shot runs was performed with closed-loop control engaged on the picomotors. While monitoring the CdTe and G-M detectors, the pulse delay of the triggered AWG was stepped in successively smaller increments until plasma self-emission was viewed on the transverse probe line. The Z-height of the beam waist was chosen so that the laser focus struck at the R-T breakup point of the jet ($\sim 300 - 350$ μm below the nozzle output). Target-normal transverse positioning was achieved by stepping across the jet while monitoring for a parabolic response in the sustained count rates measured by the radiation detectors. The focus was then commanded back to the reference position of highest flux. Longitudinal positioning of the beam waist proceeded in an identical manner but was optimized at high power using the average count rate measured by the He-3 proportional detector.

4.5 Experimental results

4.5.1 Stroboscopic confirmation of EHD jet operation

This subsection contains a sample of representative high-resolution time-resolved micrographs of the EHD nozzle during vacuum operation at f = 8.4 kHz.

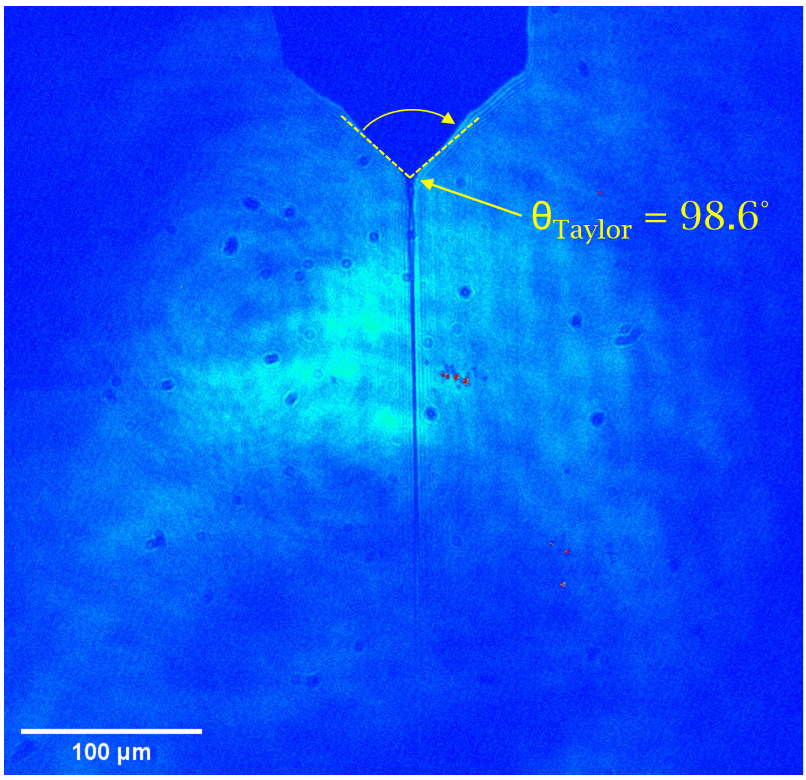

Figure 4.10: Time-resolved imaging that confirms the proper fluid flow rate associated with stable Taylor cone formation. The jet diameter was measured to be 2.7±0.5 μm prior to the onset of R-T breakup. [13]

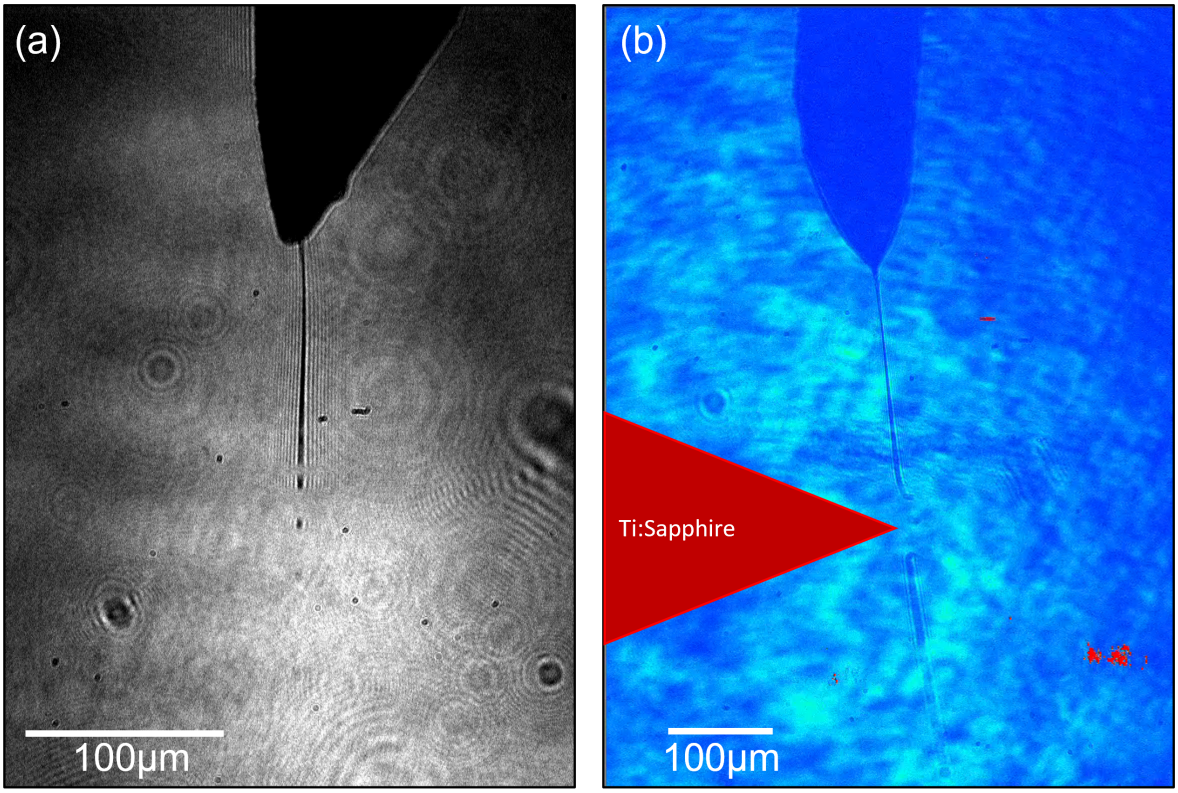

Figure 4.11: (*left*) Time-resolved images of the R-T breakup of the microjet after approximately 5 μs at a jet frequency of 8.4 kHz and (*right*) a time-resolved image of the microjet blown apart by < 10 μJ femtosecond laser pulses.

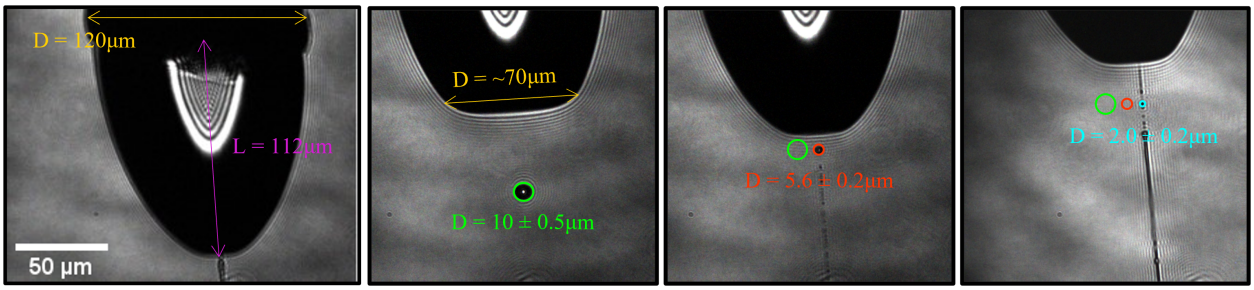

Figure 4.12: Images (*Left to Right*): Time-resolved microscopic (10x) images of EHD extraction of D_2O from a 36 Ga blunt NanoFil capillary with 1.0 μL/min flow rates. Subsequent R-T breakup induced by the Maxwell stress exceeding the fluid's capillary stress which results in ejection of a micron-scale droplet train.

4.5.2 Confirmation of jet synchronization via deterministic secondary radiation emission

Unlike the free-flowing D_2O liquid jet employed in Ref. [40], the EHD microjet operates in a kHz pulsed regime set by the arbitrary waveform generator synchronized extraction pulses. Pulsed shadowgraphy of the cone-jet in subsection 4.5.1 confirmed that, as configured, the EHD drive electronics are capable of end-to-end jetting cycles lasting less than 80 μs. In the absence of an ultra-high frame rate camera and image recognition software, coincidence detection of secondary ionizing radiation emitted during laser-plasma interactions provided quantitative confirmation of successful shot-to-shot laser hits on target. This measurement was conducted by removing the Pb shielding of the N1 EJ-309 scintillator and logging all waveforms stored during a coincidence window of $\tau_{\text{coinc}} = 512$ ns. A multichannel scaling (MCS) feature within the CAEN CoMPASS software suite was then used to plot all radiation counts with a dwell time of 1.0 seconds.

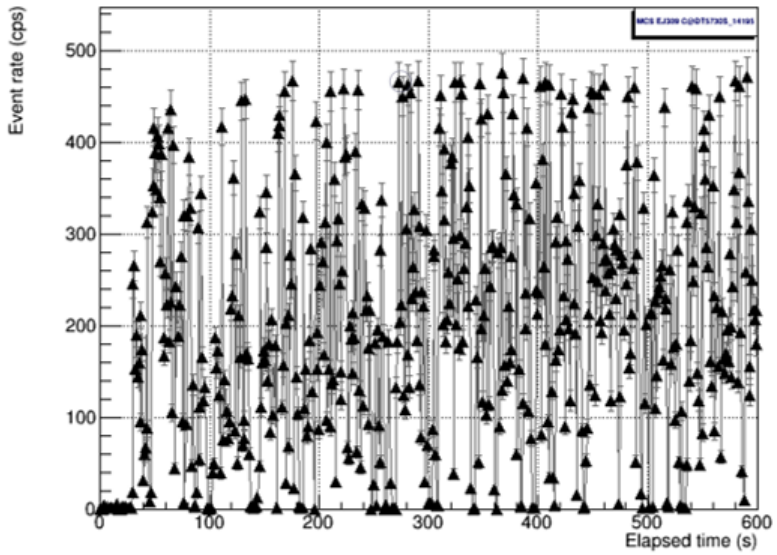

Figure 4.13: MCS readouts for laser-target radiation events registered by a triggered coincidence scintillation detector while the drive laser running at $f_{\text{rep}} = 480$ Hz.

Figure 4.13 shows total event rates (all x-ray/γ/n events) of up to the repetition rate of the drive laser. EHD target system operation was initialized 20 seconds after data acquisition

began and corresponds with the absence of events registered at the start of the MCS waterfall plot.

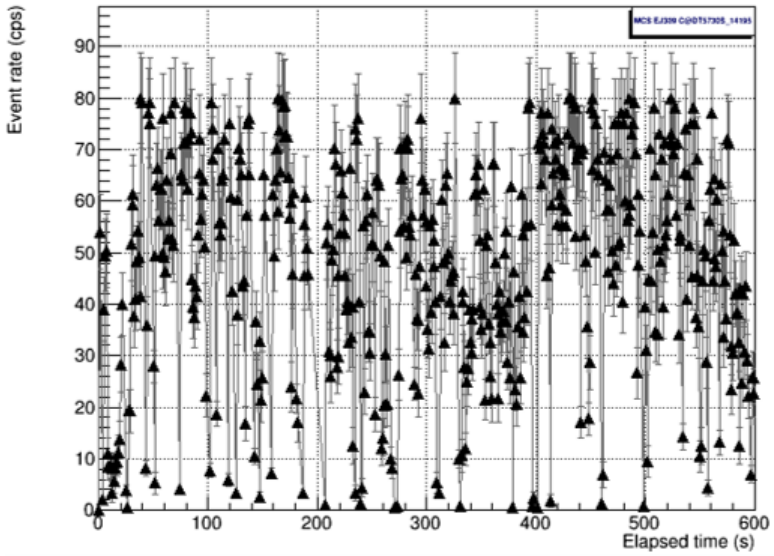

Figure 4.14: MCS readouts for laser-target radiation events registered by a triggered coincidence scintillation detector while the drive laser is chopped to an $f_{\text{rep}} = 80$ Hz.

Activation of an electronically synchronized optical chopper wheel at the output of the regenerative amplifier in the λ^3 laser allows for a 6:1 reduction the in the laser repetition rate. Figure 4.14 shows an MCS readout of radiation events measured with the chopper enabled. Again, the maximum sustained count rate shows good agreement with the modified laser frequency of $f_{\text{rep}} = 80$ Hz. Deviations from the maximum event rate are a net result of vibrational jitter caused by a lack of mechanical isolation from the vacuum pumps, and minor shot-to-shot laser pointing fluctuations intrinsic to free-air propagation of the USPL beam to the experimental chamber.

4.5.3 X-ray emission from femtosecond laser-liquid interaction

Relativistic laser interactions with an overdense target can lead to extreme acceleration gradients at the laser-plasma boundary. Resonance absorption, **JxB** heating, and Brunel heating mechanisms will create a dense plasma region at the target surface. Hot electrons

escaping in the backward direction from this region will be drawn by space-charge fields back toward the "cold" bulk target [132]. Penetration of the target and collision of these electrons with the high-Z nuclei in the target and wall materials of the vacuum chamber will generate bremsstrahlung and characteristic X-rays. Analysis of the X-ray spectra can provide valuable insight into the average temperature of the plasma and is to first order a diagnostic for characterizing the absorption of laser light into the plasma. In our experiment, a CdTe x-ray detector located d = 32.0±0.5 cm from the target center continuously monitored x-ray flux from *relativistic* laser irradiation of the deuterated jet target. While this diagnostic was not used for neutron interrogation, it aided in iterative optimization of the jet placement within the focused beam waist.

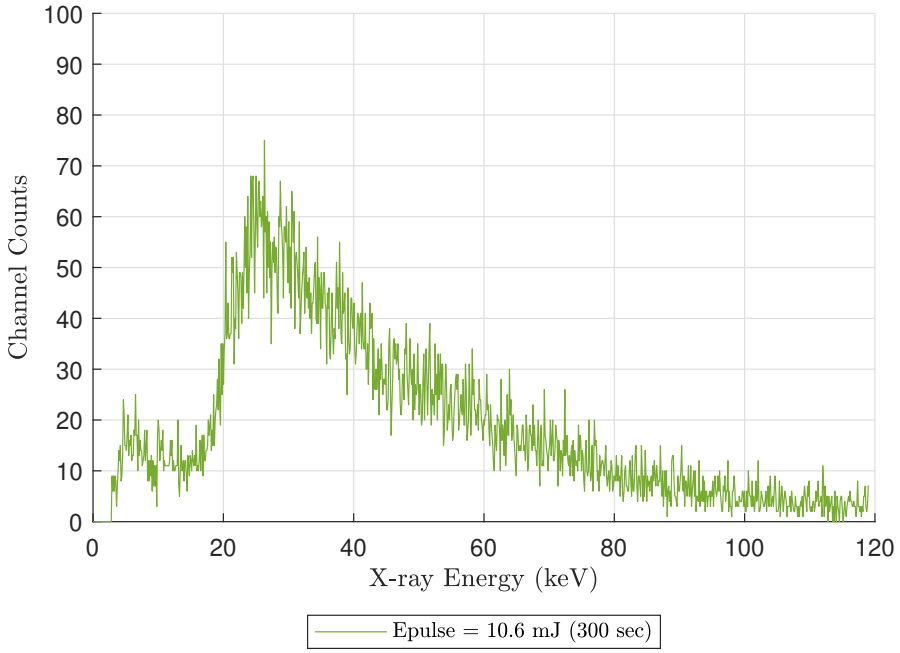

Figure 4.15: Bremsstrahlung x-ray spectra measured during a 300 second run of the EHD jet target.

The spectroscopic data shown in Figure 4.15 is representative of the x-ray flux measured during high energy laser shots correlated with isotropic D-D neutron yield of $> 4 \times 10^4$

n/s/sr. Three distinct spectral regions are shown. No binned counts are shown below 2.8 keV as this was set as the lower discrimination threshold to prevent pile-up and dead time saturation. From 2.8 keV $\leq$ E $<$ 20.3 keV, the total photon count across all channels remains well below the maximum and relatively unchanged and can be explained by considering the high attenuation of low energy photon content by the chamber walls and lossy propagation through the atmosphere. From 20.3 keV $\leq$ E $<$ 120 keV, the spectrum resembles the expected Maxwell-Boltzmann distribution attained by the plasma electrons at thermal equilibrium superimposed on a suprathermal energy tail attributed to ponderomotive acceleration.

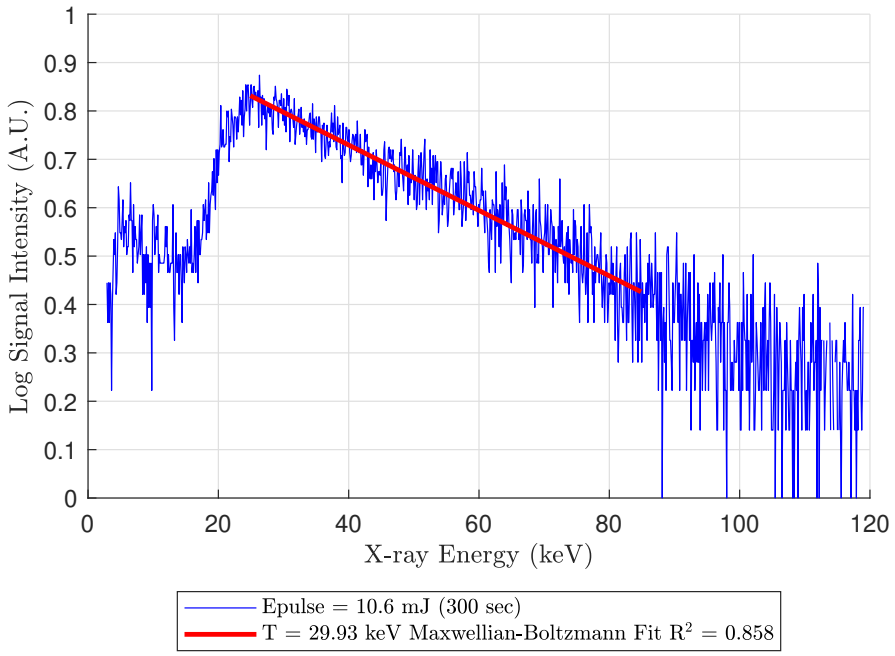

Figure 4.16: Maxwell-Boltzmann estimation of the plasma temperature.

Figure 4.16 shows the post-processing of this spectral data. By defining a region of interest (ROI) and using log-linear regression between 25-85 keV, a Maxwell-Boltzmann electron temperature of $T_e \simeq 29.93$ keV with $R^2 = 0.858$ was fit.

4.5.4 Fast neutron measurement via pulse shape discrimination

Fast neutron interrogation in the presence of intense mixed (n/γ) radiation fields poses a significant detection challenge, and additional complication is incurred when the sources emitting ionizing radiation operate in a pulsed regime. Pulse shape discrimination (PSD) addresses this detection problem by filtering voltage pulse waveforms generated during scintillation events by quantifying the ratio of the integrated charge in the pulse tail corresponding to Q_{short} and Q_{long} fluorescent decay components characteristic of the scintillating medium. The difference in this decay time in EJ-309 scintillators is quite pronounced because fast neutron-induced proton recoil events lead to a large number of molecular triplet excited states that phosphoresce over much longer ($>$ 200 ns) durations relative to fast (3.2 ns) singlet fluorescence transitions [133, 134].

In our relativistic LDNS experiment, two EJ-309 liquid scintillation detectors consisting of identical 50 mm x 50 mm cylindrical liquid scintillator cells (Eljen Technology, EJ-309) coupled to high-efficiency photo-multiplier tubes (Hamamatsu, R7724), referred to as assemblies N1 and N2 (see Fig. 4.6) were mounted with the front surfaces of detector assemblies located at a distance of 25.0$\pm$0.5 cm and 75.0$\pm$0.5 cm from the EHD nozzle. These detectors were setup for nTOF and coincidence PSD as described in Methods subsection 3.3.4.

Fig. 4.17 shows all coincident scintillation events recorded by each detector during a 16 minute shot campaign. Event discrimination is clearly evident with fast neutron and photon peaks centered at PSP values of approximately 0.25 and 0.07 respectively. The scarcity of x-ray/γ-ray events is attributed to photon rejection due to the combined filtering from 50 mm Pb bulk shielding and fine Cu mesh Faraday cages surrounding each composite detector assembly. The observed light output quenching corresponding to the D-D neutron edge at 2.45 MeV ($\leq$1.0 MeVee) and PSP ratio (0.18-0.50) for the fast neutron events measured by our pulse shape discrimination enabled scintillator assemblies was in good agreement with data collected during our D-D generator calibration runs and data published for (α,n) isotopic sources [102].

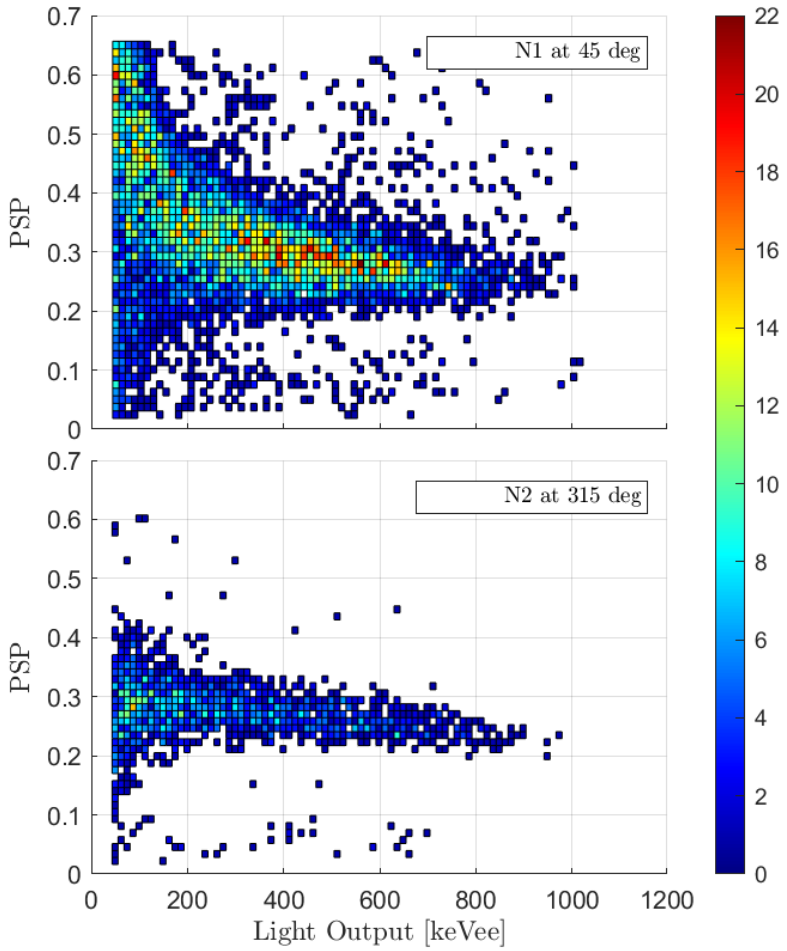

Figure 4.17: Binned coincidence scintillation events measured by the 2-inch EJ-309 liquid scintillators N1 (top) and N2 (bottom) during 4.608×10^5 laser shots at 10.6 mJ.

4.5.5 Neutron time-of-flight measurements

Within the detection coincidence window, the application of a rectangular cut on fast neutron events with $0.18 < \text{PSP} < 0.50$ and a light output distribution between 70-991 keVee allowed us to construct the γ-rejected TOF timing histograms shown in Fig. 4.18. Relativistic time-of-flight for the 2.45 MeV DD fusion neutron was calculated as 11.52 ns and 34.56 ns for the flight length to detectors N1 and N2 respectively. Fast neutron events measured during our experiments show excellent agreement with the expected transit time and energy spread measured in similar laser-driven D-D fusion campaigns [56, 59]. As expected, we see

evidence of up-scattered neutron energies associated with beam-on-target interactions from target normal sheath accelerated deuterons driven forward into the microjet. We believe that the increasing event rate past the initial edge of the pulse corresponds to pitcher-catcher reactions at the target chamber surface. This claim is supported by evidence of visible carbonization deposited on the chamber walls after only a few minutes of operation. These deuterium-rich surfaces are 8-12 mm from the geometric focus and subtend ∼1/3 of the total available solid angle. Assuming a nominal $T_i = 50$ keV from estimated yield scaling in similar experiments [40], the deuteron time of flight to the chamber wall would result in our observed fusion yield delayed by up to 5.5 ns.

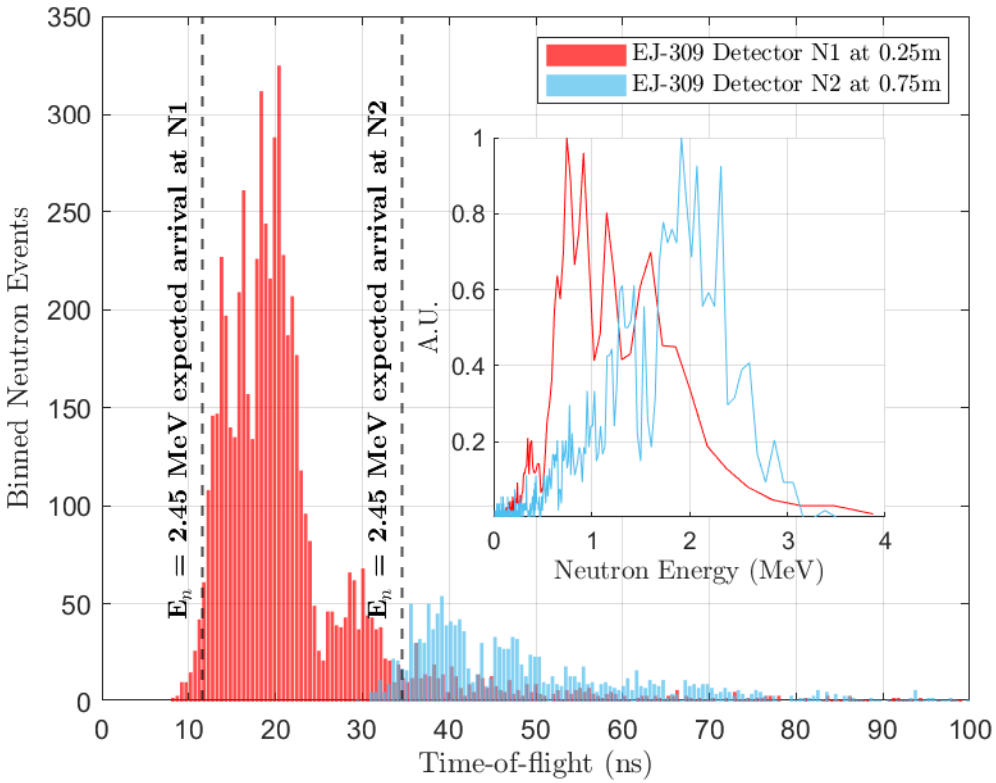

Figure 4.18: Fast neutron time-of-flight measurements performed with $\tau_{\text{coinc}} = 512$ ns coincidence. Liquid scintillation events with proper fast neutron PSP and light output characteristics are shown in 500 ps bins for detectors N1 and N2. (*Inset*) A normalized plot of neutron energies corresponding to all registered nTOF events.

4.5.6 Neutron flux measurement

Absolute neutron flux measurements were performed with an x-ray and γ blind BD-PND personal neutron dosimeters. During each flux scaling measurement, a minimum of three detectors were placed at varying distances of 4.5-12.0 cm from the target center. Timing error was reduced by the use of a second investigator to open the regenerative amplifier shutter and monitor the elapsed dosimeter exposure with a standard stopwatch. To prevent erroneous bubble generation from stray laser light reflections, the detectors were kept upright in their protective aluminum housing when uncompressed. All isotropic yield is reported with quadrature error propagation factoring in the cumulative error from manufacturer calibration, source-to-detector flight distance, and timing error. Macroscopic bubbles generated during bubble dosimeter exposure were read out by eye against a high-contrast background and an average of three unassisted readings were recorded. Figure 4.19 provides a representative fast neutron dose recorded during high-intensity laser irradiation of the EHD microjet target with 3.26×10^5 laser pulses.

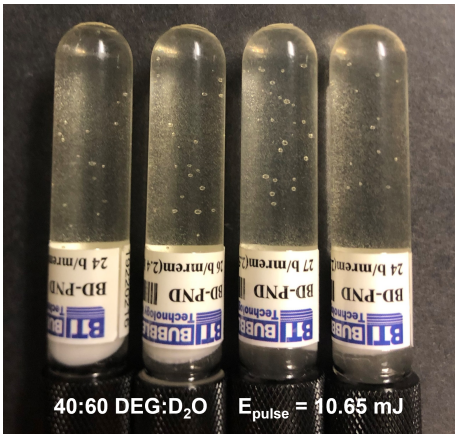

Figure 4.19: Fast neutron dose resulting in the formation of macroscopic bubbles on BD-PND dosimeters surrounding the laser-plasma target volume. The recorded dose corresponds to an isotropic flux of approximately $\Phi = 24{,}000$ n/sec/sr measured over 680 seconds.

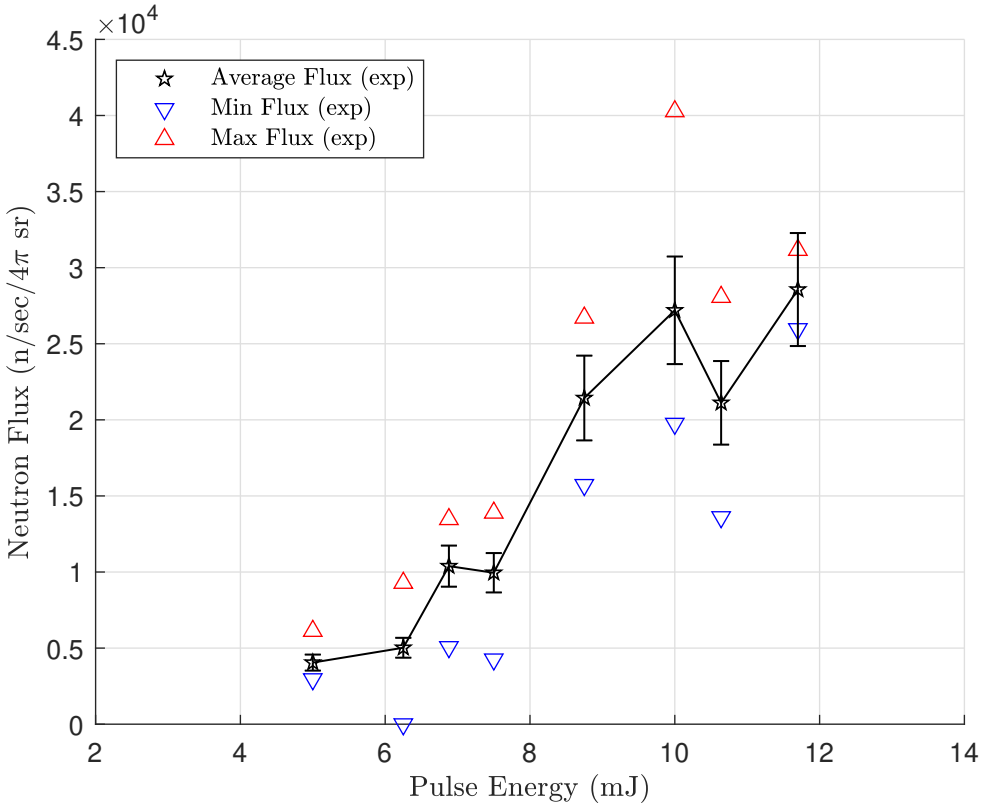

Figure 4.20: Fast neutron isotropic flux measured during a 12 minute dose accumulations from the EHD jet target at various laser energies.

The maximum isotropic flux recorded during any shot campaign was 4.0×10^4 n/s/sr. Although fusion D-D neutron yields measured during this work were lower than those previously reported for similar pulse energies in experimental work by *Hah et al.* [40], we rectify this result by considering the hydrocarbon composition of the target material used in our experiment as well as the five-decade reduction in backing pressure realized with our device. While deuterons are preferentially accelerated over carbon atoms, owing to their higher Q/M ratio up to C^{+5} [105], full stripping of the carbon in the DEG is expected with protons and C^{+6} competing for the same pondermotive energy exchange which would further enhance heating of the deuteron population. Chamber pressure was maintained at or below 5×10^{-4} Torr even for flow rates of 4.8 μL/min. At this vacuum level, it is unlikely that a significant number of 'pitcher-catcher' reactions resulted from energetic deuteron expulsion into the

chamber volume.

4.6 Conclusion

In conclusion, this experimental work is the first demonstration of an electrostatically dispensed reduced mass liquid target for relativistic laser-plasma interactions, with specific application to high average flux tabletop fast neutron sources. End-to-end system design and optimized performance for various experimentally relevant parameters were shown for micron-scale deuterated liquid target generation at multi-kHz frequencies. Irradiation of 2.7±0.5 μm pulsed jets containing 40:60 DEG:D_2O mixtures with a tightly focused Ti:Sa USPL capable of delivering up to 10.6 mJ, 39.5 fs pulses on-target at 480 Hz resulted in isotropic 2.45 MeV neutron fluxes of up to $4.02(0.54)\times10^4$ n/s/4π sr. Pulsed electrohydrodynamic target extraction also resulted in the lowest measured volumetric flow rate for a kilohertz-class target and the first use of deuterated low-vapor pressure solutions without the need for a complex fluid trap or differential pumping. Extension of the EHD extraction mechanism to the high vacuum regime facilitates microscale target synthesis from conductive nozzles with inner diameters 20-30 times larger than fluid spatial dimensions. This remarkable scaling supports clog-free target operation without the need for in-line filters. Furthermore, this work establishes a path toward the realization of synchronized microdroplets for true droplet-on-demand targets. Stroboscopic imagery confirms that the current microjet system is stable at up to 12 kHz operation and extension to higher frequencies is likely possible with increased amplifier slew rates. This bandwidth overhead suggests that the measured neutron flux of ($\sim10^5$ n/s) could quickly scale to 10^{6-7} n/s when coupled to relativistic OPCPA and fiber-based drivers supporting multi-kHz pulse repetition rates. Lastly, this system can enable high-resolution neutron radiography as the effective source size is smaller than those demonstrated in previous experimental work.

4.7 Future work

Relativistic shot campaigns on the jet emitted from the EHD nozzle demonstrated proof-of-principle for implementation of this EHD target system for tabletop scale generation of fast neutrons from the D-D fusion reaction. Further improvement of the system could realize a true droplet-on-demand (DOD) target system for vacuum generation of spatiotemporally synchronized isolated droplets with <5 μm diameter. Commercially sourced 34-36 Ga stainless steel syringe tips were used throughout this because of their short manufacturing lead time and lack of fabrication overhead. While capable of surviving millions of laser shots, ultimately the precision electro-machined edges of the syringe tip would suffer shock-induced ablation causing significant surface irregularities. In turn, these irregularities would cause severe distortions to the normally symmetric field profile and disrupt proper Taylor cone formation. Tungsten is rated as a $\sim$7 on the Mohs hardness scale (compared to 4-4.5 for SS) is highly durable while also conductive. A precision micromachined tungsten nozzle could result in improvements to target system longevity and reduced nozzle failure.

Experimental work performed in this chapter specifically focused on EHD target generation for laser-driven neutron source (LDNS) applications. The use of non-deuterated target fluid compositions could naturally extend the capability of this source to generate tunable X-ray fluxes. Experimental demonstration of high-brightness characteristic x-rays would be possible if a high molarity solution was synthesized from water-soluble elemental salts (CsI, $CuSO_4$) and mixed with low vapor pressure solvent such as chemically pure ethylene glycol or glycerol.

RCL impedance characteristics of the conductive nozzle and ground plane system were not extensively investigated during this work. The transient high-voltage rise time of the nozzle resulting from impedance mismatch resulted in temporal jetting cycles that were much longer than those estimated from the specified slew rate of the driver. The large fixed standoff distance between the ground electrode and the conductive nozzle tip required the application of peak-to-peak voltages $V_{pk-pk} \geq 1.1$ kV and resulted in significant electromagnetic pulse

(EMP) generation. This EMP and the resulting interference necessitated Faraday shielding of the liquid scintillators, installation of ferrite chokes on instrumentation cabling, and in one case, caused the permanent failure of a closed-loop motor driver due to a transient voltage spike across the earth ground to which the experiment was tied. Mounting of the ground electrode to a small translation stage or linear-servo-mounted stalk would allow for in-situ positioning adjustment in future experiments. This spatial control would serve two purposes: (1) adjustable control of the standoff height would allow for a proportional linear reduction in the applied peak pulse voltage, ultimately reducing RF power coupled into the EMP, and (2) the ability to lower and clean the stage of carbonized deposits between experimental runs without removal of the entire electrode assembly. The latter improvement would reduce spatial error in the ground plane height and positional asymmetry below the conductive nozzle.

CHAPTER 5

Orbital Angular Momentum Beam Enhanced Neutron Generation

5.1 Introduction

Vortices are most often associated with the natural motion of fluid systems, examples include hurricanes, tornadoes and whirlpools. Like fluids, electromagnetic waves and even photons can exhibit vortex motion and carry an orbital angular momentum (OAM) [15]. The concept of an optical vortex was first pioneered by Nye and Berry [135], but it was the seminal work by Allen *et al.* [136] that showed paraxial Laguerre-Gaussian (LG) modes carry a well defined OAM [15]. LG modes mathematically characterize circularly symmetric laser beam profiles through cylindrical paraxial solutions to the Helmholtz equation and are written in cylindrical coordinates using the generalized Laguerre polynomials. One of the most unique characteristics of OAM beams is that the twisting helical phase structure creates an on-axis phase singularity. This singularity manifests as an intensity null which gives such beams their 'doughnut-shaped' far-field intensity pattern [137].

Recently, there has been considerable interest in extending the application of optical vortices to the realm of ultrashort high-intensity lasers. The body of this work is primarily focused on exploring plasma dynamics resulting from an inward-facing ponderomotive component associated with the on-axis phase singularity present in OAM beams [15, 138]. Further, OAM beams exhibit an annular intensity profile which is suitable for driving ring-

shaped electron beams via LWFA [139, 140]. Lastly, ion acceleration with OAM beams has shown significant promise for ion beam radiotherapy applications due to experimentally confirmed sheath focusing effects [141–143] To date, the generation of both high-intensity and high purity OAM beams has proved challenging due to the limited number of high damage threshold phase shaping optical elements [144]. As a consequence of these material limitations, the majority of high-intensity OAM laser plasma studies to date have generally been executed via computational simulations [15, 140, 145] Recently, the development mode conversion techniques exploiting optical-grade UV fused silica spiral phase plates (SPP), and epitaxially grown spiral phase mirrors (SPM) have opened access to relativistic experimentation with intense vortex lasers beams.

In this work, we investigate the creation of high repetition tightly focused ($f/1.5$) LG_{01} and LG_{05} ultrashort laser beams carrying orbital angular momentum with near relativistic intensity. To our knowledge, this is the first experimental demonstration of deuteron acceleration using OAM laser beams incident on a microscale free-flowing D_2O liquid jet. We show that high-order LG modes propagating at grazing incidence to overdense targets result in an order of magnitude enhancement in fast neutron generation over previously reported normal incidence interactions with relativistic Gaussian beams. Through the use of particle-in-cell computational methods, we corroborate the findings of experimental results and confirm evidence of LG beam collapse due to plasma self-focusing. Following beam collapse, intense polar filamentation is shown two drive to distinct regions of locally hot ions which possibly cause late-time beam-beam interactions resulting in enhanced laser absorption into fast particles and D(d,n)^{3}He fusion yield. Polarization effects on the OAM ion acceleration dynamics are also investigated.

5.2 Methods for generating high-intensity OAM beams

By convention, vortex light beams with finite angular momentum are characterized by an angular-dependent phase $\Phi = L\phi$, a helical wavefront structure, and an intensity null on the propagation axis [136]. L (specified by l in the basis set) is the topological charge that corresponds to OAM carried by each photon and ϕ is the azimuthal angle. Mathematically, these beams are described by Laguerre-Gaussian (LG) modes, and physical implementation usually requires some method of mode conversion from Hermite-Gaussian to LG [139]. Within the $LG_{p,l}$ basis set, p defines the radial mode index and l the angular mode index respectively. All LG beams constitute a set of complete orthogonal basis vectors capable of representing any arbitrary OAM spatial profile. To the simplest approximation, higher radial order LG beams exhibit a far-field intensity profile that appears as sets of concentric rings of with radially diminishing amplitude. Likewise, higher angular order manifests a singular annular ('doughnut') mode with a radius that scales with diffraction. Figure 5.1 shows numerical far-field beam profiles for an ever-increasing topological charge.

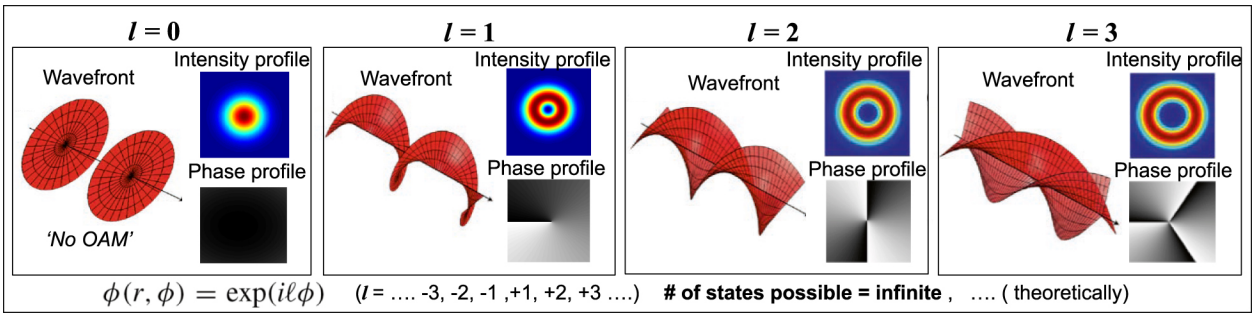

Figure 5.1: Graphical representation of the laser wavefront, intensity profile, and phase profiles of OAM modes l =0,1,2,3. Figure from Ref. [14] used with permission.

Established methods for generating the vortex light beams include beam structuring performed by q-plates [146], digital spatial light modulators (SLMs) [147, 148], spiral phase plates [137, 149] and most recently, dispersionless spiral phase mirrors [150]. For high-intensity applications, such as the experiments performed during this work, spiral phase optics (SPPs and SPMs) provide the primary means of HG to LG conversion. This fact is

primarily attributed to their high optical damage threshold and ability to shape pulses of substantial bandwidth, typical of femtosecond laser systems < 100 fs [15].

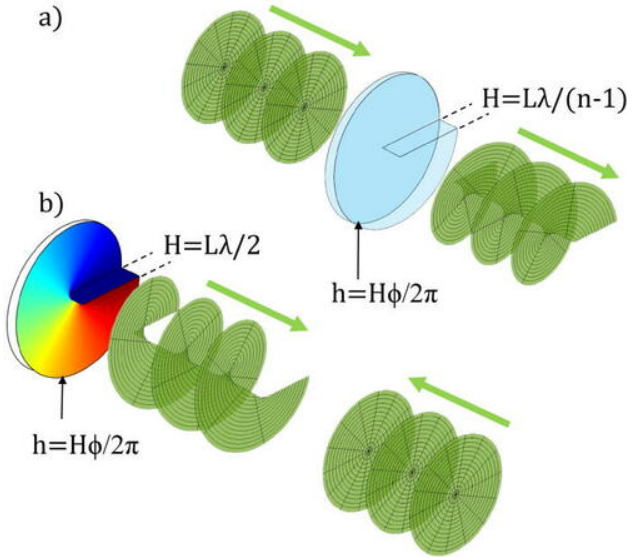

Figure 5.2: Illustration of the working principles of two classes of spiral phase optics. (a) Transmissive spiral phase plates (SPP) impart helical wavefront through an engineered azimuthally varying optical thickness. (b) A spiral phase mirror (SPM) imparts a helical wavefront through beam reflection off a helically-structured mirror surface. Figure from Ref. [15] used with permission.

The operating principle of a spiral phase mirror is straightforward and involves the reflection of a laser pulse with a planar wavefront (typically the Gaussian near-field of a USPL) off a helical mirror surface [150]. As detailed in Figure 5.2, the surface of the mirror is structured such that the optical path length changes as the azimuthal angle advances - with the spiral step height H set to the desired topological charge [15]. The topological charge of a spiral phase mirror is given by $L = 2\mathrm{H}/\lambda$, where λ is the laser's center wavelength. Local step height $\mathrm{h} = \mathrm{H}\phi/2\pi$, with ϕ defined as the azimuthal coordinate. For fabrication purposes, H is typically an integer multiple of $\lambda/2$ as it leads to enhanced symmetry in the resulting focal spot. Mode shaping in the transmission regime is carried out using a spiral phase plate and the only difference lies in the modification of the spiral step height expression to account for the material's linear optical refractive index n - giving $H = L\lambda/(n-1)$. One important factor to note is that the OAM beam chirality (direction of azimuthal phase accumulation)

is reversed following optical propagation from the mirror as opposed to the plate.

In our experiment, we used two spiral phase plates of topological charge $L = 1$ and 5 to mode convert a normally Gaussian femtosecond laser driver with a center wavelength of $\lambda = 800$ nm. Each SPP was fabricated on an optical grade 1.0 mm thick and 47 mm diameter fused silica substrate. The LG_{01} plate was uncoated while the LG_{05} plate was NIR anti-reflection coated. Each plate was retained in a standard lens mount and height indexed to the driver beam axis with a locking collar.

5.3 OAM neutron generation experiment

5.3.1 Experimental setup

This experiment was performed on the λ^3 laser systems at the University of Michigan. An overview of the vacuum target chamber, optical diagnostics, and secondary radiation detectors is shown in Figure 5.3. Under experimental conditions, the laser delivered up to 16 mJ of laser energy at $\tau_p = 66.7 \pm 1.0$ fs into a 60° $f/1.5$ OAP. Compared to the EHD jet experiment discussed in Chapter 4, longer pulse duration was used in this campaign for two reasons: (1) the reduced peak power minimizes the risk of catastrophic beam self-focusing in the spiral phase plates inserted in the compressed beam to generate OAM modes, and (2) early empirical work indicated that the optimally compressed laser would filament prior to the geometric beam waist because high non-linear phase accumulation attributed to (12 Torr) ambient chamber pressures necessitated keeping the liquid jet from freezing. Operation of the Ti:Sa USPL at a longer pulse duration also relaxes the depth of the spectral hole drilled by the DAZZLER system and saturated gain of the regenerative amplifier was obtained with one less gain round trip than required for peak compression. To ensure the day-to-day repeatability of the system compression, a chirp scan (see Fig. 5.4) was obtained by manipulation of the second-order phase imparted by the DAZZLER. This scan allowed for optimization of the FROG trace without the need for manipulation of the compressor grating

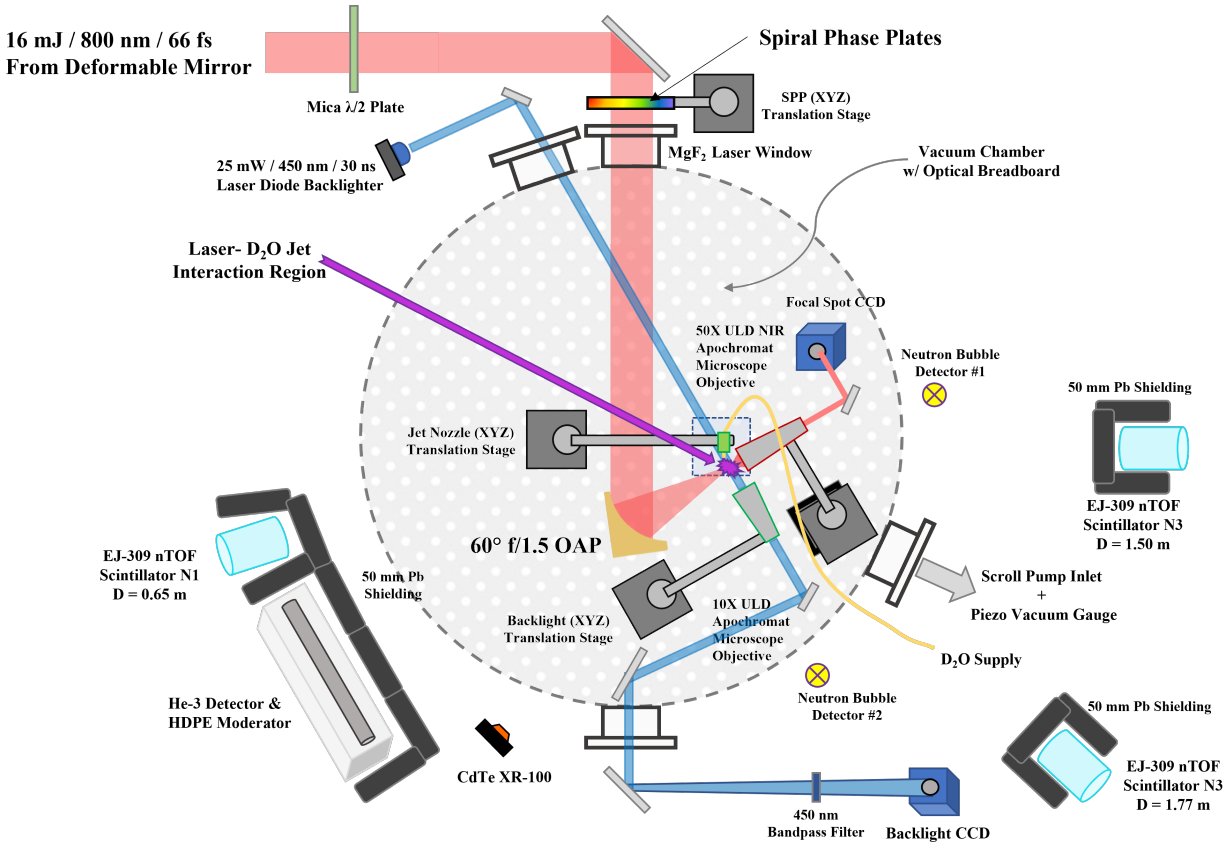

Figure 5.3: The plasma target chamber configuration for experimental investigation of OAM beam effects on ultrashort laser-driven fast neutron yield. The placement of detectors and beam optics is not to scale.

separation, thus eliminating random errors caused by hysteresis in the grating translation stage.

Following iterative beam optimization by the GA + DM, the laser was focused to a 2.86 μm 1/e^2 Gaussian spot which resulted in a maximum on-target intensity of 7.5×10^{18} W/cm^2. All beams were focused on the target as linearly P-polarized light, except as noted in the polarization study where the effects of S-Polarized light on the plasma dynamics were investigated by inserting a 100 mm diameter 78 μm thick mica half-waveplate into the optical axis of the driver beam.

Similar to work performed by Hah *et al.* in Ref. [40] a free-flowing liquid jet was used as the high repetition laser-plasma target. To create a stable, laminar jet with a diameter of

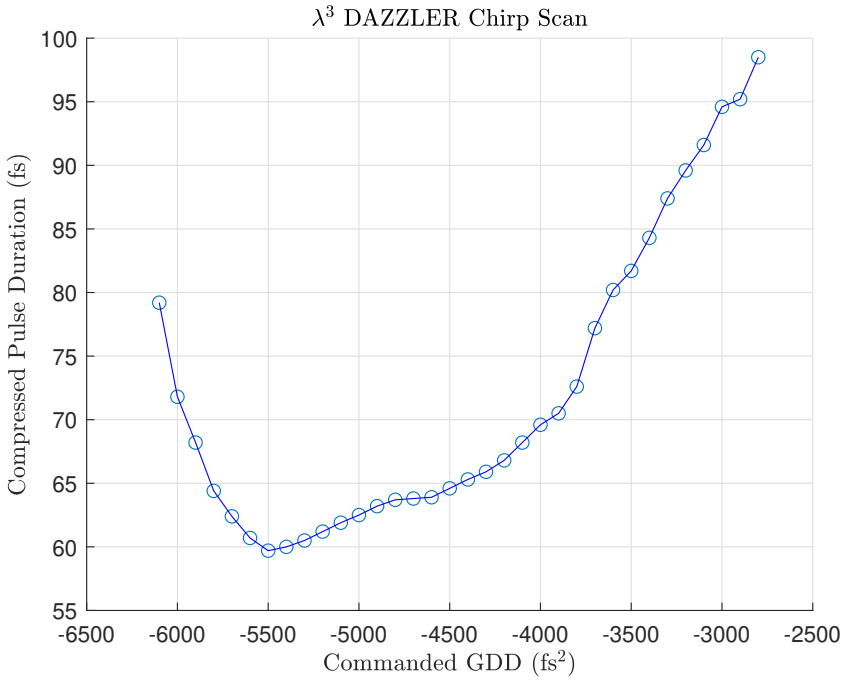

Figure 5.4: System pulse duration measured during a DAZZLER chirp scan.

15.2±0.2 μm deuterium oxide of 99.8% isotopic purity (Sigma-Aldrich, CAS:7789-20-0) was pressurized with a programmable constant displacement/constant pressure syringe pump (Teledyne Iso). To ensure clog-free jet operation, prior to filling the syringe pump reservoir all target fluid was passed through 5-micron nylon Luer lock syringe filters. Liquid exiting the pump at 185 μL/min was routed through 300/150 μm O.D./I.D. PEEK tubing and filtered by an in-line 10 μm frit filter. The jet nozzle consisted of a precision cleaved fused silica capillary with 360/15 μm O.D./I.D. (Molex Polymicro) retained in a PEEK CapTite fitting (LabSmith). The microfluidic jet assembly was rigidly held in a 3D-printed mount capable of coupling to standard optomechanical components. Absolute target alignment was performed by manipulating the jet's transverse and longitudinal position with vacuum-compatible closed-loop stepper motors (Thorlabs Z812V) connected to matched USB stepper controllers (Thorlabs KDC101). Jet height was set to ∼300 μm above the geometric focus of the beam and ensured focused laser pulses were interacting with the laminar cylindrical profile of the fluid jet, well above the R-T breakup of the stream into a fine droplet spray.

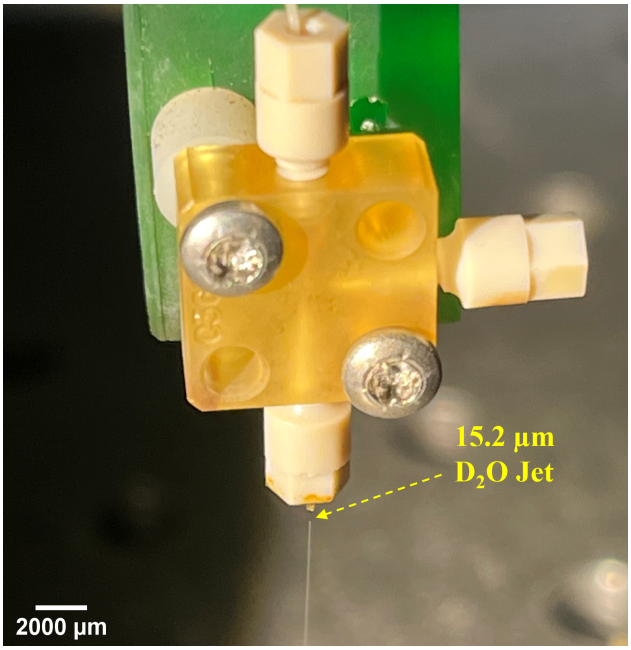

Figure 5.5: The free-flowing liquid jet target operating at ambient temperature and pressure.

During experiments, the chamber was evacuated with a 7.5 CFM dry scroll pump to just below 12 Torr as recorded on a digital piezo vacuum gauge (Thermovac TM101). D_2O was allowed to free-flow into the catch reservoir centered below the jet for a period of 20-30 minutes. During this period as ambient vapor pressure rose above 15 Torr, the chamber was repetitively evacuated back to base pressure. This process was performed 6-8 times after which the target chamber was "fully conditioned" with a dense background of pure deuterium oxide vapor. This step was critical to ensure superlative neutron yield resulting from TNSA deuterons causing pitcher-catcher fusion reactions during their flight through this distributed vapor 'catcher'.

The pulsed laser diode (LD) optical backlighting system described in subsection 4.3.1 was again used for probing laser-target interactions in this experiment. To further enhance the edge contrast between plasma self-emission and the liquid microjet structure, the central wavelength of InGaN LD and matched visible filters were changed to $\lambda = 450$ nm. Focal spot characterization of the pure Gaussian (PG), and OAM beam modes were as described in subsection 3.2.2. Procedures for the alignment and optimization of LG beams used during

this experiment is further explained in the next subsection.

5.3.2 Characterization of spiral phase plate generated OAM laser modes

Prior to commencing high-intensity laser shots on the free-flowing liquid target, the fundamental Gaussian spatial mode of the drive laser was optimized for axial symmetry and peak intensity. As in Chapter 4, the λ^3 deformable mirror and genetic algorithm were allowed to iteratively optimize the highly attenuated and magnified $f/1.5$ focal spot. Upon algorithm convergence, a 2.86±0.25 μm ($1/e^2$ diameter) Gaussian spot was obtained. SPPs with a topological charge of $l = 1, 5$ were then inserted and centered with an X-Z translation stage to the radial axis of the driver beam approximately 35 cm from the front surface of the final focusing optic. By closing an upstream 50.8 mm O.D. adjustable iris, the attenuated driver beam was apodized allowing for minute adjustment of SPP positioning in both optical planes. To compensate for the minor elliptical asymmetry of the compressed Ti:Sa spatial mode, the transverse positioning was further adjusted to yield a nominally uniform ring intensity profile. A representative result of this adjustment is shown in Figure 5.6.

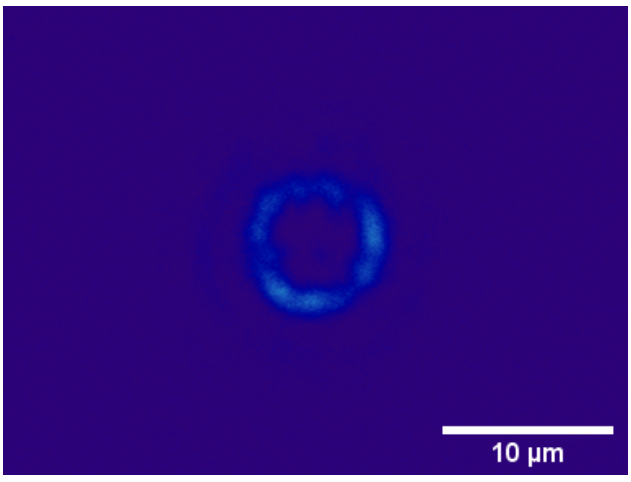

Figure 5.6: The apodized and attenuated LG_{05} beam at focus integrated over four consecutive laser shots.

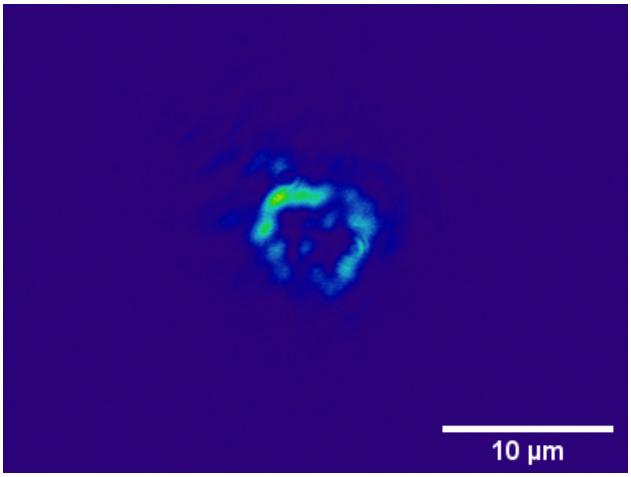

Figure 5.7: The attenuated LG_{05} at beam focus integrated over four consecutive laser shots.

HG-to-LG modal conversion is not a pure process and any spatial hot spots or asymmetry in the near-field laser mode will manifest as intensity inhomogeneities in the OAM beam. Practical visualization of this effect is shown in Figure 5.7, and the consequences on our experiment are explained in the experimental results.

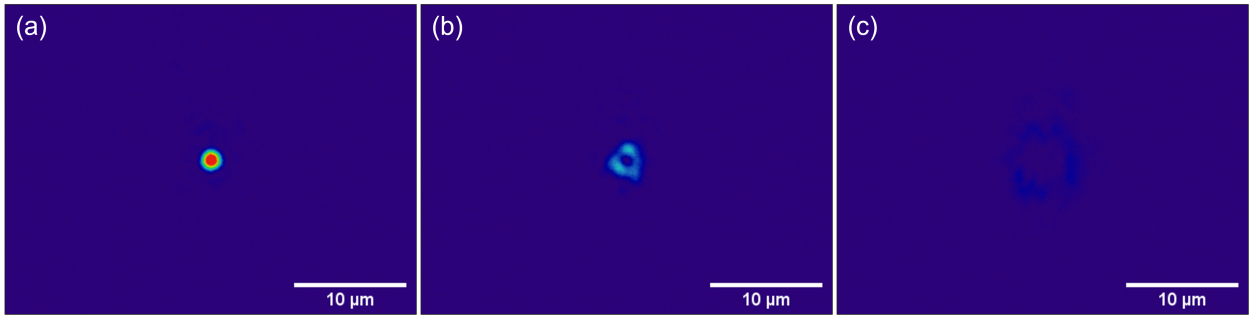

Figure 5.8: Highly attenuated focal spot images of the (a) PG, (b) LG_{01}, and (c) LG_{05} beam modes used during this experiment. All intensity images were taken as single-shot exposure with identical electronic gain.

Figure 5.8, shows a set of tightly-focused pure Gaussian, LG_{01}, and LG_{05} beam modes representative of those used to irradiate the liquid microjet at relativistic intensity.

The intensity distribution for the OAM beam of topological charge L can be analytically computed in the far-field using Fraunhofer diffraction and Fourier transforms. Assuming integer values of L, then the far-field intensity distribution of an SPP generated OAM beam

is given by [15]

$$I = I_0 \frac{\pi}{4} \frac{r^2}{w_0^2} \exp\left(-\frac{r^2}{w_0^2}\right) \left| I_{\frac{|L|-1}{2}}\left(\frac{r^2}{2w_0^2}\right) - I_{\frac{|L|-1}{2}}\left(\frac{r^2}{2w_0^2}\right) \right|^2 \tag{5.1}$$

where $I_n(X)$ is the modified Bessel function of the first kind, I_0 is the peak intensity of the PG beam and, the beam waist assumes its normal form

$$w_0 = \frac{\lambda f}{\pi R_0} \approx \frac{2}{\pi} \lambda f_{\#} \tag{5.2}$$

with $f_{\#}$ the OAP focusing f-number, f the focal length of the optic, and R_0 the near field beam radius [15]. Employing a split-step Fourier beam propagation model, we calculated theoretical intensity distributions expected for the nominally 2.86 μm Gaussian focus delivered by GA optimization of the compressed USPL driver beam. As seen in Figure 5.9, the experimentally generated OAM modes show good agreement with radial position and normalized amplitude of the peak intensity. Experimental line-outs were taken in ImageJ as the average of the beam intensity as measured in the orthogonal axes of the beam. Reduced intensity of the experimentally characterized $l = 5$ beam is attributed to the summed effects of the apparent beam ellipticity shown in Fig. 5.7 and diffractive beam propagation prior to reaching the OAP. Sensor saturation shown for the experimental PG case could not be avoided without losing the necessary dynamic range to measure a single-shot exposure of the LG_{05} beam under identical conditions. During transverse experiments investigating neutron yield as a function of beam position relative to the jet, each OAM beam mode was independently asymmetry compensated, and the differing X-Z micrometer spatial positions were recorded. Chirality effects were not investigated in this experiment and SPP orientation to the driver beam was held constant throughout this study.

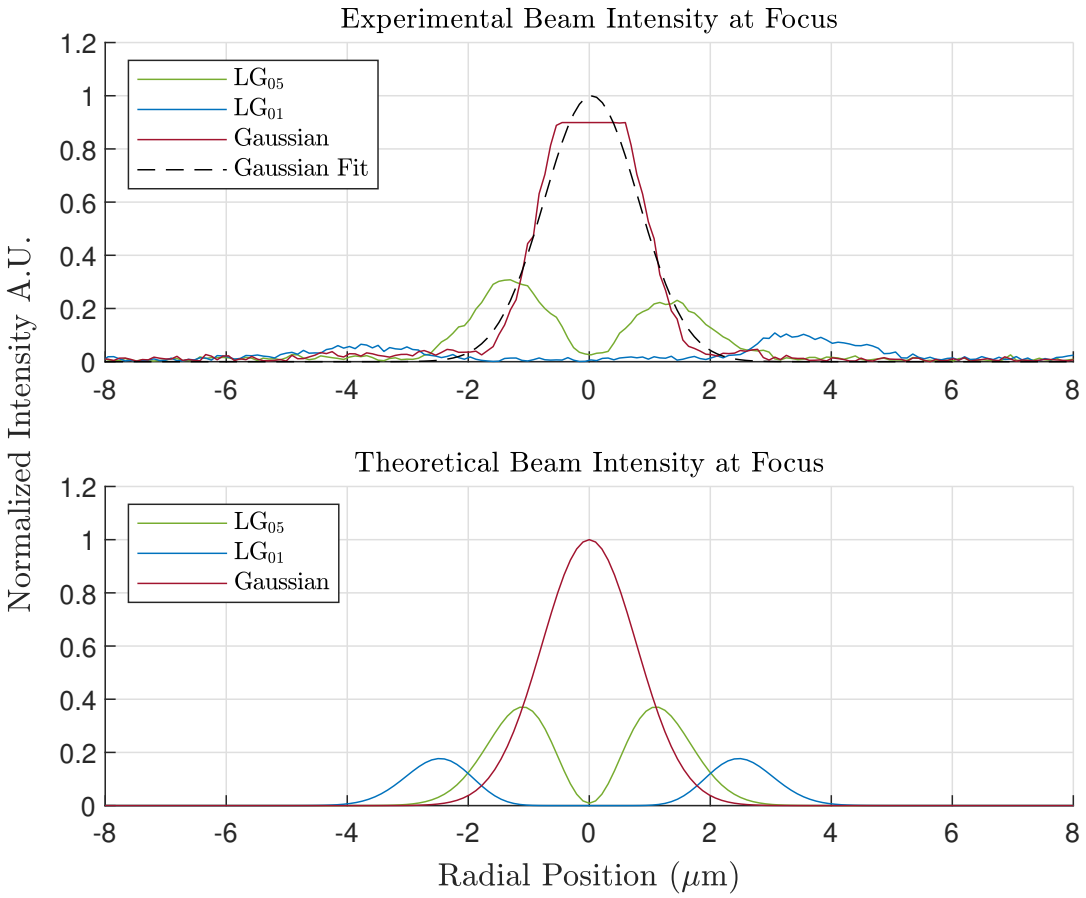

Figure 5.9: (*top*) Axis averaged, Gaussian normalized intensity line-outs of the PG, LG_{01}, and LG_{05} experimental beams and (*bottom*) Gaussian normalized theoretical beam intensity for the same modes from Fourier beam modeling.

5.3.3 Target alignment procedure

The process for aligning the free-flowing liquid jet to the focused USPL beam was straightforward and followed a similar scheme as was used in Chapter 4 but with slight modifications. Because jet operation was possible at ambient atmospheric conditions, the liquid stream was initialized by starting the microfluidic pump in constant pressure mode (3900-4500 psi) and monitoring the fluid flow rate until the target volume flow rate of 180-190 μL/min was obtained. The pump was then reprogrammed to run in a constant volume flow regime with PID control holding the target flow rate at the empirically optimized value of 185 μL/min. While

running at 480 Hz pulse repetition rate, the focus-optimized USPL driver was attenuated to 1-2 mJ and allowed to strike the jet. At atmospheric pressure, the jet position was then homed to the target center in the Thorlabs Kinesis control software. Using the handheld G-M counter in survey mode, the jet was then minutely adjusted in both transverse and longitudinal positions until a maximum count rate was recorded as measured at the edge of the vacuum chamber. At this point, the beam was shuttered and the chamber evacuated following the procedure in subsection 5.3.1. Removable lead shielding (x-ray apron) and 1.5 mm equivalent Pb-glass were then installed to prevent unnecessary dose exposure from the acrylic chamber lid. Full laser power was then delivered to the target surface. Intense laser pulses interacting with the stream at grazing incidence caused a visible generation of second-harmonic light in the near-UV. The backward propagating SHG signal was collimated by the OAP and visible on the laser system enclosure after reflecting off a 101.6 mm protected silver mirror. Similar to the method used in Ref. [40], optimization of this SHG signal corresponded with intense x-ray generation on all dose survey equipment. The longitudinal position of the jet was then manipulated until He-3 NIM count rates measured 600-800 cpm which was corroborated by measurements of 80-100 μSv/hr on a calibrated REM ball above the target chamber center.

5.4 Grazing incidence experimental results

Previous work by our group in [40] observed up to 2.2×10^5 n/s/sr D-D fusion neutron yield from relativistic Gaussian beam interaction with free-flowing D_2O liquid microjet at near normal incidence. An initial attempt to recreate the pre-plasma enhancement noted in this experiment led to confirmation that grazing incidence laser-target interaction ultimately corresponds with the highest isotropic neutron flux. In this section, we further expand the findings of this work by investigating grazing incidence interaction of sub-relativistic optical vortices with overdense free-flowing liquid jet targets at rough vacuum conditions.

5.4.1 Neutron flux measurement

The isotropic D-D flux from grazing incidence interaction with the D_2O jet was characterized using the absolute dosimetry provided by neutron bubble detectors and relative counts measured by three EJ-309 proton-recoil detectors. During each run, bubble detectors were placed at a distance of d = 30.5±0.5 cm and d = 34.2±0.5 cm from the laser-plasma interaction region. The PSD-enabled liquid scintillators N1-N3 were located at distances of d = 65.0±0.5 cm, 170.0±0.5 cm, and 150.0±0.5 cm and relative angles to the driver beam of 180°, 90°, and 355° respectively. The accumulation time for a series of PG and LG_{05} shots at full laser power (15.75±0.25 / 66.5 fs / 480.3 Hz) was 300 seconds.

During our experiments, the average isotropic flux measured for beams of topological charge $l = 5$ over 2.63×10^6 laser shots was $8.43(0.17)\times10^5$ n/s/sr and the maximum recorded dose during any single run was logged at $1.45(0.34)\times10^6$ n/s/sr. In comparison, the average isotropic flux measured for Gaussian beams over 7.78×10^5 laser shots was $2.56(0.55)\times10^5$ n/s/sr. This relative signal enhancement of 3.29±0.71 for the OAM to PG case as measured by the bubble detectors was completely unexpected. Post-processing of the parsed scintillation events corroborated this relative fast neutron signal enhancement and was additionally calculated for each detector as: N1 - 3.29±0.69, N2 - 3.18±0.67, and N3 - 3.41±0.72. Figure 5.10 and Figure 5.11 provide a representative visualization of the fast neutron signal enhancement seen with high-order OAM shots.

5.4.2 nTOF interrogation of Gaussian and high-order OAM beam-driven D-D fusion

Neutron time-of-flight (nTOF) using pulse shape discrimination enabled and time-gated EJ-309 was again fielded in this experimental study. For simplicity, we consider the dynamics of only PG and LG_{05} in this study. All PSP and coincidence parameters were the same as in the EHD experiment and minor changes to the setup included: (1) movement of the 1 ns

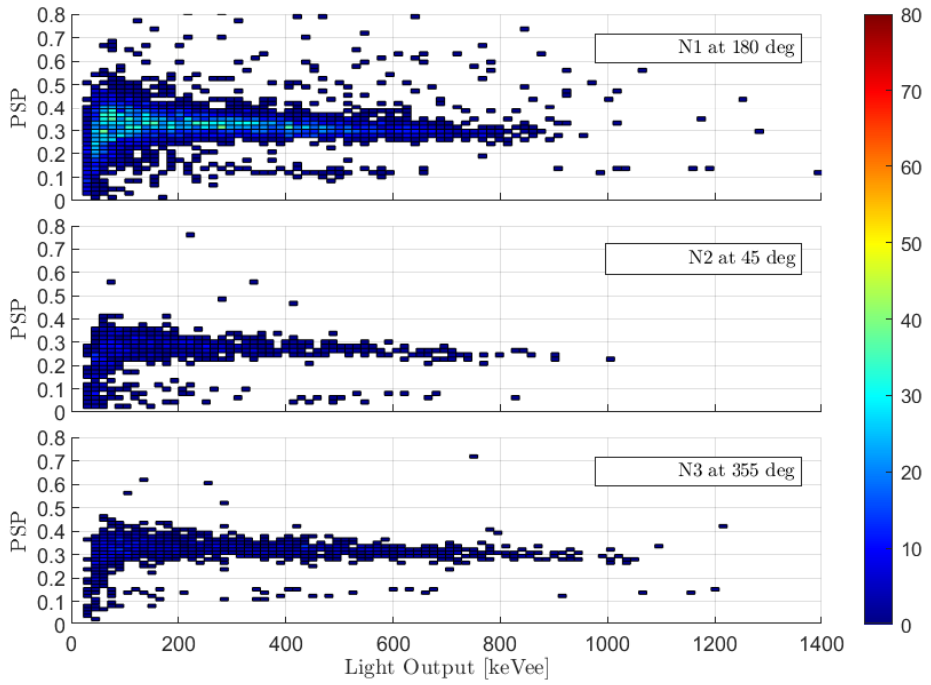

Figure 5.10: Scintillation events measured during a 300 s accumulation of 480 Hz PG shots on the heavy water jet.

fast rise-time photodiode to within close proximity of large aperture alignment iris at the entrance of the vacuum chamber, (2) addition of flight length to further resolve the < 500 keV deuteron kinetics associated with laser-jet energy coupling, and (3) addition of a third detector allowing neutron measurement in the target forward and backward direction. The flight length to the front surface of the EJ-309 detectors was d = 0.65±0.5, 1.77±0.5 and 1.55±0.5 m for detectors N1, N2, and N3 respectively.

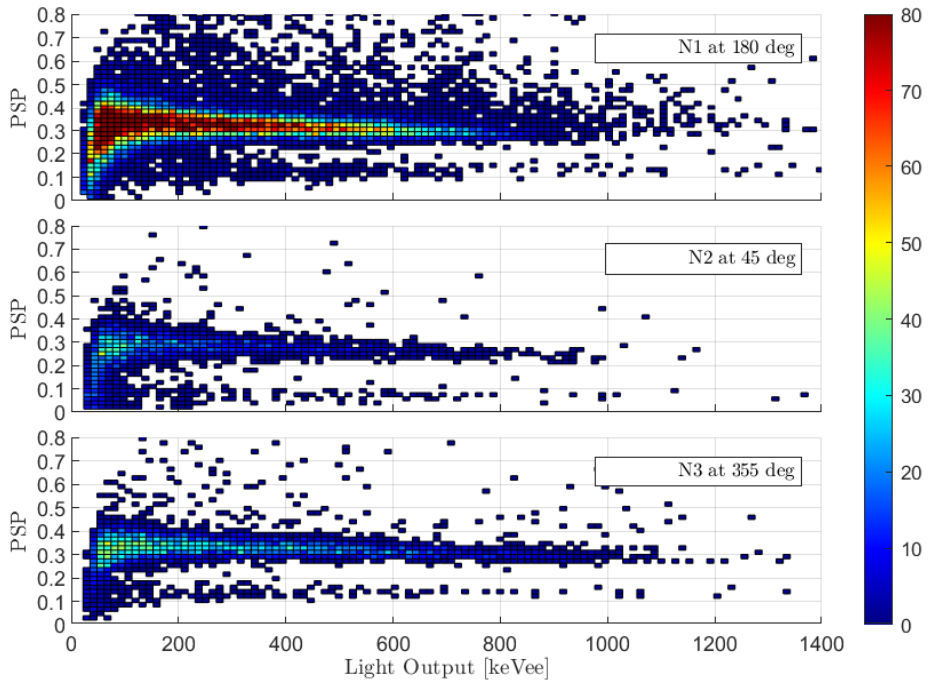

Figure 5.11: Scintillation events measured during a 300 s accumulation of 480 Hz LG_{05} shots on the heavy water jet.

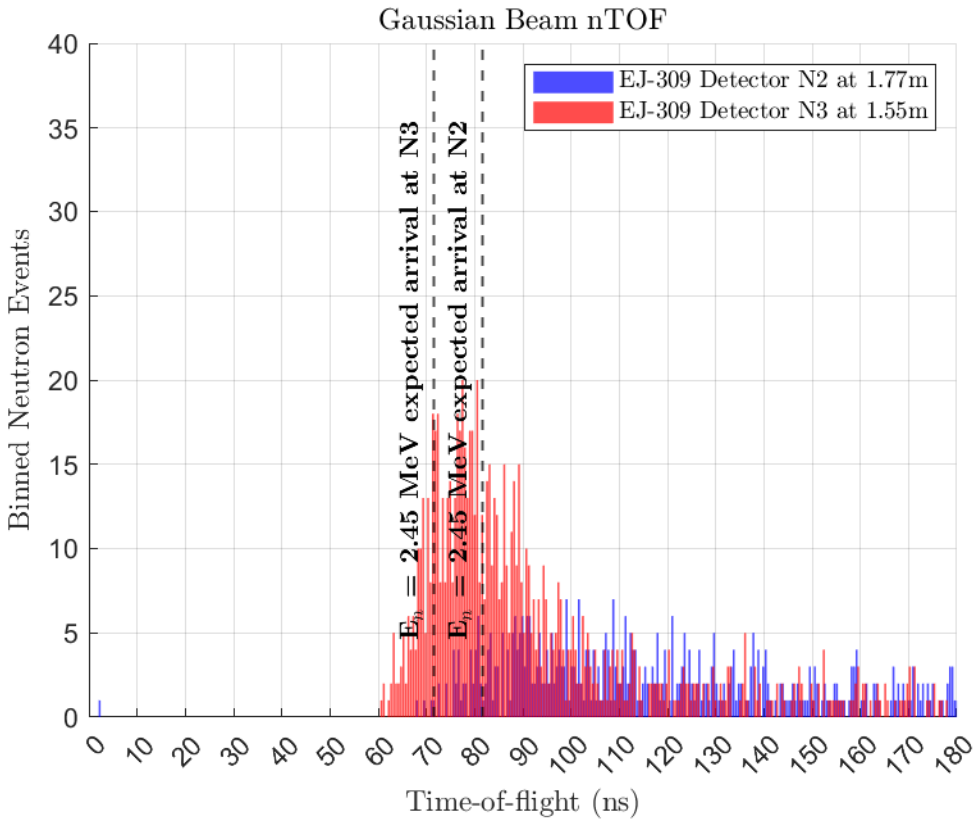

Figure 5.12: Fast neutron time-of-flight measurements performed with τ_{coinc} = 512 ns coincidence. Liquid scintillation events with proper fast neutron PSP and light output characteristics are shown in 500 ps bins for detectors N2 and N3.

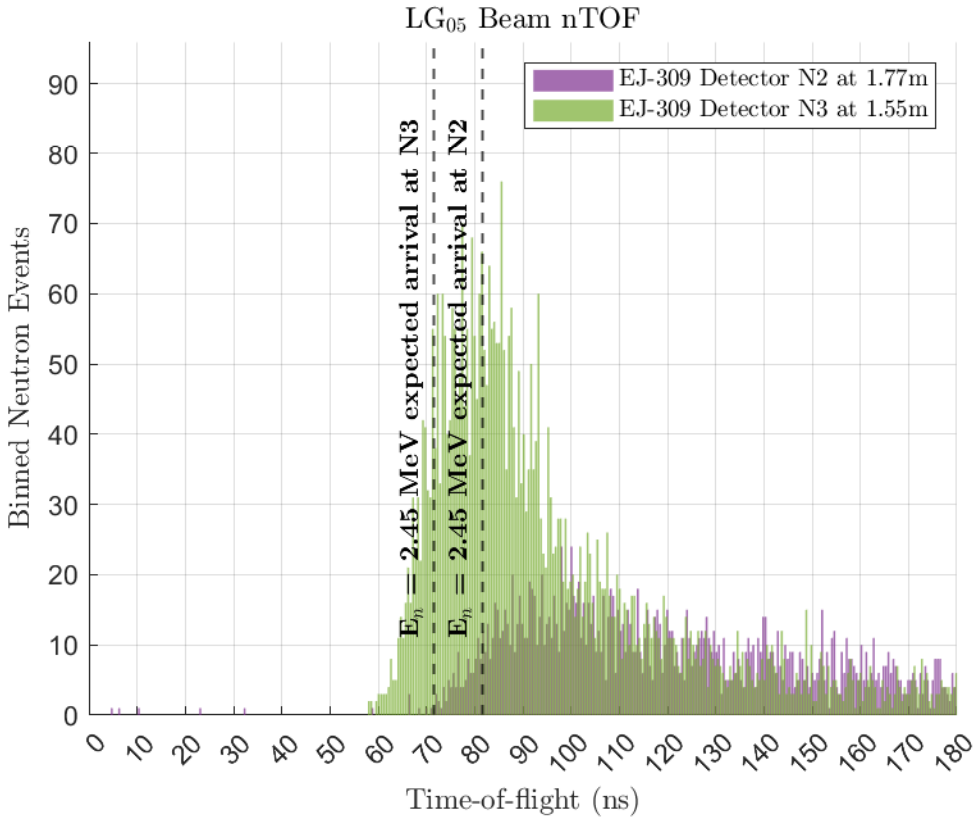

Figure 5.13: Fast neutron time-of-flight measurements performed with $\tau_{\text{coinc}} = 512$ ns coincidence. Liquid scintillation events with proper fast neutron PSP and light output characteristics are shown in 500 ps bins for detectors N2 and N3.

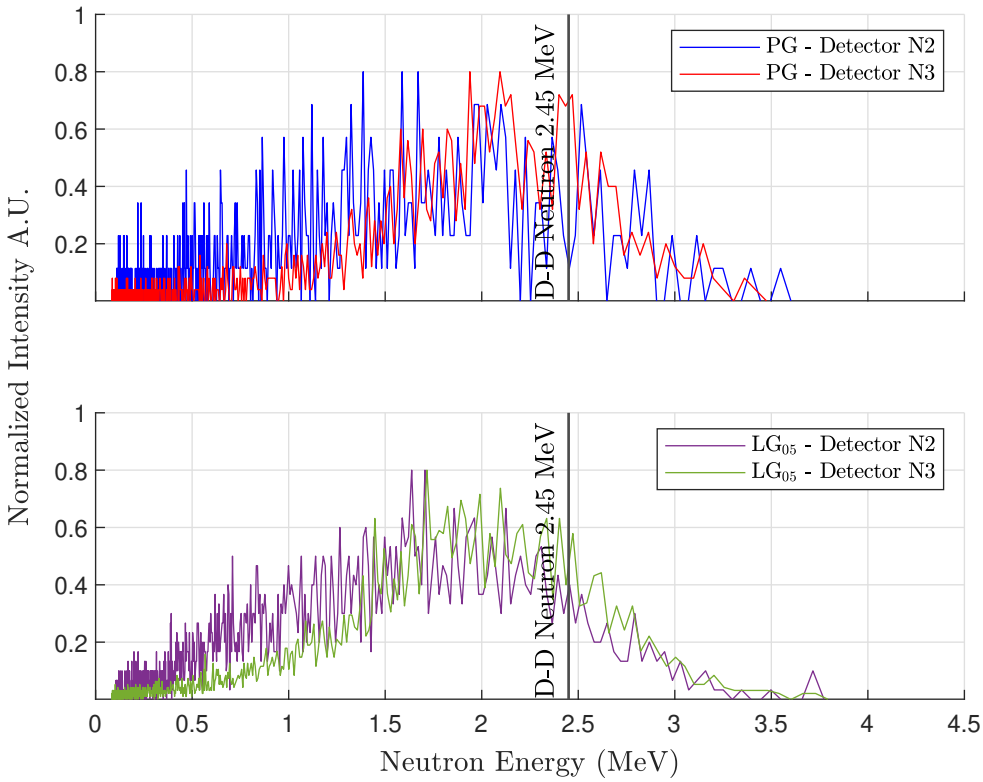

Figure 5.14: A normalized plot of neutron energies corresponding to all registered nTOF events for the PG beam (*top*) and LG_{05} beam (*bottom*).

Aside from the difference in magnitude for the total binned events between the LG_{05} and PG case, the nTOF measurement elucidates no fundamental difference in the ion population dynamics. As seen in Figure 5.14, the maximum ion energy cutoff for both beams was $\sim$1 MeV and the bulk of the characteristic E_n = 2.45 MeV D-D neutrons arrived at the detector plane with down-scattered energy. These results are consistent with similar LDNS experiments performed in the presence of a low-pressure background of deuterated vapor. [40,56]. A lack of extension to the high energy tail of the LG_{05} measured fast neutron spectra suggests the bulk ion temperatures vary little if any from the Gaussian case. This suggests that improved volumetric heating likely plays a role in the neutron flux enhancement and further investigation is carried out in a computational model.

5.5 Transverse target scan experiment

To further explore the dynamics of OAM enhancement of D-D fusion yield from the free-flowing D_2O liquid jet target, a series of transverse scans were conducted. The purpose of this experiment simultaneously investigated what effect three independent variables may play on the measured isotropic fast neutron yield. First, we considered the case of higher peak intensity in the OAM beam mode by introducing an SPP with a topological charge of $l = 1$. Second, as is often done in solid-target absorption and x-ray yield experiments [132, 151] we inserted an HWP to rotate the incoming linear polarized driver beam to the S-polarized state. Third, using the LG_{05} optimal longitudinal positions from the previous experiment, we then scanned the spatial position of the target across the tightly focused beams in an attempt to elucidate what role grazing incidence irradiation plays in the intense vortex beam interaction with the overdense target.

The experimental setup was the same as in the grazing incidence experiment. During each scan, a series of 4.00 μm closed-loop steps were made starting from the farthest transverse position of the $l = 5$ OAM beam that coincided with the x-ray yield measured above the laboratory background. At each position, total PSD filtered counts within the fast neutron ROI from the N1 EJ-309 detector located at 180° and d = 0.65±0.5 cm from the plasma target was used as the detection figure-of-merit. For a dwell time of t =40.0 seconds, coincidence neutron events from laser-jet interaction were recorded in the CAEN CoMPASS software suite. The chamber pressure was maintained at 12.0 ± 1.0 Torr, as read out on the digital vacuum gauge, throughout the entire scan. Due to the long elapsed time required for this series of measurements, ablation to the capillary nozzle would result in significant jet deflection or outright stoppage of target fluid flow. In these cases, data logging was aborted and the nozzle was replaced. Vapor pressure conditioning of the chamber followed the procedure outlined in subsection 5.3.1. Data from the previous campaign was discarded and a new baseline for grazing incidence interaction of the LG_{05} beam was taken. When two successive 300-second bubble detector dose measurements indicated nominal yield was within 10% of

the average yield measured in the grazing incidence experiment, the transverse scan was resumed. This was typically accompanied by >600 cpm as measured by the He-3 proportional counter and REM-ball survey dose rates of 70-80 μSv/hr at the surface of the chamber lid above the experiment. While N2/N3 counts were logged during this evolution, the solid angle subtended by the close proximity of the N1 detector afforded greater signal-to-background. Additionally, in all cases of target normal interaction (mid-point of the transverse position) but especially for the P-polarized Gaussian beam ($a_0 = 1.89$), bremsstrahlung and prompt γ flash were severe. This secondary radiation from the hot electron population caused detector pileup that washed out the low-frequency neutron counts typically still registered on the heavily shielded N1 detector.

From Figure 5.15, it is immediately clear that the LG_{05} beam interacts over a spatial scale that extends over $\sim$20 beam diameters ($D_{LG_{05}} = 5.0$ μm) and approximately $\sim$7 liquid jet diameters. A similar interaction scale length is also evident for the LG_{01} beam even though the measured intensity profile was $\approx$0.44 the diameter of the larger $l = 5$ LG mode. Asymmetry shown in the amplitude for the measured relative neutron yield at either edge of the jet for the OAM modes is possibly due to distortion of the annular mode profile (hotspots) or the incident chirality. All three beams show a pronounced reduction in neutron yield at target-normal incidence independent of the incident beam polarization state. This is expected due to plasma mirroring effects as the target is $n_{\text{crit}} \simeq 190$. All three scans performed with P-polarized beams show a bi-modal distribution of peak counts across the transverse scan profile but only the spatial rise and fall distances of the PG case are of the order of the $1/e^2$ beam diameter. The broad spatial range over which the OAM beams efficiently couple energy into plasma surrounding the liquid jet suggests that there is an extended region of critical density ($n_{\text{crit}} = 1.742 \times 10^{21}$ cm^{-3} for Ti:Sapphire light at λ =800 nm) vapor at the microjet's edge. This is unsurprising, as the local density changes five decades in magnitude from approximately $n_e = 3.8 \times 10^{18}$ cm^{-3} to $n_e = 3.3 \times 10^{23}$ cm^{-3} in this same region. The true magnitude of this scale length is unknown and further complicated

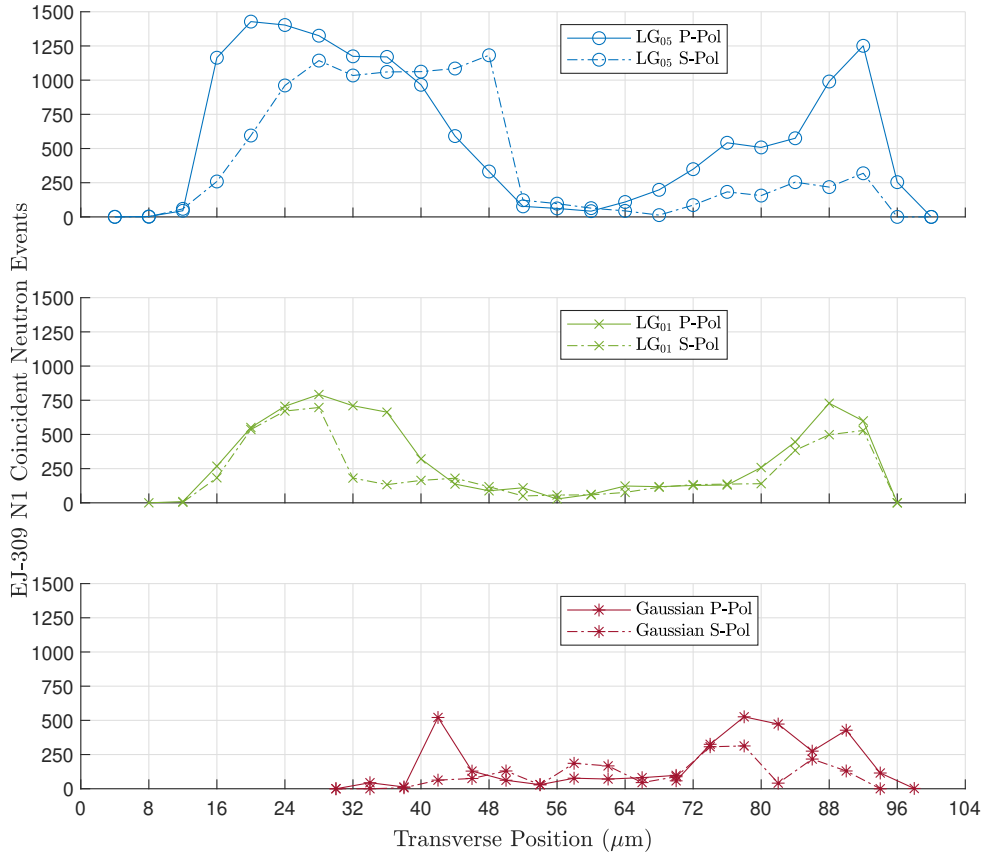

Figure 5.15: Total neutron events measured in the PSP ROI during the 40 second dwell time at each transverse position. Solid and dashed lines correspond with the P-polarization and S-Polarization of the driver beam respectively.

by the slow hydrodynamic response time of a finely atomized mist that blows out of the laser-liquid interaction volume. This extended scale length supports plasma inhomogeneity which we further study in a computational simulation that follows.

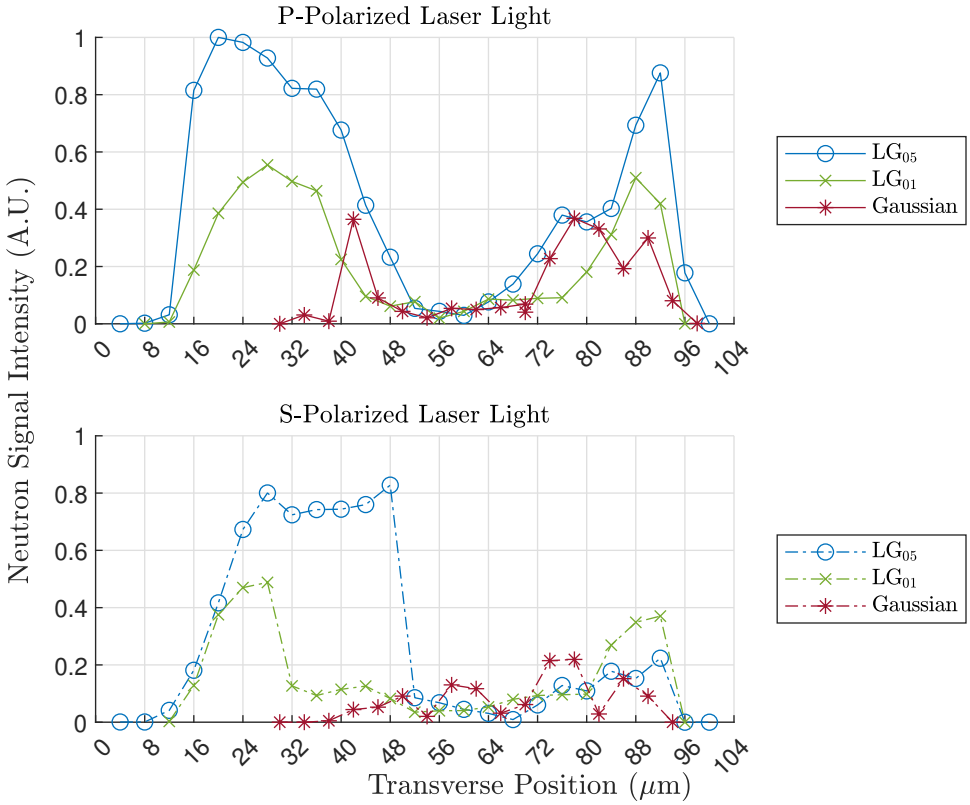

Figure 5.16: Neutron signal normalized to the maximum count recorded for the case of P-Polarized light with topological charge $l = 5$. Solid and dashed lines correspond with the P-polarization and S-Polarization of the driver beam respectively.

Following normalization of the binned fast neutron scintillation events shown for all cases in Figure 5.15 to the maximum count measured for the LG$_{05}$ scan (i.e. $\eta_{m_P=5} = 1.0$), we construct the plot shown in Figure 5.16. As expected we see that in the PG case, the P-polarized light effectively couples into the target through resonance absorption [75] at oblique incidence but S-polarized light causes negligible heating across the entire transverse profile. In sharp contrast, efficient coupling ($\eta_{m_S=5} = 0.80$ and $\eta_{m_S=1} = 0.49$) and of S-polarized light is observed for both OAM beam scans and a likely explanation arises from the advancing helical phase which drives skewed propagation of the Poynting vector [152].

5.6 Particle-in-cell simulation

Computational tools can provide valuable insight into the often complex and nonlinear dynamics of intense light-matter interactions. The particle-in-cell (PIC) computational method falls into a special class of partial differential equation solvers known as particle-mesh techniques. These codes solve the complete set of Maxwell's equations on a grid using currents and weighted charge densities corresponding to discrete particles mapped to the grid. PIC simulations are especially important in modeling the computational complexity of relativistic laser physics by means of representative macroparticles, without which the kinetic modeling of liquid jet ion densities $n_i =\sim 10^{23}$ cm^{-3} would be computationally intractable on even the most powerful high-performance computing clusters.

5.6.1 OSIRIS 4.0

OSIRIS 4.0 is a fully relativistic 3-Dimensional grid-based electromagnetic PIC code developed by a consortium including UCLA (Los Angeles, CA) and Superior Tecnico Lisboa (Lisbon, Portugal) [16, 153]. The code is object-oriented in nature but is compiled in FORTRAN prior to execution by a node. Depending on the complexity of the simulation being run, OSIRIS has the added benefit of computational efficiency necessary for execution on a single personal computer but with the capability of scaling to high-performance computing clusters. OSIRIS is capable of running a variety of high-order particle weighting schemes that allow for practical resolution of λ_D and minimizes fictitious species heating from particle-to-field and grid-to-particle interpolation steps.

As shown in Figure 5.17 OSIRIS solves for the evolving motion of representative macroparticles (fluid elements representation electron or ion species) using an iterative method:

1. Simulation loop parameters, boundary conditions, particles, and electric and magnetic fields are initialized from user-provided input decks

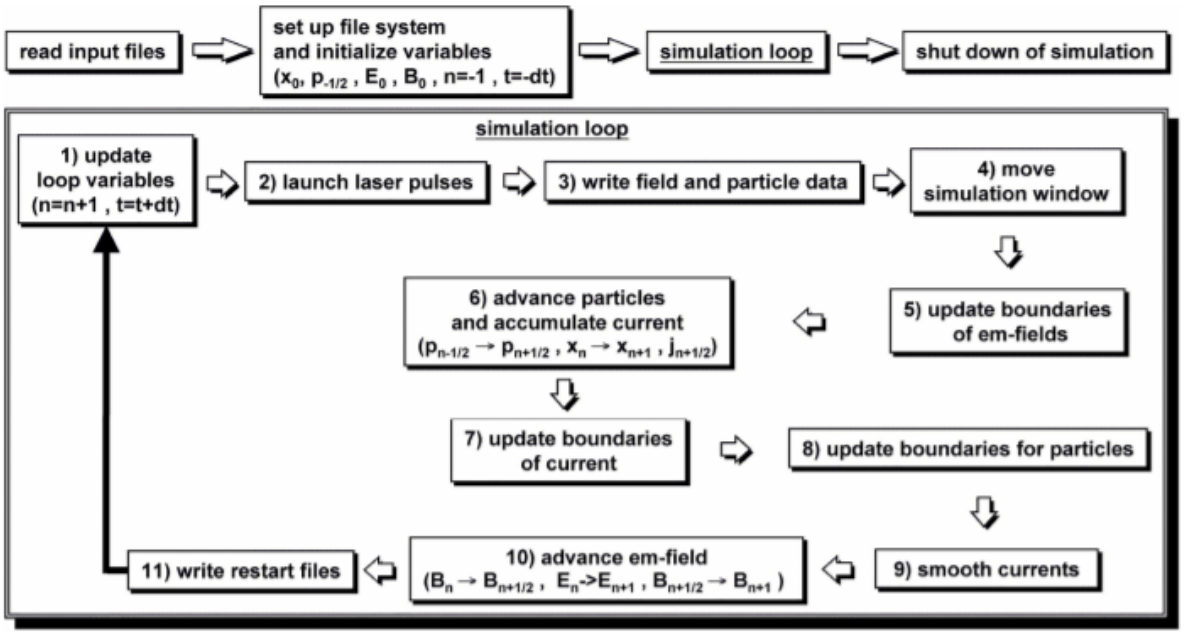

Figure 5.17: The general OSIRIS computational PIC cycle which includes relativistic electromagnetic models necessary to handle laser-plasma interactions. Figure sourced from Ref. [16] with permission.

2. Electromagnetic fields are interpolated on the grids relative to the position of macroparticles

3. Particles are 'pushed' using the Lorentz equations of motion

4. Currents and charge densities are calculated from the new macroparticle positions

5. Resulting electromagnetic fields are solved using Maxwell's equations and the new current and charge densities

6. Step in time and update loop variables as necessary

Within OSIRIS 4.0 a unit normalization scheme is used to minimize the total number of computational operations invoked during the multiplication of large floating point vector and scalar values. All units are normalized to fundamental plasma parameters which additionally have the beneficial effect of yielding minimized machine error, grid heating, and

reduced computational cost required to handle a 3D grid [153]. The normalization of key computational parameters is as follows: time is normalized to $t' = t \times \omega_p$, frequency to $\omega' = \omega/\omega_p$, and momenta $\mathbf{u'} = \mathbf{p}/m_{sp}c$ where m_{sp} is the individual species mass. Grid size selection is equally important as it the spatial sampling frequency must be higher than the smallest physical features, usually the USPL wavelength and Debye length. Lastly, the time steps used for advancing the computation loop must be small enough to resolve the shortest time scale of physically significant kinetic processes. These grid and time considerations taken together must satisfy the Courant–Friedrichs–Lewy (CFL) convergence condition for numerical stability: $\Delta t < \frac{1}{\Delta_x^2} + \frac{1}{\Delta_y^2} + \frac{1}{\Delta_z^2}$.

5.6.2 OAM laser interaction with free-flowing liquid jets

To develop a physical explanation for the marked enhancement of fusion neutron yield experimentally observed for grazing incidence irradiation of overdense targets with sub-relativistic intensity OAM beams, a basic particle-in-cell (PIC) computational model was constructed. This joint effort was supported in large part by fellow University of Michigan graduate student member Nicholas Ernst and employed the OSIRIS 4.0 PIC framework.

Before the development of a full computational 3D model of the laser-jet target interaction, we began by extending the findings of Wilson *et al.* [145] which showed analytical evidence of near relativistic Laguerre-Gaussian beam self-focusing in a homogeneous, near-critical density plasma. In our test simulation, laser pulses of $a_0 = 0.1$ and varying azimuthal mode order were launched through a linear plasma gradient from 0.1-1 n_{crit}. Results shown in Figure 5.18 confirmed that PG and higher-order OAM modes exhibit self-steepening and deflection into the density up-ramp. For the LG_{07} beam, at only $t = 655.2$ fs the initially annular shape of the beam has begun to collapse and the early onset of filamentation is evident. Hypothesizing that a similar gradient-driven collapse might occur in the presence of the overdense jet, we then developed a reduced-resolution full-3D PIC model.

This computational investigation was used to simulate the temporal evolution of the

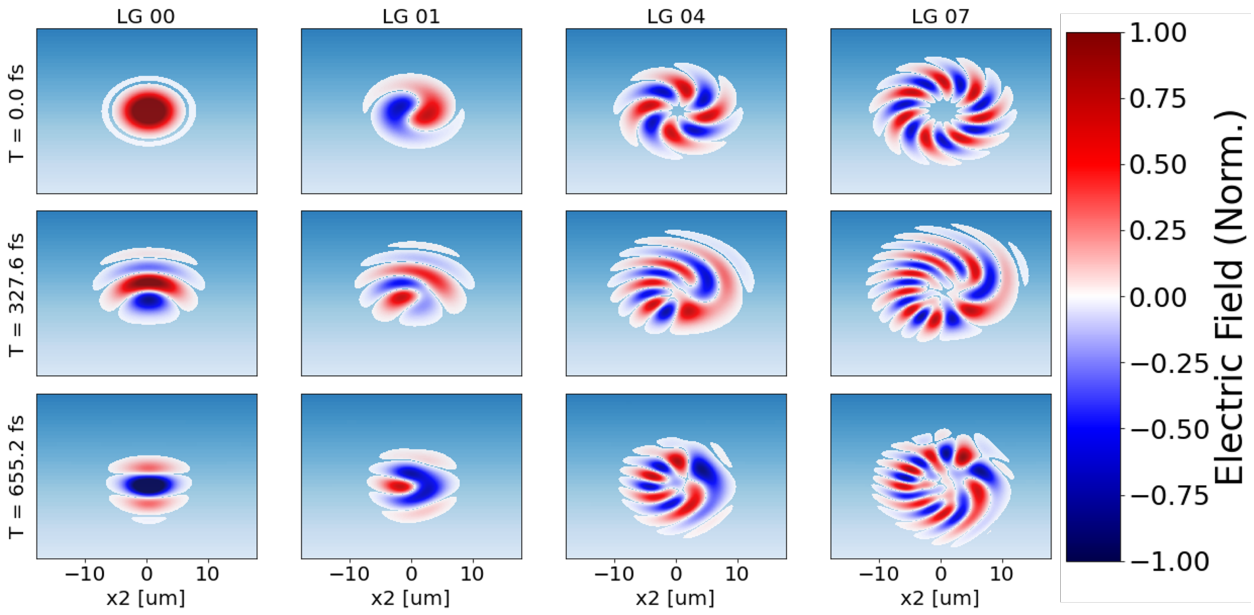

Figure 5.18: Propagation of intense laser pulses through a linear plasma gradient. Azimuthal mode order scales from left to right and time steps advance by row.

ultrashort laser propagation, complex laser-plasma interactions, and resulting particle kinetics. To our best approximation, we attempted to model the experimental parameters utilized in the λ^3 cubed shot campaigns albeit with necessary computational truncation in certain instances. A spatial interaction volume of 133.7 x 35.6 x 45.8 (μm) was built in our computational model using a simulation box with dimensions of 3312 x 128 x 164 (X1, X2, X3) cells, with a grid resolution of $\lambda/20$ in the X1 and $\lambda/4$ in the X2 and X3 dimensions respectively. In order to meet the CFL condition, time steps dt = 0.131 fs were used and our model showed no evidence of grid heating (stability) out to τ_{sim} = 350 fs.

The free-flowing D_2O jet was initialized as a cylindrical uniform cold plasma with a diameter D = 15.2 μm. Jet density was modeled as n_{crit} = 10 to relax necessary conditions to reduce numerical artifacts. The effect of finite laser pre-pulse contrast ($\leq 10^{-7}$) in tandem with a D_2O vapor pressure of 12 Torr in the physical experiment induces a pre-plasma and associated density scale length at the liquid jet's boundary. To accurately capture the plasma inhomogeneity associated with this scale length a 4^{th}-order Gaussian roll-off was applied to the heavy water jet model. Macro particles representing deuterium and oxygen ions

were initialized on the grid with a +1 charge at a density of 18 particles per cell and with normalized charge-to-mass ratios. Corresponding electron macro-particles were similarly placed with a -1 charge and grid density of 18 particles per cell.

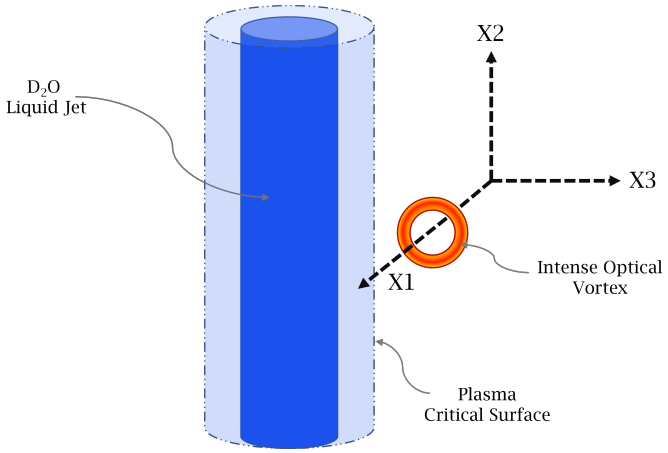

Figure 5.19: A cartoon diagram showing the beam propagation axes and orientation for data slices from the PIC OSIRIS simulation.

.

In the simulation, a Gaussian (PG) laser pulse with $E_p = 14$ mJ, $\tau_p = 66.8$ fs FWHM, and a focused beam waist of $2w_0 = 4.8$ μm FHWM were used as a relativistic ($a_0 = 1.0$) reference case. Using a built-in suite for OAM beam generation, an LG_{05} beam was launched with equivalent pulse energy and temporal duration and a properly scaled focused beam waist of $2w_0 = 8$ μm peak-to-peak. As modeled, and in good agreement with theory, the tightly focused LG_{05} mode corresponded with an initial normalized peak vacuum intensity of $a_0 = 0.41$. All laser fields were launched as linear P-polarized light unless otherwise noted. Figure 5.19 shows a basic diagram of the PIC model.

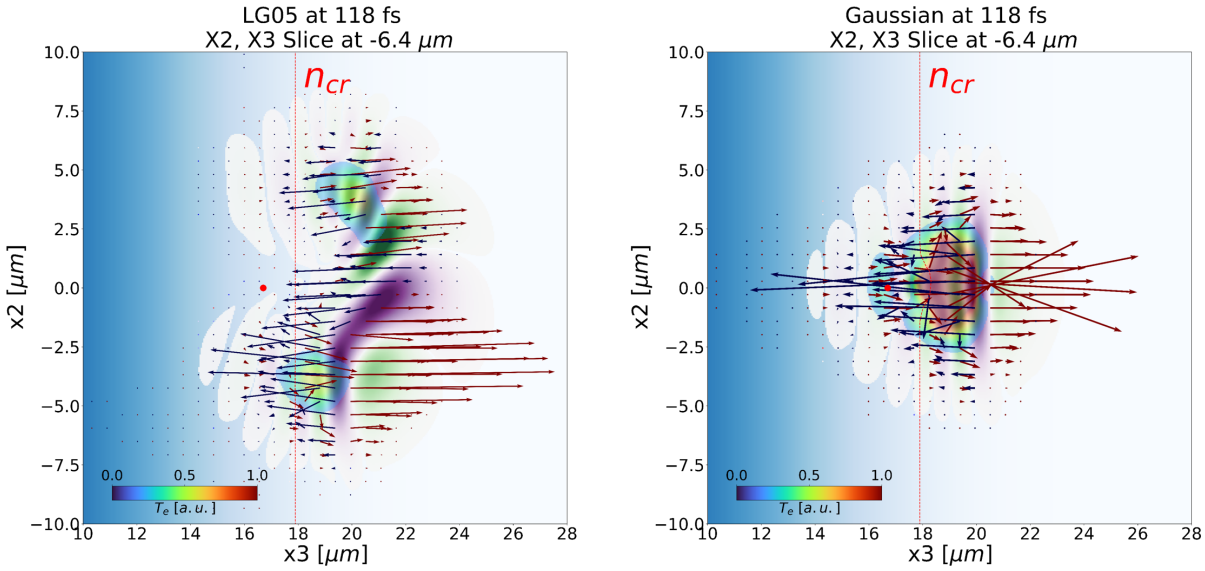

Figure 5.20: An X2-X3 transverse slice of the (*left*) LG_{05} and (*right*) PG beam offset r = 16.67 μm from the jet center. The vector arrows represent the normalized amplitude of electron current and the green-purple shading is the normalized electric field strength.

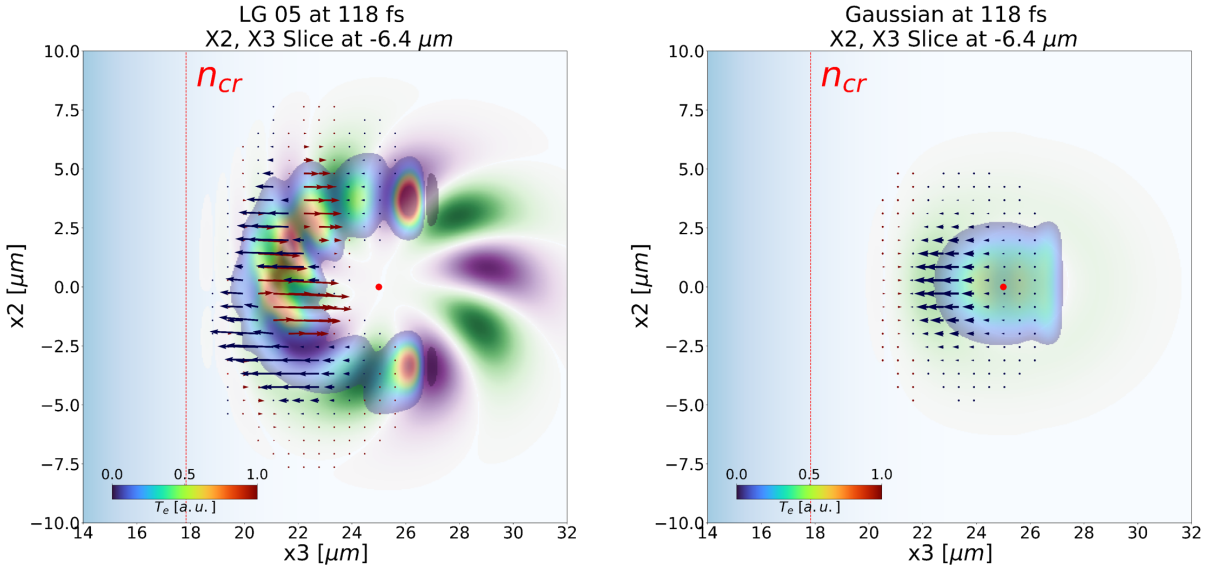

Figure 5.21: An X2-X3 transverse slice of the (*left*) LG_{05} and (*right*) PG beam offset r = 25.0 μm from the jet center. The vector arrows represent the normalized amplitude of electron current and the green-purple shading is the normalized electric field strength.

The notable differences in Figure 5.20 and Figure 5.21 provide a heuristic for the major

findings of this series of simulations. Each figure shows a comparison of transverse X2-X3 slices taken at t = 118 fs of the PG and LG_{05} beam after propagation at different radial offsets in the density down-ramp at the liquid jet's edge. At both distances, we can plainly observe that the OAM beam has self-focused and the development of two intense anti-nodes corresponding to the points where the laser energy has become concentrated during beam self-compression. This effect was previously characterized in [145, 154, 155] and is known to exhibit the characteristic bi-lateral spatial structure seen in our simulation. At the r = 16.67 μm offset position, this collapse is limited in its extent and the beam scrapes along the critical surface driving the formation of two moderate-temperature electron populations. As expected, the Gaussian beam creates an axial channel of hot electrons which ponderomotively expels suprathermal electrons orthogonally into the jet and outward into the low-density background. In contrast, fundamentally different behavior is seen when the two beams are translated further into the shallow density ramp at r = 25.0 μm. Here, the PG beam diffracts and only weakly interacts with the underdense plasma while the high-order OAM beam takes on the appearance of a cylindrical line-focus. This flattening along the critical surface creates a large volumetric region of hot electrons and large amplitude perturbations to the electric field that likely correspond to intense beamlet formation. Under the effects of this spatially optimized self-focusing, the LG_{05} attains near relativistic intensity of $a_0 \geq 0.73$. We believe this configuration, as represented in Figure 5.21, qualitatively corroborates with enhanced resonance absorption at the critical surface and increasing neutron yield at transverse beam positions exceeding 1.5 jet diameters. Lastly, the magnitude and structure of currents formed during the LG_{05} beam interaction with the jet are markedly different from those seen in the PG case. The Gaussian beam radially expels electrons forming a starburst current flow. Conversely, the self-focusing OAM beam presents with a dense region of counter-flowing electron motion that strongly resembles the efficient laser-plasma coupling of optimized resonance absorption [75, 156]. Indeed, this extended planar region of resonance absorption would lead to a large area of volumetric heating, and the shearing

current flow likely caused by helical phase rotation would impart strong plasma oscillations along the interaction region. Further modeling and confirmation of the instability growth rate of such an effect would show excellent agreement with [157], where rippling of the critical surface was shown to enhance coupling of non-normally incident laser radiation. Furthermore, this filament-induced rippling overrides the role of the incident polarization state in light-plasma coupling [151], and would explain why efficient neutron generation was seen in our experimental campaign for the case of incident S-polarized beams.

5.7 Conclusion and future works

In conclusion, we demonstrate the application of self-focusing near relativistic optical vortex beams to generate a record isotropic fast neutron yield of 1.45×10^6 n/s/sr. Beams with a topological charge of $l = 5$ were shown to deliver up to a 3.3x enhancement of fast neutron yield over the standard Gaussian beam. This completely unexpected result was achieved with only modest laser energies of 16 mJ and relaxed compressed pulse duration (τ_p = 66.7 fs) requirements suitable for laser media with narrow band gain windows. Tabletop neutron flux of this level is comparable to that characteristic of commercial sealed-tube D-D generators [83] but with a FWHM pulse duration of 20 ns. Further repetition rate scaling of this interaction could easily generate of-order 10^{7-8} n/s and would be well suited for time-resolved prompt gamma neutron activation analysis studies [158]. The marked reduction in polarization sensitivity to laser-plasma energy coupling for OAM-target interactions in our physical experiment was investigated through a simple PIC model and a rudimentary link to electron density rippling resulting in plasma wave excitation drawn.

The results of this study provide a solid groundwork for experimentation both in the laser lab and in PIC models. To reduce the effects of B-integral accumulation, the experiment should adopt the use of reflective SPMs with lower dispersion. Homogeneity of the far-field OAM spatial intensity profiles could likewise be substantially improved through the use of

iterative wavefront optimization algorithms such as those first demonstrated in our group's parallel work [144]. In terms of the PIC simulation, the use of higher macroparticle densities could further reduce numerical artifacts associated with the overdense target geometry and the added resolution would provide better insight into the critical surface rippling suggested by our preliminary model.

CHAPTER 6

High-Repetition Ultrashort Fiber Laser Experiment

6.1 Introduction

Ultrashort fiber lasers have seen widespread application in telecommunications systems [159], precision optical timing [159], frequency comb generation [160, 161], and industrial materials processing [162, 163]. Historically, breakthroughs in relativistic laser-plasma acceleration [46, 47, 50, 74, 78, 105, 164] have been dominated by solid-state CPA lasers built around Ti:Sapphire [23] and Nd^{3+}-doped phosphate glass [165, 166]. Seminal work by Snitzer et al. [167] on double-clad fibers began a revolution in high average power ultrashort fiber lasers that has rapidly accelerated by the subsequent development Yb-doped photonic crystal fiber amplifiers [168] and Yb-doped chirally coupled core (CCC) fibers [169]. In parallel to widespread progress in extractable pulse energy and average power from a single fiber channel, channel multiplexing known as coherent beam combination was successfully demonstrated [68]. Lastly, management of parasitic ultrashort pulse non-linear phase accumulation associated with the long propagation lengths of fibers was demonstrated through experimental demonstration of divided pulse amplification (DPA) [67] and coherent pulse stacking amplification (CPSA) [69, 70]. Synergistically, and taken together, these advances have led to the demonstration of kilohertz repetition-rate, multi-mJ ultrashort fiber laser architectures capable of delivering 10^{1-2} GW of peak and near kW average powers [170–174]. To

date, and to the best of our knowledge, utilization of such systems for laser-plasma acceleration or demonstration of high-field science has been limited only to hard x-ray [55,175,176] THz radiation generation [177].

In this work, we extend the application of a novel Yb-doped ultrashort fiber laser system in the University of Michigan Galvanauskas laboratory. We show that the high-power coherent beam combining and coherent pulse stacking architectures are capable of stable operation at multi-GW peak powers for elapsed laser-plasma experimental campaigns of > 1700 seconds. In a proof-of-principle demonstration, and to the best of our knowledge for the very first time, we demonstrate nuclear fusion reactions driven by an all-fiber ultrashort laser system. As part of this joint collaboration, we also show a proof-of-principle application of gain-managed nonlinear amplification (GMNA) [178] in Yb-doped fibers to engineer an ultrashort, off-color, and temporally synchronous backlighting laser for transverse optical probing of intense laser-matter interactions.

6.2 High repetition ultrashort fiber laser-driven neutron source

6.2.1 Experimental setup

This experiment utilized an almost identical target chamber configuration to the experimental work presented in Chapter 5 and the layout is shown in Figure 6.1. Modifications to the setup are noted as follows: Because this system lacks adaptive optics, tight focusing was achieved with a 50.8 mm $f/1$ 90° YAG-coated off-axis parabolic mirror (Edmund Optics). Basic operating principles of the CBC + CPSA laser driver are discussed in subsection 3.1.2 and are well characterized in [179]. During this experiment, the USPL delivered $\lambda_L = 1035\pm5$ nm nominally 2.75 mJ pulses at a pulse repetition frequency of $f_{rep} = 1.95$ kHz. Using intensity autocorrelation the compressed pulse duration of the high-intensity driver

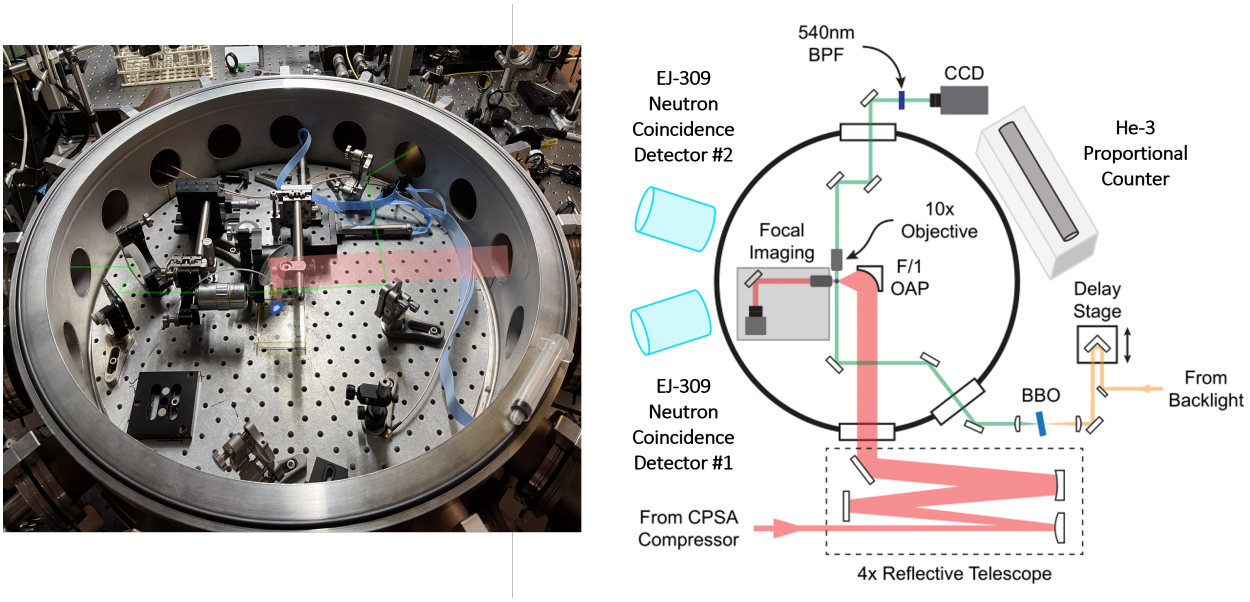

Figure 6.1: The experiment setup used for the high repetition ultrashort fiber laser-driven neutron source. (*left*) The vacuum target chamber and D_2O microjet target and (*right*) a diagram of the incoming driver and probe beam paths.

pulse was measured as $\tau_p = 501$ fs using a deconvolution factor of 1.34. As shown in Figure 6.2, the focused driver beam was measured to have a Gaussian profile of $2w_0 = 4.4 \pm 0.1$ μm resulting in peak on-target intensities of up to $7.2{\times}10^{16}$ W/cm^2 and an estimated peak power of $\sim$5.5 GW.

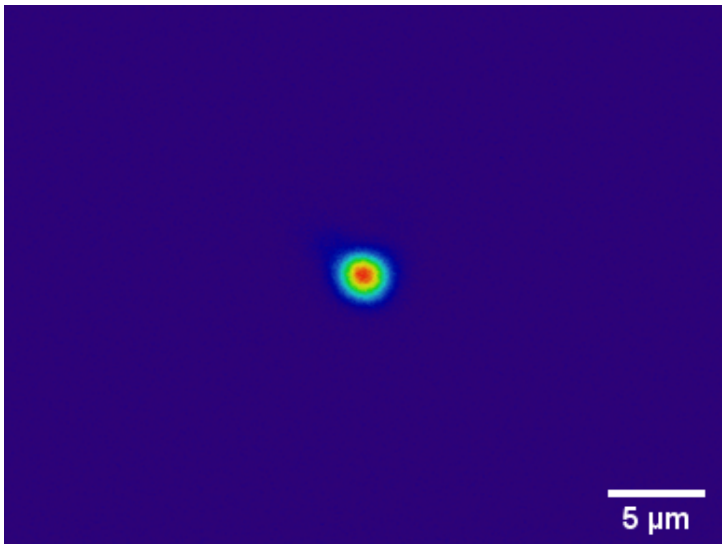

Figure 6.2: An image of the highly attenuated Yb-CPSA laser beam profile at focus.

During experimental runs, the amplified and stacked 81-pulse burst train was measured to have nanosecond pre-pulse contrast of no better than 10^{-1} and stacking efficiency was measured at η= 68.9%. An oscilloscope trace of the stacked burst sampled from a fast (< 22ps) beam sampling photodiode in the compressor is shown in Figure 6.3.

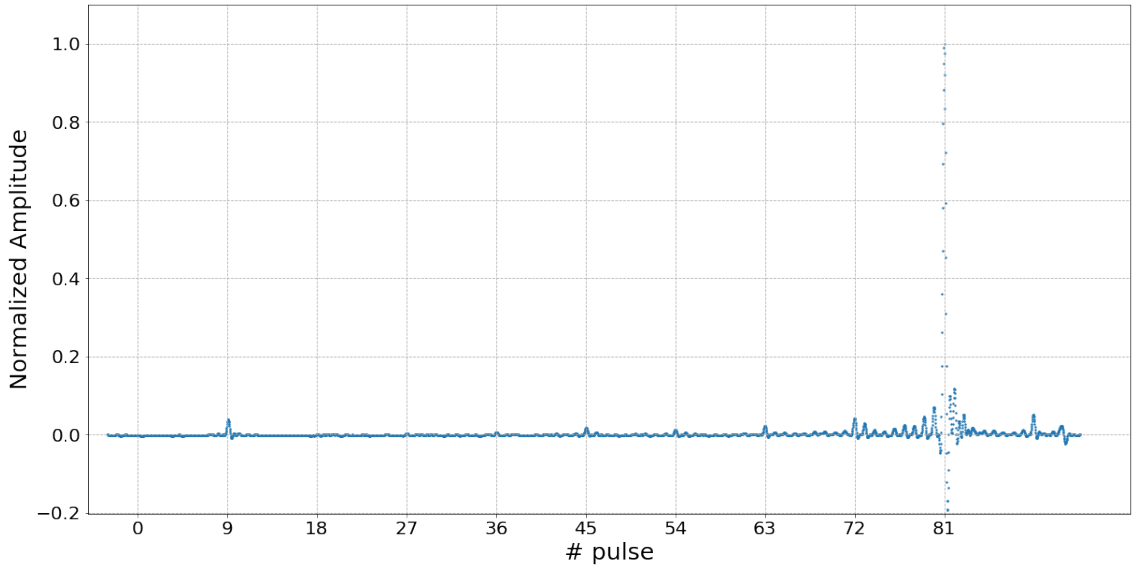

Figure 6.3: An oscilloscope trace of the high-power stacked and compressed burst train coming from the CBC and CPSA stacking setups.

Although the mass-limited characteristics of the EHD microjet target would have proved beneficial for this campaign we chose to use the free-flowing D_2O jet as our ion acceleration source. Ultimately we were concerned that high-voltage transients and EMP emitted from the EHD target system could adversely affect the phase-sensitive feedback stabilization loop running the CPSA setup, or worse damage the primary high-speed FPGAs controlling the various phase and amplitude shaping electro-optic elements in the system front end. A consumable fused silica capillary nozzle was again used to generate a d = 15.2±0.2 μm target stream with nominal flow rates of 225 μL/min. Following the basic alignment procedures outlined in the EHD and OAM chapters, the chamber was evacuated and conditioned to allow the buildup of ambient D_2O vapor pressure to ∼12 Torr.

Transverse optical probing of the laser-jet interaction was performed with an ultrashort

synchronous off-color backlight system that is further detailed in section 6.3. The fast neutron detection methodology is further discussed in the next subsection.

6.2.2 Neutron flux measurement

Given the proof-of-principle nature of this experiment, we attempted to maximize event counting by placing the fast neutron detectors as close to the target interaction volume as was spatially achievable. Similar work with sub-relativistic lasers of <1 mJ of energy in [41, 180] suggested that measured yield would be of order 1-10 n/s/sr. Neutron fluxes of this level are near the absolute noise floor of detection because of the cosmogenic neutron background present under normal conditions [181]. Fast neutron-induced proton-recoil is ideally suited for neutron interrogation under these conditions and two EJ-309 detectors N1/N2 were mounted at 10.9±0.5 and 11.4±0.5 cm from the OAP's beam waist. The detectors were operated with pulse shape discrimination enabled and with an optically triggered coincidence window of $\tau_{\text{coinc}} = 512$ ns. To maximize the solid angle subtended by the detectors' liquid wells, secondary high-Z shielding was not used and as a consequence x-ray/γ photon count rates were significant but remained below the level necessary to paralyze the detectors. This bright gamma flash coinciding with the high-intensity laser pulses interacting with the overdense D_2O jet required modification of the PSP cuts used for n/γ discrimination. For N1 the energy cut range was set to between 120-1150 keV and PSP values of 0.25-0.50 were binned as fast neutron events. Likewise, for N2 the energy cut range was set to between 120-1150 keV, and PSP values of 0.25-0.45 were binned as fast neutron events. A moderated ^{3}He proportional detector was additionally used for target positioning optimization.

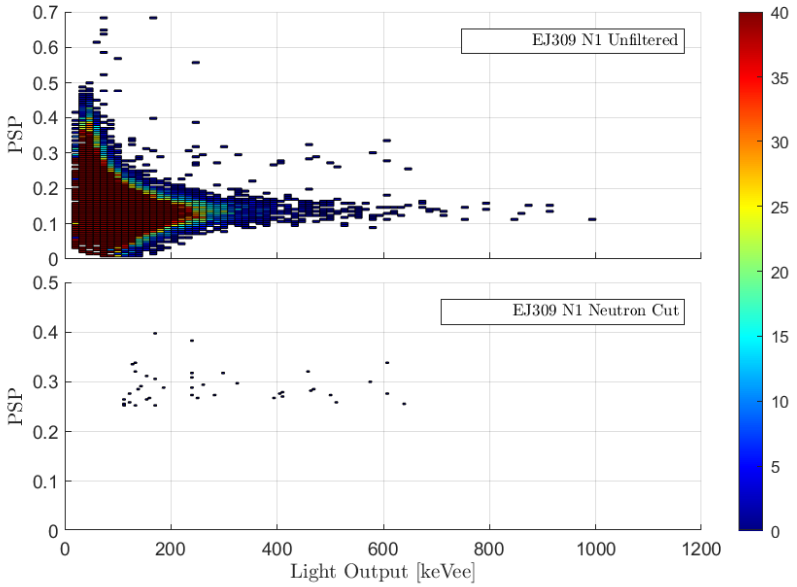

Figure 6.4: (*top*) Binned coincidence scintillation events measured by scintillator detector N1 during 1.41×10^6 Yb-CPSA laser shots at 2.75 mJ. (*bottom*) 43 fast neutron events registered in the PSP cut ROI.

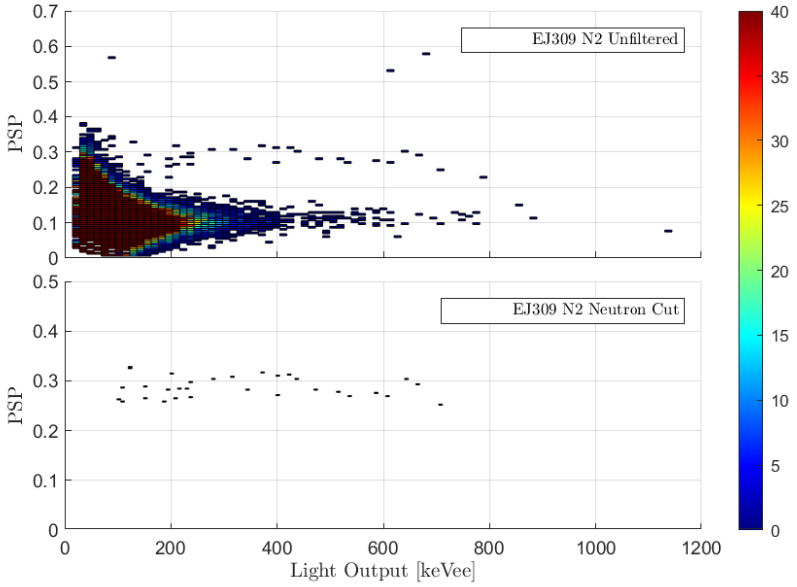

Figure 6.5: (*top*) Binned coincidence scintillation events measured by scintillator detector N2 during 1.41×10^6 Yb-CPSA laser shots at 2.75 mJ. (*bottom*) 31 fast neutron events registered in the PSP cut ROI.

Coincident ultrashort fiber laser-driven fast neutron events (PSP of 0.3) measured over a Δt = 1725 second experimental campaign are clearly shown in Figure 6.4 and Figure 6.5. Measurement of a non-coincident laboratory fast neutron background accumulated for Δt = 10,800 seconds yielded an average event rate of 0.04±0.0057 counts per second (cps) over both detectors. Assuming Poisson statistics, the total number of counts expected for worst-case chance coincidence detection within our detection window was 0.069±0.08 total events. Total region of interest (ROI) neutron events measured for N1/N2 were 43 and 31 respectively and ultrashort fiber laser-driven nuclear fusion is claimed with $> 3\sigma$ confidence.

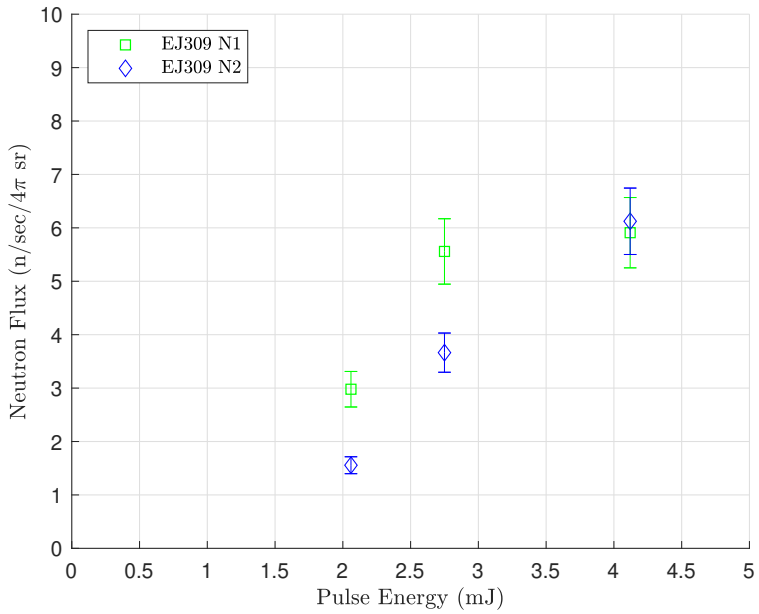

Figure 6.6: Measured isotropic neutron flux for CBC + CPSA fiber laser-driven neutron campaigns at various pulse energies.

Applying EJ-309 detector response calibration obtained in the University of Michigan Neutron Science Laboratory, the binned ROI counts were converted to a floor estimate of isotropic neutron flux. As shown in Figure 6.6, we estimate a maximum sustained isotropic flux during our experiment of $\phi = 6.12 \pm 0.62$ n/s/4π sr. This yield is in reasonable agreement with fluxes reported from LDNS experiments with low contrast or sub-10 GW peak power systems [180].

6.3 Synchronous off-color ultrashort backlight system

Optical diagnostics play a crucial role in interrogating the complex and rapidly evolving physics associated with relativistic light-matter interactions. The practical application of ultrashort and few-cycle optical probes has been reported in studies of laser-driven ion acceleration [57, 182], plasma channeling [183], and the channel structure of laser wakefield accelerators [184, 185]. To date, further adoption of these systems has been limited due to several factors: (1) most solid-state lasers use Kerr-lens modelocked oscillators with cavity repetition rates of >80 MHz and large mechanical delay stages must be used to achieve temporal delay between the >12.5 ns spaced pulses, (2) optical backlight pulses at the fundamental and second-harmonic of the driver frequency are often washed at by plasma self-emission or scattering from the energetic driver beams, and (3) 'picked' backlight pulses must be separately amplified and compressed - necessitating added system complexity and cost. In this work, we apply the recently discovered technique of gain-managed nonlinear amplification (GMNA) [178, 186] in Yb-fibers to spectrally broaden, amplify and compress off-color ultrashort laser pulses. Arbitrary delay from fs-ms temporal durations is achieved by seeding the system with pulses derived from a 1 GHz oscillator and pulse picking with a high-damage threshold quartz AOM. Operation of the system is shown through time-resolved imaging of a propagating hydrodynamic shock front.

6.3.1 Gain-managed nonlinear amplification theory of operation

Gain managed nonlinear amplification [178, 186] takes advantage of the co-evolving gain dynamics of co-pumped Yb-doped fiber lasers. As the pump light is absorbed along the length of the fiber amplifier, the gain spectrum shifts to longer wavelengths enabling spectral broadening. But unlike self-phase modulation, the resulting ultra-broadband pulses exit the fiber amplifier with a nearly quadratic spectral phase. When properly applied, this technique can result in the generation of NIR pulses with a transform-limited duration of ∼40 fs [186].

It is currently theorized that the pulse evolution during the GMNA process is due to the presence of a nonlinear attractor although this is still an open question.

6.3.2 System design

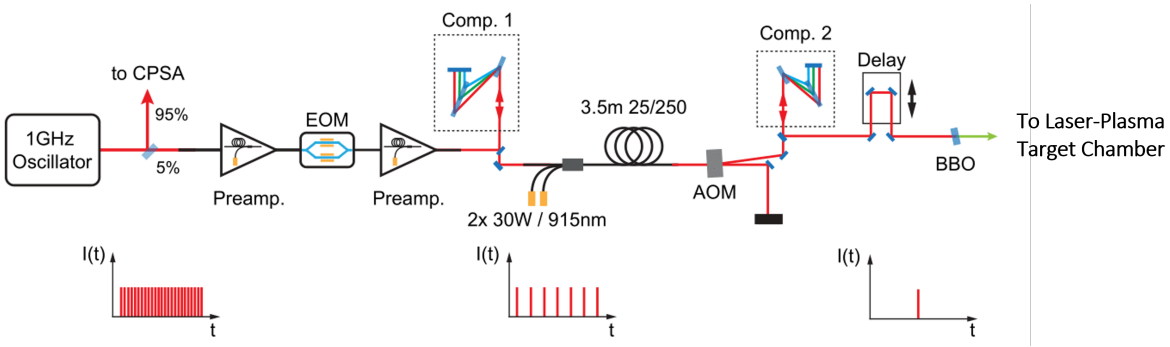

Figure 6.7: A schematic showing the fundamental components of the GMNA system. Figure courtesy of Alex Rainville.

The design of this system was substantially based on previous work by our collaborators in Frank Wise' group at Cornell [178] and is diagrammatically shown in Figure 6.7. An ultrashort seed for the system is derived from a nominally 1 GHz non-linear polarization rotation modelocked Yb-fiber oscillator generating ∼70 fs pulses. Approximately 5% of the oscillator energy is beam-split and coupled into a single-mode fiber (PM 980) for routing to the backlight setup. A single-mode pre-amplifier then boosts the energy to 10 pJ prior to burst shaping in a 10 GHz fiber-integrated EOM (iXblue). Using the Yb-CPSA FPGA back-end, we then down count the burst to 5 MHz and create a pulse windowed by 200 ns on both the leading and trailing edge. A second pre-amplifier then boosts the pulse energy to 100 pJ prior to pulse burst compression in a compact Treacy compressor featuring 1000 line/mm dielectric transmission gratings. The nominally 150-200 fs pulses are now injected into a 3.5 m long, cladding-pumped, effectively single-mode LMA fiber. This high-power amplifier is 2x CW pumped at 915 nm with up to 60W of power.

The amplified and ultra-broadband 5 MHz burst train leaves the YDFA with a pulse duration of 20-30 ps and pulse energy of ∼600 nJ. Following collimation and residual pump

stripping by a dichroic mirror, the now free space beam is launched through a 40 dB isolator. A high damage threshold quartz AOM (Gooch & Housego) then picks the 'windowed' pulse within the burst at repetition rates set by the master Yb-CPSA system (typically 1.95 kHz). The diffracted pulses are then sent through a second Treacy compressor stage containing a pair of matched gratings. Finally, the NIR 200 nJ off-harmonic pulses transit a 30 cm optical path length mechanical delay line which provides temporal scanning in the ps-fs range. Figure 6.8 shows a single-shot measurement of the compressed GMNA output.

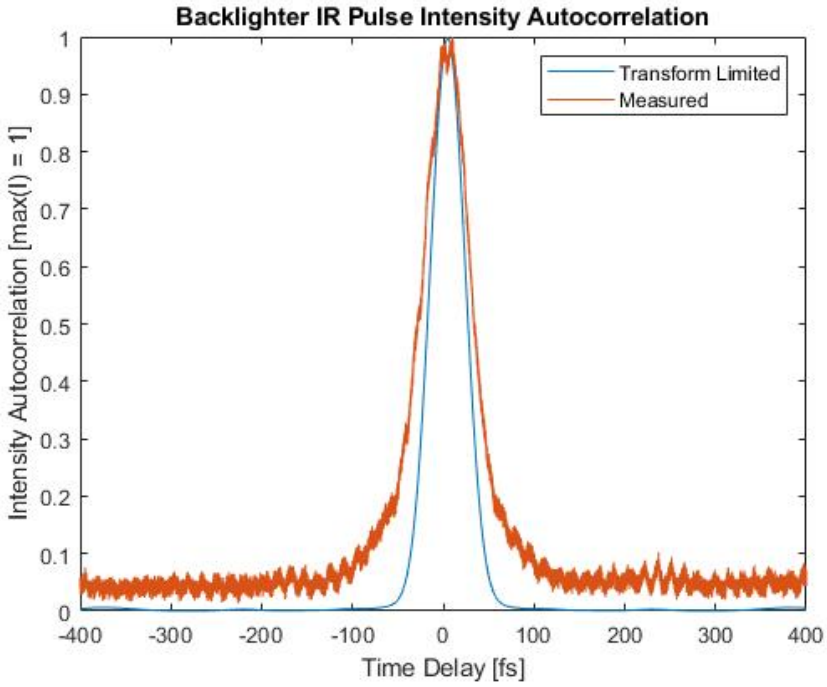

Figure 6.8: An intensity autocorrelation trace of the compressed NIR off-harmonic backlight signal. Trace deconvolution recovered a pulse duration of $\tau_p = 41$ fs at a center wavelength of $\lambda = 1080$ nm.

Focused frequency doubling in a 500 μm BBO crystal provides approximately $\sim$20 nJ of visible green light centered at 542$\pm$10 nm. This beam is then placed through a 5.0 OD hard edge YAG filter at 1064 nm to strip the residual NIR spectral content and sent to a telescope for collimation and sizing for delivery to the experimental chamber. The spectra before and after this filtering process is detailed in Figure 6.9.

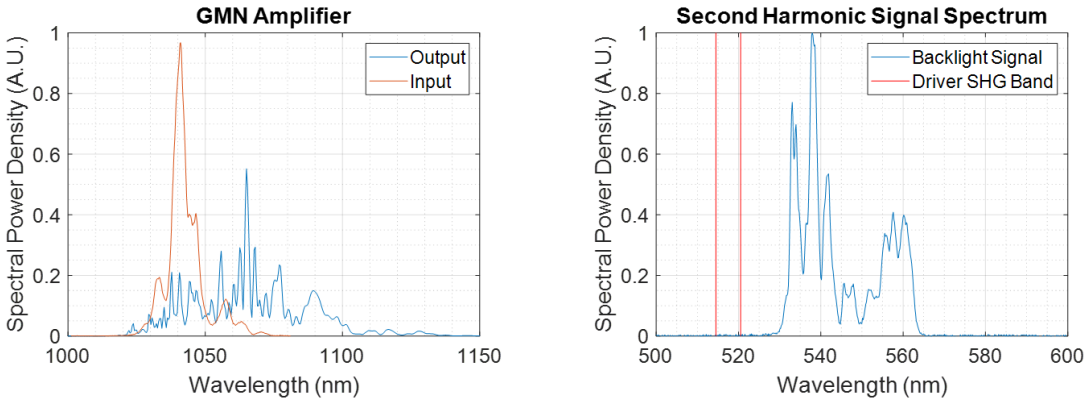

Figure 6.9: (*left*) The amplified and spectrally broadened backlight output signal and (*right*) off-harmonic light in the visible spectrum generated from SHG of the output.

This realization of this system was the result of a joint developmental effort with University of Michigan EECS graduate students Alex Rainville and Christopher Pasquale. This author aided in the implementation of the physical system and build-out of the bias electronics but the ultimate system design was performed by members of the Galvanauskas laboratory. During proof-of-principle experiments, my work focused on the successful demonstration of time-resolved imaging of ultrashort laser-plasma interactions and the temporal evolution of liquid target stability dynamics.

6.4 Proof-of-principle time-resolved imaging demonstration

The following proof-of-principle imaging sequences were taken by backlighting the irradiation of a d = 15.2 μm free-flowing liquid jet with ~1 mJ / τ = 3 ps pulses from the main CPSA system running at a repetition rate of 1.95 kHz. Images were collected with a monochrome USB CCD with 1280x960 pixel resolution (Imaging Source DMK41BU02). The camera was externally triggered from a TTL delay generator (Stanford Research DG535) and exposure was set to 1/10000 s and electronic gain was set at its maximum value of 36 dB. Micrograph

magnification is provided by an infinity-corrected 10x long working distance microscope objective (Mitutoyo). To enhance contrast and reduce image saturation due to the plasma self-emission, the off-color light is further filtered with a 4.0 OD hard edge band pass filter with a pass band of 550±20 nm FWHM.

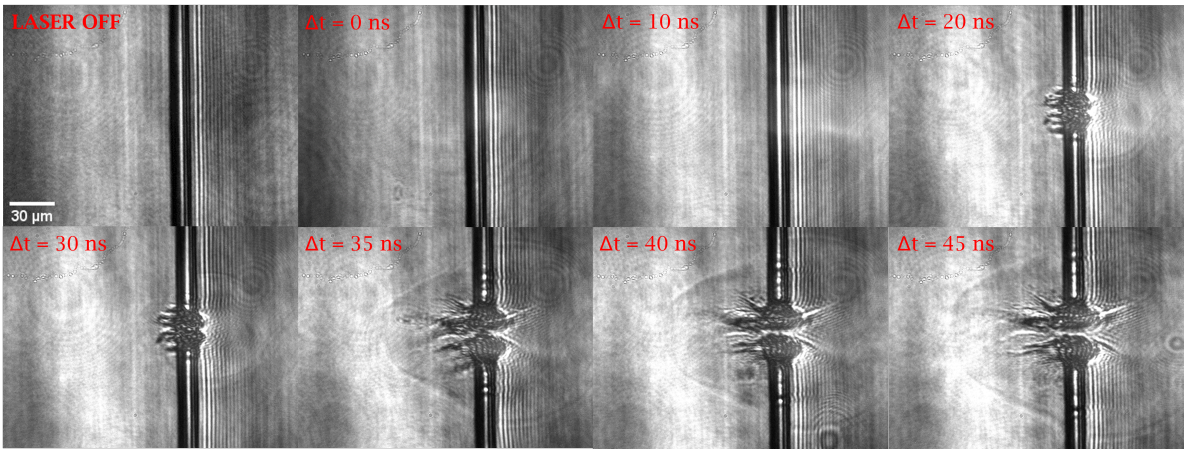

Figure 6.10: Time-resolved imagery of the hydrodynamic shock front propagation from a laser-perturbed microscale liquid jet.

In Figure 6.10 we clearly see the formation of a radially propagating hydrodynamic shock front. Through image post-processing (ImageJ), we estimate that the early time ($t \leq 20$ ns) target-normal shock velocity reaches an astounding 2,725±45 m/s (Mach = 8.22) before stagnation. In this sequence, the FPGA-to-EOM timing signal was coded with simple Python script modifications, and owing to the 1 GHz front-end seed, no additional mechanical delay was necessitated. As a point of reference, attempted acquisition of this same frame sequence with the pulsed 405/450 nm LD backlight used in the λ^3 experiments would have failed to resolve the shock as the minimum rise time for resolvable image features was at least 35.0 ns.

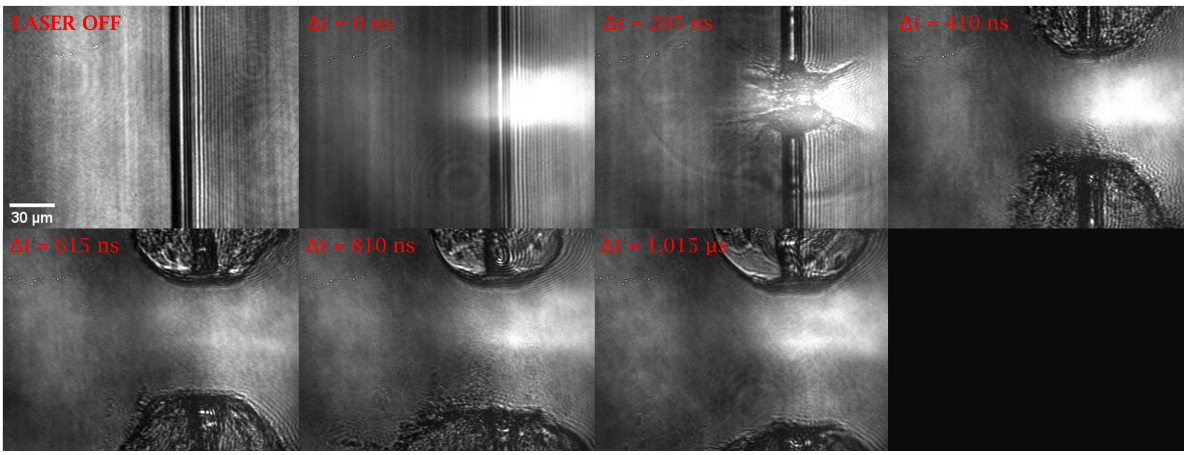

Figure 6.11: Time-resolved onset of late time liquid-target recovery.

The promise of 3FST laser drivers exceeding frequency repetition rates of 10 kHz poses a significant laser-targetry problem. To this end, Figure 6.11 reveals two critical insights. First, the space-charge effects and thermal pressure wave of the resulting intense laser-plasma interaction cause the hydrodynamic stagnation of the liquid jet. Although this sequence is truncated at $\Delta t = 1.015$ μs, the time-resolved video of this interaction reveals that the stream was not able to recover laminar flow until 18-22 μs after irradiation. At f = 45.5 kHz, this places a true ceiling on the usefulness of liquid targets. In truth, this is likely overestimating the jet response because we see the parabolic deflection of the stream outward from the focused beam waist. This causes the significant upward ejection of bulk liquid filaments and droplets seen in Fig. 6.11. Subsequent collision of these fluid fragments with the upper laminar portion of the stream could seed hydrodynamic instability and warrants further investigation as to its effects on maximum on-target shot rates.

6.5 Conclusion and outlook

In summary, this work presents a meaningful extension of the application of high-power ultrashort fiber laser systems into the realm of high-field science. To the best of our knowledge, we demonstrated for the first time a tabletop neutron source driven by an all-fiber ultra-

short driver. Irradiation of a free-flowing laminar D_2O liquid jet with 5.5 GW laser pulses at f_{rep} = 1.95 kHz resulted in statistically significant D(d,n)^{3}He fusion reactions detected through coincidence proton-recoil measurements. The GMNA synchronous off-color backlighting system is capable of time-resolving plasma dynamics and further system refinement promises increased contrast through polarization filtering. The novelty of this design resides in the arbitrary ability to delay the system from fs-ms time scales by straightforward electronic pulse delay. Furthermore, this design has wide applicability as the YDFL gain band is well aligned with Yb^{3+}-doped solid-state laser media that is now ubiquitously deployed in thin-disk systems [26].

Although the isotropic yield measured during this campaign is a fraction of that realized in the optical vortex experiments, the significance of this work should not be understated. The poor system contrast measured during this campaign is a natural consequence of the coherent pulse stacking process and recently, methods for contrast improvement to >30 dB have been shown for cases where the phase control algorithm allows burst post-pulsing at only marginal expense to the system stacking efficiency [179]. In addition, this experiment was carried out with compressed pulses that were atypical of the properly compressed system (∼330 fs) and the application of non-linear phase management techniques could further improve peak power by a factor of 3. Programmatic scaling of the system toward the 3FST stated objective of realizing a 100 mJ / <100 fs / 10 kHz all-fiber ultrashort driver would deliver relativistic peak intensities of 1.9×10^{19} W/cm^2 if used in the same experimental chamber. This exciting development could further extend ultrashort fiber laser systems to efficiently drive high-brightness tabletop fast neutron sources.

CHAPTER 7

Conclusions and Outlook

7.1 Conclusion

This experimental thesis work has demonstrated various pathways toward the generation of fast neutron sources through the engineered application of intense laser light. In three separate cases, the use of only a few mJ of tightly focused ultrashort laser energy successfully initiated D(d,n)^{3}He fusion reactions at tabletop scales. The results from these campaigns advance the field of high-field science by further characterizing the dynamics of relativistic laser interactions with near solid-density targets in the high repetition rate regime.

This work resulted in the conceptualization, design, and physical implementation of a novel high-repetition target system capable of synthesizing liquid-density deuterated targets only 2.7 μm in diameter. The pulsed electrohydrodynamic microjet target was shown to operate at beamline-quality vacuum levels ($< 10^{-5}$ Torr) without ancillary cryogenic pumping or costly high-volume flow rate turbomolecular pumps. The target fluid flow rates achieved were an order of magnitude lower than those previously reported for similar piezo-droplet target generators or for laminar free-flowing liquid jets. The EHD target system was built with commercial-off-the-shelf components and demonstrates the use of additive manufacturing technology to rapidly iterate modular vacuum components into a fielded design. Up to 4×10^4 n/s/sr isotropic flux was measured over sustained periods (>3600 s) of pulsed target operation at $f = 4.8$ kHz without degradation in output flux or target system failure.

First-of-their-kind experiments carried out with near relativistic intensity optical vortices demonstrated record fast neutron yield of 3×10^3 n/shot for modest pulse energies of only $\sim$ 16 mJ of incident S-polarized laser energy. As part of a parametric scan investigating transverse beam position and incident beam polarization, it was shown that beams of light with finite orbital angular momentum (topological charge $m = 1$ and $m = 5$) can efficiently couple into critical density plasmas in both linear polarization states. These unexpected findings build upon earlier theories regarding filamentation dynamics resulting in enhanced resonance absorption in critical density plasmas. A basic computation PIC model qualitatively validated the empirical findings of an optimized radial offset distance for OAM beam self-steepening and collapse in the presence of an inhomogeneous plasma density gradient. Experimental results suggest that volumetric plasma heating scales with topological charge and that OAM beams of higher azimuthal order could lead to lead to an even higher brightness laser-driven neutron source.

Proof-of-principle experiments demonstrated for the first time D-D fusion driven by a high average power, all-fiber, ultrashort laser driver. This extends the application of fiber optic technology to the high-field physics domain and establishes the preeminence of wall-plug efficient laser systems as practical drivers for laser-plasma particle acceleration. Lastly, the engineered application of GMNA in Yb-doped fibers led to the successful development and experimental demonstration of an off-harmonic optical backlighting system that is capable of arbitrary delay over 9 decades of temporal duration.

As a point of reference, the per/shot isotropic neutron yields estimated from the three laser-driven neutron source experiments discussed in this work are shown relative to published work in Figure 7.1.

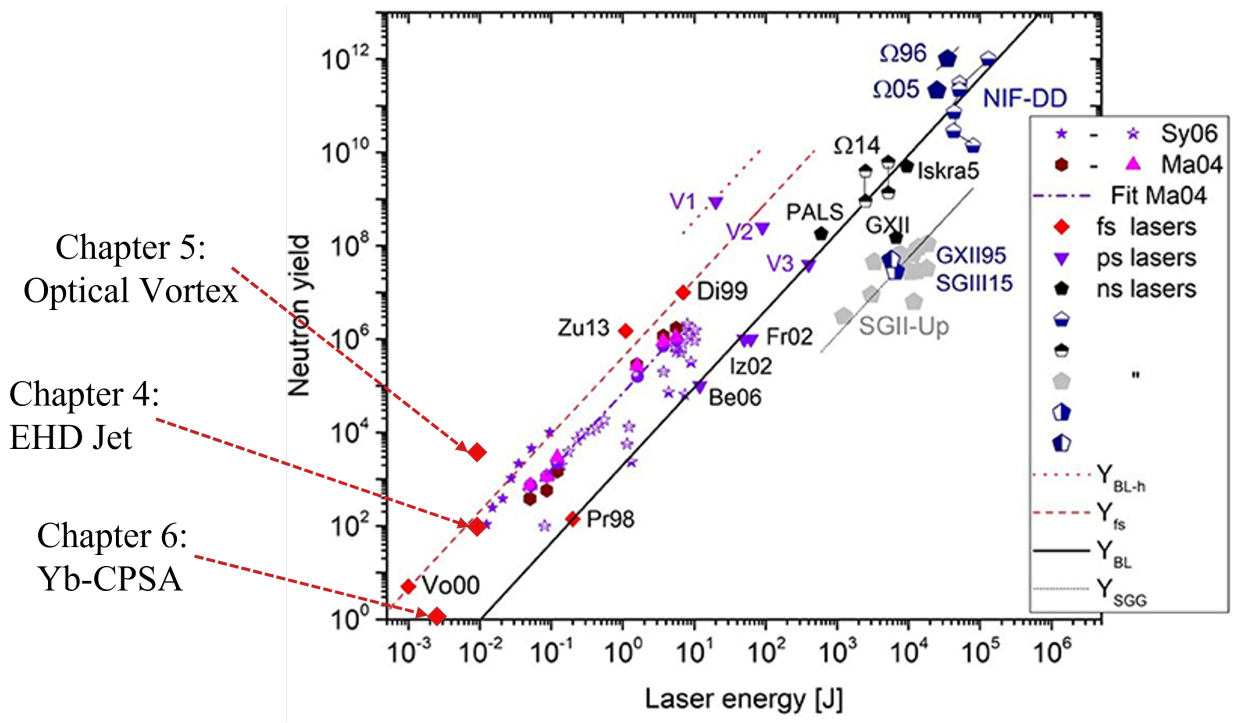

Figure 7.1: Isotropic fast neutron yield per shot across various laser-driven fast neutron experimental campaigns. Adapted from [9] with permission to show the D-D yields measured during this thesis work.

7.2 Future work

Future improvements to each individual experiment were suggested within their respective thesis chapters. This author envisages that the primary future work related to this doctoral thesis should involve coupling these complementary and parallel efforts into a single high-brightness tabletop laser-driven fast neutron source. Planned upgrades to the CBC + CPSA ultrashort fiber laser system will lead to the practical implementation of a TW-kW LPA driver. Further peak power enhancement and contrast improvement from implementing CafC techniques would deliver near-relativistic intensity. The use of a dispersionless spiral phase mirror to generate high-order optical vortices with such a beam could serve to further boost the on-target intensity to levels that were previously only feasible with legacy Ti:Sa systems. In tandem, refined multi-physics modeling would allow the EHD nozzle to operate

in a true 'droplet-on-demand' scheme and the mass-limited nature of such targets would only further enhance expected thermonuclear heating. Ultimately, the convergence of these three efforts could deliver a modular, sub-ns pulsed source of fast neutrons, with an isotropic flux of order 10^{8-9}. A high-brightness source of this scale has far-reaching implications for neutron radiography, materials testing, PGNAA, and special nuclear materials assay.

Bibliography

[1] G. A. Mourou, N. J. Fisch, V. M. Malkin, Z. Toroker, E. A. Khazanov, A. M. Sergeev, T. Tajima, and B. Le Garrec, *Exawatt-Zettawatt pulse generation and applications*, Optics Communications **285**, 720–724 (2012).

[2] M. A. Ahmed, *Development of high-power ultrafast lasers: Quo Vadis*, in W. A. Clarkson and R. K. Shori (editors), *Solid State Lasers XXX: Technology and Devices*, volume 11664, 1166404, SPIE (2021).

[3] M. A. Hickner, N. P. Siegel, K. S. Chen, D. N. McBrayer, D. S. Hussey, D. L. Jacobson, and M. Arif, *Real-Time Imaging of Liquid Water in an Operating Proton Exchange Membrane Fuel Cell*, Journal of The Electrochemical Society **153**, A902 (2006).

[4] R. Torres, *2018 Nobel prize in physics awarded for invention that drives Eupraxia*, https://www.eupraxia-project.eu/2018-nobel-prize-in-physics-awarded-for-invention-that-drives-eupraxia.html (2018), [Online; accessed 1-April-2023].

[5] A. Ruiz-De-La-Cruz and R. Rangel-Rojo, *Compact multi-pass amplifier for chirped-pulse amplification*, Journal of Modern Optics **53**, 307–311 (2006).

[6] V. Talluto, T. Blochowicz, and T. Walther, *A nanosecond regenerative Ti:Sapphire amplifier for the simultaneous generation of 940 nm and of 320 nm pulses*, Applied Physics B **122**, 132 (2016).

[7] A. Butkutė and L. Jonušauskas, *3D Manufacturing of Glass Microstructures Using Femtosecond Laser*, Micromachines **12**, 499 (2021).

[8] H.-S. Bosch and G. M. Hale, *Improved formulas for fusion cross-sections and thermal reactivities*, Nuclear Fusion **33**, 1919 (1993).

[9] J. Krása and D. Klír, *Scaling of Laser Fusion Experiments for DD-Neutron Yield*, Frontiers in Physics **8** (2020).

[10] J. Serna, A. Hamad, E. Rueda, and H. Garcia, *Autocorrelation measurement of an ultrashort optical pulse using an electrically focus-tunable lens*, Journal of optics **17**, 105505 (2015).

[11] M. Cecconello, *Liquid Scintillators Neutron Response Function: A Tutorial*, Journal of Fusion Energy **38**, 356–375 (2019).

[12] M. A. A. Rehmani and K. M. Arif, *High resolution electrohydrodynamic printing of conductive ink with an aligned aperture coaxial printhead*, The International Journal of Advanced Manufacturing Technology **115**, 2785–2800 (2021).

[13] *Disintegration of water drops in an electric field*, Proceedings of the Royal Society of London. Series A. Mathematical and Physical Sciences **280**, 383–397 (1964).

[14] A. E. Willner and C. Liu, *Perspective on using multiple orbital-angular-momentum beams for enhanced capacity in free-space optical communication links*, Nanophotonics **10**, 225–233 (2021).

[15] A. Longman and R. Fedosejevs, *Modeling of high intensity orbital angular momentum beams for laser–plasma interactions*, Physics of Plasmas **29**, 063109 (2022).

[16] R. G. Hemker, *Particle in cell modeling of plasma based accelerators in two-dimensions and three-dimensions*, Ph.D. thesis, UCLA (2000).

[17] J. Chadwick, *The existence of a neutron*, Proceedings of the Royal Society of London. Series A, Containing Papers of a Mathematical and Physical Character **136**, 692–708 (1932).

[18] T. H. Maiman, *Stimulated Optical Radiation in Ruby*, Nature **187**, 493–494 (1960).

[19] L. Nuckolls, J. H., *Early steps toward inertial fusion energy (IFE) (1952 to 1962)*, https://www.osti.gov/biblio/658936.

[20] N. Basov, P. Kriukov, S. Zakharov, Y. Senatsky, and S. Tchekalin, *Experiments on the observation of neutron emission at a focus of high-power laser radiation on a lithium deuteride surface*, IEEE Journal of Quantum Electronics **4**, 864–867 (1968).

[21] J. Nuckolls, L. Wood, A. Thiessen, and G. Zimmerman, *Laser Compression of Matter to Super-High Densities: Thermonuclear (CTR) Applications*, Nature **239**, 139–142 (1972).

[22] D. Strickland and G. Mourou, *Compression of amplified chirped optical pulses*, Optics Communications **56**, 219–221 (1985).

[23] P. F. Moulton, *Spectroscopic and laser characteristics of Ti:Al2O3*, J. Opt. Soc. Am. B **3**, 125–133 (1986).

[24] G. Cerullo, S. D. Silvestri, and V. Magni, *Self-starting Kerr-lens mode locking of a Ti:sapphire laser*, Opt. Lett. **19**, 1040–1042 (1994).

[25] J. Herrmann, *Theory of Kerr-lens mode locking: role of self-focusing and radially varying gain*, J. Opt. Soc. Am. B **11**, 498–512 (1994).

[26] H. Fattahi, H. G. Barros, M. Gorjan, T. Nubbemeyer, B. Alsaif, C. Y. Teisset, M. Schultze, S. Prinz, M. Haefner, M. Ueffing, A. Alismail, L. Vámos, A. Schwarz, O. Pronin, J. Brons, X. T. Geng, G. Arisholm, M. Ciappina, V. S. Yakovlev, D.-E.

Kim, A. M. Azzeer, N. Karpowicz, D. Sutter, Z. Major, T. Metzger, and F. Krausz, *Third-generation femtosecond technology*, Optica **1**, 45–63 (2014).

[27] T. Zhou, J. Ruppe, C. Zhu, I.-N. Hu, J. Nees, and A. Galvanauskas, *Coherent pulse stacking amplification using low-finesse Gires-Tournois interferometers*, Optics Express **23**, 7442–7462 (2015).

[28] H. Stark, J. Buldt, M. Müller, A. Klenke, A. Tünnermann, and J. Limpert, *23 mJ high-power fiber CPA system using electro-optically controlled divided-pulse amplification*, Optics Letters **44**, 5529–5532 (2019).

[29] W. Sha, J.-C. Chanteloup, and G. Mourou, *Ultrafast Fiber Technologies for Compact Laser Wake Field in Medical Application*, Photonics **9**, 423 (2022).

[30] E. A. Khazanov, S. Y. Mironov, and G. Mourou, *Nonlinear compression of high-power laser pulses: compression after compressor approach*, Physics-Uspekhi **62**, 1096 (2019).

[31] M. Kaumanns, D. Kormin, T. Nubbemeyer, V. Pervak, and S. Karsch, *Spectral broadening of 112 mJ, 1.3 ps pulses at 5 kHz in a LG10 multipass cell with compressibility to 37 fs*, Optics Letters **46**, 929–932 (2021).

[32] V. Ginzburg, I. Yakovlev, A. Zuev, A. Korobeynikova, A. Kochetkov, A. Kuzmin, S. Mironov, A. Shaykin, I. Shaikin, E. Khazanov, and G. Mourou, *Fivefold compression of 250-TW laser pulses*, Phys. Rev. A **101**, 013829 (2020).

[33] S. Tóth, R. S. Nagymihály, I. Seres, L. Lehotai, J. Csontos, L. T. Tóth, P. P. Geetha, T. Somoskői, B. Kajla, D. Abt, V. Pajer, A. Farkas, . Mohácsi, . Börzsönyi, and K. Osvay, *Single thin-plate compression of multi-TW laser pulses to 3.9 fs*, Optics Letters **48**, 57–60 (2023).

[34] G. Stibenz, N. Zhavoronkov, and G. Steinmeyer, *Self-compression of millijoule pulses to 7.8 fs duration in a white-light filament*, Optics Letters **31**, 274–276 (2006).

[35] E. Schulz, T. Binhammer, D. S. Steingrube, S. Rausch, M. Kovacev, and U. Morgner, *Intense few-cycle laser pulses from self-compression in a self-guiding filament*, Applied Physics B **95**, 269–272 (2009).

[36] G. Fan, P. A. Carpeggiani, Z. Tao, G. Coccia, R. Safaei, E. Kaksis, A. Pugzlys, F. Légaré, B. E. Schmidt, and A. Baltuška, *70 mJ nonlinear compression and scaling route for an Yb amplifier using large-core hollow fibers*, Optics Letters **46**, 896–899 (2021).

[37] I. Prencipe, J. Fuchs, S. Pascarelli, D. W. Schumacher, R. B. Stephens, N. B. Alexander, R. Briggs, M. Büscher, M. O. Cernaianu, A. Choukourov, and et al., *Targets for high repetition rate laser facilities: needs, challenges and perspectives*, High Power Laser Science and Engineering **5**, e17 (2017).

[38] T. Ma, D. Mariscal, R. Anirudh, T. Bremer, B. Z. Djordjevic, T. Galvin, E. Grace, S. Herriot, S. Jacobs, B. Kailkhura, R. Hollinger, J. Kim, S. Liu, J. Ludwig, D. Neely, J. J. Rocca, G. G. Scott, R. A. Simpson, B. S. Spears, T. S. Spinka, K. Swanson,

J. J. Thiagarajan, B. V. Essen, S. Wang, S. C. Wilks, G. J. Williams, J. Zhang, M. C. Herrmann, and C. Haefner, *Accelerating the rate of discovery: toward high-repetition-rate HED science*, Plasma Physics and Controlled Fusion **63**, 104003 (2021).

[39] S. Vallières, J. Powell, T. Connell, M. Evans, S. Fourmaux, S. Payeur, P. Lassonde, F. Fillion-Gourdeau, S. MacLean, and F. Légaré, *High Dose-Rate Ionizing Radiation Source from Tight Focusing in Air of a mJ-class Femtosecond Laser* (2022), arXiv:2207.05773 [physics].

[40] J. Hah, G. M. Petrov, J. A. Nees, Z.-H. He, M. D. Hammig, K. Krushelnick, and A. G. R. Thomas, *High repetition-rate neutron generation by several-mJ, 35 fs pulses interacting with free-flowing D2O*, Applied Physics Letters **109**, 144102 (2016).

[41] N. Basov, P. Kriukov, S. Zakharov, Y. Senatsky, and S. Tchekalin, *Experiments on the observation of neutron emission at a focus of high-power laser radiation on a lithium deuteride surface*, IEEE Journal of Quantum Electronics **4**, 864–867 (1968).

[42] G. W. Gobeli, J. C. Bushnell, P. S. Peercy, and E. D. Jones, *Observation of Neutrons Produced by Laser Irradiation of Lithium Deuteride*, Physical Review **188**, 300–302 (1969).

[43] M. Passoni, L. Bertagna, and A. Zani, *Target normal sheath acceleration: theory, comparison with experiments and future perspectives*, New Journal of Physics **12**, 045012 (2010).

[44] M. Roth and M. Schollmeier, *Ion Acceleration—Target Normal Sheath Acceleration*, CERN Yellow Reports 1–231 (2016).

[45] J. T. Morrison, S. Feister, K. D. Frische, D. R. Austin, G. K. Ngirmang, N. R. Murphy, C. Orban, E. A. Chowdhury, and W. M. Roquemore, *MeV proton acceleration at kHz repetition rate from ultra-intense laser liquid interaction*, New Journal of Physics **20**, 022001 (2018).

[46] R. A. Snavely, M. H. Key, S. P. Hatchett, T. E. Cowan, M. Roth, T. W. Phillips, M. A. Stoyer, E. A. Henry, T. C. Sangster, M. S. Singh, S. C. Wilks, A. MacKinnon, A. Offenberger, D. M. Pennington, K. Yasuike, A. B. Langdon, B. F. Lasinski, J. Johnson, M. D. Perry, and E. M. Campbell, *Intense High-Energy Proton Beams from Petawatt-Laser Irradiation of Solids*, Physical Review Letters **85**, 2945–2948 (2000).

[47] T. Ditmire, J. Zweiback, V. P. Yanovsky, T. E. Cowan, G. Hays, and K. B. Wharton, *Nuclear fusion in gases of deuterium clusters heated with a femtosecond laser*, Physics of Plasmas **7**, 1993–1998 (2000).

[48] J. Zweiback, R. A. Smith, T. E. Cowan, G. Hays, K. B. Wharton, V. P. Yanovsky, and T. Ditmire, *Nuclear Fusion Driven by Coulomb Explosions of Large Deuterium Clusters*, Phys. Rev. Lett. **84**, 2634–2637 (2000).

[49] G. Grillon, P. Balcou, J.-P. Chambaret, D. Hulin, J. Martino, S. Moustaizis, L. Notebaert, M. Pittman, T. Pussieux, A. Rousse, J.-P. Rousseau, S. Sebban, O. Sublemontier, and M. Schmidt, *Deuterium-Deuterium Fusion Dynamics in Low-Density Molecular-Cluster Jets Irradiated by Intense Ultrafast Laser Pulses*, Physical Review Letters **89**, 065005 (2002).

[50] S. Fritzler, Z. Najmudin, V. Malka, K. Krushelnick, C. Marle, B. Walton, M. S. Wei, R. J. Clarke, and A. E. Dangor, *Ion Heating and Thermonuclear Neutron Production from High-Intensity Subpicosecond Laser Pulses Interacting with Underdense Plasmas*, Physical Review Letters **89**, 165004 (2002).

[51] Y. Gershuni, D. Roitman, I. Cohen, E. Porat, Y. Danan, M. Elkind, A. Levanon, R. Louzon, D. Reichenberg, A. Tsabary, E. Urisman, S. Vaisman, and I. Pomerantz, *A gatling-gun target delivery system for high-intensity laser irradiation experiments*, Nuclear Instruments and Methods in Physics Research Section A: Accelerators, Spectrometers, Detectors and Associated Equipment **934**, 58–62 (2019).

[52] J. Bin, L. Obst-Huebl, J.-H. Mao, K. Nakamura, L. D. Geulig, H. Chang, Q. Ji, L. He, J. De Chant, Z. Kober, A. J. Gonsalves, S. Bulanov, S. E. Celniker, C. B. Schroeder, C. G. R. Geddes, E. Esarey, B. A. Simmons, T. Schenkel, E. A. Blakely, S. Steinke, and A. M. Snijders, *A new platform for ultra-high dose rate radiobiological research using the BELLA PW laser proton beamline*, Scientific Reports **12**, 1484 (2022).

[53] N. Xu, M. J. V. Streeter, O. C. Ettlinger, H. Ahmed, S. Astbury, M. Borghesi, N. Bourgeois, C. B. Curry, S. J. D. Dann, N. P. Dover, T. Dzelzainis, V. Istokskaia, M. Gauthier, L. Giuffrida, G. D. Glenn, S. H. Glenzer, R. J. Gray, J. S. Green, G. S. Hicks, C. Hyland, M. King, B. Loughran, D. Margarone, O. McCusker, P. McKenna, C. Parisuaña, P. Parsons, C. Spindloe, D. R. Symes, F. Treffert, C. a. J. Palmer, and Z. Najmudin, *Versatile tape-drive target for high-repetition rate laser-driven proton acceleration*, High Power Laser Science and Engineering 1–12 (2023).

[54] M. Zimmer, S. Scheuren, A. Kleinschmidt, N. Mitura, A. Tebartz, G. Schaumann, T. Abel, T. Ebert, M. Hesse, Ş. Zähter, S. C. Vogel, O. Merle, R.-J. Ahlers, S. D. Pinto, M. Peschke, T. Kröll, V. Bagnoud, C. Rödel, and M. Roth, *Demonstration of non-destructive and isotope-sensitive material analysis using a short-pulsed laser-driven epi-thermal neutron source*, Nature Communications **13** (2022).

[55] L. Rimkus, I. Stasevičius, M. Barkauskas, L. Giniūnas, V. Barkauskas, S. Butkus, and M. Vengris, *Compact high-flux X-ray source based on irradiation of solid targets by gigahertz and megahertz bursts of femtosecond laser pulses*, Optics Continuum **1**, 1819–1836 (2022).

[56] S. Karsch, S. Düsterer, H. Schwoerer, F. Ewald, D. Habs, M. Hegelich, G. Pretzler, A. Pukhov, K. Witte, and R. Sauerbrey, *High-Intensity Laser Induced Ion Acceleration from Heavy-Water Droplets*, Physical Review Letters **91**, 015001 (2003).

[57] J. T. Morrison, S. Feister, K. D. Frische, D. R. Austin, G. K. Ngirmang, N. R. Murphy, C. Orban, E. A. Chowdhury, and W. M. Roquemore, *MeV proton acceleration at kHz*

repetition rate from ultra-intense laser liquid interaction, New Journal of Physics **20**, 022001 (2018).

[58] G. A. Becker, M. B. Schwab, R. Lötzsch, S. Tietze, D. Klöpfel, M. Rehwald, H.-P. Schlenvoigt, A. Sävert, U. Schramm, M. Zepf, and M. C. Kaluza, *Characterization of laser-driven proton acceleration from water microdroplets*, Scientific Reports **9**, 17169 (2019).

[59] S. Ter-Avetisyan, M. Schnürer, D. Hilscher, U. Jahnke, S. Busch, P. V. Nickles, and W. Sandner, *Fusion neutron yield from a laser-irradiated heavy-water spray*, Physics of Plasmas **12**, 012702–012702–5 (2005).

[60] F. Treffert, C. B. Curry, T. Ditmire, G. D. Glenn, H. J. Quevedo, M. Roth, C. Schoenwaelder, M. Zimmer, S. H. Glenzer, and M. Gauthier, *Towards High-Repetition-Rate Fast Neutron Sources Using Novel Enabling Technologies*, Instruments **5**, 38 (2021).

[61] M. Roth, D. Jung, K. Falk, N. Guler, O. Deppert, M. Devlin, A. Favalli, J. Fernandez, D. Gautier, M. Geissel, R. Haight, C. E. Hamilton, B. M. Hegelich, R. P. Johnson, F. Merrill, G. Schaumann, K. Schoenberg, M. Schollmeier, T. Shimada, T. Taddeucci, J. L. Tybo, F. Wagner, S. A. Wender, C. H. Wilde, and G. A. Wurden, *Bright Laser-Driven Neutron Source Based on the Relativistic Transparency of Solids*, Phys. Rev. Lett. **110**, 044802 (2013).

[62] Andrew M. Weiner, *Ultrafast Optics*, 202, 411–412, John Wiley and Sons, Hoboken, NJ (2009).

[63] Walter Koechner, *Solid-state laser engineering*, 200–209, Springer, New York, NY (2006).

[64] O. Martinez, *3000 times grating compressor with positive group velocity dispersion: Application to fiber compensation in 1.3-1.6 μm region*, IEEE Journal of Quantum Electronics **23**, 59–64 (1987).

[65] I. V. Yakovlev, *Stretchers and compressors for ultra-high power laser systems*, Quantum Electronics **44**, 393–414 (2014).

[66] K.-H. Liao, M.-Y. Cheng, E. Flecher, V. I. Smirnov, L. B. Glebov, and A. Galvanauskas, *Large-aperture chirped volume Bragg grating based fiber CPA system*, Optics Express **15**, 4876–4882 (2007).

[67] S. Zhou, F. W. Wise, and D. G. Ouzounov, *Divided-pulse amplification of ultrashort pulses*, Opt. Lett. **32**, 871–873 (2007).

[68] A. Klenke, M. Müller, H. Stark, M. Kienel, C. Jauregui, A. Tünnermann, and J. Limpert, *Coherent Beam Combination of Ultrafast Fiber Lasers*, IEEE Journal of Selected Topics in Quantum Electronics **24**, 1–9 (2018).

[69] T. Zhou, J. Ruppe, C. Zhu, I.-N. Hu, J. Nees, and A. Galvanauskas, *Coherent pulse stacking amplification using low-finesse Gires-Tournois interferometers*, Optics Express **23**, 7442–7462 (2015).

[70] J. Ruppe, H. Pei, M. Sheikhsofla, S. Chen, R. Wilcox, W. Leemans, J. Nees, and A. Galvanauskas, *Coherent pulse stacking amplification — Extending chirped pulse amplification by orders of magnitude*, in *2017 Conference on Lasers and Electro-Optics (CLEO)*, 1–1 (2017).

[71] Guo, Chunlei and Singh, Subhash Chandra and Moulton, Peter F and Fry, Alan R and Fendel, Peter, *Ti:sapphire: Material, Lasers and Amplifiers*, 69–81, CRC Press (2021), 2nd edition.

[72] Gibbon, Paul, *Short Pulse Laser Interactions with Matter*, 18, 166, Published by Imperial College Press and Distributed by World Scientific Publishing Co., London (2005).

[73] L. V. Keldysh, *Ionization in the field of a strong electromagnetic wave*, Zh. Eksperim. i Teor. Fiz. **Vol: 47** (1964), institution: Lebedev Inst. of Physics, Moscow.

[74] M. Roth, D. Jung, K. Falk, N. Guler, O. Deppert, M. Devlin, A. Favalli, J. Fernandez, D. Gautier, M. Geissel, R. Haight, C. E. Hamilton, B. M. Hegelich, R. P. Johnson, F. Merrill, G. Schaumann, K. Schoenberg, M. Schollmeier, T. Shimada, T. Taddeucci, J. L. Tybo, F. Wagner, S. A. Wender, C. H. Wilde, and G. A. Wurden, *Bright Laser-Driven Neutron Source Based on the Relativistic Transparency of Solids*, Physical Review Letters **110**, 044802 (2013).

[75] N. G. Denisov, *On a singularity of the field of an electromagnetic wave propagated in an inhomogeneous plasma*, JETP **4**, 544–553 (1957).

[76] G. J. Morales and Y. C. Lee, *Ponderomotive-Force Effects in a Nonuniform Plasma*, Phys. Rev. Lett. **33**, 1016–1019 (1974).

[77] S. C. Wilks, A. B. Langdon, and T. E. Cowan, *Energetic proton generation in ultra-intense laser–solid interactions*, Phys. Plasmas **8** (2001).

[78] A. Maksimchuk, S. Gu, K. Flippo, D. Umstadter, and V. Y. Bychenkov, *Forward Ion Acceleration in Thin Films Driven by a High-Intensity Laser*, Physical Review Letters **84**, 4108–4111 (2000).

[79] J. Badziak, *Laser-driven ion acceleration: methods, challenges and prospects*, Journal of Physics: Conference Series **959**, 012001 (2018).

[80] J. Hornung, Y. Zobus, P. Boller, C. Brabetz, U. Eisenbarth, T. Kühl, Z. Major, J. Ohland, M. Zepf, B. Zielbauer, and et al., *Enhancement of the laser-driven proton source at PHELIX*, High Power Laser Science and Engineering **8**, e24 (2020).

[81] T. Ditmire, J. W. G. Tisch, E. Springate, M. B. Mason, N. Hay, R. A. Smith, J. Marangos, and M. H. R. Hutchinson, *High-energy ions produced in explosions of superheated atomic clusters*, Nature **386**, 54–56 (1997).

[82] M. Borghesi, *Laser-driven ion acceleration: State of the art and emerging mechanisms*, Nuclear Instruments and Methods in Physics Research Section A: Accelerators, Spectrometers, Detectors and Associated Equipment **740**, 6–9 (2014).

[83] *IAEA-Tecdoc-1981 : Compact Accelerator Based Neutron Sources*, Tecdoc Series, International Atomic Energy Agency, Vienna (2021).

[84] H. Abu-Shawareb, R. Acree, P. Adams, J. Adams, B. Addis, R. Aden, P. Adrian, B. B. Afeyan, M. Aggleton, L. Aghaian, A. Aguirre, D. Aikens, J. Akre, F. Albert, M. Albrecht, B. J. Albright, J. Albritton, J. Alcala, C. Alday, D. A. Alessi, N. Alexander, J. Alfonso, N. Alfonso, E. Alger, S. J. Ali, Z. A. Ali, W. E. Alley, P. Amala, P. A. Amendt, P. Amick, S. Ammula, C. Amorin, D. J. Ampleford, R. W. Anderson, T. Anklam, N. Antipa, B. Appelbe, C. Aracne-Ruddle, E. Araya, M. Arend, P. Arnold, T. Arnold, J. Asay, L. J. Atherton, D. Atkinson, R. Atkinson, J. M. Auerbach, B. Austin, L. Auyang, A. S. Awwal, J. Ayers, S. Ayers, T. Ayers, S. Azevedo, B. Bachmann, C. A. Back, J. Bae, D. S. Bailey, J. Bailey, T. Baisden, K. L. Baker, H. Baldis, D. Barber, M. Barberis, D. Barker, A. Barnes, C. W. Barnes, M. A. Barrios, C. Barty, I. Bass, S. H. Batha, S. H. Baxamusa, G. Bazan, J. K. Beagle, R. Beale, B. R. Beck, J. B. Beck, M. Bedzyk, R. G. Beeler, R. G. Beeler, W. Behrendt, L. Belk, P. Bell, M. Belyaev, J. F. Benage, G. Bennett, L. R. Benedetti, L. X. Benedict, R. Berger, T. Bernat, L. A. Bernstein, B. Berry, L. Bertolini, G. Besenbruch, J. Betcher, R. Bettenhausen, R. Betti, B. Bezzerides, S. D. Bhandarkar, R. Bickel, J. Biener, T. Biesiada, K. Bigelow, J. Bigelow-Granillo, V. Bigman, R. M. Bionta, N. W. Birge, M. Bitter, A. C. Black, R. Bleile, D. L. Bleuel, E. Bliss, E. Bliss, B. Blue, T. Boehly, K. Boehm, C. D. Boley, R. Bonanno, E. J. Bond, T. Bond, M. J. Bonino, M. Borden, J.-L. Bourgade, J. Bousquet, J. Bowers, M. Bowers, R. Boyd, A. Bozek, D. K. Bradley, K. S. Bradley, P. A. Bradley, L. Bradley, L. Brannon, P. S. Brantley, D. Braun, T. Braun, K. Brienza-Larsen, T. M. Briggs, J. Britten, E. D. Brooks, D. Browning, M. W. Bruhn, T. A. Brunner, H. Bruns, G. Brunton, B. Bryant, T. Buczek, J. Bude, L. Buitano, S. Burkhart, J. Burmark, A. Burnham, R. Burr, L. E. Busby, B. Butlin, R. Cabeltis, M. Cable, W. H. Cabot, B. Cagadas, J. Caggiano, R. Cahayag, S. E. Caldwell, S. Calkins, D. A. Callahan, J. Calleja-Aguirre, L. Camara, D. Camp, E. M. Campbell, J. H. Campbell, B. Carey, R. Carey, K. Carlisle, L. Carlson, L. Carman, J. Carmichael, A. Carpenter, C. Carr, J. A. Carrera, D. Casavant, A. Casey, D. T. Casey, A. Castillo, E. Castillo, J. I. Castor, C. Castro, W. Caughey, R. Cavitt, J. Celeste, P. M. Celliers, C. Cerjan, G. Chandler, B. Chang, C. Chang, J. Chang, L. Chang, R. Chapman, T. Chapman, L. Chase, H. Chen, H. Chen, K. Chen, L.-Y. Chen, B. Cheng, J. Chittenden, C. Choate, J. Chou, R. E. Chrien, M. Chrisp, K. Christensen, M. Christensen, A. R. Christopherson, M. Chung, J. A. Church, A. Clark, D. S. Clark, K. Clark, R. Clark, L. Claus, B. Cline, J. A. Cline, J. A. Cobble, K. Cochrane, B. Cohen, S. Cohen, M. R. Collette, G. Collins, L. A. Collins, T. J. B. Collins, A. Conder, B. Conrad, M. Conyers, A. W. Cook, D. Cook, R. Cook, J. C. Cooley, G. Cooper, T. Cope, S. R. Copeland, F. Coppari, J. Cortez, J. Cox, D. H. Crandall, J. Crane, R. S. Craxton, M. Cray, A. Crilly, J. W. Crippen, D. Cross, M. Cuneo, G. Cuotts, C. E. Czajka, D. Czechowicz, T. Daly, P. Danforth, R. Darbee, B. Darlington, P. Datte, L. Dauffy,

G. Davalos, S. Davidovits, P. Davis, J. Davis, S. Dawson, R. D. Day, T. H. Day, M. Dayton, C. Deck, C. Decker, C. Deeney, K. A. DeFriend, G. Deis, N. D. Delamater, J. A. Delettrez, R. Demaret, S. Demos, S. M. Dempsey, R. Desjardin, T. Desjardins, M. P. Desjarlais, E. L. Dewald, J. DeYoreo, S. Diaz, G. Dimonte, T. R. Dittrich, L. Divol, S. N. Dixit, J. Dixon, E. S. Dodd, D. Dolan, A. Donovan, M. Donovan, T. Döppner, C. Dorrer, N. Dorsano, M. R. Douglas, D. Dow, J. Downie, E. Downing, M. Dozieres, V. Draggoo, D. Drake, R. P. Drake, T. Drake, G. Dreifuerst, D. F. DuBois, P. F. DuBois, G. Dunham, R. Dylla-Spears, A. K. L. Dymoke-Bradshaw, B. Dzenitis, C. Ebbers, M. Eckart, S. Eddinger, D. Eder, D. Edgell, M. J. Edwards, P. Efthimion, J. H. Eggert, B. Ehrlich, P. Ehrmann, S. Elhadj, C. Ellerbee, N. S. Elliott, C. L. Ellison, F. Elsner, M. Emerich, K. Engelhorn, T. England, E. English, P. Epperson, R. Epstein, G. Erbert, M. A. Erickson, D. J. Erskine, A. Erlandson, R. J. Espinosa, C. Estes, K. G. Estabrook, S. Evans, A. Fabyan, J. Fair, R. Fallejo, N. Farmer, W. A. Farmer, M. Farrell, V. E. Fatherley, M. Fedorov, E. Feigenbaum, M. Feit, W. Ferguson, J. C. Fernandez, A. Fernandez-Panella, S. Fess, J. E. Field, C. V. Filip, J. R. Fincke, T. Finn, S. M. Finnegan, R. G. Finucane, M. Fischer, A. Fisher, J. Fisher, B. Fishler, D. Fittinghoff, P. Fitzsimmons, M. Flegel, K. A. Flippo, J. Florio, J. Folta, P. Folta, L. R. Foreman, C. Forrest, A. Forsman, J. Fooks, M. Foord, R. Fortner, K. Fournier, D. E. Fratanduono, N. Frazier, T. Frazier, C. Frederick, M. S. Freeman, J. Frenje, D. Frey, G. Frieders, S. Friedrich, D. H. Froula, J. Fry, T. Fuller, J. Gaffney, S. Gales, B. Le Galloudec, K. K. Le Galloudec, A. Gambhir, L. Gao, W. J. Garbett, A. Garcia, C. Gates, E. Gaut, P. Gauthier, Z. Gavin, J. Gaylord, M. Geissel, F. Génin, J. Georgeson, H. Geppert-Kleinrath, V. Geppert-Kleinrath, N. Gharibyan, J. Gibson, C. Gibson, E. Giraldez, V. Glebov, S. G. Glendinning, S. Glenn, S. H. Glenzer, S. Goade, P. L. Gobby, S. R. Goldman, B. Golick, M. Gomez, V. Goncharov, D. Goodin, P. Grabowski, E. Grafil, P. Graham, J. Grandy, E. Grasz, F. Graziani, G. Greenman, J. A. Greenough, A. Greenwood, G. Gregori, T. Green, J. R. Griego, G. P. Grim, J. Grondalski, S. Gross, J. Guckian, N. Guler, B. Gunney, G. Guss, S. Haan, J. Hackbarth, L. Hackel, R. Hackel, C. Haefner, C. Hagmann, K. D. Hahn, S. Hahn, B. J. Haid, B. M. Haines, B. M. Hall, C. Hall, G. N. Hall, M. Hamamoto, S. Hamel, C. E. Hamilton, B. A. Hammel, J. H. Hammer, G. Hampton, A. Hamza, A. Handler, S. Hansen, D. Hanson, R. Haque, D. Harding, E. Harding, J. D. Hares, D. B. Harris, J. A. Harte, E. P. Hartouni, R. Hatarik, S. Hatchett, A. A. Hauer, M. Havre, R. Hawley, J. Hayes, J. Hayes, S. Hayes, A. Hayes-Sterbenz, C. A. Haynam, D. A. Haynes, D. Headley, A. Heal, J. E. Heebner, S. Heerey, G. M. Heestand, R. Heeter, N. Hein, C. Heinbockel, C. Hendricks, M. Henesian, J. Heninger, J. Henrikson, E. A. Henry, E. B. Herbold, M. R. Hermann, G. Hermes, J. E. Hernandez, V. J. Hernandez, M. C. Herrmann, H. W. Herrmann, O. D. Herrera, D. Hewett, R. Hibbard, D. G. Hicks, D. Hill, K. Hill, T. Hilsabeck, D. E. Hinkel, D. D. Ho, V. K. Ho, J. K. Hoffer, N. M. Hoffman, M. Hohenberger, M. Hohensee, W. Hoke, D. Holdener, F. Holdener, J. P. Holder, B. Holko, D. Holunga, J. F. Holzrichter, J. Honig, D. Hoover, D. Hopkins, L. Berzak Hopkins, M. Hoppe, M. L. Hoppe, J. Horner, R. Hornung, C. J. Horsfield, J. Horvath, D. Hotaling, R. House, L. Howell, W. W. Hsing, S. X. Hu, H. Huang, J. Huckins, H. Hui, K. D. Humbird, J. Hund, J. Hunt, O. A. Hurricane, M. Hutton, K. H.-K. Huynh, L. Inandan, C. Iglesias, I. V. Igumenshchev, N. Izumi, M. Jackson, J. Jackson, S. D. Jacobs,

G. James, K. Jancaitis, J. Jarboe, L. C. Jarrott, D. Jasion, J. Jaquez, J. Jeet, A. E. Jenei, J. Jensen, J. Jimenez, R. Jimenez, D. Jobe, Z. Johal, H. M. Johns, D. Johnson, M. A. Johnson, M. Gatu Johnson, R. J. Johnson, S. Johnson, S. A. Johnson, T. Johnson, K. Jones, O. Jones, M. Jones, R. Jorge, H. J. Jorgenson, M. Julian, B. I. Jun, R. Jungquist, J. Kaae, N. Kabadi, D. Kaczala, D. Kalantar, K. Kangas, V. V. Karasiev, M. Karasik, V. Karpenko, A. Kasarky, K. Kasper, R. Kauffman, M. I. Kaufman, C. Keane, L. Keaty, L. Kegelmeyer, P. A. Keiter, P. A. Kellett, J. Kellogg, J. H. Kelly, S. Kemic, A. J. Kemp, G. E. Kemp, G. D. Kerbel, D. Kershaw, S. M. Kerr, T. J. Kessler, M. H. Key, S. F. Khan, H. Khater, C. Kiikka, J. Kilkenny, Y. Kim, Y.-J. Kim, J. Kimko, M. Kimmel, J. M. Kindel, J. King, R. K. Kirkwood, L. Klaus, D. Klem, J. L. Kline, J. Klingmann, G. Kluth, P. Knapp, J. Knauer, J. Knipping, M. Knudson, D. Kobs, J. Koch, T. Kohut, C. Kong, J. M. Koning, P. Koning, S. Konior, H. Kornblum, L. B. Kot, B. Kozioziemski, M. Kozlowski, P. M. Kozlowski, J. Krammen, N. S. Krasheninnikova, B. Kraus, W. Krauser, J. D. Kress, A. L. Kritcher, E. Krieger, J. J. Kroll, W. L. Kruer, M. K. G. Kruse, S. Kucheyev, M. Kumbera, S. Kumpan, J. Kunimune, B. Kustowski, T. J. T. Kwan, G. A. Kyrala, S. Laffite, M. Lafon, K. LaFortune, B. Lahmann, B. Lairson, O. L. Landen, J. Langenbrunner, L. Lagin, T. Land, M. Lane, D. Laney, A. B. Langdon, S. H. Langer, A. Langro, N. E. Lanier, T. E. Lanier, D. Larson, B. F. Lasinski, D. Lassle, D. LaTray, G. Lau, N. Lau, C. Laumann, A. Laurence, T. A. Laurence, J. Lawson, H. P. Le, R. R. Leach, L. Leal, A. Leatherland, K. LeChien, B. Lechleiter, A. Lee, M. Lee, T. Lee, R. J. Leeper, E. Lefebvre, J.-P. Leidinger, B. LeMire, R. W. Lemke, N. C. Lemos, S. Le Pape, R. Lerche, S. Lerner, S. Letts, K. Levedahl, T. Lewis, C. K. Li, H. Li, J. Li, W. Liao, Z. M. Liao, D. Liedahl, J. Liebman, G. Lindford, E. L. Lindman, J. D. Lindl, H. Loey, R. A. London, F. Long, E. N. Loomis, F. E. Lopez, H. Lopez, E. Losbanos, S. Loucks, R. Lowe-Webb, E. Lundgren, A. P. Ludwigsen, R. Luo, J. Lusk, R. Lyons, T. Ma, Y. Macallop, M. J. MacDonald, B. J. MacGowan, J. M. Mack, A. J. Mackinnon, S. A. MacLaren, A. G. MacPhee, G. R. Magelssen, J. Magoon, R. M. Malone, T. Malsbury, R. Managan, R. Mancini, K. Manes, D. Maney, D. Manha, O. M. Mannion, A. M. Manuel, E. Mapoles, G. Mara, T. Marcotte, E. Marin, M. M. Marinak, C. Mariscal, D. A. Mariscal, E. F. Mariscal, E. V. Marley, J. A. Marozas, R. Marquez, C. D. Marshall, F. J. Marshall, M. Marshall, S. Marshall, J. Marticorena, D. Martinez, I. Maslennikov, D. Mason, R. J. Mason, L. Masse, W. Massey, P.-E. Masson-Laborde, N. D. Masters, D. Mathisen, E. Mathison, J. Matone, M. J. Matthews, C. Mattoon, T. R. Mattsson, K. Matzen, C. W. Mauche, M. Mauldin, T. McAbee, M. McBurney, T. Mccarville, R. L. McCrory, A. M. McEvoy, C. McGuffey, M. Mcinnis, P. McKenty, M. S. McKinley, J. B. McLeod, A. McPherson, B. Mcquillan, M. Meamber, K. D. Meaney, N. B. Meezan, R. Meissner, T. A. Mehlhorn, N. C. Mehta, J. Menapace, F. E. Merrill, B. T. Merritt, E. C. Merritt, D. D. Meyerhofer, S. Mezyk, R. J. Mich, P. A. Michel, D. Milam, C. Miller, D. Miller, D. S. Miller, E. Miller, E. K. Miller, J. Miller, M. Miller, P. E. Miller, T. Miller, W. Miller, V. Miller-Kamm, M. Millot, J. L. Milovich, P. Minner, J.-L. Miquel, S. Mitchell, K. Molvig, R. C. Montesanti, D. S. Montgomery, M. Monticelli, A. Montoya, J. D. Moody, A. S. Moore, E. Moore, M. Moran, J. C. Moreno, K. Moreno, B. E. Morgan, T. Morrow, J. W. Morton, E. Moses, K. Moy, R. Muir, M. S. Murillo, J. E. Murray, J. R. Murray, D. H. Munro, T. J. Murphy, F. M. Munteanu, J. Nafziger,

T. Nagayama, S. R. Nagel, R. Nast, R. A. Negres, A. Nelson, D. Nelson, J. Nelson, S. Nelson, S. Nemethy, P. Neumayer, K. Newman, M. Newton, H. Nguyen, J.-M. G. Di Nicola, P. Di Nicola, C. Niemann, A. Nikroo, P. M. Nilson, A. Nobile, V. Noorai, R. Nora, M. Norton, M. Nostrand, V. Note, S. Novell, P. F. Nowak, A. Nunez, R. A. Nyholm, M. O'Brien, A. Oceguera, J. A. Oertel, J. Okui, B. Olejniczak, J. Oliveira, P. Olsen, B. Olson, K. Olson, R. E. Olson, Y. P. Opachich, N. Orsi, C. D. Orth, M. Owen, S. Padalino, E. Padilla, R. Paguio, S. Paguio, J. Paisner, S. Pajoom, A. Pak, S. Palaniyappan, K. Palma, T. Pannell, F. Papp, D. Paras, T. Parham, H.-S. Park, A. Pasternak, S. Patankar, M. V. Patel, P. K. Patel, R. Patterson, S. Patterson, B. Paul, M. Paul, E. Pauli, O. T. Pearce, J. Pearcy, B. Pedrotti, A. Peer, L. J. Pelz, B. Penetrante, J. Penner, A. Perez, L. J. Perkins, E. Pernice, T. S. Perry, S. Person, D. Petersen, T. Petersen, D. L. Peterson, E. B. Peterson, J. E. Peterson, J. L. Peterson, K. Peterson, R. R. Peterson, R. D. Petrasso, F. Philippe, T. J. Phipps, E. Piceno, Y. Ping, L. Pickworth, J. Pino, R. Plummer, G. D. Pollack, S. M. Pollaine, B. B. Pollock, D. Ponce, J. Ponce, J. Pontelandolfo, J. L. Porter, J. Post, O. Poujade, C. Powell, H. Powell, G. Power, M. Pozulp, M. Prantil, M. Prasad, S. Pratuch, S. Price, K. Primdahl, S. Prisbrey, R. Procassini, A. Pruyne, B. Pudliner, S. R. Qiu, K. Quan, M. Quinn, J. Quintenz, P. B. Radha, F. Rainer, J. E. Ralph, K. S. Raman, R. Raman, P. Rambo, S. Rana, A. Randewich, D. Rardin, M. Ratledge, N. Ravelo, F. Ravizza, M. Rayce, A. Raymond, B. Raymond, B. Reed, C. Reed, S. Regan, B. Reichelt, V. Reis, S. Reisdorf, V. Rekow, B. A. Remington, A. Rendon, W. Requieron, M. Rever, H. Reynolds, J. Reynolds, J. Rhodes, M. Rhodes, M. C. Richardson, B. Rice, N. G. Rice, R. Rieben, A. Rigatti, S. Riggs, H. G. Rinderknecht, K. Ring, B. Riordan, R. Riquier, C. Rivers, D. Roberts, V. Roberts, G. Robertson, H. F. Robey, J. Robles, P. Rocha, G. Rochau, J. Rodriguez, S. Rodriguez, M. Rosen, M. Rosenberg, G. Ross, J. S. Ross, P. Ross, J. Rouse, D. Rovang, A. M. Rubenchik, M. S. Rubery, C. L. Ruiz, M. Rushford, B. Russ, J. R. Rygg, B. S. Ryujin, R. A. Sacks, R. F. Sacks, K. Saito, T. Salmon, J. D. Salmonson, J. Sanchez, S. Samuelson, M. Sanchez, C. Sangster, A. Saroyan, J. Sater, A. Satsangi, S. Sauers, R. Saunders, J. P. Sauppe, R. Sawicki, D. Sayre, M. Scanlan, K. Schaffers, G. T. Schappert, S. Schiaffino, D. J. Schlossberg, D. W. Schmidt, M. J. Schmitt, D. H. G. Schneider, M. B. Schneider, R. Schneider, M. Schoff, M. Schollmeier, M. Schölmerich, C. R. Schroeder, S. E. Schrauth, H. A. Scott, I. Scott, J. M. Scott, R. H. H. Scott, C. R. Scullard, T. Sedillo, F. H. Seguin, W. Seka, J. Senecal, S. M. Sepke, L. Seppala, K. Sequoia, J. Severyn, J. M. Sevier, N. Sewell, S. Seznec, R. C. Shah, J. Shamlian, D. Shaughnessy, M. Shaw, R. Shaw, C. Shearer, R. Shelton, N. Shen, M. W. Sherlock, A. I. Shestakov, E. L. Shi, S. J. Shin, N. Shingleton, W. Shmayda, M. Shor, M. Shoup, C. Shuldberg, L. Siegel, F. J. Silva, A. N. Simakov, B. T. Sims, D. Sinars, P. Singh, H. Sio, K. Skulina, S. Skupsky, S. Slutz, M. Sluyter, V. A. Smalyuk, D. Smauley, R. M. Smeltser, C. Smith, I. Smith, J. Smith, L. Smith, R. Smith, R. Sohn, S. Sommer, C. Sorce, M. Sorem, J. M. Soures, M. L. Spaeth, B. K. Spears, S. Speas, D. Speck, R. Speck, J. Spears, T. Spinka, P. T. Springer, M. Stadermann, B. Stahl, J. Stahoviak, L. G. Stanton, R. Steele, W. Steele, D. Steinman, R. Stemke, R. Stephens, S. Sterbenz, P. Sterne, D. Stevens, J. Stevers, C. B. Still, C. Stoeckl, W. Stoeffl, J. S. Stolken, C. Stolz, E. Storm, G. Stone, S. Stoupin, E. Stout, I. Stowers, R. Strauser, H. Streckart, J. Streit, D. J. Strozzi,

T. Suratwala, G. Sutcliffe, L. J. Suter, S. B. Sutton, V. Svidzinski, G. Swadling, W. Sweet, A. Szoke, M. Tabak, M. Takagi, A. Tambazidis, V. Tang, M. Taranowski, L. A. Taylor, S. Telford, W. Theobald, M. Thi, A. Thomas, C. A. Thomas, I. Thomas, R. Thomas, I. J. Thompson, A. Thongstisubskul, C. B. Thorsness, G. Tietbohl, R. E. Tipton, M. Tobin, N. Tomlin, R. Tommasini, A. J. Toreja, J. Torres, R. P. J. Town, S. Townsend, J. Trenholme, A. Trivelpiece, C. Trosseille, H. Truax, D. Trummer, S. Trummer, T. Truong, D. Tubbs, E. R. Tubman, T. Tunnell, D. Turnbull, R. E. Turner, M. Ulitsky, R. Upadhye, J. L. Vaher, P. VanArsdall, D. VanBlarcom, M. Vandenboomgaerde, R. VanQuinlan, B. M. Van Wonterghem, W. S. Varnum, A. L. Velikovich, A. Vella, C. P. Verdon, B. Vermillion, S. Vernon, R. Vesey, J. Vickers, R. M. Vignes, M. Visosky, J. Vocke, P. L. Volegov, S. Vonhof, R. Von Rotz, H. X. Vu, M. Vu, D. Wall, J. Wall, R. Wallace, B. Wallin, D. Walmer, C. A. Walsh, C. F. Walters, C. Waltz, A. Wan, A. Wang, Y. Wang, J. S. Wark, B. E. Warner, J. Watson, R. G. Watt, P. Watts, J. Weaver, R. P. Weaver, S. Weaver, C. R. Weber, P. Weber, S. V. Weber, P. Wegner, B. Welday, L. Welser-Sherrill, K. Weiss, K. Widmann, G. F. Wheeler, W. Whistler, R. K. White, H. D. Whitley, P. Whitman, M. E. Wickett, C. Widmayer, J. Wiedwald, R. Wilcox, S. Wilcox, C. Wild, B. H. Wilde, C. H. Wilde, K. Wilhelmsen, M. D. Wilke, H. Wilkens, P. Wilkins, S. C. Wilks, E. A. Williams, G. J. Williams, W. Williams, W. H. Williams, D. C. Wilson, B. Wilson, E. Wilson, R. Wilson, S. Winters, J. Wisoff, M. Wittman, J. Wolfe, A. Wong, K. W. Wong, L. Wong, N. Wong, R. Wood, D. Woodhouse, J. Woodruff, D. T. Woods, S. Woods, B. N. Woodworth, E. Wooten, A. Wootton, K. Work, J. B. Workman, J. Wright, M. Wu, C. Wuest, F. J. Wysocki, H. Xu, M. Yamaguchi, B. Yang, S. T. Yang, J. Yatabe, C. B. Yeamans, B. C. Yee, S. A. Yi, L. Yin, B. Young, C. S. Young, C. V. Young, P. Young, K. Youngblood, R. Zacharias, G. Zagaris, N. Zaitseva, F. Zaka, F. Ze, B. Zeiger, M. Zika, G. B. Zimmerman, T. Zobrist, J. D. Zuegel, and A. B. Zylstra, *Lawson Criterion for Ignition Exceeded in an Inertial Fusion Experiment*, Phys. Rev. Lett. **129**, 075001 (2022).

[85] Archie A. Harms, David R. Kingdon, K. F. Schoepf, and George H. Miley, *Principles of Fusion Energy*, 15–29, World Scientific (2000).

[86] A. K. Schwemmlein, C. Stoeckl, C. J. Forrest, W. T. Shmayda, S. P. Regan, and W. U. Schröder, *First demonstration of a triton beam using target normal sheath acceleration*, Nuclear Instruments and Methods in Physics Research Section B: Beam Interactions with Materials and Atoms **522**, 27–31 (2022).

[87] X. Jiao, J. Shaw, T. Wang, X. Wang, H. Tsai, P. Poth, I. Pomerantz, L. Labun, T. Toncian, M. Downer, and B. Hegelich, *A tabletop, ultrashort pulse photoneutron source driven by electrons from laser wakefield acceleration*, Matter and Radiation at Extremes **2**, 296–302 (2017).

[88] M. Allen, P. K. Patel, A. Mackinnon, D. Price, S. Wilks, and E. Morse, *Direct Experimental Evidence of Back-Surface Ion Acceleration from Laser-Irradiated Gold Foils*, Physical Review Letters **93**, 265004 (2004).

[89] B. Hou, J. A. Nees, Z. He, G. Petrov, J. Davis, J. H. Easter, A. G. R. Thomas, and K. M. Krushelnick, *Laser-ion acceleration through controlled surface contamination*, Physics of Plasmas **18**, 040702 (2011).

[90] A. Maksimchuk, A. Raymond, F. Yu, G. M. Petrov, F. Dollar, L. Willingale, C. Zulick, J. Davis, and K. Krushelnick, *Dominant deuteron acceleration with a high-intensity laser for isotope production and neutron generation*, Applied Physics Letters **102**, 191117 (2013).

[91] J. Davis, G. M. Petrov, T. Petrova, L. Willingale, A. Maksimchuk, and K. Krushelnick, *Neutron production from 7Li(d,xn) nuclear fusion reactions driven by high-intensity laser–target interactions*, Plasma Physics and Controlled Fusion **52**, 045015 (2010).

[92] J. Davis and G. M. Petrov, *Neutron production from ultrashort pulse lasers using linear and circular polarization*, Physics of Plasmas **18**, 073109 (2011).

[93] V. Horný, S. N. Chen, X. Davoine, V. Lelasseux, L. Gremillet, and J. Fuchs, *High-flux neutron generation by laser-accelerated ions from single- and double-layer targets*, Scientific Reports **12**, 19767 (2022).

[94] X. Jiao, C. B. Curry, M. Gauthier, H.-G. J. Chou, F. Fiuza, J. B. Kim, D. D. Phan, E. McCary, E. C. Galtier, G. M. Dyer, B. K. Ofori-Okai, L. Labun, O. Z. Labun, C. Schoenwaelder, R. Roycroft, G. Tiwari, G. D. Glenn, F. Treffert, S. H. Glenzer, and B. M. Hegelich, *High deuteron and neutron yields from the interaction of a petawatt laser with a cryogenic deuterium jet*, Frontiers in Physics **10** (2023).

[95] M. Storm, S. Jiang, D. Wertepny, C. Orban, J. Morrison, C. Willis, E. McCary, P. Belancourt, J. Snyder, E. Chowdhury, W. Bang, E. Gaul, G. Dyer, T. Ditmire, R. R. Freeman, and K. Akli, *Fast neutron production from lithium converters and laser driven protons*, Physics of Plasmas **20**, 053106 (2013).

[96] D. Papp, A. Necas, N. Hafz, T. Tajima, S. Gales, G. Mourou, G. Szabo, and C. Kamperidis, *Laser Wakefield Photoneutron Generation with Few-Cycle High-Repetition-Rate Laser Systems*, Photonics **9**, 826 (2022).

[97] G. Mourou, N. Naumova, E. Power, V. Yanovsky, and J. Nees, *Relativistic optics in the lambda-cubed regime and applications to attosecond physics*, in *CLEO/Europe. 2005 Conference on Lasers and Electro-Optics Europe, 2005.*, 691–691 (2005).

[98] D. Kane and R. Trebino, *Characterization of arbitrary femtosecond pulses using frequency-resolved optical gating*, IEEE Journal of Quantum Electronics **29**, 571–579 (1993).

[99] H. Geiger and W. Müller, *Elektronenzählrohr zur Messung schwächster Aktivitäten*, Naturwissenschaften **16**, 617–618 (1928).

[100] Knoll, Glenn F., *Radiation detection and measurement*, 207–208, 565, Wiley New York (1989), 2nd edition.

[101] D. S. McGregor, W. J. McNeil, S. L. Bellinger, T. C. Unruh, and J. K. Shultis, *Microstructured semiconductor neutron detectors*, Nuclear Instruments and Methods in Physics Research Section A: Accelerators, Spectrometers, Detectors and Associated Equipment **608**, 125–131 (2009).

[102] J. Nattress and I. Jovanovic, *Response and calibration of organic scintillators for gamma-ray spectroscopy up to 15-MeV range*, Nuclear Instruments and Methods in Physics Research Section A: Accelerators, Spectrometers, Detectors and Associated Equipment **871**, 1–7 (2017).

[103] T. Marchi, F. Pino, C. L. Fontana, A. Quaranta, E. Zanazzi, M. Vesco, M. Cinausero, N. Daldosso, V. Paterlini, F. Gramegna, S. Moretto, G. Collazuol, M. Degerlier, D. Fabris, and S. M. Carturan, *Optical properties and pulse shape discrimination in siloxane-based scintillation detectors*, Scientific Reports **9** (2019).

[104] K. M. George, J. T. Morrison, S. Feister, G. K. Ngirmang, J. R. Smith, A. J. Klim, J. Snyder, D. Austin, W. Erbsen, K. D. Frische, and et al., *High-repetition-rate ($\geqslant$ kHz) targets and optics from liquid microjets for high-intensity laser–plasma interactions*, High Power Laser Science and Engineering **7**, e50 (2019).

[105] C. Zulick, F. Dollar, V. Chvykov, J. Davis, G. Kalinchenko, A. Maksimchuk, G. M. Petrov, A. Raymond, A. G. R. Thomas, L. Willingale, V. Yanovsky, and K. Krushelnick, *Energetic neutron beams generated from femtosecond laser plasma interactions*, Applied Physics Letters **102**, 124101 (2013).

[106] R. E. Apfel and S. C. Roy, *Instrument to detect vapor nucleation of superheated drops*, Review of Scientific Instruments **54**, 1397–1400 (1983).

[107] F. d'Errico, *Fundamental Properties of Superheated Drop (Bubble) Detectors*, Radiation Protection Dosimetry **84**, 55–62 (1999).

[108] H. R. Andrews, R. A. Noulty, H. Ing, F. d'Errico, B. J. Lewis, L. G. I. Bennett, and A. R. Green, *LET dependence of bubble detector response to heavy ions*, Radiation Protection Dosimetry **120**, 480–484 (2006).

[109] M. Haines, M. Wei, F. Beg, and R. Stephens, *Hot-Electron Temperature and Laser-Light Absorption in Fast Ignition*, Physical review letters **102**, 045008 (2009).

[110] F. Rigaut, *Astronomical Adaptive Optics*, Publications of the Astronomical Society of the Pacific **127**, 1197 (2015).

[111] G. Vdovin, P. M. Sarro, and S. Middelhoek, *Technology and applications of micromachined adaptive mirrors*, Journal of Micromechanics and Microengineering **9**, R8 (1999).

[112] Z.-H. He, B. Hou, V. Lebailly, J. Nees, K. Krushelnick, and A. Thomas, *Coherent control of plasma dynamics*, Nature Communications **6** (2015).

[113] O. Albert, H. Wang, D. Liu, Z. Chang, and G. Mourou, *Generation of relativistic intensity pulses at a kilohertz repetition rate*, Optics Letters **25**, 1125–1127 (2000).

[114] T. Nayuki, Y. Oishi, T. Fujii, K. Nemoto, T. Kayoiji, Y. Okano, Y. Hironaka, K. G. Nakamura, K.-i. Kondo, and K.-i. Ueda, *Thin tape target driver for laser ion accelerator*, Review of Scientific Instruments **74**, 3293–3296 (2003).

[115] L. Martín, J. Benlliure, D. Cortina, J. J. Llerena, D. González, and C. Ruiz, *Optimization of a fast rotating target to produce kHz X-ray pulses from laser-plasma interaction*, Journal of Physics: Conference Series **1079**, 012008 (2018).

[116] P. L. Poole, C. Willis, G. E. Cochran, R. Hanna, C. D. Andereck, and D. W. Schumacher, *Moderate repetition rate ultra-intense laser targets and optics using variable thickness liquid crystal films*, Applied Physics Letters **109**, 151109 (2016).

[117] K. W. Madison, P. K. Patel, D. Price, A. Edens, M. Allen, T. E. Cowan, J. Zweiback, and T. Ditmire, *Fusion neutron and ion emission from deuterium and deuterated methane cluster plasmas*, Physics of Plasmas **11**, 270–277 (2004).

[118] L. Obst, S. Göde, M. Rehwald, F.-E. Brack, J. Branco, S. Bock, M. Bussmann, T. E. Cowan, C. B. Curry, F. Fiuza, M. Gauthier, R. Gebhardt, U. Helbig, A. Huebl, U. Hübner, A. Irman, L. Kazak, J. B. Kim, T. Kluge, S. Kraft, M. Loeser, J. Metzkes, R. Mishra, C. Rödel, H.-P. Schlenvoigt, M. Siebold, J. Tiggesbäumker, S. Wolter, T. Ziegler, U. Schramm, S. H. Glenzer, and K. Zeil, *Efficient laser-driven proton acceleration from cylindrical and planar cryogenic hydrogen jets*, Scientific Reports **7**, 10248 (2017).

[119] J. Polz, A. P. L. Robinson, A. Kalinin, G. A. Becker, R. A. C. Fraga, M. Hellwing, M. Hornung, S. Keppler, A. Kessler, D. Klöpfel, H. Liebetrau, F. Schorcht, J. Hein, M. Zepf, R. E. Grisenti, and M. C. Kaluza, *Efficient Laser-Driven Proton Acceleration from a Cryogenic Solid Hydrogen Target*, Scientific Reports **9** (2019).

[120] M. Schnürer, D. Hilscher, U. Jahnke, S. Ter-Avetisyan, S. Busch, M. Kalachnikov, H. Stiel, P. V. Nickles, and W. Sandner, *Explosion characteristics of intense femtosecond-laser-driven water droplets*, Phys. Rev. E **70**, 056401 (2004).

[121] T. Kluge, W. Enghardt, S. D. Kraft, U. Schramm, K. Zeil, T. E. Cowan, and M. Bussmann, *Enhanced laser ion acceleration from mass-limited foils*, Physics of Plasmas **17**, 123103 (2010).

[122] J.-U. Park, M. Hardy, S. J. Kang, K. Barton, K. Adair, D. kishore Mukhopadhyay, C. Y. Lee, M. S. Strano, A. G. Alleyne, J. G. Georgiadis, P. M. Ferreira, and J. A. Rogers, *High-resolution electrohydrodynamic jet printing*, Nature Materials **6**, 782–789 (2007).

[123] S. Mishra, K. L. Barton, A. G. Alleyne, P. M. Ferreira, and J. A. Rogers, *High-speed and drop-on-demand printing with a pulsed electrohydrodynamic jet*, Journal of Micromechanics and Microengineering **20**, 095026 (2010).

[124] H. Kim, J. Song, J. Chung, and D. Hong, *Onset condition of pulsating cone-jet mode of electrohydrodynamic jetting for plane, hole, and pin type electrodes*, Journal of Applied Physics **108**, 102804 (2010).

[125] A. Jaworek and A. Sobczyk, *Electrospraying route to nanotechnology: An overview*, Journal of Electrostatics **66**, 197–219 (2008).

[126] S. Lee, J. Song, H. Kim, and J. Chung, *Time resolved imaging of electrohydrodynamic jetting on demand induced by square pulse voltage*, Journal of Aerosol Science **52**, 89–97 (2012).

[127] C.-H. Chen, D. A. Saville, and I. A. Aksay, *Scaling laws for pulsed electrohydrodynamic drop formation*, Applied Physics Letters **89**, 124103 (2006).

[128] S. N. Jayasinghe and M. J. Edirisinghe, *Electric-field driven jetting from dielectric liquids*, Applied Physics Letters **85**, 4243–4245 (2004).

[129] G. I. Taylor, *Disintegration of water drops in an electric field*, Proceedings of the Royal Society of London. Series A. Mathematical and Physical Sciences **280**, 383–397 (1964).

[130] A. L. Yarin, S. Koombhongse, and D. H. Reneker, *Taylor cone and jetting from liquid droplets in electrospinning of nanofibers*, Journal of Applied Physics **90**, 4836–4846 (2001).

[131] F. Paschen, *Ueber die zum Funkenübergang in Luft, Wasserstoff und Kohlensäure bei verschiedenen Drucken erforderliche Potentialdifferenz*, Annalen der Physik **273**, 69–96 (1889).

[132] B. Hou, J. Easter, A. M. K. Krushelnick, and J. A. Nees, *Vacuum-free x-ray source based on ultrashort laser irradiation of solids*, Optics Express **16**, 17695–17705 (2008).

[133] A. Tomanin, J. Paepen, P. Schillebeeckx, R. Wynants, R. Nolte, and A. Lavietes, *Characterization of a cubic EJ-309 liquid scintillator detector*, Nuclear Instruments and Methods in Physics Research Section A: Accelerators, Spectrometers, Detectors and Associated Equipment **756**, 45–54 (2014).

[134] S. A. Pozzi, S. D. Clarke, M. Flaska, and P. Peerani, *Pulse-height distributions of neutron and gamma rays from plutonium-oxide samples*, Nuclear Instruments and Methods in Physics Research Section A: Accelerators, Spectrometers, Detectors and Associated Equipment **608**, 310–315 (2009).

[135] J. F. Nye and M. V. Berry, *Dislocations in Wave Trains*, Proceedings of the Royal Society of London. Series A, Mathematical and Physical Sciences **336**, 165–190 (1974).

[136] L. Allen, M. W. Beijersbergen, R. J. C. Spreeuw, and J. P. Woerdman, *Orbital angular momentum of light and the transformation of Laguerre-Gaussian laser modes*, Phys. Rev. A **45**, 8185–8189 (1992).

[137] K. Sueda, G. Miyaji, N. Miyanaga, and M. Nakatsuka, *Laguerre-Gaussian beam generated with a multilevel spiral phase plate for high intensity laser pulses*, Optics Express **12**, 3548–3553 (2004).

[138] H. Dong, W. P. Wang, Z. X. Lv, C. Jiang, J. Z. He, Y. X. Leng, R. X. Li, and Z. Z. Xu, *Topological structure effects of Laguerre-Gaussian laser on self-collimation acceleration mechanism*, Frontiers in Physics **10** (2022).

[139] L. B. Ju, C. T. Zhou, K. Jiang, T. W. Huang, H. Zhang, T. X. Cai, J. M. Cao, B. Qiao, and S. C. Ruan, *Manipulating the topological structure of ultrarelativistic electron beams using Laguerre–Gaussian laser pulse*, New Journal of Physics **20**, 063004 (2018).

[140] J. Luís Martins, J. Vieira, J. Ferri, and T. Fülöp, *Radiation emission in laser-wakefields driven by structured laser pulses with orbital angular momentum*, Scientific Reports **9**, 9840 (2019).

[141] C. Brabetz, S. Busold, T. Cowan, O. Deppert, D. Jahn, O. Kester, M. Roth, D. Schumacher, and V. Bagnoud, *Laser-driven ion acceleration with hollow laser beams*, Physics of Plasmas **22**, 013105 (2015).

[142] K. H. Pae, H. Song, C.-M. Ryu, C. H. Nam, and C. M. Kim, *Low-divergence relativistic proton jet from a thin solid target driven by an ultra-intense circularly polarized Laguerre–Gaussian laser pulse*, Plasma Physics and Controlled Fusion **62**, 055009 (2020).

[143] W. Wang, C. Jiang, H. Dong, X. Lu, J. Li, R. Xu, Y. Sun, L. Yu, Z. Guo, X. Liang, Y. Leng, R. Li, and Z. Xu, *Hollow Plasma Acceleration Driven by a Relativistic Reflected Hollow Laser*, Physical Review Letters **125**, 034801 (2020).

[144] M. Burger, J. M. Murphy, L. A. Finney, N. Peskosky, J. A. Nees, K. Krushelnick, and I. Jovanovic, *Iterative wavefront optimization of ultrafast laser beams carrying orbital angular momentum*, Optics Express **30**, 26315–26323 (2022).

[145] T. C. Wilson, Z.-M. Sheng, P. McKenna, and B. Hidding, *Self-focusing, compression and collapse of ultrashort weakly-relativistic Laguerre–Gaussian lasers in near-critical plasma*, Journal of Physics Communications **7**, 035002 (2023).

[146] L. Marrucci, C. Manzo, and D. Paparo, *Optical Spin-to-Orbital Angular Momentum Conversion in Inhomogeneous Anisotropic Media*, Physical Review Letters **96**, 163905 (2006).

[147] J. M. Andersen, S. N. Alperin, A. A. Voitiv, W. G. Holtzmann, J. T. Gopinath, and M. E. Siemens, *Characterizing vortex beams from a spatial light modulator with collinear phase-shifting holography*, Applied Optics **58**, 404–409 (2019).

[148] M. T. Gruneisen, W. A. Miller, R. C. Dymale, and A. M. Sweiti, *Holographic generation of complex fields with spatial light modulators: application to quantum key distribution*, Applied Optics **47**, A32–A42 (2008).

[149] S. S. R. Oemrawsingh, J. A. W. van Houwelingen, E. R. Eliel, J. P. Woerdman, E. J. K. Verstegen, J. G. Kloosterboer, and G. W. 't Hooft, *Production and characterization of spiral phase plates for optical wavelengths*, Applied Optics **43**, 688 (2004).

[150] A. Longman, C. Salgado, G. Zeraouli, J. I. Apiñaniz, J. A. Pérez-Hernández, M. K. Eltahlawy, L. Volpe, and R. Fedosejevs, *Off-axis spiral phase mirrors for generating high-intensity optical vortices*, Optics Letters **45**, 2187–2190 (2020).

[151] P. P. Rajeev, S. Banerjee, A. S. Sandhu, R. C. Issac, L. C. Tribedi, and G. R. Kumar, *Role of surface roughness in hard-x-ray emission from femtosecond-laser-produced copper plasmas*, Physical Review A **65**, 052903 (2002).

[152] S. Qiu, Y. Ren, T. Liu, Z. Liu, C. Wang, Y. Ding, Q. Sha, and H. Wu, *Directly observing the skew angle of a Poynting vector in an OAM carrying beam via angular diffraction*, Optics Letters **46**, 3484–3487 (2021).

[153] R. Fonseca, L. O. Silva, F. Tsung, V. K. Decyk, W. Lu, C. Ren, W. Mori, S. Deng, S. Lee, T. Katsouleas, and J. Adam, *OSIRIS: A Three-Dimensional, Fully Relativistic Particle in Cell Code for Modeling Plasma Based Accelerators*, 342–351 (2002).

[154] L. T. Vuong, T. D. Grow, A. Ishaaya, A. L. Gaeta, G. W. 't Hooft, E. R. Eliel, and G. Fibich, *Collapse of Optical Vortices*, Phys. Rev. Lett. **96**, 133901 (2006).

[155] N. Kant and V. Thakur, *Enhanced self-focusing of Laguerre-Gaussian laser beam in relativistic plasma under exponential plasma density transition*, Chinese Journal of Physics **70**, 182–187 (2021).

[156] S. Wilks and W. Kruer, *Absorption of ultrashort, ultra-intense laser light by solids and overdense plasmas*, IEEE Journal of Quantum Electronics **33**, 1954–1968 (1997).

[157] E. J. Valeo and K. G. Estabrook, *Stability of the Critical Surface in Irradiated Plasma*, Phys. Rev. Lett. **34**, 1008–1011 (1975).

[158] M. M. Günther, O. N. Rosmej, P. Tavana, M. Gyrdymov, A. Skobliakov, A. Kantsyrev, S. Zähter, N. G. Borisenko, A. Pukhov, and N. E. Andreev, *Forward-looking insights in laser-generated ultra-intense -ray and neutron sources for nuclear application and science*, Nature Communications **13**, 170 (2022).

[159] Y. Han, Y. Guo, B. Gao, C. Ma, R. Zhang, and H. Zhang, *Generation, optimization, and application of ultrashort femtosecond pulse in mode-locked fiber lasers*, Progress in Quantum Electronics **71**, 100264 (2020).

[160] A. Ruehl, A. Marcinkevicius, M. Fermann, and I. Hartl, *80 W, 120 fs Yb-fiber frequency comb*, Optics letters **35**, 3015–7 (2010).

[161] N. Nishizawa, *Ultrashort pulse fiber lasers and their applications*, Japanese Journal of Applied Physics **53**, 090101 (2014).

[162] Y. Yu, S. Bai, S. Wang, and A. Hu, *Ultra-Short Pulsed Laser Manufacturing and Surface Processing of Microdevices*, Engineering **4**, 779–786 (2018).

[163] G. Račiukaitis, *Ultra-Short Pulse Lasers for Microfabrication: A Review*, IEEE Journal of Selected Topics in Quantum Electronics **27**, 1–12 (2021).

[164] J. Limpert, F. Roeser, T. Schreiber, and A. Tunnermann, *High-power ultrafast fiber laser systems*, Selected Topics in Quantum Electronics, IEEE Journal of **12**, 233–244 (2006).

[165] W. Seka, J. Soures, O. Lewis, J. Bunkenburg, D. Brown, S. Jacobs, G. Mourou, and J. Zimmermann, *High-power phosphate-glass laser system: design and performance characteristics*, Applied Optics **19**, 409–419 (1980).

[166] C. Yamanaka, Y. Kato, Y. Izawa, K. Yoshida, T. Yamanaka, T. Sasaki, M. Nakatsuka, T. Mochizuki, J. Kuroda, and S. Nakai, *Nd-doped phosphate glass laser systems for laser-fusion research*, IEEE Journal of Quantum Electronics **17**, 1639–1649 (1981).

[167] E. Snitzer, H. Po, F. Hakimi, R. Tumminelli, and B. C. McCollum, *Double clad, offset core Nd fiber laser*, in *Optical Fiber Sensors (1988), paper PD5*, PD5, Optica Publishing Group (1988).

[168] J. Limpert, A. Liem, M. Reich, T. Schreiber, S. Nolte, H. Zellmer, A. Tünnermann, J. Broeng, A. Petersson, and C. Jakobsen, *Low-nonlinearity single-transverse-mode ytterbium-doped photonic crystal fiber amplifier*, Optics Express **12**, 1313–1319 (2004).

[169] X. Ma, C. Zhu, I.-N. Hu, A. Kaplan, and A. Galvanauskas, *Single-mode chirally-coupled-core fibers with larger than 50μm diameter cores*, Optics Express **22**, 9206–9219 (2014).

[170] G. Mourou, B. Brocklesby, T. Tajima, and J. Limpert, *The future is fibre accelerators*, Nature Photonics **7**, 258–261 (2013).

[171] M. Kienel, M. Müller, A. Klenke, J. Limpert, and A. Tünnermann, *12 mJ kW-class ultrafast fiber laser system using multidimensional coherent pulse addition*, Optics Letters **41**, 3343–3346 (2016).

[172] H. Stark, J. Buldt, M. Müller, A. Klenke, A. Tünnermann, and J. Limpert, *23 mJ high-power fiber CPA system using electro-optically controlled divided-pulse amplification*, Optics Letters **44**, 5529–5532 (2019).

[173] M. Müller, C. Aleshire, A. Klenke, E. Haddad, F. Légaré, A. Tünnermann, and J. Limpert, *10.4 kW coherently combined ultrafast fiber laser*, Optics Letters **45**, 3083–3086 (2020).

[174] H. Pei, J. Ruppe, S. Chen, M. Sheikhsofla, J. Nees, Y. Yang, R. Wilcox, W. Leemans, and A. Galvanauskas, *10mJ Energy Extraction from Yb-doped 85μm core CCC Fiber using Coherent Pulse Stacking Amplification of fs Pulses*, in *Laser Congress 2017 (ASSL, LAC) (2017), paper AW4A.4*, AW4A.4, Optica Publishing Group (2017).

[175] K.-H. Liao, A. G. Mordovanakis, B. Hou, G. Chang, M. Rever, G. Mourou, J. Nees, and A. Galvanauskas, *Generation of hard X-rays using an ultrafast fiber laser system*, Optics Express **15**, 13942–13948 (2007).

[176] D. Metzner, M. Olbrich, P. Lickschat, A. Horn, and S. Weißmantel, *X-ray generation by laser ablation using MHz to GHz pulse bursts*, Journal of Laser Applications **33**, 032014 (2021).

[177] J. Buldt, M. Mueller, H. Stark, C. Jauregui, and J. Limpert, *Fiber laser-driven gas plasma-based generation of THz radiation with 50-mW average power*, Applied Physics B **126**, 2 (2019).

[178] P. Sidorenko, W. Fu, and F. Wise, *Nonlinear ultrafast fiber amplifiers beyond the gain-narrowing limit*, Optica **6**, 1328–1333 (2019).

[179] M. Whittlesey, *Advanced Techniques for Spectral and Temporal Ultrashort Pulse Synthesis in Coherent Pulse Stacking Amplification*, Ph.D. thesis, University of Michigan, Ann Arbor, MI (2022).

[180] R. V. Volkov, D. M. Golishnikov, V. M. Gordienko, P. M. Mikheev, A. B. Savel'ev, V. D. Sevast'yanov, V. S. Chernysh, and O. V. Chutko, *Neutron generation in dense femtosecond laser plasma of a structured solid target*, Journal of Experimental and Theoretical Physics Letters **72**, 401–404 (2000).

[181] S. Collaboration, B. Aharmim, S. Ahmed, A. Anthony, N. Barros, E. Beier, A. Bellerive, B. Beltran, M. Bergevin, S. Biller, R. Bonventre, K. Boudjemline, M. Boulay, B. Cai, E. Callaghan, J. Caravaca, Y. Chan, D. Chauhan, M. Chen, B. Cleveland, G. Cox, R. Curley, X. Dai, H. Deng, F. Descamps, J. Detwiler, P. Doe, G. Doucas, P.-L. Drouin, M. Dunford, S. Elliott, H. Evans, G. Ewan, J. Farine, H. Fergani, F. Fleurot, R. Ford, J. Formaggio, N. Gagnon, K. Gilje, J. Goon, K. Graham, E. Guillian, S. Habib, R. Hahn, A. Hallin, E. Hallman, P. Harvey, R. Hazama, W. Heintzelman, J. Heise, R. Helmer, A. Hime, C. Howard, M. Huang, P. Jagam, B. Jamieson, N. Jelley, M. Jerkins, C. Kéfélian, K. Keeter, J. Klein, L. Kormos, M. Kos, A. Krüger, C. Kraus, C. Krauss, T. Kutter, C. Kyba, B. Land, R. Lange, J. Law, I. Lawson, K. Lesko, J. Leslie, I. Levine, J. Loach, R. MacLellan, S. Majerus, H. Mak, J. Maneira, R. Martin, A. Mastbaum, N. McCauley, A. McDonald, S. McGee, M. Miller, B. Monreal, J. Monroe, B. Nickel, A. Noble, H. O'Keeffe, N. Oblath, C. Okada, R. Ollerhead, G. Orebi Gann, S. Oser, R. Ott, S. Peeters, A. Poon, G. Prior, S. Reitzner, K. Rielage, B. Robertson, R. Robertson, M. Schwendener, J. Secrest, S. Seibert, O. Simard, D. Sinclair, P. Skensved, T. Sonley, L. Stonehill, G. Tešić, N. Tolich, T. Tsui, R. Van Berg, B. VanDevender, C. Virtue, B. Wall, D. Waller, H. Wan Chan Tseung, D. Wark, J. Wendland, N. West, J. Wilkerson, J. Wilson, T. Winchester, A. Wright, M. Yeh, F. Zhang, and K. Zuber, *Cosmogenic neutron production at the Sudbury Neutrino Observatory*, Physical Review D **100**, 112005 (2019).

[182] C. Bernert, S. Assenbaum, F.-E. Brack, T. E. Cowan, C. B. Curry, M. Garten, L. Gaus, M. Gauthier, S. Göde, I. Goethel, S. H. Glenzer, T. Kluge, S. Kraft, F. Kroll,

M. Kuntzsch, J. Metzkes-Ng, M. Loeser, L. Obst-Huebl, M. Rehwald, H.-P. Schlenvoigt, C. Schoenwaelder, U. Schramm, M. Siebold, F. Treffert, T. Ziegler, and K. Zeil, *Off-harmonic optical probing of high intensity laser plasma expansion dynamics in solid density hydrogen jets*, Scientific Reports **12**, 7287 (2022).

[183] M. B. Schwab, A. Sävert, O. Jäckel, J. Polz, M. Schnell, T. Rinck, L. Veisz, M. Möller, P. Hansinger, G. G. Paulus, and M. C. Kaluza, *Few-cycle optical probe-pulse for investigation of relativistic laser-plasma interactions*, Applied Physics Letters **103**, 191118 (2013).

[184] M. Downer, R. Zgadzaj, A. Debus, U. Schramm, and M. Kaluza, *Diagnostics for plasma-based electron accelerators*, Reviews of Modern Physics **90**, 035002 (2018).

[185] M. Gilljohann, H. Ding, A. Döpp, J. Götzfried, S. Schindler, G. Schilling, S. Corde, A. Debus, T. Heinemann, B. Hidding, S. Hooker, A. Irman, O. Kononenko, T. Kurz, A. Martinez de la Ossa, U. Schramm, and S. Karsch, *Direct Observation of Plasma Waves and Dynamics Induced by Laser-Accelerated Electron Beams*, Physical Review X **9**, 011046 (2019).

[186] P. Sidorenko and F. Wise, *Generation of 1 μJ and 40 fs pulses from a large mode area gain-managed nonlinear amplifier*, Optics Letters **45**, 4084–4087 (2020).